REPORT NO.
UCB/SEMM-2021/03

STRUCTURAL ENGINEERING,
MECHANICS AND MATERIALS

ON THE MODELING OF RESTRAINED TORSIONAL WARPING IN PRISMATIC ELASTIC SHAFTS
(A Full Report)

BY

F. ARMERO

JULY 2021

DEPARTMENT OF CIVIL AND ENVIRONMENTAL ENGINEERING
UNIVERSITY OF CALIFORNIA
BERKELEY, CALIFORNIA

On the Modeling of Restrained Torsional Warping in Prismatic Elastic Shafts (A Full Report)

F. Armero

Department of Civil and Environmental Engineering,

University of California at Berkeley,

Berkeley CA 94720-1710, USA

Abstract

This paper considers the modeling of torsion in elastic shafts accounting for the non–uniform warping of their cross sections. In particular, it studies (1) the original formulation of Timoshenko-Wagner-Kappus-Vlasov, consisting of the underlying Saint–Venant torsion but with a non–constant rate of twist driving the warping, (2) the alternative formulation first proposed by Reissner-Benscoter-Vlasov involving an independent field for the warping amplitude, and (3) a mixed treatment with the axial strain and stress resulting of the restrained warping, extending an early idea of Reissner. In fact, the paper presents a new structural mixed formulation of restrained warping, with its complete numerical evaluation comparing it with those previous formulations and with full three–dimensional solid finite element solutions. To this purpose, the model problem of a prismatic linear elastic shaft is considered, with different cross sections topologies, including solid and thin–walled, the latter for both open and closed (hollow) sections. The whole treatment accounts for general distributions of the material, hence including composite sections, a case also considered in the numerical evaluation. The appropriateness of the newly proposed mixed formulation is concluded.

Keywords: Torsion, Saint–Venant problem, restrained warping, solid and thin–walled composite sections.

Email address: armero@berkeley.edu (F. Armero)

August 5, 2021 version

Table of Contents

1. Introduction

The torsion of shafts and, in a more general sense, of bars, beams, rods or columns is a problem of great practical importance whose understanding goes back to the fundamental work of Saint–Venant in Saint-Venant [1855]. In these early days of modern elasticity theory, Saint–Venant considered a prismatic/cylindrical three–dimensional solid and studied its deformation and state of stress, the so–called Saint–Venant problem, through what is now known as Saint–Venant semi–inverse method. In this way, he identified the warping of the shaft's cross section out of its plane as a main characteristic of the torsion part of the problem for a general geometry of the cross section, extending in this way the early results by Coulomb [1784] on the torsion of thin circular wires, where warping does not occur. We limit our comments and considerations in this paper to isotropic elastic solids in the infinitesimal deformation range.

The resulting problem and its solution is now well–known, covered in all textbooks on (or even just related to) elasticity theory; see e.g. Timoshenko & Goodier [1951], Sokolnikoff [1956], Oden & Ripperger [1981] to cite just a few classical references. The solution consists of the shaft's plane cross sections rotating without distortion in their plane, the twist rotation around the shaft axis, with the section's warping displacement along this axial direction proportional to the rate of this twist rotation along the shaft length. The actual distribution of this warping displacement on the cross section itself is given by the so–called Saint–Venant warping function, an harmonic function on the plane domain defined by the cross section. We refer to this solution simply as Saint–Venant torsion.

This original solution received a great deal of attention leading to a number of refinements and extensions, among which the classical treatment by Prandtl in Prandtl [1903] in terms of the alternative stress function and the well–known membrane analogy must be pointed out. This allowed the easy treatment of important practical cases like thin–walled sections where the effects of torsion are significant in general, as studied in Föppl [1917] for thin–walled sections with open (or simply–connected) topology, and in the classical work of Bredt [1896] for closed (or multiply–connected) hollow sections. In both cases, away from any wall ends, junctions or kinks, the dominant stress component follows the direction of the wall middle line, but the first case of open sections is known to lead in the limit of thin walls (i.e. neglecting second order terms as in Popov [1970]) to a linear distribution of

the shear stress through the thickness (centered so it vanishes along the wall's middle line), whereas closed hollow sections result in a constant distribution instead. We refer to Zbirohowski-Koscia [1967], Gjelsvik [1981] among others for monographs focused on thin–walled beams.

In Saint–Venant torsion, equilibrium considerations require the rate of twist giving the amplitude of the section's warping to remain constant along the shaft length. This situation implies not only that no normal axial stresses appear (so only shear stresses on the cross section are involved), but it also restricts the exactness of this three–dimensional solution to configurations involving such uniform distribution of the warping along the length of the shaft. In particular, no supports restraining the warping of the section can be accounted for. The restrainment of the warping (by the supports, stiffeners or otherwise) creates a non–uniform distribution of this axial displacement of the cross sections along the shaft and, hence, it leads to normal axial strains and stresses, resulting in a different structural response of the shaft. Given the practical interest of these configurations, this clear limitation of pure Saint–Venant torsion, although local to those restraining conditions, motivated the development of extensions of this theory accommodating a non–uniform warping along the shaft, leading to the so–called *torsion with restrained warping* or simply, as it is often called in short, *warping torsion*, notwithstanding that the original Saint–Venant torsion does involve warping, even if just a uniform one; see e.g. Connor [1976], Oden & Ripperger [1981], Pilkey [2002], Salmon et al. [2009] among many references in the field, including professional manuals like Seaburg & Carter [1997].

With this background in mind, the main objective here is to develop a structural model of the shaft (or, more generally, rod or other structural members in torsion) that incorporates the effects of restrained warping. The most important aspect in accomplishing this goal is to develop an appropriate approximation of the warping displacement of the cross sections, crucially identifying its link with the twist rotation of the cross sections along the shaft. In the process, the considered arguments must also identify both the normal and shear strains and stresses involved in the approximation, as well as the resulting properties of the structural member like its flexibility, altogether pointing to the adequacy of the formulation based on the assumed approximation.

Historically, early treatments accommodating restrained warping in torsion were presented by Timoshenko in Timoshenko [1905, 1906, 1910], with a focus on thin–walled sections and, in particular, on the observed bending

of the flanges in these sections when warping is restrained; see the case of an I-beam discussed in Timoshenko & Gere [1961], page 213. These early analyses were later extended and formalized by Wagner [1936] and Kappus [1938], where the main assumption underlying the final formulation was identified as simply assuming a non–constant rate of twist in the Saint–Venant torsion solution, including the use of that same harmonic Saint–Venant warping function over the cross section. These considerations are usually referred to as the *Wagner assumption;* see e.g. Goodier [1942], Gjelsvik [1981]. Hence, and as we explore in detail in this work, the amplitude of the warping is constrained to be the rate of twist of the cross sections along the shaft: a kinematic constraint in our point of view here.

Even if this may not be a correct solution for the three–dimensional elastic problem, it is a valid starting point for an structural model of torsion in shafts, although it may result in anomalies, especially when comparing the resulting state of stress with the full three–dimensional one. Indeed, if stresses are proportional to that rate of twist because it defines the amplitude of the warping displacement, restraining the warping to vanish may lead to both vanishing stresses and its resultants (like the resultant torque), a situation sometimes referred to as the torque anomaly, and discussed in Section 2.2 below. As shown in Section 3.2, the structural formulation of warping torsion considered so far resolves this anomaly, at least partially, by the appearance of additional (warping or, sometimes also called, secondary) shear stresses arising from the Wagner assumption when viewed as a kinematic constraint. With the non–uniform warping, the characteristic normal stresses on the cross sections appear. These warping shear and normal stresses are self–equilibrated, but lead to new stress resultants, the so–called bishear (or warping torque) and bimoment.

Additional important contributions for this treatment of restrained warping were made in Goodier [1942], Kármán & Christensen [1944], Vlasov [1961]. This last monograph has had, in particular, a great influence in the field. Interestingly, Vlasov considered a different starting point when analyzing open thin–walled sections under torsion, namely, the vanishing of the shear strain between the local tangential direction to the wall's middle line (the idealization of the thin–walled section) and the axial direction of the shaft. This assumption/approximation is often referred to as the *Vlasov assumption.* Note that this situation is consistent with the centered linear distribution of the shear stress through the thickness indicated above for open thin–walled sections. This assumption can be seen to lead to the same

kinematics encompassed by the Wagner assumption (see Gjelsvik [1981]), and it leads to an elegant treatment for thin–walled sections, incorporating the consideration of the so–called sectorial coordinate along the section's middle line. This approach gives convenient explicit expressions for thin–wall limit estimates of the different section constants involved in the torsion problem, to the point that it has become an standard treatment in the field. Besides the excellent monograph by Vlasov itself, we refer to Oden & Ripperger [1981], Zbirohowski-Koscia [1967], Gjelsvik [1981] among other volumes considering these developments in detail. Because of all these historic considerations, in this work we refer to this first approximation of torsion with restrained warping as the TWKV formulation for Timoshenko–Wagner–Kappus–Vlasov.

Given the above argument linking the vanishing of the shear strain and stress along the wall middle line with the basic kinematic assumption underlying the TWKV formulation, we can see that this formulation may be well–suited for open thin–walled sections, at least in the thin limit, but not so for closed (hollow) thin–walled sections given their aforementioned different state of stress in basic Saint–Venant torsion and, similarly, for general solid/hollow sections. Still, one may also treat closed thin–walled sections with extensions of the considerations above, involving also the sectorial coordinate along the middle line while accounting for the constant shear flow through the thickness observed in the thin–wall limit for these sections; see e.g. Gjelsvik [1981], and references therein.

Nevertheless, a clear alternative is provided by leaving the parameter controlling the amplitude of the restrained warping as an independent field along the shaft, sometimes in combination with distributions over the cross section itself different that the harmonic Saint–Venant warping function. This more general approximation based on an independent warping field was indeed considered early by Reissner in Reissner [1952] as a general option, by Benscoter in Benscoter [1954] for multicell sections, and again by Vlasov in Vlasov [1961] for general solid and closed sections. Hence, we refer to the resulting formulation as the RBV formulation in this work. The direct link (or constraint) between the amplitude of the warping displacement and the rate of twist along the shaft is then relaxed. This more general treatment of restrained torsional warping makes this formulation also very appealing for the incorporation of torsion in general models of beams and rods. This is especially the case in the geometrically nonlinear range, with a marked interest in accommodating it in computational models, as illustrated by Simo &

Vu-Quoc [1991], Gruttmann et al. [2000] to name just two more recent works.

We refer to both the TWKV and RBV as direct formulations since they involve a single field ("displacement–like") variational functional approximating the restrained warping displacement directly. Alternative approximations are possible. For example, Reissner indicated in that cited early work Reissner [1952] a possible mixed treatment of the problem at hand, considering a mixed variational principle of the generally non–uniform warping displacement and the resulting normal axial stresses. As he actually indicates in the introduction to that paper, this idea was presented as an illustration of his recently developed (at the time) mixed variational principle in elasticity, a principle known now as the Hellinger–Reissner variational principle; see e.g. Washizu [1982] for a full account in the context of other problems in elasticity. He did not elaborate on several details of the resulting formulation for the torsion problem (e.g. specific distributions of the warping, cross section stresses and stress resultants,...) nor did he evaluate it for different shaft configurations. We cannot find any reference to this particular proposal in his later work on the subject (e.g. Reissner [1983] and references therein), nor in any other author's work for that matter.

It is precisely the main goal of the work presented here to explore an alternative mixed treatment of restrained warping in the torsion of shafts and to evaluate it in comparison with the two early approximations described above, namely, the TWKV and RBV formulations. Specifically, we propose new Hu–Washizu type mixed formulations, not relying on the complementary energy of the material model needed in that Hellinger–Reissner treatment; see again Washizu [1982] for general ideas on this type of variational treatment. We consider such approach first in a three–dimensional setting, with a general distribution of the axial displacement in the 3D shaft, allowing us to identify the consequences on the kinematics of the shaft's deformation that a particular mixed (assumed) form of the axial strain and stress has. In this way, we discover an enriched form of the warping displacement itself, allowing a varying form of the section distribution of the warping along the shaft, in contrast with the kinematics encompassed by both the TWKV and RBV formulation, both showing a fixed form of the distribution of the warping displacement over all the sections of the shaft. The insight gained by these considerations allows us to develop a new fully structural mixed formulation of restrained warping, a formulation that shows a better resolution of this phenomenon for all sections topologies, as demonstrated by the numerical

evaluations considered in this work.

In addition, we want to study the constrained character of the original TWKV formulation identified above, and fully characterize how both the RBV and mixed formulations relax the involved constraint. The developments presented here show that the TWKV formulation leads to an over–stiff prediction of the shaft's response, especially for solid and closed (hollow) sections, precisely because of its constrained character. Similarly, our results show that the widely–used RBV formulation leads to a less stiff response of the shaft for general section topologies, relaxing that constraint but, as shown here, by considering incorrect shear stresses over the cross section in the sense that they are not in equilibrium. The newly proposed mixed formulation will be shown to accomplish a much better structural response when compared with full three–dimensional finite element simulations of the solid at hand, while providing correct (equilibrated) section stresses. This improved performance is particularly pronounced for shafts with solid and closed thin–walled sections where the three formulations lead to significant differences. Even for open thin–walled sections, the use of the new mixed formulation is also motivated, as it occurs with the RBV formulation, by the freedom gained with the introduction of additional warping fields, reducing the order of the governing boundary–value problem when compared with the original TWKV formulation and, thus, making this treatment very appealing in those more recent works involving general geometrically nonlinear extensions with their computational implementation, as noted above. Even though this extension is not explored in this paper, a main motivation in considering the new and more general mixed formulation of retrained warping presented here is the adequacy of this type of formulations in the general nonlinear range. We plan to explore that extension in future publications.

An outline of the rest of the paper is as follows. Section 2 introduces the basic problem of a linear elastic prismatic shaft in torsion. More specifically, Section 2.1 includes a complete definition of the physical problem under study, with Section 2.3 presenting the Saint–Venant solution of torsion with uniform warping, after considering the case of general warping and its associated anomalies in Section 2.2. The center of twist, ubiquitous in all the considerations in this work, is discussed in Section 2.4. Section 3 presents the TWKV formulation of restrained warping, identifying the governing equations in Section 3.1, and with Section 3.2 analyzing the role played by the additional stress resultants, the aforementioned bimoment and bishear, over the basic torque of Saint–Venant torsion in defining the warping and total

stresses. Section 4 considers the RBV formulation, developing the governing equations in Section 4.1, with Section 4.2 identifying the limit process leading to the original constrained TWKV formulation. The aforementioned incorrect shear stresses predicted by this formulation are studied in Section 4.3. The newly proposed mixed formulation of restrained warping in torsion is developed in Section 5. After presenting the mixed treatment in Section 5.1 for a general three–dimensional distribution of the warping displacement, we develop in Section 5.2 the newly proposed mixed formulation involving only structural fields along the shaft as fundamental generalized displacements. There we fully characterize the distributions of the torque, bishear and bimoment predicted by the new theory, as well as present complete details of the stresses involved at the cross section level. This allows us to identify in Section 5.3 the limit process by which the original TWKV formulation is recovered as the constrained limit from the proposed mixed formulation.

The evaluation of all these theoretical considerations is undertaken in the context of the model problem of a straight linear elastic shaft with a constant cross section, subjected to an imposed torque/twist rotation at its tip while the section at the opposite end is being kept fixed in both rotation and warping. This model problem is studied in detail Section 6, obtaining closed–form exact solutions for the above three different formulations, all depending of the section constants appropriate for each formulation. We obtain complete expressions of the resulting shaft's flexibility as well as the section stresses, the latter depending on the warping functions associated to the particular cross section under consideration. This setting allows the full numerical evaluation of the different formulations, obtaining those warping functions and the resulting needed section constants via finite element simulations on the cross section. We include specific remarks to this task in Appendix A. This numerical evaluation is presented in Section 7, considering solid (rectangular) cross sections in Section 7.1, open thin–walled (channel) cross sections in Section 7.2, closed thin–walled (box) cross sections in Section 7.3, and multi–cell cross sections in Section 7.4. All the developments in the paper consider linear elastic response for the material but not necessarily homogeneous, with general spatial distributions of the inhomogeneity. This aspect is illustrated in Section 7.5 which includes the analysis of a composite cross section. All these evaluations are carried out comparing the different formulations under study among themselves and with full three–dimensional finite element simulations of the elastic solids. This allows to draw a number of conclusions on the properties and overall adequacy of the three different

formulations of restrained torsional warping under study in Section 8.

Since the consideration of thin–walled sections is of clear practical importance, we provide in Appendix B a complete evaluation of thin–wall estimates for the different torsional constants involved in the considered formulations. This includes new torsional constants involved in the newly proposed mixed formulation not available in the literature. These considerations also allow to identify the orders of magnitude of the different constants as the wall thickness becomes small depending on the type of section involved and, as elaborated in that appendix, the so–called primary and secondary warpings, allowing in turn to understand how the different formulations treat the constraint underlying restrained warping in the original TWKV formulation. The developments presented in this work do not need the final formulas giving these thin–wall limits. Instead, it relies on their exact evaluation by solving numerically the boundary–value problems in the different cross sections, thin or thick, for the warping functions defining those section constants. This approach provides not only a more general and accurate evaluation of the different constants, but the availability of the warping functions themselves, leading to a complete characterization of the stresses, shear and normal, acting on the cross sections of the shaft, as we undertake in detail in what follows.

2. The Saint–Venant problem in torsion

After defining the physical problem of interest in Section 2.1, Section 2.2 develops its mathematical treatment accounting for a general torsional warping of the shaft's cross sections. The Saint–Venant torsion solution with unrestrained warping is summarized then in Section 2.3. A fundamental part of this solution, and further developments in this work, is the rotation of the shaft's cross sections around its axis, a rotation about the center of twist whose characterization is discussed in Section 2.4.

2.1. The physical problem

The fundamental problem considered in this work consists of a straight shaft or, more generally, rod of constant cross section $\Omega \subset \mathbb{R}^2$ and length L subjected to torsional loading; see Figure 1. As depicted in this figure, we consider a Cartesian coordinate system (x, y, z), with the coordinate z along the axis of the shaft and the points $(x, y) \in \Omega$ on a generic cross section Ω. As noted below (see Remark 2.1), we shall not assume the origin of this Cartesian

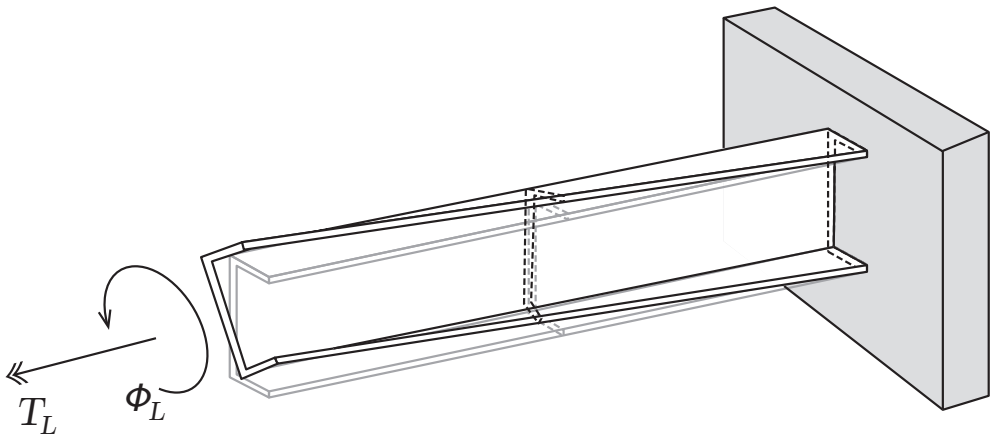

Figure 1: Prismatic shaft subjected to an end torque/rotation at its tip, fixed at its root. The shaft develops a non-uniform twist rotation and warping.

system on the section Ω to have a specific property (e.g. the centroid) nor the axis directions themselves (e.g. principal directions of inertia) given the generality that this choice represents, especially when setting numerical solutions of the problem at hand. We shall assume an isotropic linear elastic response for the material, and the standard infinitesimal assumption of small displacements and strains in all our developments in this paper.

With that coordinate system in mind, we are interested in modeling the shear stresses $\boldsymbol{\tau} = [\tau_{xz}, \tau_{yz}]^T$ and the normal (axial) stress σ_z on the shaft's cross sections created by the assumed torsional loading, the normal stress caused by the non–uniform warping of the sections. For the elastic rod of interest, the material response can be formulated in terms of a stored energy function $\Psi(\varepsilon_z, \boldsymbol{\gamma})$, resulting in

$$\boldsymbol{\tau} = \frac{\partial \Psi}{\partial \boldsymbol{\gamma}} \quad \text{and} \quad \sigma_z = \frac{\partial \Psi}{\partial \varepsilon_z} \,, \tag{1}$$

in terms of the transverse shear strain $\boldsymbol{\gamma} = [\gamma_{xz}, \gamma_{yz}]^T$ and axial strain ε_z, conjugate to $\boldsymbol{\tau}$ and σ_z, respectively. In particular, the standard isotropic linear elastic relations $\sigma_z = E\varepsilon_z$ and $\boldsymbol{\tau} = G\boldsymbol{\gamma}$ correspond to the quadratic energy functions

$$\Psi(\varepsilon_z, \boldsymbol{\gamma}) = \frac{1}{2}\, E\, \varepsilon_z^2 + \frac{1}{2}\, G\, \boldsymbol{\gamma} \cdot \boldsymbol{\gamma} \,, \tag{2}$$

for the shear modulus $G > 0$ and the Young modulus $E > 0$ (under the usual

additional assumption of uniaxial normal stress in the beam/shaft response). An effective elastic modulus E (like the usual plane strain value $E/(1-\nu^2)$ for the Poisson's ratio ν of the material) can be considered alternatively, if preferred; see e.g. Benscoter [1954]. We do not assume constant moduli even on a given cross section, as elaborated below. In equation (2), we have denoted by "$\cdot$" the standard Euclidean scalar product of two vectors and we shall also use below the notation $\|\boldsymbol{\gamma}\|^2 = \boldsymbol{\gamma}\cdot\boldsymbol{\gamma}$ for the associated Euclidean norm of vectors.

To accommodate general composite sections in our developments, we consider moduli distributions of the form

$$E(x,y) = \bar{E}\; n_{_E}(x,y) \qquad \text{and} \qquad G(x,y) = \bar{G}\; n_{_G}(x,y)\;, \tag{3}$$

for reference values $\bar{E}$ and $\bar{G}$, and (non-dimensional) distributions $n_{_E}(x,y)$ and $n_{_G}(x,y)$ on the cross section Ω. The actual choice of the reference values $\bar{E}$ and $\bar{G}$, and so the normalized distributions $n_{_E}(x,y)$ and $n_{_G}(x,y)$, is arbitrary, not affecting the developments to follow.

Finally, and as shown in Figure 1, the shaft is loaded at the end $z = L$ with an applied torque T_L or, equivalently, an applied twist rotation ϕ_L, while that end section is free to warp and, hence, with no axial stress $\sigma_z(x,y,L) = 0$. At the opposite end $z = 0$, its root, the shaft is fixed in the sense that it is not allowed to rotate nor warp, with a reacting torque $T(0)$ appearing to impose the former condition and a normal stress σ_z for the latter. The shaft is also, possibly, loaded by a distributed torque $t_{ex}(z)$ (torque/length) along its length $z \in [0, L]$.

As noted above, we focus our considerations to the effects of the assumed torsional loading on the shaft, namely, twisting and warping of the cross sections. Axial or bending effects must not appear. Hence, the distribution of the normal stress σ_z along the axial direction need to satisfy the relations

$$\int_\Omega \sigma_z \; d\Omega = 0\;, \tag{4}$$

and

$$\int_\Omega x_{_E}\; \sigma_z \; d\Omega = \int_\Omega y_{_E}\; \sigma_z \; d\Omega = 0\;, \tag{5}$$

where $x_{_E} := x - \bar{x}_{_E}$ and $y_{_E} := y - \bar{y}_{_E}$ for the centroid $\bar{\boldsymbol{x}}_{_E} = (\bar{x}_{_E}, \bar{y}_{_E})$ of the Young's modulus distribution $n_{_E}(x,y)$; see Remark 2.1 below. Clearly, the use of this centroid in the relations (5) is not necessary because of the

condition (4), corresponding to a zero resultant force on the cross sections Ω, makes the choice of any other point completely equivalent. Similarly, equations (5) imply the absence of bending moments on the cross sections as well. The satisfaction of the conditions (4) and (5) is automatic at the free end with $\sigma_z = 0$, but these conditions need to be taken into account inside the shaft in the forthcoming developments. A result derived at the end of Section 2.2 below shows that the two conditions (5) will also lead to the vanishing of the resultant shear force on the cross sections Ω due to the torsional shear stresses $\boldsymbol{\tau}$.

Remark 2.1. *For the sake of generality, we consider an independent distribution of the Young and shear moduli over the cross section Ω, and avoid the use of a prescribed centroid as the origin of the coordinate system. Even if this option would simplify some of the expressions below, its identification and use complicates the setting of the problem in the numerical simulations, as presented in Section 7. In general, we have two different centroids, one associated with each distribution. In this way, we have the centroid $\bar{\boldsymbol{x}}_{_E} = (\bar{x}_{_E}, \bar{y}_{_E})$ with coordinates*

$$\bar{x}_{_E} := \frac{1}{A_{n_{_E}}} \int_\Omega x \; n_{_E}(x,y) \; d\Omega \quad \textit{and} \quad \bar{y}_{_E} := \frac{1}{A_{n_{_E}}} \int_\Omega y \; n_{_E}(x,y) \; d\Omega \; , \tag{6}$$

where

$$A_{n_{_E}} := \int_\Omega n_{_E}(x,y) \; d\Omega \; , \tag{7}$$

for the Young modulus distribution $n_{_E}(x,y)$, and $\bar{\boldsymbol{x}}_{_G} = (\bar{x}_{_G}, \bar{y}_{_G})$ with coordinates

$$\bar{x}_{_G} := \frac{1}{A_{n_{_G}}} \int_\Omega x \; n_{_G}(x,y) \; d\Omega \quad \textit{and} \quad \bar{y}_{_G} := \frac{1}{A_{n_{_G}}} \int_\Omega y \; n_{_G}(x,y) \; d\Omega \; , \tag{8}$$

where

$$A_{n_{_G}} := \int_\Omega n_{_G}(x,y) \; d\Omega \; , \tag{9}$$

for the shear modulus distribution $n_{_G}$. We will often use the notation

$$\left\{ \begin{array}{c} x_{_E} := x - \bar{x}_{_E} \\ \\ y_{_E} := y - \bar{y}_{_E} \end{array} \right\} \quad \textit{and} \quad \left\{ \begin{array}{c} x_{_G} := x - \bar{x}_{_G} \\ \\ y_{_G} := y - \bar{y}_{_G} \end{array} \right\} \tag{10}$$

for the shifted coordinates (x, y), when convenient. In the next section, we introduce a third point on the cross section Ω, the center of twist $\bar{\boldsymbol{x}}_{_T} = (\bar{x}_{_T}, \bar{y}_{_T})$ and follow a similar notation $(x_{_T}, y_{_T}) := (x - \bar{x}_{_T}, y - \bar{y}_{_T})$. Finally, we will make use of the moment of inertia

$$\left.\begin{aligned} I_{n_{_E}x} &:= \int_\Omega y_{_E}^2 \; n_{_E}(x,y) \; d\Omega \; , \quad I_{n_{_E}y} := \int_\Omega x_{_E}^2 \; n_{_E}(x,y) \; d\Omega \; , \\ I_{n_{_E}xy} &:= -\int_\Omega x_{_E} \; y_{_E} \; n_{_E}(x,y) \; d\Omega \; , \end{aligned}\right\} \tag{11}$$

since we shall not necessarily consider principal axes of inertia for the coordinate directions, again because of the simplicity that this option implies in the setting of the numerical simulations of interest. □

2.2. Torsion with general warping

Following Saint–Venant's semi–inverse method, we look for a solution of the problem at hand with the assumed three–dimensional displacements

$$\left.\begin{aligned} u_x(x,y,z) &= -\,(y - \bar{y}_{_T}) \;\; \phi(z) \; , \\ u_y(x,y,z) &= \quad (x - \bar{x}_{_T}) \;\; \phi(z) \; , \\ u_z(x,y,z) &= \quad w(x,y,z) \; , \end{aligned}\right\} \tag{12}$$

along each of the Cartesian directions, in terms of two generalized displacements: the twist rotation $\phi(z)$ along the shaft, and the warping displacement $w(x, y, z)$, both for the cross section at $z \in [0, L]$ along the shaft. Physically, the formulas $(12)_{1,2}$ correspond to an infinitesimal rotation of magnitude $\phi(z)$ for the section Ω at $z \in [0, L]$ about the shaft's axis direction at the center of twist $\bar{\boldsymbol{x}}_{_T} := (\bar{x}_{_T}, \bar{y}_{_T})$ (to be identified below), while the section remains rigid with no distortion in its plane. The axial displacement component $(12)_3$ models a general out-of-plane warping of that section along that same shaft's axial direction marked as z in our notation. Restraining the warping at $z = 0$ imposes $w(x, y, 0) = 0$.

The infinitesimal strains associated to the displacement field (12) are

$$\left.\begin{aligned} \gamma_{xz} &= \frac{\partial u_z}{\partial x} + \frac{\partial u_x}{\partial z} = \frac{\partial w}{\partial x} - (y - \bar{y}_{_T}) \;\; \phi'(z) \; , \\ \gamma_{yz} &= \frac{\partial u_z}{\partial y} + \frac{\partial u_y}{\partial z} = \frac{\partial w}{\partial y} + (x - \bar{x}_{_T}) \;\; \phi'(z) \; , \end{aligned}\right\} \tag{13}$$

for the transverse shear strains, and

$$\varepsilon_z = \frac{\partial u_z}{\partial z} = w'(x,y,z) \ , \tag{14}$$

for the axial normal strain, all other components vanishing (this fact corresponding to the assumed no distortion of the section in its plane). Here we have denoted by $(\cdot)' = \partial(\cdot)/\partial z$ (so $\phi' := d\phi/dz$). We further write the shear strains (13) in compact notation as

$$\boldsymbol{\gamma} := \begin{bmatrix} \gamma_{xz} \\ \gamma_{yz} \end{bmatrix} = \nabla w + \phi' \, \mathbb{J} \qquad \text{with} \quad \mathbb{J} := \begin{bmatrix} -y_{_T} \\ x_{_T} \end{bmatrix} := \begin{bmatrix} -(y - \bar{y}_{_T}) \\ (x - \bar{x}_{_T}) \end{bmatrix} \ , \tag{15}$$

for the assumed Cartesian coordinates (x, y) in the section's plane, and the corresponding plane gradient operator $\nabla(\cdot)$.

For the elastic shaft of interest here, the formulation of the boundary value problem is best obtained by considering the potential energy

$$\Pi(\phi, w) := \int_V \Psi \left(\varepsilon_z(w), \boldsymbol{\gamma}(w, \phi) \right) dv + \Pi_{ext}(\phi) \ , \tag{16}$$

for the shaft's volume $V = \Omega \times [0, L]$, and the potential Π_{ext} associated to the external loading, assumed conservative for convenience in the presentation here, but not required in general treatments of the problem under consideration. As usual, what matters is not so much the actual variational functional but the resulting governing equations, like equations (18) below. For the case depicted in Figure 1, we have

$$\Pi_{ext}(\phi) = - \int_0^L t_{ex}(z) \, \phi(z) \, dz - T_L \phi(L) \ , \tag{17}$$

for the distribute torque $t_{ex}(z)$ along the shaft's length and the applied torque T_L at the end $z = L$ otherwise free. If the equivalent loading by an imposed twist rotation ϕ_L at $z = L$ is considered, the last term in (17) is not to be included, imposing $\phi(L) = \phi_L$ with the then reacting torque T_L obtained as a postprocessing, as usual. Details for this alternative are omitted in what follows.

In this way, taking the variations of the potential energy (16) for all admissible variations (i.e. $\delta\phi(0) = 0$ and $\delta w(x, y, 0) = 0$, corresponding to

the assumed kinematic boundary condition at the root), we obtain

$$\left.\begin{aligned} \delta_\phi \Pi &= \int_0^L \underbrace{\left(\int_\Omega \boldsymbol{\tau} \cdot \mathbb{J} \; d\Omega \right)}_{:=T(z)} \delta\phi'(z) \, dz - \int_0^L t_{ex}(z) \delta\phi(z) \, dz - T_L \delta\phi(L) = 0 \; , \\ \delta_w \Pi &= \int_V \left(\boldsymbol{\tau} \cdot \nabla(\delta w) + \sigma_z \delta w' \right) \, dv = 0 \; , \end{aligned} \right\} \tag{18}$$

where we have introduced the internal torque $T(z)$ along the shaft $z \in [0, L]$. The variational equation $(18)_1$ corresponds to the weak form of the balance of moment around the shaft's axis, and it results in the strong form equation

$$\boxed{\frac{dT}{dz}(z) + t_{ex}(z) = 0 \quad \forall z \in [0, L] \; , \quad \text{with} \quad T(L) = T_L \quad \text{at } z = L \; ,} \tag{19}$$

after a standard use of integration by parts. A similar argument reduces equation $(18)_2$ to

$$\begin{aligned} - \int_V \left[\nabla \cdot \boldsymbol{\tau} + \sigma_z' \right] \delta w \; dV + \int_0^L \left(\int_{\partial\Omega} \boldsymbol{\tau} \cdot \boldsymbol{\nu} \; \delta w \; d\Gamma \right) dz \\ + \left[\int_\Omega \sigma_z \; \delta w \; d\Omega \right]_0^L = 0 \; , \end{aligned} \tag{20}$$

for the boundary $\partial\Omega$ of the plane domain Ω defined by the cross section, with (outward) unit normal $\boldsymbol{\nu}$. We obtain then the (strong) equations

$$\nabla \cdot \boldsymbol{\tau} + \sigma_z' = 0 \quad \text{in } \Omega \; , \quad \text{with} \quad \boldsymbol{\tau} \cdot \boldsymbol{\nu} = 0 \quad \text{along } \partial\Omega \; , \tag{21}$$

for all sections in $[0, L]$, together with $\sigma_z = 0$ at the end with free warping

For the linear elastic material model in shear, the shear stresses are give by

$$\boldsymbol{\tau} = G\boldsymbol{\gamma} = G \left[\nabla w + \phi' \; \mathbb{J} \right] \; , \tag{22}$$

so the problem (21) reduces to

$$\boxed{\begin{aligned} &\nabla \cdot \big(G \big(\nabla w + \phi' \mathbb{J} \big) \big) + \sigma_z' = 0 && \text{in } \Omega \; , \\ &\frac{\partial w}{\partial \nu} = -\phi'(z) \; \mathbb{J} \cdot \boldsymbol{\nu} && \text{along } \partial\Omega \; , \end{aligned}} \tag{23}$$

defining the characteristic Neumann type boundary condition on the boundary $\partial\Omega$ of the cross section Ω for the derivative along its normal direction $\partial w/\partial\nu := \nabla w \cdot \boldsymbol{\nu}$. Assuming a constant moduli $\bar{G}$ and $\bar{E}$ for the whole shaft, including over the cross section Ω (i.e. assuming $n_{_G}(x,y) = n_{_E}(x,y) = 1$), the problem (23) reduces to finding the function $w(x,y,z)$

$$\left.\begin{aligned} \Delta w + \frac{\bar{E}}{\bar{G}}\, w'' &= 0 \qquad && \text{in } \Omega\ , \\ \frac{\partial w}{\partial \nu} &= -\phi'(x)\ \mathbb{J}\cdot\boldsymbol{\nu} \qquad && \text{along } \partial\Omega\ , \end{aligned}\right\} \tag{24}$$

for the Laplace operator $\Delta(\cdot) = \nabla\cdot\nabla(\cdot)$ in the (x,y) plane of the section Ω.

Integration of equation (21) over the cross section Ω readily leads to the relation

$$\frac{d}{dz}\left(\int_\Omega \sigma_z\ d\Omega\right) = -\int_\Omega \nabla\cdot\boldsymbol{\tau}\ d\Omega = -\int_{\partial\Omega} \underbrace{\boldsymbol{\tau}\cdot\boldsymbol{\nu}}_{=0}\ d\Gamma = 0 \tag{25}$$

so

$$\int_\Omega \sigma_z\ d\Omega = 0 \quad \forall z\in[0,L]\ , \tag{26}$$

after imposing the boundary condition $\sigma_z = 0$ at the free end $z = L$. Hence, the condition (4), the absence of an axial force in the shaft, is automatically satisfied. In the same way, multiplying equation (21) by $x_{_E}$ and integrating, we obtain

$$\begin{aligned} \frac{d}{dz}\left(\int_\Omega x_{_E}\ \sigma_z\ d\Omega\right) &= -\int_\Omega x_{_E}\ \nabla\cdot\boldsymbol{\tau}\ d\Omega = -\int_\Omega \left[\nabla\cdot(x_{_E}\boldsymbol{\tau}) - \tau_{xz}\right]\ d\Omega \\ &= -\int_{\partial\Omega} x_{_E}\ \underbrace{\boldsymbol{\tau}\cdot\boldsymbol{\nu}}_{=0}\ d\Gamma + \int_\Omega \tau_{xz}\ d\Omega = \int_\Omega \tau_{xz}\ d\Omega\ , \end{aligned} \tag{27}$$

and, similarly, multiplying by $y_{_E}$,

$$\frac{d}{dz}\left(\int_\Omega y_{_E}\ \sigma_z\ d\Omega\right) = \int_\Omega \tau_{yz}\ d\Omega\ , \tag{28}$$

corresponding to the x and y components of the resultant shear force of the shear stresses $\boldsymbol{\tau}$ on the cross sections Ω along the shaft $[0,L]$. Hence, imposing the conditions (5) on the distribution of the normal stress σ_z appearing on the cross sections due to torsional warping, lead to the vanishing of that resultant force as required from physical considerations.

Remark 2.2. *Note that the above arguments, based on the assumed displacements (12), can be rephrased as finding the best approximate solution to the exact elasticity problem with those displacements, best in the sense of minimizing the functional (16). The resulting equations (19) and (21) correspond physically to the balance of moments and forces, respectively, along the axial direction z of the shaft. The problem at hand does not impose the other two partial differential equations of three–dimensional elasticity, which would reduce for the assumed non-zero stress components to $\tau'_{xz} = \tau'_{yz} = 0$. This is a common situation in beam/rod models of structural mechanics and, in our case, can be traced back to the assumption of the cross section being rigid in its plane, an unphysical but a realistic and very useful approximation in typical applications. Similarly, our focus on the torsional response of the shaft, including the warping of the sections, allows us to consider only those equilibrium relations, global equilibrium in the transversal directions being imposed by the integral conditions (5) on all cross sections.* □

Remark 2.3. *The torque anomaly. In fact, the assumed displacements (12) are not an appropriate option in general. We observe that, for a section at z for which $w(x, y, z) = 0$ for all $(x, y) \in \Omega$, the shear stresses (22) reduce to $\boldsymbol{\tau} = G\phi'(z)\mathbb{J}$. Therefore, the boundary condition $(21)_2$ of the boundary–value problem in the cross section plane Ω implies*

$$\boldsymbol{\tau} \cdot \boldsymbol{\nu} = G\ \phi'(z)\ \mathbb{J} \cdot \boldsymbol{\nu} = 0 \quad \textit{along } \partial\Omega \quad \Longrightarrow \quad \phi'(z) = 0\ , \tag{29}$$

for a general section geometry (i.e. non-circular, so $\mathbb{J} \cdot \boldsymbol{\nu} \neq 0$ at some point along $\partial\Omega$), hence implying $\boldsymbol{\tau} = 0$ altogether on the whole cross section. In fact, the boundary condition $w(x, y, 0) = 0$ for the restrained support at $z = 0$ is such a case and, as a consequence, no shear stresses would develop there and hence no torque, something physically unfeasible. This situation was denoted in Burgoyne & Brown *[1994] as the torque anomaly, although the authors proceeded with the consideration of the resulting three–dimensional equation (24) in the analysis of response of different sections to restrained warping, treating it as one more contradiction in the assumed structural approximation of the three–dimensional problem as noted in the previous remark. This anomaly can be traced back again to the inadequacy of the assumed rigid rotation of the cross section on its plane when the warping is restrained. Circular symmetric sections, or unrestrained warping of general sections (general warping but constant along the shaft's axis), do not lead to this anomaly. One of the goals of this paper is to evaluate the avoidance of*

these difficulties by different additional approximations to the three–dimensional displacements (12) in its axial component $w(x, y, z)$. □

2.3. The Saint–Venant solution with unrestrained warping

The free out-of-plane warping of the cross section Ω in the absence of normal axial stress σ_z is referred by as unrestrained warping. With the considerations above, this situation occurs when

$$\varepsilon_z = w'(x, y, z) = 0 \ , \tag{30}$$

in the isotropic case of interest, that is, for a constant warping displacement along the length of the shaft for all $z \in [0, L]$. In this case, equation (21) is satisfied with shear stresses constant in z by considering the case

$$\phi'(z) = \overline{\phi'} = \text{constant} \qquad \forall z \in [0, L] \ , \tag{31}$$

that is, a constant rate of twist along the shaft. The resulting problem was first considered in this form in the classical work by Saint–Venant in Saint-Venant [1855] as discussed in the introduction presented in Section 1.

For the linear elastic case in shear, the warping displacement $w(x, y, z)$ can then be written as

$$w(x, y, z) = \overline{\phi'}\ W_{SV}(x, y) \ , \tag{32}$$

as a simple calculation shows. The new function $W_{SV}(x, y)$ defines the distribution of the warping displacement over the cross section Ω. This function will appear in all our developments below, and we refer to it as the *Saint–Venant warping function*. Noting the presence of the (non-dimensional) twist rotation $\phi(z)$ and its derivative in the axial displacement (32), we observe that, in terms of units, $W_{SV} \sim (\text{length})^2$, that is, area, as it becomes apparent when considering approximations for thin–walled sections in terms of the sectorial coordinate; see Appendix B.

Inserting relation (32) in the governing equation (23), we see that the Saint–Venant warping function $W_{SV}(x, y)$ is a solution of the problem

$$\boxed{\begin{aligned} &\nabla \cdot \big(n_G(x, y)\ \big(\nabla W_{SV} + \mathbb{J}\big)\big) = 0 \quad \text{in } \Omega \ , \\ &\frac{\partial W_{SV}}{\partial \nu} = -\mathbb{J} \cdot \boldsymbol{\nu} \qquad\qquad\qquad\quad \text{along} \quad \partial\Omega \ , \end{aligned}} \tag{33}$$

with the characteristic Neumann boundary condition along the boundary $\partial\Omega$ of the section Ω. The problem (33) reduces to the standard Laplace equation

$$\left.\begin{aligned} \Delta W_{SV} &= 0 \qquad\quad \text{in } \Omega \,, \\ \frac{\partial W_{SV}}{\partial \nu} &= -\mathbb{J}\cdot\boldsymbol{\nu} \quad \text{along} \quad \partial\Omega \,, \end{aligned}\right\} \tag{34}$$

for the case of constant shear modulus G in Ω so $n_{G}(x,y)=1$, making the Saint–Venant warping function $W_{SV}(x,y)$ an harmonic function in this case, as noted in the introduction; see many standard expositions on the subject, like Timoshenko & Goodier [1951], Sokolnikoff [1956], Connor [1976], Oden & Ripperger [1981], Pilkey [2002], among many others.

Continuing with the linear elastic response in shear, with stresses then given by

$$\boldsymbol{\tau} = G\,\overline{\phi'}\,\left(\nabla W_{SV} + \mathbb{J}\right) \,, \tag{35}$$

with $G=\bar{G}\,n_{G}(x,y)$, the torque $T(z)$ in $(18)_1$ reads

$$T(z) = \int_{\Omega} \boldsymbol{\tau}\cdot\mathbb{J}\; d\Omega = \bar{G}J\;\overline{\phi'} \,, \tag{36}$$

for the Saint–Venant torsional constant J of the section Ω defined by

$$\begin{aligned} J &:= \int_{\Omega} n_{G}(x,y)\,[\nabla W_{SV} + \mathbb{J}]\cdot\mathbb{J}\; d\Omega \\ &= \int_{\Omega} n_{G}(x,y)\left[x_{T}^{2} + y_{T}^{2} + x_{T}\frac{\partial W_{SV}}{\partial y} - y_{T}\frac{\partial W_{SV}}{\partial x}\right] d\Omega \,, \end{aligned} \tag{37}$$

for, again, $x_{T}=x-\bar{x}_{T}$ and $y_{T}=y-\bar{y}_{T}$, and a general distribution $n_{G}(x,y)$ of the shear modulus. The constant torque distribution (36) corresponds to the solution of the differential equation (19) for a zero distributed torque $t_{ex}(z)=0$, thus leading to $T(z)=T_{L}$, the torque applied at the shaft's free end, identifying in this semi-inverse approach the Saint–Venant problem in torsion. Expression (37) identifies the well-known Saint–Venant torsional constant J of the cross section Ω defining the stiffness of the shaft in torsion accounting for uniform (unrestrained) warping in terms of the Saint–Venant warping function $W_{SV}(x,y)$; see e.g. Sokolnikoff [1956], Connor [1976], Pilkey [2002], among others, for the case of constant elastic modulus.

Remark 2.4. *We note the orthogonality relation*

$$\int_\Omega n_{_G}\left(\nabla W_{_{SV}}+\mathbb{J}\right)\cdot\nabla W_{_{SV}}d\Omega=\int_{\partial\Omega} n_{_G}\underbrace{\left(\nabla W_{_{SV}}+\mathbb{J}\right)\cdot\boldsymbol{\nu}}_{=0}W_{_{SV}}d\Gamma$$

$$-\int_\Omega\underbrace{\nabla\cdot\left(n_{_G}\left(\nabla W_{_{SV}}+\mathbb{J}\right)\right)}_{=0}W_{_{SV}}d\Omega=0\;, \qquad (38)$$

after the use of the divergence theorem and the governing equations (23) defining the Saint–Venant warping function $W_{_{SV}}(x,y)$. Then, a straightforward calculation shows that

$$J:=\int_\Omega n_{_G}\left(\nabla W_{_{SV}}+\mathbb{J}\right)\cdot\mathbb{J}\;d\Omega=\int_\Omega n_{_G}\|\nabla W_{_{SV}}+\mathbb{J}\|^2\;d\Omega>0\;, \qquad (39)$$

giving an alternative expression for the Saint–Venant torsional constant J, an expression that explicitly shows $J>0$. □

Remark 2.5. *The absence of normal stresses σ_z altogether for this case implies that $\int_\Omega \boldsymbol{\tau}\;d\Omega=0$ exactly here after using the arguments in (27)-(28). Alternatively, those same arguments in combination with the equations (33) defining the Saint–Venant warping function $W_{_{SV}}(x,y)$ shows that*

$$\int_\Omega n_{_G}(x,y)\left(\nabla W_{_{SV}}+\mathbb{J}\right)\;d\Omega=0\;, \qquad (40)$$

in purely mathematical terms for the function $W_{_{SV}}(x,y)$ as defined. We conclude then that

$$\int_\Omega n_{_G}(x,y)\left(\frac{\partial W_{_{SV}}}{\partial x}-y_{_T}\right)d\Omega=0$$

$$\Longrightarrow\quad\int_\Omega n_{_G}(x,y)\frac{\partial W_{_{SV}}}{\partial x}d\Omega=\quad A_{n_{_G}}\;\left(\bar{y}_{_G}-\bar{y}_{_T}\right)\;, \qquad (41)$$

$$\int_\Omega n_{_G}(x,y)\left(\frac{\partial W_{_{SV}}}{\partial y}+x_{_T}\right)d\Omega=0$$

$$\Longrightarrow\quad\int_\Omega n_{_G}(x,y)\frac{\partial W_{_{SV}}}{\partial y}d\Omega=-A_{n_{_G}}\;\left(\bar{x}_{_G}-\bar{x}_{_T}\right)\;, \qquad (42)$$

for the weighted area A_{n_G} of the section Ω in (9) and the centroid $(\bar{x}_G, \bar{y}_G)$ of the shear modulus distribution $n_G(x, y)$ in (8). Equations (41)-(42) also imply, after straightforward calculations, that the Saint–Venant torsional constant J in (37) can be written equivalently as

$$J = \int_\Omega n_G(x,y) \left[x^2 + y^2 + x \frac{\partial W_{SV}}{\partial y} - y \frac{\partial W_{SV}}{\partial x} \right] \, d\Omega$$

$$- A_{n_G} (\bar{x}_T \bar{x}_G + \bar{y}_T \bar{y}_G) \, , \tag{43}$$

recovering the standard expression (the integral in this expression) when the shear modulus centroid is chosen as origin of the coordinate system (i.e. when $\bar{x}_G = \bar{y}_G = 0$); see Sokolnikoff *[1956], page 112. This torsional constant seems to be dependent on the center of twist $\boldsymbol{x}_T$ (explicitly in this equation and, in principle, implicitly through the function $W_{SV}(x, y)$, solution of the boundary-value problem (33) involving this point), but this is not the case as shown next.* □

2.4. The center of twist

The above developments do not identify the center of twist $\bar{\boldsymbol{x}}_T = (\bar{x}_T, \bar{y}_T)$. In fact, such a point is not determined in the Saint–Venant's torsion problem with unrestrained warping; see Sokolnikoff [1956], page 113. In fact, as noted in this reference, different centers of twist lead to solutions differing by a rigid body displacement. Hence, the center of twist in actual realizations of the problem will be determined on how the shaft is supported at its ends; see also Oden & Ripperger [1981] in this respect.

Indeed, if we consider a different center of twist $\bar{\boldsymbol{x}}^*_T = (\bar{x}^*_T, \bar{y}^*_T)$, a straightforward calculation shows that

$$W_{SV}(x,y) = W^*_{SV}(x,y) + (\bar{x}_T - \bar{x}^*_T) \, y_E - (\bar{y}_T - \bar{y}^*_T) \, x_E + C \, , \tag{44}$$

for the solutions $W_{SV}(x, y)$ and $W^*_{SV}(x, y)$ of the linear boundary-value problem (33) with respect to $\bar{\boldsymbol{x}}_T$ and $\bar{\boldsymbol{x}}^*_T$, respectively. In equation (44), we have used the shifted coordinates $(x_E, y_E) = (x - \bar{x}_E, y - \bar{y}_E)$ for later convenience, since the terms involving the centroid $(\bar{x}_E, \bar{y}_E)$ of the Young modulus distribution $n_E(x, y)$ (or any other point for that matter) could have been lumped in the constant C in (44). This additional constant is a consequence of the arbitrariness of an additional constant into these functions given the presence of only their derivatives in the problem (33). This constant and the two

additional linear terms in (44) are nothing else but the additional superposed rigid body displacement noted above.

The stresses arising from both functions coincide

$$\boldsymbol{\tau} = G\overline{\phi'}\,(\nabla W_{SV} + \mathbb{J}) = G\overline{\phi'}\,(\nabla W^*_{SV} + \mathbb{J}^*) \ , \tag{45}$$

and so is the Saint–Venant torsional constant $J = J^*$, as a simple calculation shows using the expression (43) with the relation (44). Note that the constant C and the centroid $(\bar{x}_{_E}, \bar{y}_{_E})$ disappear after taking the derivatives of the function $W_{SV}(x, y)$. Hence, the Saint–Venant torsion solution is independent of the center of twist, even for sections with general distribution of the shear modulus (and independent Young modulus distribution), a fact not often pointed out in the vast literature on the subject.

The arbitrariness of the constant C and the center of twist $\bar{\boldsymbol{x}}_{_T} = (\bar{x}_{_T}, \bar{y}_{_T})$ given by (44) (that is, three arbitrary values total), allows us to impose the three conditions

$$\int_\Omega n_{_E}(x, y)\ W_{SV}(x, y)\ d\Omega = 0 \ , \tag{46}$$

and

$$\int_\Omega x_{_E}\ n_{_E}(x, y)\ W_{SV}(x, y)\ d\Omega = \int_\Omega y_{_E}\ n_{_E}(x, y)\ W_{SV}(x, y)\ d\Omega = 0 \ , \tag{47}$$

on the Saint–Venant warping function $W_{SV}(x, y)$. Indeed, these conditions are satisfied by choosing the constant in (44) as $C = -Q^*/A_{n_{_E}}$, and the center of twist by

$$\left.\begin{aligned} \bar{x}_{_T} &= \bar{x}^*_{_T} - \frac{1}{\Delta}\left[I_{n_{_E}y}\ Q^*_y + I_{n_{_E}xy}\ Q^*_x\right] \ , \\ \bar{y}_{_T} &= \bar{y}^*_{_T} + \frac{1}{\Delta}\left[I_{n_{_E}x}\ Q^*_x + I_{n_{_E}xy}\ Q^*_y\right] \ , \end{aligned}\right\} \tag{48}$$

after having calculated the function $W^*_{SV}(x, y)$ solution of problem (33) for an arbitrary $\bar{\boldsymbol{x}}^*_{_T}$. Here, we have introduced the notation

$$Q^* := \int_\Omega n_{_E}(x, y)\ W^*_{SV}(x, y)\ d\Omega \ , \tag{49}$$

$$Q^*_y := \int_\Omega x_{_E}\ n_{_E}(x, y)\ W^*_{SV}(x, y)\ d\Omega \ , \tag{50}$$

$$Q^*_x := \int_\Omega y_{_E}\ n_{_E}(x, y)\ W^*_{SV}(x, y)\ d\Omega \ , \tag{51}$$

and $\Delta := I_{n_E x} I_{n_E y} - I_{n_E xy}$ for the moment of inertia of the cross section Ω introduced in (11).

Expressions like (48) to impose the conditions (46)-(47) can be found in, e.g., Connor [1976] for the case of an homogeneous section in its principal directions of inertia. In the general case considered in this paper, the (so-far arbitrary) use of the distribution $n_E(x, y)$ for the Young modulus in (46) and (47) is required in the developments to follow for the case of restrained warping. Again, the Saint–Venant torsional problem with unrestrained warping (same warping for all sections) is independent of the choice of the center of twist $\bar{\boldsymbol{x}}_T$, but the specific point identified by the relations (48) will have important consequences in the developments below. To begin with, that point corresponds to the shear center of the cross section Ω as proposed by Trefftz in Trefftz [1935], a fact originally pointed out by Weinstein [1947]; see e.g. Pilkey [2002], page 254, for a detailed discussion (here we have presented it in a general, non–centroidal coordinate system).

3. Direct formulation 1: the Timoshenko–Wagner–Kappus–Vlasov (TWKV) approximation of restrained warping

The general treatment presented in Section 2 leads to the three dimensional partial differential equation (23) for the three-dimensional function $w(x, y, z)$ (or the simpler problem (24) for the case of constant material moduli). The goal in any structural mechanics treatment of the shaft of interest is to reduce the problem to an ordinary differential equation along its length $z \in [0, L]$, while still accounting for its torsional/warping response at the section level $(x, y) \in \Omega$. In fact, this has been accomplished in the Saint –Venant solution presented in Section 2.3 since the warping displacement naturally reduces to $w(x, y, z) = \overline{\phi'}\, W_{SV}(x, y)$, for a constant rate of twist $\overline{\phi'}$ and, hence, only requiring the section function $W_{SV}(x, y)$.

To accomplish this reduction in the general case of non-uniform rate of twist, we explore in this and the next sections two different direct approximations of this warping displacement on a cross section. It is worth studying how the different approximations address the torque anomaly noted in Remark 2.3 for the original general three-dimensional treatment of the warping function. We start with the classical treatment of restrained warping, going back to the initial contributions by Timoshenko in Timoshenko [1905, 1906, 1910].

3.1. The governing equations of the TWKV formulation

The older and more direct approximation for the non-constant warping along the shaft is to consider the axial displacement

$$\boxed{u_z(x,y,z) = \phi'(z)\; W_{SV}(x,y)\;,} \tag{52}$$

that is, the Saint–Venant solution (32) with a general non-constant rate of twist $\phi'(z)$. The form of the distribution of the axial displacement on a given section is assumed fixed, and given by the Saint–Venant warping function $W_{SV}(x,y)$, the solution of the problem (33) (or simply (34) for a constant shear modulus distribution). We choose the particular function $W_{SV}(x,y)$ satisfying the conditions (46) and (47), fixing then the center of twist $\bar{\boldsymbol{x}}_T$ as discussed in Section 2.4. Hence, together with the lateral displacements $(12)_{1,2}$ we have a single degree of freedom field, namely, the twist rotation $\phi(z)$. As noted in the introduction, the resulting formulation was originally considered by Wagner [1936], Kappus [1938] extending early considerations by Timoshenko in Timoshenko [1905, 1906, 1910], and later considered in Vlasov [1961] for thin–walled sections, although starting from an alternative but equivalent assumption for these cross sections; see Section 1 above. The particular form (52) of the warping displacement corresponds to the Wagner assumption indicated in that section, as it can be found referred to in Goodier [1942], Benscoter [1954], Gjelsvik [1981], among others.

The potential energy in this case reads then

$$\Pi_{dir,1}(\phi) = \int_V \Psi\left(\varepsilon_z(\phi), \boldsymbol{\gamma}(\phi)\right) dv + \Pi_{ext}(\phi)\;, \tag{53}$$

where now

$$\varepsilon_z(\phi) = \phi''(z)\; W_{SV}(x,y) \qquad \text{and} \qquad \boldsymbol{\gamma} = \phi'(z)\,(\nabla W_{SV} + \mathbb{J})\;. \tag{54}$$

The potential of the external loading $\Pi_{ext}(\phi)$ is still given by (17). Note that the formulation considered here, given by the warping displacement (52), assumes a fixed distribution of that warping displacement on any given cross section Ω, a distribution given by the Saint–Venant warping function $W_{SV}(x,y)$ simply modulated in amplitude by the derivative of the twist rotation $\phi(z)$, the only generalized displacement in the theory at hand.

Taking the variation of the functional (53) leads to

$$\boxed{\int_0^L \left(T_{SV}(z)\,\delta\phi'(z) + B_W(z)\,\delta\phi''\right)\, dz = \int_0^L t_{ex}(z)\,\delta\phi(z)\,dz + T_L\;\delta\phi(L)\;,} \tag{55}$$

for the *Saint–Venant torque*

$$T_{SV}(z) := \int_\Omega \boldsymbol{\tau}_{SV} \cdot (\nabla W_{SV} + \mathbb{J}) \; d\Omega \; , \tag{56}$$

and the so-called *bimoment*

$$B_W(z) := \int_\Omega \sigma_z(x,y,z)\, W_{SV}(x,y)\, d\Omega \; , \tag{57}$$

following Vlasov [1961]; see Section 3.2 below for an additional discussion of the terminology used here. In equation (56), different than the developments in the previous section, we have denoted by $\boldsymbol{\tau}_{SV} = \partial\Psi/\partial\boldsymbol{\gamma}$ the stresses arising from the strain energy of the material, given in terms of the shear strain $(54)_2$, and the corresponding resultant torque $T_{SV}(z)$, (instead of simply $\boldsymbol{\tau}$ and $T(z)$), since additional shear stresses and torque are identified below in this formulation. Note that the balance of moments about the shaft's axis (balance of torque) (55) involves both the torque $T_{SV}(z)$ and the bimoment $B_W(z)$, through different derivatives of the variation of the twist rotation $\delta\phi(z)$.

For the linear elastic material of interest here, we have

$$\boldsymbol{\tau}_{SV} = G\, \phi'(z)\; (\nabla W_{SV} + \mathbb{J}) \; , \tag{58}$$

and note that

$$\nabla \cdot \boldsymbol{\tau}_{SV} = \bar{G}\; \nabla \cdot (n_{_G}\, (\nabla W_{SV} + \mathbb{J})) = 0 \qquad\qquad \text{in } \Omega \; , \tag{59}$$

$$\boldsymbol{\tau}_{SV} \cdot \boldsymbol{\nu} = G\; (\nabla W_{SV} + \mathbb{J}) \cdot \boldsymbol{\nu} = 0 \qquad\qquad \text{along } \partial\Omega \; , \tag{60}$$

by the equations (33) defining the Saint–Venant warping function $W_{SV}(x,y)$. The relations (59)-(60) indicate that the shear stresses $\boldsymbol{\tau}_{SV}$ are in equilibrium, without additional stresses σ_z. We also have

$$\begin{aligned} T_{SV}(z) &= \int_\Omega \boldsymbol{\tau}_{SV} \cdot (\nabla W_{SV} + \mathbb{J}) \; d\Omega = \int_\Omega \boldsymbol{\tau}_{SV} \cdot \mathbb{J} \; d\Omega \\ &= \bar{G}\; \phi'(z) \; \underbrace{\int_\Omega n_{_G}(x,y) \; (\nabla W_{SV} + \mathbb{J}) \cdot \mathbb{J} \; d\Omega}_{=J} = \bar{G}\; J\; \phi'(z) \; , \end{aligned} \tag{61}$$

the first equality following from the divergence theorem and the equilibrium relations (59)-(60). Hence, both the stresses $\boldsymbol{\tau}_{SV}$ and their resultant torque T_{SV} on a cross section Ω follow the same expressions as for the Saint–Venant solution, even with a general (non-constant) rate of twist $\phi'(z)$. In fact, combining equations (58) and (61) we obtain the alternative formula

$$\boxed{\boldsymbol{\tau}_{SV} = G\,\phi'(z)\;(\nabla W_{SV} + \mathbb{J}) = n_{G}(x,y)\,\frac{T_{SV}(z)\;(\nabla W_{SV} + \mathbb{J})}{J}}\;, \tag{62}$$

showing the relation between these shear stresses $\boldsymbol{\tau}_{SV}$ and its resultant torque T_{SV} more explicitly.

Similarly, from equation (57) combined with the stress $\sigma_z = E\varepsilon_z$ for the axial strain $(54)_1$, we obtain

$$B_{W}(z) = \bar{E}\,I_{W_{SV}}\,\phi''(z)\;, \tag{63}$$

for the bimoment, where we have introduced the parameter

$$I_{W_{SV}} := \int_{\Omega} n_{E}(x,y)\;\Big(W_{SV}(x,y)\Big)^{2}\;d\Omega\;, \tag{64}$$

a new constant of the section Ω. We note that, by definition, $I_{W_{SV}} > 0$ and the "inertia nature" of its expression if $W_{SV}(x,y)$ is understood as a coordinate on the section Ω, the sectorial coordinate for the thin–walled sections. Vlasov in Vlasov [1961] calls this section constant the "sectorial moment of inertia" for thin–walled sections, while the technical literature refers to it as the "warping constant" and it is often denoted by C_W; see e.g. Salmon et al. [2009], Seaburg & Carter [1997], among others.

For the fixed support at $z = 0$ with no rotation $\phi(0) = 0$, the restraining of the warping is easily enforced by imposing in (52) $\phi'(0) = 0$. The corresponding admissible variations in (55) satisfy then $\delta\phi(0) = 0$ and $\delta\phi'(0) = 0$. Integrating by parts twice in (55) results in the strong form of the governing equation

$$\frac{dT}{dz}(z) + t_{ex}(z) = 0 \quad \forall z \in [0,L]\;, \quad \text{with} \quad T(L) = T_{L} \quad \text{at } z = L\;, \tag{65}$$

that is, the same equation as (19) (physically, the balance of moments about the axis of the shaft), but now with the internal (total) torque $T(z)$ given by

$$T(z) := T_{SV}(z) + T_{W}(z) \qquad \text{for} \quad T_{W}(z) = -\frac{d}{dz}B_{W}(z)\;, \tag{66}$$

the so-called *bishear*, often called the *warping torque* too; see Section 3.2 below. In addition, we obtain the natural boundary condition $B_W(L) = 0$ at the end $z = L$ with no restraining of the warping and, similarly, with a reacting bimoment $B_W(0)$ at the shaft's root $z = 0$ where the warping is restrained.

Combining equations (66) with (63), we obtain

$$T(z) = \bar{G}J\phi'(z) - \frac{d}{dz}\Big(\bar{E}I_{W_{SV}}\phi''(z)\Big) = \bar{G}J\phi'(z) - \bar{E}I_{W_{SV}}\phi'''(z) \ , \tag{67}$$

for the linear elastic case of interest, the latter expression assuming $\bar{E}I_{W_{SV}}$ constant in z. The differential equation (65) reads then

$$\boxed{\frac{d}{dz}\left[\bar{G}J\phi'(z) - \frac{d}{dz}\Big(\bar{E}I_{W_{SV}}\phi''(z)\Big)\right] + t_{ex}(z) = 0 \ ,} \tag{68}$$

a fourth-order ordinary differential equation for the twist rotation distribution $\phi(z)$, with the boundary conditions

$$\phi(0) = 0 \ , \qquad \phi'(0) = 0 \ , \tag{69}$$

and

$$\phi''(L) = 0 \ , \qquad T(L) = T_L \ , \tag{70}$$

or, alternatively, $\phi(L) = \phi_L$ instead of the latter condition if the shaft is loaded by an imposed twist rotation ϕ_L at that end. The condition $(70)_1$ is given by the free warping at the tip of the shaft, corresponding to zero normal strain/stress by $(54)_1$ and, consequently, to $B_W(L) = 0$ by (57).

Remark 3.1. *The introduction of the assumed displacements (12) with the axial displacement given by (52) for a fixed spatial distribution on* Ω *(specifically, the Saint–Venant warping function* $W_{SV}(x, y)$ *for the assumed particular formulation) reduces the problem from a problem in three-dimensional elasticity to an structural mechanics theory for the shaft of interest, the latter in terms of the twist rotation field* $\phi(z)$ *in this case. All the arguments in the above developments, and the ones below, involving particular stress distributions and other considerations at the section level* Ω *must be understood as arguments to justify the connection of those two treatments, the approximation in the structural theory. In fact, the structural model can be simply characterized by the potential energy*

$$\Pi^{(TWKV)}(\phi) = \int_0^L \left[\frac{1}{2}\,\bar{G}J\,(\phi')^2 + \frac{1}{2}\,\bar{E}I_{W_{SV}}\,(\phi'')^2\right] dz + \Pi_{ext}(\phi) \ , \tag{71}$$

in terms of the section constants J and $I_{W_{SV}}$ for the linear elastic case considered here. The equality of this functional with the original (three-dimensional) functional (53) follows easily. Similarly, the governing weak equation (55), for the section resultant torques defined by (56) and (57), follows directly from the (one-dimensional) potential energy (71), and so is equation (68). □

Remark 3.2. *The functional (71) also indicates when to expect the effects of restrained warping to be less dominant, the second term in this expression, with the response of the shaft reducing to Saint–Venant torsion, the first term, in the limit. Indeed, factoring $G\,J$ in (71), we can easily see that for long shafts, namely, for*

$$L \gg L_T^{(TWKV)} := \sqrt{\frac{\bar{E} I_{W_{SV}}}{\bar{G} J}\,\alpha^{(TWKV)}} \qquad \textit{with} \quad \alpha^{(TWKV)} := 1\,, \tag{72}$$

the underlying Saint–Venant torsion will dominate in the overall (global) structural response of the shaft. This also indicates that, in general, the effects of restrained warping are local in nature, as measured by the characteristic length $L_T^{(TWKV)}$. However, note that general shafts, even such as (72), may require special practical considerations locally near restrained sections (by supports, stiffeners, or other conditions), hence the motivation behind this work in modeling its effects correctly. In the definition (72), we have introduced the trivial parameter $\alpha^{(TWKV)} = 1$ for later comparisons with other formulations. Similarly, for later use, the governing equation for the case shown in Figure 1 (i.e. prismatic shaft with non–varying section constants, with an imposed torque T_L at its end, and no distributed loading $t_{ex}(z) = 0$) can be reduced to the equation

$$\tilde{\phi'} + \left(\frac{L_T^{(TWKV)}}{L}\right)^2 \tilde{\phi'''} = f_T^{(SV)}\,T_L\,, \qquad \textit{for} \quad f_T^{(SV)} := \frac{L}{\bar{G} J}\,, \tag{73}$$

and the non–dimensional derivatives $(\cdot)\tilde{}' = d(\cdot)/d\tilde{z}$ with $\tilde{z} = z/L$. The limit marked by the condition (72), recovering Saint–Venant torsion, becomes apparent in this expression too, as it is the flexibility of the shaft $f_T^{(SV)}$ given by this basic torsion solution. □

3.2. The bimoment, the bishear, and the associated stresses in the TWKV formulation

As discussed in detail in Zbirohowski-Koscia [1967] or Oden & Ripperger [1981], the bimoment can be understood physically as a couple of

balanced moments acting on the cross section Ω, corresponding to the statically balanced distribution of the normal stress $\sigma_z = E\phi''(z)W_{SV}(x,y)$, that is, with zero resultant force (4) and moments (5)

$$\int_\Omega \sigma_z, d\Omega = \bar{E}\,\phi''(z) \int_\Omega n_{_E}(x,y)\, W_{SV}(x,y)\, d\Omega = 0\ , \tag{74}$$

and similarly

$$\left.\begin{aligned} \int_\Omega x_{_E}\,\sigma_z\, d\Omega = \bar{E}\,\phi''(z) \int_\Omega x_{_E}\, n_{_E}(x,y)\, W_{SV}(x,y)\, d\Omega = 0\ , \\ \int_\Omega y_{_E}\,\sigma_z\, d\Omega = \bar{E}\,\phi''(z) \int_\Omega y_{_E}\, n_{_E}(x,y)\, W_{SV}(x,y), d\Omega = 0\ , \end{aligned}\right\} \tag{75}$$

after using the Saint–Venant warping function $W_{SV}(x,y)$ in the assumed warping displacement (52) normalized with the conditions (46) and (47). We refer also to Epstein & Segev [2019] for a mathematical, more abstract, interpretation of the bimoment and bishear.

The typical illustration of the bimoment $B_{_W}(z)$ is an open thin–walled section, like a I-beam or channel section, warping with a pair of same but opposite moments bending the flanges. Hence the appearance of the associated (same and opposite) shear forces acting transversely on the flanges and creating a torque on the whole section, the bishear $T_{_W}(z)$; see e.g. Oden & Ripperger [1981], page 226, for details, including an illustrating figure for a channel section. In fact, this was how the incorporation of the effects of restrained warping in torsion was accomplished originally; see Timoshenko [1906, 1910]. This is why some authors have traditionally referred to the bishear $T_{_W}(z)$ as the flexural torque, as opposed to the twisting torque $T_{_{SV}}(z)$, given its origin in thin–walled sections; see Vlasov [1961], Zbirohowski-Koscia [1967]. Some other authors call $T_{_W}(z)$ the warping shear (Oden & Ripperger [1981]), the warping torque (Gjelsvik [1981]), or even the Vlasov torque in this last reference too, referring implicitly to restrained warping since the twisting torque $T_{_{SV}}(z)$ also involves (uniform) warping. We shall refer to $T_{_{SV}}(z)$ and $T_{_W}(z)$ as the Saint–Venant torque and the bishear, respectively. Their sum, the total internal torque $T(z)$, is the one satisfying the balance (of moments) equation (65). The term bishear has been used in Simo & Vu-Quoc [1991], motivated by the "transverse shear-type" role that $T_{_W}(z)$ plays for the bimoment $B_{_W}(z)$ in equation $(66)_2$.

The assumed three–dimensional warping displacement (52) does not satisfy equations (23) or (24), so it is indeed an approximation of the problem described in Section 2.2 or, better, an alternative treatment of the torsional problem with restrained warping. It may appear that the torque anomaly described in Remark 2.3 still applies to this approximation since restraining the warping displacement at the support $z = 0$ also implies $\phi'(0) = 0$ and, hence, zero shear strains $\boldsymbol{\gamma}$ by $(54)_2$, zero stresses $\boldsymbol{\tau}_{SV}$ by (58), and zero resulting Saint–Venant torque $T_{SV}(0)$ by (61). In fact, such observation can be found in Reissner [1952], motivating somehow the alternative approximation discussed in the Section 4. However, this torque is only part of the total torque $T(0)$ appearing at that support, balancing by (65) the applied torsional loading on the shaft. In other words, the appearance of the bishear $T_W(z)$ resolves the anomaly (at least partially since, again, the Saint–Venant part of the stress and torque still vanishes).

Still, the above developments do not identify a particular shear stress distribution due to this torque on the cross section Ω, say $\boldsymbol{\tau}_W$, but the illustrative case presented in the previous remark clearly points out to the existence of such stresses associated to the bending caused by the bimoment $B_W(z)$ on parts of the section (e.g the flanges of an I-beam). We can proceed as follows to identify these stresses.

First, we note that the normal stress $\sigma_z = E\varepsilon_z$ on the cross section can be written as

$$\boxed{\sigma_z(x,y,z) = E\,\phi''(z)\,W_{SV}(x,y) = n_{_E}(x,y)\;\frac{B_W(z)\;W_{SV}(x,y)}{I_{W_{SV}}}\;,} \tag{76}$$

after combining equations $(54)_1$ and (63). By equilibrium (i.e by equation (21)), these stresses identify the transverse shear stresses $\boldsymbol{\tau}_W$ as

$$\left.\begin{array}{ll} \nabla\cdot\boldsymbol{\tau}_W + \sigma_z' = 0 & \text{in} \quad \Omega\;, \\ \\ \boldsymbol{\tau}_W\cdot\boldsymbol{\nu} = 0 & \text{along} \quad \partial\Omega\;. \end{array}\right\} \tag{77}$$

By inspection, we can write these stresses as

$$\boxed{\boldsymbol{\tau}_W = n_{_G}(x,y)\;\frac{T_W(z)\;\nabla W_\sigma(x,y)}{I_{W_{SV}}}\;,} \tag{78}$$

for the function $W_\sigma(x,y)$ solution of the boundary-value problem

$$\boxed{\begin{aligned} &\nabla\cdot(n_{_G}(x,y)\ \nabla W_\sigma) = n_{_E}(x,y)\ W_{_{SV}}(x,y) && \text{in } \Omega\ , \\ &\frac{\partial W_\sigma}{\partial \nu} = 0 && \text{along } \partial\Omega\ , \end{aligned}} \tag{79}$$

where the Saint–Venant $W_{_{SV}}(x,y)$ enters this problem as data defining the new function $W_\sigma(x,y)$. The claim that the shear stresses (78) satisfy the equilibrium equations (77) for the normal stress σ_z in (76) follows easily by simply inserting them in those equations after noting that $T_{_W}(z) = -B'_{_W}(z)$ by (66). Note that we need here to assume that indeed the warping constant $I_{_{W_{SV}}}$ does not depend on z as in, e.g., the prismatic shafts of interest here; in this respect, see Remark 5.4 in Section 5.2 below.

Up to an irrelevant constant the function $W_\sigma(x,y)$, the well-posedness of the Neumann problem (79) is assured after noting the compatibility condition

$$\begin{aligned} 0 = \int_\Omega n_{_E}(x,y)\ W_{_{SV}}(x,y)\ d\Omega &= \int_\Omega \nabla\cdot(n_{_G}(x,y)\ \nabla W_\sigma)\ d\Omega \\ &= \int_{\partial\Omega} n_{_G}(x,y)\ \frac{\partial W_\sigma}{\partial\nu}\ d\Gamma = 0\ , \end{aligned} \tag{80}$$

since the condition (46) is imposed on the Saint–Venant warping function $W_{_{SV}}(x,y)$. The function $W_\sigma(x,y)$ plays a crucial role in the developments of Section 5 below, and further details of it we will discussed there (including a motivation for the symbol used for it). We also refer to Remark 5.2 at the end of Section 5.1 for further details on the arbitrary constant in the definition of the warping function $W_\sigma(x,y)$.

The stresses $\boldsymbol{\tau}_{_W}$, often called the warping shear stresses, and their distribution function, have been studied in Gjelsvik [1981], Zbirohowski-Koscia [1967], Pilkey [2002], being called sometimes as the complementary in Vlasov [1961] or secondary in Kármán & Christensen [1944], Vlasov [1961], Oden & Ripperger [1981] shear stresses. Their derivation from purely static (equilibrium) considerations like equation (77) and not from a material constitutive relation with associated strains clearly points their origin to the imposition of a kinematic constraint. This setting will become apparent in the alternative formulation considered in the next section as well as in its generalization to mixed formulations of the problem at hand

later in the paper, a formulation that incorporates additional terms to the warping displacements themselves with associated shear strains.

The resultant torque of the stresses $\boldsymbol{\tau}_W$ in (78) is the bishear T_W. Indeed, noting the result

$$\begin{aligned}
\int_\Omega n_{_G}\ \nabla W_\sigma \cdot \mathbb{J}\ d\Omega &= \int_\Omega \left[\nabla \cdot (n_{_G}\ W_\sigma \mathbb{J}) - W_\sigma\ \nabla n_{_G} \cdot \mathbb{J}\right] d\Omega \quad (\text{since } \nabla \cdot \mathbb{J} = 0) \\
&= \int_{\partial\Omega} n_{_G}\ W_\sigma\ \mathbb{J} \cdot \boldsymbol{\nu}\ d\Gamma - \int_\Omega W_\sigma\ \nabla n_{_G} \cdot \mathbb{J}\ d\Omega \\
&= \int_{\partial\Omega} n_{_G}\ W_\sigma\ \underbrace{(-\nabla W_{_{SV}} \cdot \boldsymbol{\nu})}_{=\mathbb{J}\cdot\nu \ by\ (33)_2}\ d\Gamma - \int_\Omega W_\sigma\ \nabla n_{_G} \cdot \mathbb{J}\ d\Omega \\
&= \int_\Omega \left[-\nabla \cdot (n_{_G}\ W_\sigma\ \nabla W_{_{SV}}\ )\right]\ d\Omega - \int_\Omega W_\sigma\ \nabla n_{_G} \cdot \mathbb{J}\ d\Omega \\
&= -\int_\Omega W_\sigma\ \underbrace{\nabla \cdot (n_{_G}\ (\nabla W_{_{SV}} + \mathbb{J}))}_{=0\ by\ (33)_1}\ d\Omega \\
&\qquad\qquad - \int_\Omega n_{_G}\ \nabla W_\sigma\ \nabla W_{_{SV}}\ d\Omega \\
&= \int_\Omega W_{_{SV}}\ \underbrace{\nabla \cdot (n_{_G}\ \nabla W_\sigma)}_{=n_{_E} W_{_{SV}}\ by\ (79)_1}\ d\Omega - \int_{\partial\Omega} n_{_G} W_{_{SV}} \underbrace{\nabla W_\sigma \cdot \boldsymbol{\nu}}_{=0\ by\ (79)_2}\ d\Gamma \\
&= \int_\Omega n_{_E}\ \left(W_{_{SV}}\right)^2\ d\Omega = I_{W_{_{SV}}}\ , \qquad (81)
\end{aligned}$$

after a repeated use of the divergence theorem, we have

$$\int_\Omega \boldsymbol{\tau}_W \cdot \mathbb{J}\ d\Omega = \frac{T_W(z)}{I_{W_{_{SV}}}}\ \underbrace{\int_\Omega n_{_G}\ \nabla W_\sigma \cdot \mathbb{J}\ d\Omega}_{=I_{W_{_{SV}}}} = T_W(z)\ , \qquad (82)$$

as claimed.

We can then identify the total shear stress acting on the cross section Ω

as

$$\boldsymbol{\tau} = \boldsymbol{\tau}_{SV} + \boldsymbol{\tau}_{W} = n_{G}(x,y)\ \left(\frac{T_{SV}(z)\,(\nabla W_{SV} + \mathbb{J})}{J} + \frac{T_{W}(z)\ \nabla W_{\sigma}}{I_{W_{SV}}} \right)\ , \tag{83}$$

in equilibrium with the normal stress σ_z in (76), that is,

$$\left.\begin{array}{ll} \nabla \cdot \boldsymbol{\tau} + \sigma_{z}' = 0 & \text{in} \quad \Omega\ , \\ \boldsymbol{\tau} \cdot \boldsymbol{\nu} = 0 & \text{along} \quad \partial\Omega\ , \end{array}\right\} \tag{84}$$

and with the resultant torque

$$\int_{\Omega} \boldsymbol{\tau} \cdot \mathbb{J}\ d\Omega = T(z) = T_{SV}(z) + T_{W}(z) = \bar{G}J\phi'(z) - \frac{d}{dz}\Big(\bar{E}I_{W_{SV}}\phi''(z)\Big)\ , \tag{85}$$

for each cross section Ω $z \in [0, L]$.

Furthermore, using the condition $(47)_1$ on the Saint–Venant function $W_{SV}(x,y)$, we have

$$\begin{aligned} 0 &= \int_{\Omega} x_{E} n_{E}(x,y,) W_{SV}(x,y) d\Omega = \int_{\Omega} x_{E} \nabla \cdot (n_{G} \nabla W_{\sigma})\, d\Omega \\ &= \int_{\partial\Omega} x_{E} n_{G}\ \underbrace{\nabla W_{\sigma} \cdot \boldsymbol{\nu}}_{=0} d\Gamma - \int_{\Omega} n_{G} \frac{\partial W_{\sigma}}{\partial x}\ d\Omega = -\int_{\Omega} n_{G} \frac{\partial W_{\sigma}}{\partial x}\ d\Omega\ , \end{aligned} \tag{86}$$

with a similar expression for the $y-$derivative, thus concluding

$$\int_{\Omega} n_{G}(x,y)\ \nabla W_{\sigma}(x,y)\ d\Omega = 0\ . \tag{87}$$

This result, together with the relation (40) for the Saint–Venant part $\boldsymbol{\tau}_{SV}$ of the total stress $\boldsymbol{\tau}$ in (83), directly shows the vanishing of the total resultant tangential force $\int_{\Omega} \boldsymbol{\tau} d\Omega = 0$, also implied by the absence of bending contribution of the normal stresses σ_z as given by (75).

All these arguments indicate that, as noted above, even if the Saint–Venant component part of the stresses $\boldsymbol{\tau}_{SV}$ vanishes at a particular cross section because of the restraining of the warping, forcing the vanishing of the rate of twist too, (e.g. a fully fixed support) the warping stress component $\boldsymbol{\tau}_{W}$ appears if needed from equilibrium considerations. The same arguments apply to their respective resultant torques, the Saint–Venant torque $T_{SV}(z)$ and

bishear $T_W(z)$, with the former vanishing entirely in such a fully fixed cross section so the bishear is only determined by equilibrium considerations. The torque anomaly discussed in Remark 2.3 for the full three–dimensional treatment may be avoided then by the presence of the warping stress component $\boldsymbol{\tau}_W$ and the corresponding bishear $T_W(z)$, but this constrained setting may distort the distribution of this stress resultant and related bimoment $B_W(z)$ along the shaft. It is for this reason that we think of the current TWKV formulation as resolving the original torque anomaly only partially, and refer to the new (constrained) situation characterized by a necessary vanishing of the Saint–Venant component of the shear stress and torque still as the torque anomaly. It has the same origin as in the full three–dimensional setting, namely, the direct control of the warping by the twisting (or rather, its rate), a kinematic constraint underlying the TWKV formulation identified below. As shown in the following sections, the other two formulations considered in this work will avoid the torque anomaly in its entirety by relaxing this constraint.

In this respect, it is worth noting that, in contrast to the original Saint–Venant shear stresses $\boldsymbol{\tau}_{SV}$ produced by the twisting of the shaft (if not fully restrained by the warping) and obtained through the associated shear strains $(54)_2$ by the constitutive relation of the material, the warping stresses $\boldsymbol{\tau}_W$ appear by equilibrium from the distribution of the normal stress σ_z distribution, with no direct use of the constitutive relation of the material. Note that the expression (78) depends at most on the non-dimensional distributions $n_{_E}(x,y)$ and $n_{_G}(x,y)$ of the material moduli. This situation points to the origin of these stresses as coming from a kinematic constraint in the assumed displacements (52), a constraint identified in the following section.

Remark 3.3. *For later use, we also note that*

$$\int_\Omega \boldsymbol{\tau}\cdot\nabla W_{SV}d\Omega = \int_\Omega \boldsymbol{\tau}_W\cdot\nabla W_{SV}d\Omega = \frac{T_W(z)}{I_{W_{SV}}}\underbrace{\int_\Omega n_{_G}\ \nabla W_\sigma\cdot\nabla W_{SV}d\Omega}_{=-I_{W_{SV}}}\,, \tag{88}$$

with $\boldsymbol{\tau}_{SV}=\boldsymbol{\tau}-\boldsymbol{\tau}_W$ dropping after using the orthogonality relation (38). The identification of the last integral in (88) with $\left(-I_{W_{SV}}\right)$ is proven as part of the long developments in (81). Hence, we obtain the relation

$$T_W(z) = -\int_\Omega \boldsymbol{\tau}\cdot\nabla W_{SV}\ d\Omega\,, \tag{89}$$

an alternative expression for the bishear $T_W(z)$. We note the consistency of this relation with the general expression

$$T(z) = \int_\Omega \boldsymbol{\tau} \cdot \mathbb{J}\ d\Omega = \underbrace{\int_\Omega \boldsymbol{\tau} \cdot (\nabla W_{SV} + \mathbb{J})\, d\Omega}_{T_{SV}(z)} + \underbrace{\left(- \int_\Omega \boldsymbol{\tau} \cdot \nabla W_{SV} d\Omega \right)}_{T_W(z)}, \quad (90)$$

employed above for the total torque $T(z)$ as the sum of the Saint–Venant $T_{SV}(z)$ and warping (bishear) $T_W(z)$ torques. □

Remark 3.4. *The conditions (74) and (75) were shown in Section 2.4 to determine a particular center of twist $\bar{\boldsymbol{x}}_T$ for the Saint–Venant torsional problem with unrestrained warping ($\sigma_z = 0$), undefined otherwise and with an irrelevant definition in that problem. The need to impose those conditions, physically balance equations, in the general problem involving restrained warping implies that the center of twist is precisely determined in this problem. This situation effectively decouples the torsional problem considered in this paper with the bending/transverse shear problem of the shaft, not considered here. It is then of no surprise that this particular center of twist, defined by the formulas (48), coincides with the shear center as defined by Trefftz in* Trefftz *[1935], who used this decoupling as the defining condition for the shear center.* □

4. Direct formulation 2: the Reissner-Benscoter-Vlasov (RBV) approximation of restrained warping

As indicated in the previous section, the derivation of the restrained warping part $\boldsymbol{\tau}_W$ of the total shear stresses $\boldsymbol{\tau}$ on a cross section from purely static considerations of equilibrium (not involving any strains nor the material parameters per se) points to the presence of a constraint in the original TWKV formulation. Actually, this suspicion is corroborated by the governing differential equation (68) being of high order (fourth order to be precise), a usual feature of mechanical formulations were a hidden constraint is involved. In fact, the original motivation presented by Timoshenko & Gere [1961], based on the aforementioned bending of the flanges in an I-beam, considers (high-order) Euler-Bernoulli beam theory, with no transverse shear strain along those flanges when bending due to the restrained warping of the cross sections. Revisiting the original assumption in this formulation, namely equation (52) where the warping displacement is assumed proportional to the

rate of twist $\phi'(z)$, identifies the constraint connecting the amplitude of this displacement and the twisting of the shaft.

In a similar way, the equivalent Vlasov assumption considers directly the vanishing of the longitudinal shear strain along the middle line of open thin–walled cross sections. As noted above, this leads directly to the Wagner assumption (52), thus constraining the warping to the rate of twist of the section, besides the approximation of the Saint–Venant warping function with the sectorial coordinate along that middle lime for those cross sections; see the developments in Appendix B.

4.1. The governing equations of the RBV formulation

With this insight, we can see that the motivation behind the alternative starting assumption

$$\boxed{u_z(x,y,z) = \lambda(z)\; W_{SV}(x,y)\;,} \tag{91}$$

for a general function $\lambda(z)$, thus considering a formulation based on two generalized displacements: the warping parameter $\lambda(z)$ and the twist rotation $\phi(z)$. As in the previous section, the distribution of the warping displacements on a cross section Ω is given by the Saint–Venant warping function $W_{SV}(x,y)$, defined by the boundary-value problem (33) on Ω and the additional normalizing conditions (46) and (47), the latter with the proper choice of the center of twist.

For later reference, it is interesting to observe that

$$\lambda(z) = \frac{1}{I_{W_{SV}}} \int_\Omega n_{_E}(x,y)\; W_{SV}(x,y)\; u_z(x,y,z)\; d\Omega\;, \tag{92}$$

after using the definition (64) of the warping constant $I_{W_{SV}}$. Equation (92) identifies the parameter $\lambda(z)$ with a weighted average over the cross section of the warping displacement along the shaft.

The consideration of the independently scaled warping displacement (91) was originally considered by Reissner in Reissner [1952] for a general section (in fact, without elaboration), in Benscoter [1954] for hollow multi–cell sections, and independently by Vlasov in Vlasov [1961] for general solid sections, the latter after considering the original TWKV formulation for open thin–walled sections. We refer to the final formulation as the Reissner–Benscoter–Vlasov, or RBV formulation in short.

Note that the warping of all the sections in the shaft are assumed to be proportional to each other, of the same shape or form, only differing by their amplitude as defined by the unknown function $\lambda(z)$. The use of alternative distributions, still constant along the shaft but based on other functions $W(x,y)$, usually approximations of $W_{SV}(x,y)$, has been considered in Vlasov [1961], Connor [1976].

Given the discussion above, we expect that the hidden constraint in the original TWKV formulation presented in the previous section is

$$\lambda(z) = \phi'(z) \qquad \text{in the constrained limit.} \tag{93}$$

This relation is clearly kinematic in nature, involving two kinematic fields: the warping amplitude $\lambda(z)$ and the rate of twist $\phi'(z)$. Given this, we refer to (93) as the *warping–twist constraint*, by which the twisting controls directly the warping. It is of interest then under what conditions this constraint is physically appropriate, motivating or not the use of this formulation in front of the original TWKV treatment. One clear motivation for considering this alternative treatment of the warping is the avoidance of a higher order problem for the twist rotation $\phi(z)$, as we will see below, at the price of solving for the additional degree of freedom $\lambda(z)$.

The formulation based on the assumed axial displacement (91) can be derived in the same way as presented in the previous sections. We start then with the identification of the associated strains, namely,

$$\varepsilon_z(\lambda) = \lambda'(z)\; W_{SV}(x,y) \qquad \text{and} \qquad \boldsymbol{\gamma}(\phi,\lambda) = \lambda'(z)\; \nabla W_{SV} + \phi'(z)\; \mathbb{J}\;, \tag{94}$$

for the axial normal and transverse shear strains, respectively. The potential energy now reads

$$\Pi_{dir,2}(\phi,\lambda) = \int_V \Psi\left(\varepsilon_z(\lambda), \boldsymbol{\gamma}(\phi,\lambda)\right) dv + \Pi_{ext}(\phi)\;, \tag{95}$$

a two-field formulation in this case. For the representative problem of interest here, the essential boundary conditions on the generalized displacement fields read $\phi(0) = 0$ for the fixed rotation and

$$\lambda(0) = 0 \qquad \text{for the restrained warping,} \tag{96}$$

at the support $z = 0$. The corresponding kinematically admissible variations $\delta\phi(z)$ and $\delta\lambda(z)$ are to satisfy then the same homogeneous boundary conditions. Crucially, restraining the warping by (96) involves the independent

field $\lambda(z)$ rather than the rate of twist $\phi'(0)$ as the TWKV formulation does, with this rate left free in the current RBV formulation.

Taking variations of the functional (95), we obtain

$$\left.\begin{aligned} \delta_\phi \Pi_{dir,2} &= \int_0^L T(z)\ \delta\phi'(z)\ dz - \int_0^L t_{ex}(z)\delta\phi(z)\ dz - \delta\phi(L)\ T_L = 0\ , \\ \delta_\lambda \Pi_{dir,2} &= \int_0^L \Big[B_W(z)\ \delta\lambda'(z) - T_W(z)\ \delta\lambda(z)\Big] dz = 0\ , \end{aligned}\right\} \tag{97}$$

for, again,

$$T(z) = \int_\Omega \boldsymbol{\tau}\cdot\mathbb{J}\ d\Omega\ , \qquad T_W(z) = -\int_\Omega \boldsymbol{\tau}\cdot\nabla W_{SV}\ d\Omega\ , \tag{98}$$

and

$$B_W(z) = \int_\Omega \sigma_z\ W_{SV}\ d\Omega\ , \tag{99}$$

the total internal torque, bishear and bimoment, respectively, with the stresses given now by

$$\boldsymbol{\tau} = G\ \left[\lambda(z)\ \nabla W_{SV} + \phi'(z)\ \mathbb{J}\right]\ , \quad \text{and} \quad \sigma_z = E\ \lambda'(z)\ W_{SV}(x,y)\ , \tag{100}$$

for the linear elastic case of interest. We then have the stresses in terms of the two unknown fields $\phi(z)$ and $\lambda(z)$, and now their *first* derivative only. We have reverted to our original notation $\boldsymbol{\tau} = \partial\Psi/\partial\boldsymbol{\gamma}$ and its resultant torque $T(z)$, since no additional stress and torque appear explicitly in the development of this formulation; see Section 4.2 below for a connection with the developments in the previous section, including the separate shear stresses and torque identified in that case.

The strong form of the governing equations associated with (97) read then

$$\left.\begin{aligned} \frac{dT}{dz}(z) + t_{ex}(z) &= 0\ , \\ \frac{dB_W}{dz}(z) + T_W(z) &= 0\ , \end{aligned}\right\} \tag{101}$$

for all $z \in [0, L]$, with the corresponding natural boundary conditions $T(L) = T_L$ and $B_W(L) = 0$ for the problem of interest here. As we would expect, the

same equilibrium equations as in the previous formulation apply, noting the role of $T(z)$ in (98) as the total internal torque.

To write the governing equations (101) in terms of the generalized displacements, it proves convenient to introduce the section constant

$$I_{\nabla W_{SV}} := \int_\Omega n_{_G}(x,y)\ \|\nabla W_{SV}\|^2 d\Omega > 0\ , \tag{102}$$

which we can also write as

$$I_{\nabla W_{SV}} = -\int_\Omega n_{_G}(x,y)\ \nabla W_{SV}\cdot \mathbb{J}\ d\Omega\ , \tag{103}$$

an equality easily obtained by following the same arguments as the few first lines of the calculations in (81) (with W_{SV} instead of W_σ).

With this notation at hand, inserting the stresses (100) in the relations (98), we obtain

$$B_{_W}(z) = \bar{E}\, I_{W_{SV}}\, \lambda'(z)\ , \tag{104}$$

for the bimoment $B_{_W}(z)$, and

$$\left.\begin{aligned} T(z) &= \bar{G}\, J\, \phi'(z) + \bar{G}\, I_{\nabla W_{SV}}\, \varpi(z)\ , \\ T_{_W}(z) &= \bar{G}\, I_{\nabla W_{SV}}\, \varpi(z)\ , \end{aligned}\right\} \tag{105}$$

for the total torque $T(z)$ and the bishear $T_{_W}(z)$, where we have introduced the notation

$$\varpi(z) := \phi'(z) - \lambda(z)\ , \tag{106}$$

a quantity that we refer to as the "warping lag". Clearly, $\varpi(z)$ measures the extent that the warping–twist constraint (93) is not satisfied. We note the direct relation of this "generalized strain" with the bishear $T_{_W}(z)$ through the new torsional constant $I_{\nabla W_{SV}}$ in $(105)_2$.

Inserting the relations (104)-(105) into the equations (101), we obtain the system of ordinary differential equations

$$\boxed{\left.\begin{aligned} \frac{d}{dz}\left[\bar{G}J\left(\phi'(z) + \frac{I_{\nabla W_{SV}}}{J}\big(\phi'(z)-\lambda(z)\big)\right)\right] + t_{ex}(z) = 0\ , \\ \frac{d}{dz}\left[\bar{E} I_{W_{SV}} \lambda'(z)\right] + \bar{G} I_{\nabla W_{SV}}\big(\phi'(z)-\lambda(z)\big) = 0\ , \end{aligned}\right\}} \tag{107}$$

a second order system in terms of the original functions $\phi(z)$ and $\lambda(z)$. The weak equations (97) in combination with the constitutive relations (104)-(105) are to be favored for a general numerical treatment of the problem at hand, especially for varying section parameters J, $I_{W_{SV}}$ and $I_{\nabla W_{SV}}$ along the shaft's length if such extension is considered.

As opposed to the fourth-order differential equation (68) in terms of the twist rotation $\phi(z)$ alone governing the original TWKV formulation presented in Section 3, the current formulation results in the second-order problem (107), but with the added field $\lambda(z)$. We investigate next the connection of the two formulations.

4.2. The TWKV formulation as the constrained limit of the RBV formulation.

The structural formulation considered in this section is characterized by the potential energy (95) reduced to the (one-dimensional) axis to the shaft. In fact, the orthogonality of the two components of the shear strain (94), namely,

$$\boldsymbol{\gamma} = \underbrace{\phi'(z)\ (\nabla W_{SV} + \mathbb{J})}_{\boldsymbol{\gamma}_{SV}} \underbrace{- \varpi\, \nabla W_{SV}}_{\boldsymbol{\gamma}_{W}} , \tag{108}$$

given by relation (38), allows to write (95) as

$$\Pi^{(RBV)}(\lambda, \phi) = \int_0^L \left[\frac{1}{2} \bar{G} J \big(\phi'\big)^2 + \frac{1}{2} \bar{G} I_{\nabla W_{SV}} \big(\underbrace{\phi' - \lambda}_{\varpi} \big)^2 \right.$$

$$\left. + \frac{1}{2} \bar{E} I_{W_{SV}} \big(\lambda'\big)^2 \right] dz + \Pi_{ext}(\phi) , \tag{109}$$

as a straightforward calculation shows. The weak equations (97), with the constitutive relations (98) and (99) for the different resultant torques, are easily obtained by considering the variations of the functional (109).

Comparing this functional with the potential energy (71) for the original TWKV formulation, based on the assumed axial displacement (52), we clearly see that the current formulation corresponds to a penalty treatment of the warping–twist constraint $\varpi(z) = \lambda(z) - \phi'(z) = 0$ characteristic of that original formulation. In particular, factoring $\bar{G}J$ in (109), we readily

identify the (penalty) parameter

$$\kappa_t^{(RBV)} := \frac{I_{\nabla W_{SV}}}{J} \ , \tag{110}$$

recovering the original formulation when $\kappa_t^{(RBV)} \to \infty$.

The parameter $\kappa_t^{(RBV)}$ is clearly a property of the geometry of the cross section. Note that dimensionally

$$J \sim (length)^4 \quad \text{and} \quad I_{\nabla W_{SV}} \sim (length)^4 \ , \tag{111}$$

for a characteristic length of the cross section (say its height h), as a simple inspection of the definitions of these constants show. As illustrated in the numerical evaluations presented in Section 7, the limit $\kappa_t^{(RBV)} \to \infty$ is approached for typical open thin–walled sections in the limit $t/h = thickness/section\ height \to 0$ (motivating the symbol used for $\kappa_t^{(RBV)}$). Thus the TWKV is recovered for these sections in that limit, regardless of the length of the shaft. Interestingly this will not be the case for closed (hollow) thin–walled section, where $t/h \to 0$ will not lead to $\kappa_t^{(RBV)} \to \infty$.

We also observe that, as occurred for the TWKV formulation, the total torque $(98)_1$ for this RBV formulation can also be written as

$$T(z) = T_{SV}(z) + T_W(z) \ , \quad \text{for} \quad T_{SV}(z) = \bar{G}\, J\, \phi'(z), \tag{112}$$

that is, following the same relation with the rate of twist $\phi'(z)$ as in that formulation, but with the bishear $T_W(z)$ given now by $(98)_1$. Remember that the bishear had no constitutive relation in the TWKV formulation, being defined entirely by equilibrium considerations, as shown in Section 3.2. On the other hand, the bishear in the current formulation is given by the constitute relation (105), with

$$T_W = \bar{G} I_{\nabla W_{SV}} \varpi \to \text{finite value} \ , \tag{113}$$

as $\varpi \to 0$ for $I_{\nabla W_{SV}} \to \infty$ for the limit case $\kappa_t^{(RBV)} \to \infty$. Note that the section constant $I_{\nabla W_{SV}}$ never appeared in the original TWKV formulation. The classical role of the bishear $T_W(z)$ as the Lagrange multiplier enforcing the warping–twist constraint $\varpi(z) = 0$ in that original formulation becomes clear.

Remark 4.1. *As occurred with the TWKV formulation and given the locality of the effects of restrained warping observed in Remark 3.2, the current RBV formulation also predicts that the response of long shafts will be dominated by Saint–Venant torsion at the global level and, in this way, also recover the TWKV formulation in that limit. To quantify this limiting process, we consider again the case of a prismatic shaft with a single applied torque T_L considered in that remark, that is, the shaft depicted in Figure 1. This allows to reduce the governing system of equations (107) to a single (high order) equation, exactly like (73) but with the characteristic length L_T given now by*

$$L_T^{(RBV)} := \sqrt{\frac{\bar{E}I_{W_{SV}}}{\bar{G}J}\,\alpha^{(RBV)}}\,, \qquad \text{for} \quad \alpha^{(RBV)} := 1 + \frac{J}{I_{W_{SV}}} = 1 + \frac{1}{\kappa_t^{(RBV)}} \quad \left(> 1 = \alpha^{(TWKV)} \right), \tag{114}$$

after eliminating the field $\lambda(z)$ with some straightforward algebraic manipulations in this particular model problem; further details are omitted. Hence, long shafts in the sense of being dominated at the global structural level by Saint–Venant torsion (i.e., with flexibility close to the value $f_T^{(SV)}$ in (73)) correspond to $L \gg L_T^{(RBV)}$. The result (114) agrees with our previous considerations in this section, namely, that the TWKV formulation is recovered from the RBV formulation in the limit $\kappa_t^{(RBV)} \to \infty$ and, in fact, tells us that

$$L_T^{(TWKV)} < L_T^{(RBV)}\,, \tag{115}$$

for real shafts not in that limit. Interestingly, this inequality is also controlled by the same parameter $\kappa_t^{(RBV)}$ by (114), characterizing the two different limit processes that recover the TWKV formulation form the RBV formulation. In the process involving long shafts as marked by these characteristic lengths (or, more trivially, a negligible warping constant in (114)), both formulations recover effectively Saint–Venant torsion, involving no bishear nor any bimoment. As illustrated in the numerical evaluations presented in Section 7 below, the approach behind the RBV formulation in recovering the Saint–Venant torsion for long shafts will prove to be more effective. This is largely because, as noted in Section 3.2 above, the original TWKV formulation can only rely on the bishear $T_W(0)$ at supports restraining the warping ($z = 0$ here) since the Saint–Venant torque vanishes entirely there ($T_{SV}(0) = 0$). This is not the case for the current RBV formulation. □

4.3. The stresses in the RBV formulation.

The developments of the previous section show the clear connection of the TWKV and RBV formulations at the structural level. However, the two formulations differ significantly at the section level as it refers to the stresses involved in their development.

The normal stresses σ_z over the cross sections for the RBV formulation are obtained by combining equations $(94)_1$ and (104) as

$$\boxed{\sigma_z(x,y,z) = E\,\lambda'(z)\,W_{SV}(x,y) = n_{_E}(x,y)\,\frac{B_W(z)\;W_{SV}(x,y)}{I_{W_{SV}}}}\;, \tag{116}$$

thus recovering the same relation (76) for the TWKV formulation when written in terms of the bimoment $B_W(z)$. Note, though, that each formulation will produce, in general, different diagrams of the bimoment $B_W(z)$, and the different parts of the torque (the bishear $T_W(z)$, in particular), along the shaft in a given problem.

Even then, the distribution of the shear stresses over a cross section predicted by the RBV formulation differs considerably to the one given by the TWKV formulation, and the mixed formulation developed in the next section. The decomposition (112) for the total torque in the RBV formulation does translate in a similar decomposition for the total stresses (100), that is,

$$\boldsymbol{\tau} = G\,(\lambda\nabla W_{SV} + \phi'\mathbb{J}) = \underbrace{G\phi'(z)\,(\nabla W_{SV} + \mathbb{J})}_{=:\boldsymbol{\tau}_{SV}}\;\underbrace{-\;G\,\varpi(z)\nabla W_{SV}}_{=:\boldsymbol{\tau}_W}\;, \tag{117}$$

in terms of the warping lag $\varpi(z)$. The calculations behind the relations (105) identify the resultant torque of these two stresses as $T_{SV}(z)$ and $T_W(z)$, respectively. In this respect, note that

$$T_W(z) = -\int_\Omega \boldsymbol{\tau}\cdot\nabla W_{SV}d\Omega = \int_\Omega \boldsymbol{\tau}_W\cdot\mathbb{J}\;d\Omega\;, \tag{118}$$

as a straightforward calculation shows. An alternative expression of the shear stresses (117) is then given by

$$\boldsymbol{\tau}_{SV} = G\,\phi'(z)\;(\nabla W_{SV} + \mathbb{J}) = n_{_G}(x,y)\,\frac{T_{SV}(z)\,(\nabla W_{SV} + \mathbb{J})\,(x,y)}{J}\;, \tag{119}$$

for the Saint–Venant component, as equation (62) for the TWKV formulation, and

$$\boxed{\boldsymbol{\tau}_{W} = -G\left(\phi'(z) - \lambda(z)\right)\nabla W_{SV}(x,y) = -n_{G}(x,y)\,\frac{T_{W}(z)\nabla W_{SV}(x,y)}{I_{\nabla W_{SV}}}}\,, \tag{120}$$

after using the definition of each part of the torque in equation (105).

These stresses do resemble the stresses (83) for the TWKV formulation, but with a clear difference for the warping stress $\boldsymbol{\tau}_{W}$. The distribution of this stress on a typical section is given now by $\nabla W_{SV}/I_{\nabla W_{SV}}$ while it is given by $\nabla W_{\sigma}/I_{W_{SV}}$ for the original TWKV formulation.

The main consequence of this result is that, in general, the stresses in the RBV formulation will not be in equilibrium, that is, they will not satisfy the relations (84), as they did in the TWKV formulation. A simple calculation shows that

$$\left.\begin{aligned} &\nabla\cdot\boldsymbol{\tau} + \sigma'_{z} = -T_{W}(z)\;\nabla\cdot\left[n_{G}\left(\frac{\nabla W_{SV}}{I_{\nabla W_{SV}}} + \frac{\nabla W_{\sigma}}{I_{W_{SV}}}\right)\right] && \text{in}\quad \Omega\,,\\ &\boldsymbol{\tau}\cdot\boldsymbol{\nu} = -n_{G}(x,y)\;T_{W}(z)\frac{\mathbb{J}\cdot\boldsymbol{\nu}}{I_{\nabla W_{SV}}} && \text{along}\quad \partial\Omega\,, \end{aligned}\right\} \tag{121}$$

which will not vanish in the RBV formulation unless $T_{W}(z) = 0$, that is, $\varpi(z) = 0$. Defining the difference appearing in (121) by

$$\boldsymbol{\tau}_{W}^{noeq} := -n_{G}(x,y)\;T_{w}(z)\;\left(\frac{\nabla W_{SV}}{I_{\nabla W_{SV}}} + \frac{\nabla W_{\sigma}}{I_{W_{SV}}}\right) \qquad \text{in}\quad \Omega\,, \tag{122}$$

and noting that $\boldsymbol{\tau}_{W}^{noeq}\cdot\boldsymbol{\nu}$ along $\partial\Omega$ is given by $(121)_{2}$, a straightforward calculation shows that

$$\int_{\Omega}\boldsymbol{\tau}_{W}^{noeq}\cdot\mathbb{J}d\Omega = -T_{W}(z)\left[\frac{1}{I_{\nabla W_{SV}}}\underbrace{\int_{\Omega} n_{G}\nabla W_{SV}\cdot\mathbb{J}d\Omega}_{=-I_{\nabla W_{SV}}\text{ by (103)}}\right.$$

$$\left. + \frac{1}{I_{W_{SV}}}\underbrace{\int_{\Omega} n_{G}\nabla W_{\sigma}\cdot\mathbb{J}d\Omega}_{=I_{W_{SV}}\text{ by (81)}}\right] = 0\,, \tag{123}$$

that is, having a zero resultant torque. However, after using the relations (40) and (87), we have

$$\int_\Omega \boldsymbol{\tau}_{W}^{noeq} d\Omega = -\frac{T_{W}(z)}{I_{\nabla W_{SV}}} \int_\Omega n_{G} \nabla W_{SV} d\Omega = \frac{T_{W}(z)}{I_{\nabla W_{SV}}} \int_\Omega n_{G} \mathbb{J} \; d\Omega$$

$$= \frac{T_{W}(z)}{I_{\nabla W_{SV}}} \; A_{n_{G}} \; (\bar{\boldsymbol{x}}_{G} - \bar{\boldsymbol{x}}_{T}) \neq 0 \; , \tag{124}$$

in general, showing again the lack of equilibrium of the stresses underlying the RBV formulation. Note that this deficiency of the RBV formulation occurs even for prismatic shafts, involving a constant cross section and corresponding warping function $W_{SV}(x, y)$ in z along the shaft, the focus of this work. This is in contrast to the original TWKV formulation (and the mixed formulation to be developed below) where any discrepancy from equilibrium is linked to a tapering of the shaft, in the geometry of the cross section or material distribution on it. This would affect, in particular, the section torsional constants along the shaft, being functions of z.

Imposing no warping in the RBV formulation at, say, the support $z = 0$ for the problem at hand is accomplished by setting $\lambda(0) = 0$, leaving free $\phi'(0)$. This allows a non-zero stress at that fixed end, namely, the Saint–Venant shear stresses $\boldsymbol{\tau}_{SV}(0)$ and the corresponding torque $T_{SV}(0)$, resolving then the torque anomaly indicated in Remark 2.3 in its entirety, as opposed to the situation discussed at the end of Section 3.2 for the TWKV formulation. However, this is accomplished by considering stresses that are not in equilibrium.

In any case, as indicated several times above and, in particular, in Remark 2.2, the goal of any structural model is to capture the response of the structural member at the global (structural) level, with necessarily a number of contradictions/anomalies at the local (section) level forced by the nature of the approximation. Despite these observations, the RBV formulation developed in this section is widely used in the literature, even in the nonlinear range as discussed in the introduction presented in Section 1. We shall evaluate in Section 7 its performance in comparison with the original TWKV formulation and the alternative mixed approximations developed next.

Remark 4.2. *We note that the use of the orthogonality relation (38) and definition (102) for the section constant $I_{\nabla W_{SV}}$ easily makes us conclude that*

the expressions (119)-(120) for the shear stress components in the RBV formulation are consistent with the general relation (90), also applicable to the original TWKV formulation. This equation gives the Saint–Venant $T_{SV}(z)$ and warping (bishear) $T_W(z)$ parts of the total torque $T(z)$ in terms of the total shear stress $\boldsymbol{\tau}$ on the cross section and the gradient of the Saint–Venant warping function $\nabla W_{SV}(x, y)$, on the cross section as well. □

5. A mixed formulation of restrained warping

The two formulations considered so far are based on a direct approximation of the warping displacement in the shaft to accommodate the effects of its restrainment. In both cases, the warping distribution on the cross section Ω is common for all sections in the shaft, being all proportional to each other. The proportionality factor is given by the generally varying rate of twist $\phi'(z)$ in the original TWKV formulation, but that resulted in a fourth order problem for this twist rotation, with the warping part of the torque not coming from associated shear strains in the shaft.

This structure of the original TWKV has been shown to be a consequence of its constrained origin. In this way, the alternative RBV formulation accomplishes the reduction to a more convenient (certainly numerically) second order boundary-value problem by releasing the warping–twist constraint on that proportionality factor from $\phi'(z)$ to a general (unknown) function $\lambda(z)$ along the shaft. However, the feasibility of the formulation has been shown to be at the price of the accuracy of the shear stresses at the section level.

These different shortcomings for both formulations can be linked to the assumption of a fixed distribution of the warping displacement over the cross section along the shaft length, both with the Saint–Venant warping function $W_{SV}(x, y)$. In the case of the TWKV formulation, shear stresses in equilibrium involving a different function (the alternate distribution $W_\sigma(x, y)$) could be obtained since, due to the aforementioned constrained character of the problem, the warping stresses $\boldsymbol{\tau}_W$ appear then from equilibrium (static) considerations rather than from material constitutive relations involving shear strains arising from the assumed approximation of the warping displacement, as the RBV formulation does. The consideration of mixed treatments, with separate approximations of the warping displacements and the strains/stresses, seems then of great interest.

This type of framework was precisely proposed in Reissner [1952], in the context of a Hellinger-Reissner treatment with assumed distributions of

the warping displacement and the axial stress. To the author's knowledge, the proposal has not received much attention in the literature, as opposed to the previous formulations based on a direct approximation of the warping displacements. Perhaps, this has been the case because the original presentation in Reissner [1952] does not consider particular distributions for the different fields, nor elaborates in the consequences of different choices.

Here we shall first reformulate this mixed treatment in a Hu-Washizu type formulation in terms of assumed both strains and stresses. This type of formulations has been shown to be more amenable to generalization to nonlinear problems, avoiding altogether the use of complementary energy densities, even though we continue focused on linear elastic problems in this paper. We start by considering in Section 5.1 the formulation in terms of a general (three–dimensional) warping displacement. The insight gained in these developments allows to identify the proper form of the assumed fields, including both the warping displacement and the normal strains and stresses. We then develop in Section 5.2 a reformulation of these ideas only in terms of structural fields along the shaft, leading to a new structural treatment of restrained warping in torsion.

5.1. Preliminary considerations: the mixed treatment in the three–dimensional setting

The staring point of the mixed formulation is an assumed distribution for both the axial strain ε_z and stress σ_z due to restrained warping, a distribution that we write as

$$\varepsilon_z = \varepsilon(z)\ \Sigma_\varepsilon(x,y)\ , \qquad \text{and} \qquad \sigma_z = \sigma(z)\ \Sigma_\sigma(x,y)\ , \tag{125}$$

for two (fixed) distribution functions $\Sigma_\varepsilon(x,y)$ and $\Sigma_\sigma(x,y)$ over the cross section, and two unknown structural fields $\varepsilon(z)$ and $\sigma(z)$ along the shaft. The notation used here should not be understood that these two fields have units of strain and stress, respectively, as this will depend on the choice of the assumed distributions $\Sigma_\varepsilon(x,y)$ and $\Sigma_\sigma(x,y)$. In fact, they will not physically have the corresponding units. They should be simply understood as the "amplitudes" of the axial strains and stresses, respectively. We leave the two distribution functions $\Sigma_\varepsilon(x,y)$ and $\Sigma_\sigma(x,y)$ open for now, only imposing the conditions

$$\int_\Omega \Sigma_\sigma(x,y)\ d\Omega = 0 \quad \text{and} \quad \int_\Omega x_{_E} \Sigma_\sigma(x,y)\ d\Omega = \int_\Omega y_{_E} \Sigma_\sigma(x,y)\ d\Omega = 0\ , \tag{126}$$

on physical grounds, following relations (4) and (5) for the normal stress σ_z.

Note that underlying the assumed distributions (125) is the same spatial shape or form of the axial strain and stress on all the cross sections of the shaft, with varying amplitude along the shaft in general. Hence, we assume that the distribution functions $\Sigma_\varepsilon(x,y)$ and $\Sigma_\sigma(x,y)$ are independent of the axis coordinate z in the calculations that follow, as implied by the employed notation, although one may perfectly consider them for the particular cross section at z for general non–prismatic shafts; see Remark 5.4 below for further comments in this respect. Specific choices for these fixed distribution functions will be made explicit in the following section; they will depend on the particular section under consideration, its geometry and material distribution.

As shown below, the uniformity of the section distributions for these quantities along the shaft will allow a varying form of the distribution of the warping displacements for different cross sections of the shaft, a crucial feature we saw missing in the previous direct approximations. In fact, we assume the same displacements as in the 3D displacement (12) with a completely general (three–dimensional) warping function $w(x,y,z)$ as our starting point. Hence, the two fundamental assumptions in building the (approximate) structural model from full three–dimensional elasticity are (1) the original assumption of the cross sections suffering an infinitesimal rigid rotation of generally varying amplitude $\phi(z)$ in their planes around the shaft's axis z, as encompassed by the 3D displacements $(12)_{1,2}$, and (2) the assumed distributions of the normal strain and stress, of uniform form and varying amplitude marked by the parameters $\varepsilon(z)$ and $\sigma(z)$, but again a general warping displacement $u_z = w(x,y,z)$.

With this in mind, and for the elastic case of interest here, the formulation under consideration can be developed from the Hu-Washizu type functional

$$\Pi_{HW,1}(\phi,w,\varepsilon,\sigma) = \int_V \Big[\Psi\left(\varepsilon_z(\varepsilon),\boldsymbol{\gamma}(\phi,w)\right) + \sigma\Sigma_\sigma\left(w' - \varepsilon\Sigma_\varepsilon\right)\Big]dv \\ +\Pi_{ext}(\phi)\ , \qquad (127)$$

for the standard shear strains $\boldsymbol{\gamma}(\phi,w) = \nabla w + \phi'\mathbb{J}$. The same external potential $\Pi_{ext}(\phi)$ as in (17). is involved in (127).

The variations of the functional (127) lead to the weak equations

$$\delta_\phi\Pi_{HW,1} = \int_0^L \left[T(z)\ \delta\phi'(z) - t_{ex}(z)\delta\phi(z)\right]dz - \delta\phi(L)T_L = 0\ , \qquad (128)$$

$$\delta_w \Pi_{HW,1} = \int_V \Big[\boldsymbol{\tau} \cdot \nabla \delta w + \sigma \; \Sigma_\sigma \; \delta w' \Big] \; dv = 0 \; , \tag{129}$$

$$\delta_\varepsilon \Pi_{HW,1} = \int_V \left[\frac{\partial \Psi}{\partial \varepsilon_z} - \sigma \Sigma_\sigma \right] \Sigma_\varepsilon \; \delta\varepsilon \; dv = 0 \; , \tag{130}$$

$$\delta_\sigma \Pi_{HW,1} = \int_V \Big[w' - \varepsilon \Sigma_\varepsilon \Big] \Sigma_\sigma \; \delta\sigma \; dv = 0 \; , \tag{131}$$

where we have introduced the (total) internal torque $T(z) = \int_\Omega \boldsymbol{\tau} \cdot \mathbb{J} \; d\Omega$ for the shear stresses $\boldsymbol{\tau} = \partial \Psi / \partial \boldsymbol{\gamma}$. These equations consider admissible variations for the different supports, consisting of the same $\delta\phi(z)$ and δw as in Section 2.2, and general variations $\delta\varepsilon$ and $\delta\sigma$ of the new mixed fields.

The weak equation (128) leads to the same equation (19) capturing the balance of moments about the axis of the shaft for the internal torque $T(z)$. Equation (130) leads to

$$\sigma(z) = \frac{1}{I_{\Sigma_\sigma \Sigma_\varepsilon}} \int_\Omega \Sigma_\varepsilon(x,y) \; \frac{\partial \Psi}{\partial \varepsilon_z} \; d\Omega = \bar{E}_{\varepsilon\sigma} \; \varepsilon(z) \; , \tag{132}$$

the latter equality for the linear elastic case of interest, with the notation

$$I_{\Sigma_\sigma \Sigma_\varepsilon} := \int_\Omega \Sigma_\varepsilon(x,y) \; \Sigma_\sigma(x,y) \; d\Omega \; , \tag{133}$$

and

$$\bar{E}_{\varepsilon\sigma} := \frac{\bar{E}}{I_{\Sigma_\sigma \Sigma_\varepsilon}} \int_\Omega n_{_E}(x,y) \; \big(\Sigma_\varepsilon(x,y) \big)^2 \; d\Omega \; , \tag{134}$$

for the mixed distribution functions assumed in equations (125).

Similarly, equation (131) results in

$$\varepsilon(z) = \lambda_\varepsilon'(z) \qquad \text{for} \quad \lambda_\varepsilon(z) := \frac{1}{I_{\Sigma_\sigma \Sigma_\varepsilon}} \int_\Omega \Sigma_\sigma(x,y) \; w(x,y,z) \; d\Omega \; , \tag{135}$$

a weighted average of the warping displacement on the cross section Ω. This equation has to be compared with relation (92), thus motivating the employed notation in the warping amplitude $\lambda_\varepsilon(z)$. Here we have assumed, as pointed out above, that the starting distribution functions (125) are indeed constant in z along the length of the shaft or, in other words, that we have a constant cross section Ω including the material distributions $n_{_G}(x,y)$ and $n_{_E}(x,y)$, so

the constant $I_{\Sigma_\sigma \Sigma_\varepsilon}$ is also independent of z. We refer to Section 5.2 below for an alternative treatment accommodating this more general situation and, in particular, to the additional arguments in Remark 5.4 of that section.

For equation (129), we proceed by integrating by parts, as in (20), to obtain

$$-\int_V \Big[\nabla\cdot\boldsymbol{\tau}+\sigma'\ \Sigma_\sigma\Big]\delta w\ dv+\int_0^L\int_{\partial\Omega}\boldsymbol{\tau}\cdot\boldsymbol{\nu}\ \delta w\ d\Omega dz+\Big[\sigma\,\delta\lambda_\varepsilon\Big]_0^L=0\ , \quad (136)$$

after using the definition $(135)_2$ for the last boundary term. Hence, we arrive at the differential equation

$$\nabla\cdot\boldsymbol{\tau}+\sigma'\ \Sigma_\sigma=0\quad \text{in }\Omega\ ,\quad \text{with}\quad \boldsymbol{\tau}\cdot\boldsymbol{\nu}=0\quad \text{along }\partial\Omega\ , \quad (137)$$

an equation to be compared with (21), and the identification of the proper boundary conditions at both end of the end for the warping fields. Namely, we have $\sigma(L)=0$ for the end with free warping, and $\lambda_\varepsilon(0)=0$ at the end $z=0$ with restrained warping. Note that the considered formulation imposes this condition through the weighted amplitude $(135)_2$, avoiding the anomalies observed above when imposing $\phi'(0)=0$ to restrain the warping. The usual boundary conditions need to be imposed on the rotation field and total internal torque, that is, $\phi(0)=0$ for the fixed support at $z=0$, and $T(L)=T_L$ for the imposed torque T_L at the free end at $z=L$, as obtained below.

For the linear elastic case, the differential equation (137) reads

$$\left.\begin{aligned}&\nabla\cdot\big(G\big(\nabla w+\phi'(z)\,\mathbb{J}\big)\big)+\sigma'(z)\ \Sigma_\sigma(x,y)=0 && \text{in }\Omega\ ,\\ &\frac{\partial w}{\partial\nu}=-\phi'(z)\ \mathbb{J}\cdot\boldsymbol{\nu} && \text{along }\partial\Omega\ ,\end{aligned}\right\} \quad (138)$$

for the fixed section Ω at z, a problem to be compared with (23). Considering again a shear modulus of the form $G=\bar{G}\,n_{_G}(x,y)$, the solution of equation (138) can be easily seen to be given as

$$w(x,y,z)=\phi'(z)\ W_{_{SV}}(x,y)-\frac{1}{\bar{G}}\ \sigma'(z)\ W_{\Sigma_\sigma}(x,y)\ , \quad (139)$$

in terms of the rate of twist $\phi'(z)$ and the stress parameter $\sigma(z)$, the Saint–Venant warping function $W_{_{SV}}(x,y)$ defined by (33), and the function $W_{\Sigma_\sigma}(x,y)$

defined by boundary-value problem

$$\left.\begin{aligned} &\nabla \cdot (n_{_G}(x,y)\ \nabla W_{\Sigma_\sigma}) = \Sigma_\sigma(x,y) && \text{in } \Omega\ , \\ &\frac{\partial W_{\Sigma_\sigma}}{\partial \nu} = 0 && \text{along } \partial\Omega\ , \end{aligned}\right\} \tag{140}$$

a Poisson problem of the Neumann type to be compared with (79). The condition $(126)_1$ assures that the Neumann boundary-value problem (140) is well-posed, following the same argument as in (80); see Remark 5.2 below for the arbitrary constant defining the warping function $W_{\Sigma_\sigma}(x,y)$.

Given the expression (139) for the warping displacement involved in the formulation under consideration, the shear stress $\boldsymbol{\tau} = G(\nabla w + \phi'\mathbb{J})$ is given, for the linear elastic case considered here, by

$$\boldsymbol{\tau} = n_{_G}(x,y)\left[\bar{G}\phi'(z)\,(\nabla W_{_{SV}} + \mathbb{J}) - \sigma'(z)\,\nabla W_{\Sigma_\sigma}\right]\ , \tag{141}$$

which results in the total torque

$$T(z) := \int_\Omega \boldsymbol{\tau}\cdot\mathbb{J}\ d\Omega = T_{_{SV}}(z) + T_{_W}(z)\ , \tag{142}$$

for the Saint–Venant torque $T_{_{SV}}(z) = \bar{G}J\phi'(z)$ with the torsional constant J defined exactly as above, and the bishear $T_{_W}(z)$ given now by

$$T_{_W}(z) = -I_{\Sigma_\sigma W_{SV}}\sigma'(z) = -\frac{d}{dz}B_{_W}(z)\ , \tag{143}$$

for the bimoment $B_{_W}(z)$ defined by

$$B_{_W}(z) = I_{\Sigma_\sigma W_{SV}}\ \sigma(z) = \bar{E}_{\varepsilon\sigma}\ I_{\Sigma_\sigma W_{SV}}\varepsilon(z)\ , \tag{144}$$

in terms of the mixed normal strain field $\varepsilon(z)$. Here we have used the notation

$$I_{\Sigma_\sigma W_{SV}} := \int_\Omega \Sigma_\sigma(x,y)\ W_{_{SV}}(x,y)\ d\Omega = \int_\Omega n_{_G}(x,y)\nabla W_{\Sigma_\sigma}\cdot\mathbb{J}\ d\Omega\ , \tag{145}$$

the last equality following from the same arguments as used in (81) for the functions considered in the current section. Equation (144) defining the bimoment $B_{_W}(z)$ is to be contrasted with the constitutive relation (104) for the RBV formulation. Note that we still can write (144)

$$B_{_W}(z) = I_{\Sigma_\sigma W_{SV}}\sigma(z) = \int_\Omega \underbrace{\sigma(z)\ \Sigma_\sigma(x,y)}_{=\sigma_z}\ W_{_{SV}}(x,y)\ d\Omega\ , \tag{146}$$

recovering the original definition of the bimoment (99) from the assumed axial stress distribution.

The result (143) allows to write the shear stresses (141) as

$$\boldsymbol{\tau} = n_{G}(x,y)\left(\frac{T_{SV}(z)\ (\nabla W_{SV} + \mathbb{J})}{J} + \frac{T_{W}(z)\,\nabla W_{\Sigma_\sigma}}{I_{\Sigma_\sigma W_{SV}}}\right)\ , \tag{147}$$

recovering the form of equation (83) for the original TWKV formulation. Each term in this expression also identifies the two parts of the shear stresses $\boldsymbol{\tau}_{SV}$ and $\boldsymbol{\tau}_{W}$, the Saint–Venant and warping stresses, respectively, for the current mixed formulation. Similarly, the normal stresses σ_z can be written as

$$\sigma_z = \frac{B_{W}(z)\ \Sigma_\sigma(x,y)}{I_{\Sigma_\sigma\Sigma_\varepsilon}}\ , \tag{148}$$

directly linked to the bimoment $B_{W}(z)$. In contrast with the stresses involved in the previous RBV formulation, the stresses (147) and (148) are indeed in equilibrium, having been derived precisely from the equilibrium relation (137). Again, this situation is exact for the prismatic shafts with constant cross section focus of this work; see Remark 5.4 for additional details.

The mixed normal strain field $\varepsilon(z)$ with associated stress field $\sigma(z) = \bar{E}_{\varepsilon\sigma}\varepsilon(z)$ appearing in all these expressions are obtained by expanding the compatibility relation $\varepsilon = \lambda'_\varepsilon$ in (135), combined with the relation (139). We carry out these calculations in the next section. Here instead, we note again the similarity of the expressions (147) and (148) of the stresses in terms of the functions $W_{\Sigma_\sigma}(x,y)$ and $\Sigma_\sigma(x,y)$ for the current mixed formulation, with $W_{\Sigma_\sigma}(x,y)$ being the solution of the Poisson problem defined by the latter function $\Sigma_\sigma(x,y)$, with similar considerations for equations (83) and (76) for the TWKV formulation in terms of the functions $W_\sigma(x,y)$ and $n_{E}(x,y)W_{SV}(x,y)$ with, similarly, the latter function being the solution of the same Poisson problem defined by the former function. In other words, the natural choices for the assumed mixed functions are

$$\Sigma_\varepsilon(x,y) = W_{SV}(x,y)\ , \quad \text{and} \quad \Sigma_\sigma(x,y) = n_{E}(x,y)\ W_{SV}(x,y)\ , \tag{149}$$

(the first choice motivated by the relation $\varepsilon = \sigma/E$), resulting also in

$$W_{\Sigma_\sigma}(x,y) = W_\sigma(x,y)\ , \tag{150}$$

the warping function defined by the Poisson problem (79) in terms of the original Saint–Venant warping function $W_{SV}(x,y)$. Note that the conditions

(126) on $\Sigma_\sigma(x,y)$ are indeed satisfied by the choice $(149)_2$, since the Saint –Venant warping function is, again, assumed to be normalized by the conditions (46) and (47). We explore the choice of functions (149) next, in the context of a fully structural derivation of the mixed formulation at hand.

Remark 5.1. *We note that, with the choices (149), we have*

$$\Sigma_\varepsilon(x,y) \sim \Sigma_\sigma(x,y) \sim W_{SV}(x,y) \sim (length)^2 \ . \tag{151}$$

in terms of units. Hence, we have

$$\varepsilon(z) \sim (length)^{-2} \qquad and \qquad \sigma(z) \sim stress \cdot (length)^{-2} \ , \tag{152}$$

for the two considered amplitude parameters. Similarly, with the choices (149), the different section constants considered in this section reduce to

$$I_{\Sigma_\sigma \Sigma_\varepsilon} = I_{\Sigma_\sigma W_{SV}} = I_{W_{SV}} \ , \quad and \quad \bar{E}_{\varepsilon\sigma} = \bar{E} \ , \tag{153}$$

for the warping function $I_{W_{SV}}$ in (64) and the reference Young modulus $\bar{E}$, respectively, both used repeatedly in previous formulations. □

Remark 5.2. *The Poisson problems of the Neumann type (79) and (140) define the functions $W_\sigma(x,y)$ and $W_{\Sigma_\sigma}(x,y)$, respectively, up to an arbitrary additive constant. The TWKV formulation only depends on the former function through its gradient, in expression (83) for the warping stresses, hence this constant is irrelevant for the TWKV formulation. These functions play no role in the RBV formulation. For the mixed formulation considered in this section, the warping stresses in (147) also depend on $\nabla W_{\Sigma_\sigma}(x,y)$ (or $W_\sigma(x,y)$ if the choices (149) are considered), so that arbitrary constant has no effect either. However, the function $W_{\Sigma_\sigma}(x,y)$ (or, as before, $W_\sigma(x,y)$) does appear explicitly in the warping displacement given by the expression (139). The first term in that expression, depending on the Saint–Venant warping function $W_{SV}(x,y)$, is imposed to have a zero ($n_{_E}$-weighted) average. We consider the same condition on the second term of that expression and, hence, impose*

$$\int_\Omega n_{_E}(x,y)\ W_\sigma(x,y)\ d\Omega = 0 \ , \tag{154}$$

and similarly for $W_{\Sigma_\sigma}(x,y)$, defining uniquely either function. Physically, this condition is motivated by the axial force balance relation $\int_\Omega E u_z' d\Omega = 0$ along the shaft for the three–dimensional displacement $u_z(x,y,z)$. □

5.2. A new mixed formulation of restrained warping in terms of structural fields only

To our purpose, the main outcome of the preliminary considerations presented in the previous section developing a mixed treatment in the three–dimensional setting is the resulting distribution (139) of the warping displacement. This distribution, involving now a non–uniform section form along the shaft, is a direct consequence of the assumed distributions (125) for the axial strain and stress, both of a uniform form along the shaft. Furthermore, the explicit expression (139) allows us to formulate a purely structural model of restrained warping.

We develop such formulation using the specific choices (149) for the assumed mixed distributions. Hence, we have

$$\boxed{\varepsilon_z = \varepsilon(z)\, W_{SV}(x,y)\ ,} \qquad \text{and} \qquad \boxed{\sigma_z = \sigma(z)\, n_{_E}(x,y)\ W_{SV}(x,y)\ ,} \tag{155}$$

for the unknown fields $\varepsilon(z)$ and $\sigma(z)$, with section distributions given by the Saint–Venant warping function $W_{SV}(x,y)$ in all the sections along the shaft. Since we assume that this function satisfies the normalizing conditions (46) and (47), the resulting normal stress distribution $(155)_2$ satisfies then the equilibrium relations (4) and (5) by construction. With these choices, the second warping function in the warping displacement (139) reduces to the function $W_\sigma(x,y)$, the unique solution of the Poisson problem (79) depending on that same Saint–Venant warping function $W_{SV}(x,y)$ after imposing the condition (154).

Together with (155), the proposed mixed formulation starts by expressing the 3D warping displacement as

$$\boxed{u_z(x,y,z) = \phi'(z)\ W_{SV}(x,y) + \frac{I_{W_{SV}}}{I_{\nabla W_\sigma}}\,(\phi'(z) - \lambda_\varepsilon(z))\ W_\sigma(x,y)\ ,} \tag{156}$$

in terms of the twist rotation field $\phi(z)$ and a new and independent structural field $\lambda_\varepsilon(z)$, besides the combination of section constants $I_{W_{SV}}/I_{\nabla W_\sigma}$ specified below. Hence, we have replaced the general three–dimensional warping function $w(x,y,z)$ considered in the previous section by an explicit expression in terms of the unknown independent structural fields $\phi(z)$ and $\lambda_\varepsilon(z)$. It is worth pointing out again that, in contrast to the TWKV and RBV formulations, the assumed expression (156) allows to have a warping displacement whose form or shape of the distribution over the cross sections varies along

the shaft. In particular, it assumes two components with fixed forms, one in the form given by the Saint–Venant warping functions $W_{SV}(x,y)$ and the other by the second warping function $W_\sigma(x,y)$. We recognize the classical Saint–Venant solution depending on the rate of twist $\phi'(z)$ in that first component, with the new added component defined by that second warping function depending on the difference of the rate of twist $\phi'(z)$ with the new field $\lambda_\varepsilon(z)$,

The assumed warping distribution (156) uses the warping constant $I_{W_{SV}}$ of the cross section, namely again,

$$I_{W_{SV}} = \int_\Omega n_{_E}(x,y)\left(W_{SV}(x,y)\right)^2 d\Omega > 0\,, \tag{157}$$

and a new section constant $I_{\nabla W_\sigma}$ associated with the second warping function $W_\sigma(x,y)$ defined as

$$I_{\nabla W_\sigma} := \int_\Omega n_{_G}(x,y)\,\|\nabla W_\sigma\|^2\, d\Omega > 0\,, \tag{158}$$

strictly positive by construction with the proper choice of that function (actually, $W_{SV}(x,y)$ driving its definition through the defining problem (79)). The introduction of this new section constant is motivated by the relation

$$I_{\nabla W_\sigma} = \int_\Omega n_{_G}(x,y)\,\nabla W_\sigma\cdot\nabla W_\sigma d\Omega = \int_{\partial\Omega} n_{_G}\underbrace{\nabla W_\sigma\cdot\boldsymbol{\nu}}_{=0} W_\sigma\, d\Gamma$$

$$-\int_\Omega \underbrace{\nabla\cdot(n_{_G}\nabla W_\sigma)}_{=\,n_{_E}W_{SV}} W_\sigma\, d\Omega = -\int_\Omega n_{_E}(x,y)\,W_{SV}\,W_\sigma\, d\Omega\,, \tag{159}$$

using again problem (79) defining the function $W_\sigma(x,y)$.

With this result at hand, the choice of the combination of these normalizing constants in (156) readily leads to the identity

$$\frac{1}{I_{W_{SV}}}\int_\Omega n_{_E}(x,y)W_{SV}(x,y)u_z(x,y,z)d\Omega = \phi'(z)\underbrace{\frac{1}{I_{W_{SV}}}\int_\Omega n_{_E}\,(W_{SV})^2 d\Omega}_{=\,1\text{ by (157)}}$$

$$+\,(\phi'(z)-\lambda_\varepsilon(z))\underbrace{\frac{1}{I_{\nabla W_\sigma}}\int_\Omega n_{_E}\,W_{SV}\,W_\sigma\,d\Omega}_{=\,-1\text{ by (159)}}$$

$$= \lambda_\varepsilon(z) \ , \tag{160}$$

identifying the field $\lambda_\varepsilon(z)$ with the weighted average of the warping direction when one looks at its distribution over the cross section Ω, a quantity that also appeared in (135) during the general considerations of the last section but not as an independent field. Hence, the notation we have employed in naming the new independent field here. In (160), we have crucially used the relation (159). Note that this last result or, directly, the original expression (156), implies that the units of this field are $\lambda_\varepsilon \sim (length)^{-1}$

The shear strain associated to the assumed warping displacement (156), always in combination with the in–plane displacements $(12)_{1,2}$ for an infinitesimal rigid rotation $\phi(z)$ of the section in its plane, is given by

$$\boldsymbol{\gamma} = \underbrace{\phi'(z)\ (\nabla W_{SV} + \mathbb{J})}_{\boldsymbol{\gamma}_{SV}} + \underbrace{\frac{I_{W_{SV}}}{I_{\nabla W_\sigma}}\ (\phi'(z) - \lambda_\varepsilon(z))\ \nabla W_\sigma}_{\boldsymbol{\gamma}_{W}} \ , \tag{161}$$

thus involving the usual Saint–Venant component $\boldsymbol{\gamma}_{SV}$ and a new warping component $\boldsymbol{\gamma}_{W}$. We can see that, crucially, this warping component involves the gradient ∇W_σ of the second warping function $W_\sigma(x, y)$. This situation is to be contrasted with expression (108) of this shear strain for the RBV formulation, involving instead the gradient ∇W_{SV} of the Saint–Venant warping function. The new warping strain component mimics the same distribution of the warping shear stresses (78) of the TWKV formulation, but recall that these stresses appear in that formulation in order to impose the warping–twist constraint, with the resulting constrained TWKV formulation involving no warping shear strains whatsoever.

The two components of the shear strain in (161) are $n_{G}-$orthogonal. Indeed, a simple application of integration by parts leads to

$$\int_\Omega n_{G}\ (\nabla W_{SV} + \mathbb{J}) \cdot \nabla W_\sigma \, d\Omega = - \int_\Omega \underbrace{\nabla \cdot (n_{G}\ (\nabla W_{SV} + \mathbb{J}))}_{=0}\ W_\sigma \, d\Omega$$

$$+ \int_{\partial_\Omega} n_{G}\ \underbrace{(\nabla W_{SV} + \mathbb{J}) \cdot \boldsymbol{\nu}}_{=0}\ W_\sigma \, d\Omega = 0 \ , \tag{162}$$

both vanishing because of the problem (33) defining the Saint–Venant function $W_{SV}(x, y)$. Although not crucial to the developments presented here,

this property leads to a decoupling of each component again in the material part of the functional (127) for the isotropic linear elastic case (2) of interest.

Summarizing the above developments so far, once we have the cross section of the shaft, its geometry and material distribution over it through the non–dimensional distributions $n_{_G}(x,y)$ and $n_{_E}(x,y)$, we proceed with the evaluation of the Saint–Venant warping function $W_{SV}(x,y)$ by solving the Laplace problem (33), followed by the determination of the second warping function $W_\sigma(x,y)$ by solving the Poisson problem (79), which in turn allows the evaluation of the involved section constants, namely, the Saint–Venant torsional constant J, the warping constant $I_{W_{SV}}$ and the new gradient constant $I_{\nabla W_\sigma}$. For the elastic shafts of interest here, these are all kept fixed in the analysis of the shaft, involving a purely structural problem for the four (one-dimensional or structural) fields $\phi(z)$, $\lambda_\varepsilon(z)$ and the two mixed fields $\varepsilon(z)$ and $\sigma(z)$. These last two fields will be eventually eliminated locally in terms of the first two.

To derive the governing equations relating these different fields, we introduce the fully structural functional

$$\boxed{\begin{aligned}\Pi_{HW}^{(MIX)}(\phi,\lambda_\varepsilon,\varepsilon,\sigma) = \int_0^L \Big[&\frac{1}{2}\,\bar{G}J\,(\phi')^2 + \frac{1}{2}\,\bar{G}\frac{\left(I_{W_{SV}}\right)^2}{I_{\nabla W_\sigma}}\,(\phi'-\lambda_\varepsilon)^2 \\ &+ \frac{1}{2}\,\bar{E}I_{W_{SV}}\varepsilon^2 + \sigma I_{W_{SV}}\,(\lambda_\varepsilon'-\varepsilon)\Big]dz + \Pi_{ext}(\phi)\;,\end{aligned}} \tag{163}$$

where the Saint–Venant torsional constant $J = \int_\Omega n_{_G}\|\nabla W_{SV}+\mathbb{J}\|^2 d\Omega$ appears naturally in this context as measuring the magnitude of the Saint–Venant component $\boldsymbol{\gamma}_{_{SV}}$ of the shear strain in (161). Here, and to be specific to the problem later considered in the evaluation of the resulting model, we have assumed again an isotropic linear elastic model, with the expression (163) clearly showing the noted orthogonality of the Saint–Venant and warping shear strain components.

Taking variation of the functional (163), we obtain the weak equations

$$\delta_\phi \Pi_{HW}^{(MIX)} = \int_0^L \left[T\;\delta\phi' - t_{ex}\delta\phi\right] dz - \delta\phi(L)T_L = 0\;, \tag{164}$$

$$\delta_{\lambda_\varepsilon}\Pi_{HW}^{(MIX)} = \int_0^L \Big[-\bar{G}\frac{\left(I_{W_{SV}}\right)^2}{I_{\nabla W_\sigma}}\,(\phi'-\lambda_\varepsilon)\,\delta\lambda_\varepsilon + I_{W_{SV}}\,\sigma\,\delta\lambda_\varepsilon'\Big]\;dz = 0\;, \tag{165}$$

$$\delta_\varepsilon \Pi_{HW}^{(MIX)} = \int_0^L I_{W_{SV}} \left[\bar{E}\varepsilon - \sigma\right] \delta\varepsilon \; dz = 0 \; , \quad (166)$$

$$\delta_\sigma \Pi_{HW}^{(MIX)} = \int_0^L I_{W_{SV}} \left[\lambda_\varepsilon' - \varepsilon\right] \delta\sigma \; dz = 0 \; , \quad (167)$$

for all admission variations (e.g. $\delta\phi(0) = 0$ and $\delta\lambda_\varepsilon(0) = 0$ for the considered fixed support at the root of the shaft with no warping).

In equation (164), we have introduced the short hand notation for

$$T(z) = \underbrace{\bar{G} J \, \phi'}_{T_{SV}(z)} + \underbrace{\bar{G} \frac{\left(I_{W_{SV}}\right)^2}{I_{\nabla W_\sigma}} \left(\phi' - \lambda_\varepsilon\right)}_{T_W(z)} \; , \quad (168)$$

incorporating again the Saint–Venant torque $T_{SV}(z)$ and bishear $T_W(z)$ parts of the total torque $T(z)$. Equation (164) is again the weak form of balance of moments about the shaft axis for this total torque $T(z)$.

Equation (165) allows to introduce the bimoment $B_W(z)$ and its relation with the bishear $T_W(z)$ in (168), recovering the strong form relation

$$T_W(z) = -\frac{d}{dz} B_W(z) \qquad \text{for} \quad B_W(z) = I_{W_{SV}} \, \sigma \; , \quad (169)$$

after integrating by parts the weak equation (165), together with the natural boundary condition $B_W(L) = B_{WL} = 0$ for the assumed free end at the shaft's tip $z = L$ or, equivalently (since $I_{W_{SV}} > 0$), $\sigma(L) = 0$. This same calculation also identifies that essential boundary condition corresponding to restrained warping at the opposite end, namely,

$$\lambda_\varepsilon(0) = 0 \qquad \text{for restrained warping at } z = 0, \quad (170)$$

fixing the new independent field $\lambda_\varepsilon(z)$ at that end. Physically, this corresponds to fixing the average of the warping displacement (weighted by the warping function $W_{SV}(x, y)$ as given by relation (160)), rather than a pointwise imposition as it occurred in the TWKV and RBV formulations, despite how similar condition (170) is with the corresponding condition (96) for the RBV formulation. Note that $\phi'(0) \neq 0$ necessarily, resolving the torque anomaly discussed in Remark 2.3 allowing a non–zero Saint–Venant torque $T_{SV}(0) \neq 0$ too, hence avoiding the observed limitation of the original TWKV formulation.

The last two weak equations (166) and (167) allow to eliminate the mixed parameters $\varepsilon(z)$ and $\sigma(z)$ pointwise along the shaft (note that no derivatives are involved for these fields). Namely, we obtain

$$\varepsilon(z) = \lambda'_\varepsilon(z) \qquad \text{and} \qquad \sigma(z) = \bar{E}\varepsilon(z) \; . \tag{171}$$

The first of these relations identifies the compatibility relation underlying the assumed mixed treatment, linking directly the amplitude of the axial strain along the shaft with the rate of the average of the warping of the cross sections. Rather than having the three–dimensional relation $\varepsilon_z = u'_z$ pointwise over the cross section, equation $(171)_1$ corresponds to the weighted average relation

$$\frac{1}{I_{W_{SV}}} \int_\Omega \varepsilon_z \, W_{SV} \, d\Omega = \varepsilon(z) = \lambda'_\varepsilon(z) = \frac{d}{dz} \left(\frac{1}{I_{W_{SV}}} \int_\Omega u_z \, W_{SV} \, d\Omega \right) \; , \tag{172}$$

after using the assumed distribution (155) for the axial strain $\varepsilon_z(x, y, z)$ and the result (160). Note that these considerations are consistent with the essential boundary condition (170), involving that same average through the new field $\lambda_\varepsilon(z)$.

These results allow to write the bishear $T_W(z)$ and bimoment $B_W(z)$ in (169) alternatively as

$$T_W(z) = -\frac{d}{dz} \left(\bar{E} \, I_{W_{SV}} \, \lambda'_\varepsilon \right) \quad \text{and} \quad B_W(z) = \bar{E} \, I_{W_{SV}} \, \lambda'_\varepsilon \; . \tag{173}$$

This last relation is to be compared with the corresponding expressions (63) and (104) for the bimoment distribution $B_W(z)$ in the TWKV and RBV formulations, respectively.

Then, the additional governing equation in the proposed formulation is obtained by equating the bishear $T_W(z)$ in relation (173) with the same bishear given by (168). The final system of ordinary differential equations for the mixed formulation, involving the resulting equation with the strong form of the equilibrium equation (164), reads then

$$\boxed{\begin{aligned} &\frac{d}{dz} \left[\bar{G} J \left(\phi'(z) + \frac{\left(I_{W_{SV}} \right)^2}{J \, I_{\nabla W_\sigma}} \Big(\phi'(z) - \lambda_\varepsilon(z) \Big) \right) \right] + t_{ex}(z) = 0 \; , \\ &\frac{d}{dz} \Big[\bar{E} I_{W_{SV}} \lambda'_\varepsilon(z) \Big] + \bar{G} \frac{\left(I_{W_{SV}} \right)^2}{I_{\nabla W_\sigma}} \Big(\phi'(z) - \lambda_\varepsilon(z) \Big) = 0 \; , \end{aligned}} \tag{174}$$

a second order system on the unknown fields $\phi(z)$ and $\lambda_{\varepsilon}(z)$, with the boundary conditions discussed above. The high–order problem (68) of the constrained TWKV formulation is then avoided. Note that the weak form of the system (174), namely, the variational equations (164) and (165) involve only first derivative of the unknown fields $\phi(z)$ and $\lambda_{\varepsilon}(z)$.

After solving this system of equations for these two fields along the shaft, one can recover the stresses on the cross sections as a post–processing. Indeed, the availability of the shear strains (161) leads directly to

$$\boldsymbol{\tau}_{SV} = G\phi'(z)\ (\nabla W_{SV} + \mathbb{J}) = n_{G}(x,y)\,\frac{T_{SV}(z)\ (\nabla W_{SV} + \mathbb{J})}{J}\ , \tag{175}$$

for the Saint–Venant component $\boldsymbol{\tau}_{SV}$, following then the same form as in the previous two considered direct formulations, and

$$\boxed{\boldsymbol{\tau}_{W} = G\,\frac{I_{W_{SV}}}{I_{\nabla W_{\sigma}}}\Big(\phi'(z) - \lambda_{\varepsilon}(z)\Big)\,\nabla W_{\sigma} = n_{G}(x,y)\,\frac{T_{W}(z)\,\nabla W_{\sigma}(x,y)}{I_{W_{SV}}}\ ,} \tag{176}$$

for the warping component $\boldsymbol{\tau}_{W}$ of the total shear stress $\boldsymbol{\tau} = \boldsymbol{\tau}_{SV} + \boldsymbol{\tau}_{W}$. The last relations in (175) and (176) have been obtained after using the constitutive structural relations (168) for the Saint–Venant torque $T_{SV}(z)$ and the bishear $T_{W}(z)$. Similarly, equations $(155)_2$ and (171) result in the expression

$$\boxed{\sigma_{z} = E\,\lambda'_{\varepsilon}(z)\,W_{SV}(x,y) = n_{E}(x,y)\,\frac{B_{W}(z)\,W_{SV}(x,y)}{I_{W_{SV}}}\ ,} \tag{177}$$

of the normal stress distribution on the cross section, with the last equality obtained from the constitutive structural relation $(169)_2$ for the bimoment $B_{W}(z)$. As expected, expressions (175) to (177) for the different stresses correspond to the analogous expressions for the same stresses derived in the previous section for the general distribution functions $\Sigma_{\varepsilon}(x,y)$ and $\Sigma_{\sigma}(x,y)$ considered in that section.

Notwithstanding, its is interesting to verify directly that these stresses are in equilibrium among themselves, regardless of the three–dimensional

arguments considered in the previous section. Indeed, we have

$$\nabla\cdot\boldsymbol{\tau} = \nabla\cdot(\boldsymbol{\tau}_{SV}+\boldsymbol{\tau}_{W}) = \frac{T_{SV}(z)}{J}\underbrace{\nabla\cdot(n_{G}(x,y)\ (\nabla W_{SV}+\mathbb{J}))}_{=0\text{ by (33)}}$$
$$+\frac{T_{W}(z)}{I_{W_{SV}}}\underbrace{\nabla\cdot(n_{G}(x,y)\,\nabla W_{\sigma})}_{=n_{E}\,W_{SV}\text{ by (79)}} = -\frac{1}{I_{W_{SV}}}\underbrace{\frac{d}{dz}\Big(\underbrace{I_{W_{SV}}\sigma(z)}_{B_{W}(z)}\Big)}_{-T_{W}(z)}\ n_{E}\,W_{SV}$$
$$= -\sigma'(z)\,n_{E}(x,y)\,W_{SV}(x,y) = -\sigma'_{z}\ , \tag{178}$$

on a cross section Ω and, similarly,

$$\boldsymbol{\tau}\cdot\boldsymbol{\nu} = \frac{T_{SV}(z)}{J}\underbrace{n_{G}(x,y)\ (\nabla W_{SV}+\mathbb{J})\cdot\boldsymbol{\nu}}_{=0\text{ by (33)}}+\frac{T_{W}(z)}{I_{W_{SV}}}\underbrace{n_{G}(x,y)\,\nabla W_{\sigma}\cdot\boldsymbol{\nu}}_{=0\text{ by (79)}}$$
$$= 0\ , \tag{179}$$

along the cross section boundary $\partial\Omega$. As occurred with the original TWKV formulation (see comments after equation (79)), the final arguments in (178) requires that the warping constant $I_{W_{SV}}$ (and, for that matter, the Saint–Venant warping function $W_{SV}(x,y)$) is, indeed, independent of z as in the considered prismatic shafts; see Remark 5.4 below.

We also note that the relation (87) of a vanishing weighted average of the gradient ∇W_{σ} in the warping stresses $\boldsymbol{\tau}_{W}$, together with the divergence free characteristic of the Saint–Venant stresses $\boldsymbol{\tau}_{SV}$, leads easily to $\int_{\Omega}\boldsymbol{\tau}d\Omega = 0$, that is, the total shear stresses in the proposed mixed formulation have indeed a zero resultant force. The expressions (175) and (176) giving these two components of the shear stress in terms of the Saint–Venant torque $T_{SV}(z)$ and the bishear $T_{W}(z)$ are the same as expressions for the original TWKV formulation. Hence, the arguments presented in Remark 3.3 in Section 3.2 above for that formulation apply exactly to the mixed formulation and so we conclude that the shear stresses (175)-(176) do have the correct resultant torque, the total internal torque $T(z)$ (i.e. $\int_{\Omega}\boldsymbol{\tau}\cdot\mathbb{J}d\Omega = T_{SV}(z)+T_{W}(z) = T(z)$ by (168)). Similarly, the resultant axial force and bending moments associated to the normal stress (177) vanish trivially given the normalizing conditions (46) and (47) imposed from the beginning on the Saint–Venant warping function $W_{SV}(x,y)$, its distribution function on the cross section (consistently weighted by $n_{E}(x,y)$).

All these results show that the proposed mixed formulation resolves the torque anomaly originally identified in Remark 2.3 for a general three–dimensional treatment of torsion with restrained warping and the stresses and strains created. Furthermore, in contrast with the direct approximations of the warping developed in Sections 3 and 4, this is accomplished with both avoiding a higher-order problem for the driving fields as well as vanishing stress and torque components like in the original TWKV formulation, involving in addition shear and axial stresses in equilibrium in contrast with the RBV formulation.

Remark 5.3. *The system of differential equations (174) driving the newly proposed mixed formulation is to be compared with the system of governing equations (107) for the RBV formulation. In fact, we see that we can we recover one from the other by switching*

$$\left\{\begin{matrix} RBV \\ formulation \end{matrix}\right\} \quad I_{\nabla W_{SV}} \quad \longleftrightarrow \quad \left(I_{W_{SV}}\right)^2 / I_{\nabla W_\sigma} \quad \left\{\begin{matrix} mixed \\ formulation \end{matrix}\right\} , \tag{180}$$

in their respective equations. As observed in the numerical evaluations presented in Section 7, this will have a significant overall effect in the predicted structural response of the shaft, like its flexibility. But note that the equations (107) or (174) are only used in determining the generalized displacements of the formulation $\phi(z)$ and $\lambda(z)$ or $\lambda_\varepsilon(z)$ which, in turn, define the amplitude of other quantities like stresses and warping displacements. At that level, the RBV and mixed formulations consider completely different distributions. In particular, the stresses for the RBV have been shown in Section 4.3 not to be in equilibrium, as opposed to the stresses predicted by the current mixed formulation, as described in this section. □

Remark 5.4. *A careful look at the developments presented in this section shows that the resulting structural model based on the fields $\phi(z)$ and $\lambda_\varepsilon(z)$ applies to a shaft exhibiting a varying cross section or material parameters in z, along the shaft's length L. Even though we have not reflected this in the notation employed, the starting assumed distributions (155) and (156) are built with the particular warping functions $W_{SV}(x,y)$ and $W_\sigma(x,y)$ obtained for the particular cross section at any fixed $z \in [0,L]$, also involving the particular material distributions $n_{_G}(x,y)$ and $n_{_E}(x,y)$ and material parameters $\bar{G}$ and $\bar{E}$ for that section at z. All the calculations leading from there to the functional (163) are to be understood for a particular cross section at any*

given $z \in [0, L]$. The resulting section constants and material parameters involved in this functional may then be functions of z, a fact that have been taken into account in deriving the governing equations from it, leading to the final system of equations (174) where the different derivatives in z are to be understood applying to the different expressions as grouped. Note also the validity of the argument behind the relation (172) between averages over the cross sections in this more general setting. In general, then, one may consider the trivial extension of varying section with simply $J(z)$, $I_{W_{SV}}(z)$ and $I_{\nabla W_\sigma}(z)$, neglecting other effects of the tapering of the shaft, as it is customary in similar simplified treatments of tapered beams in beam theory. See e.g. Timoshenko & Goodier *[1951], page 341, or* Sokolnikoff *[1956], page 186, for the analysis of shaft of varying circular cross section. Still, one must be aware that the equilibrium relations for the section stresses are then only approximation as pointed out in deriving equation (178), even though the differences are usually neglected on practical grounds. Similar comments apply exactly to the direct formulations discussed in previous sections.* □

5.3. The TWKV formulation as the constrained limit of the mixed formulation.

As we did for the RBV formulation, it is interesting to understand the limit process (or processes) that recover the original TWKV constrained formulation in this case for the current mixed formulation. To this purpose, it proves convenient to eliminate the mixed fields $\varepsilon(z)$ and $\sigma(z)$ in the Hu–Washizu functional (163), obtaining the two–field functional

$$\Pi^{(MIX)}(\phi, \lambda_\varepsilon) = \int_0^L \Big[\frac{1}{2}\,\bar{G}J\,(\phi')^2 + \frac{1}{2}\,\bar{G}\frac{\big(I_{W_{SV}}\big)^2}{I_{\nabla W_\sigma}}\,(\phi' - \lambda_\varepsilon)^2 + \frac{1}{2}\,\bar{E}I_{W_{SV}}\,(\lambda_\varepsilon')^2\Big]dz + \Pi_{ext}(\phi)\;, \qquad (181)$$

in the two unknown fields $\phi(z)$ and $\lambda_\varepsilon(z)$. Taking the variation of this functional results directly in the system of differential equations (174) in weak form. In this way, the functional (181) defines a new direct formulation for restrained warping based on the kinematics defined by the assumed warping displacement (156). This is indeed the case but hidden in all this are the mixed distributions (155) for the normal strain and stresses, the (average) mixed treatment required for the compatibility relation in the formulation

and, similarly, the proper (mixed) average boundary condition (170). For all these reasons, we still refer to such direct formulation as mixed, and actually prefer to consider the original Hu–Washizu functional (163).

In any case, the availability of the functional (181) allows us to easily compare the current mixed formulation with the TWKV formulation of Section 3. Indeed, comparing the direct functional (181) with the functional (71) for the original TWKV formulation, we see that the latter formulation is recovered if one imposes the constraint

$$\varpi_\varepsilon(z) := \phi'(z) - \lambda_\varepsilon(z) = 0 \quad \Longrightarrow \quad \lambda_\varepsilon(z) = \phi'(z) \,, \tag{182}$$

in the constrained limit. This expression defines the warping lag $\varpi_\varepsilon(z)$ encompassed by the mixed formulation, similar to the warping lag $\varpi(z)$ in (106) for the RBV formulation. Note that not only we recover the functional of the TWKV formulation by imposing the constraint (182), but also the assumed warping displacement (52) (that is, $\phi'(z)\, W_{SV}(x,y)$ along the shaft) from the new expression (156) and, thus, the boundary condition restraining the warping (that is, $\phi'(0) = 0$).

In turn, and as occurred for the RBV formulation discussed in Section 4.2, we can see that the functional (181) enforces the constraint (182) in two ways. That is, it accomplishes its enforcement with large values of the non–dimensional penalty parameter

$$\kappa_t^{(MIX)} := \frac{\left(I_{W_{SV}}\right)^2}{J\; I_{\nabla W_\sigma}} \,, \tag{183}$$

and by recovering the underlying Saint–Venant torsion for long shafts, encountering the two previous direct formulations in that limit too. The parameter $\kappa_t^{(MIX)}$ is easily obtained by writing the functional (181) in non-dimensional form; further details are omitted. Note only that

$$I_{\nabla W_\sigma} \sim (length)^8 \quad \text{and, again,} \quad I_{W_{SV}} \sim (length)^6 \,,\; J \sim (length)^4 \,, \tag{184}$$

for the dimensions of the involved section constants. See Remark 5.5 for details on the limiting process for long shafts.

The parameter $\kappa_t^{(MIX)}$ in (183) is the counterpart of the penalty parameter (110) obtained for the previous RBV formulation, after comparing their corresponding definitions. In fact, this relation is clear given the analogy

(180), depending only on the cross section geometry. Furthermore, as occurred for the RBV formulation, the numerical evaluations presented in Section 7 show that it drives the limit $\kappa_t^{(MIX)} \to \infty$ for open thin–walled sections as $t/h \to 0$, whereas it remains finite for closed (hollow) thin–walled sections and, thus, the mixed and TWKV produce significantly different results when modeling the restrained warping of solid/hollow shafts.

It is interesting to compare in more detail the penalty parameter (183) identified for the current mixed formulation with the corresponding parameter (110) for the RBV formulation. In fact, we easily observe that

$$\frac{\kappa_t^{(RBV)}}{\kappa_t^{(MIX)}} = \frac{I_{\nabla W_{SV}}/J}{\left(I_{W_{SV}}\right)^2/(JI_{\nabla W_\sigma})} = \frac{I_{\nabla W_{SV}}\, I_{\nabla W_\sigma}}{\left(I_{W_{SV}}\right)^2} \geq 1 \tag{185}$$

$$\Longrightarrow \quad \boxed{\kappa_t^{(RBV)} \geq \kappa_t^{(MIX)}}\,, \tag{186}$$

where the inequality in equation (185) follows from

$$\underbrace{\left|\int_\Omega n_{_E}\,(W_{SV})^2\,d\Omega\right|^2}_{\left(I_{W_{SV}}\right)^2} = \left|\int_\Omega n_{_G} \nabla W_\sigma \cdot \nabla W_{SV} d\Omega\right|^2$$

$$\leq \underbrace{\left(\int_\Omega n_{_G} \|\nabla W_\sigma\|^2 d\Omega\right)}_{I_{\nabla W_\sigma}} \underbrace{\left(\int_\Omega n_{_G} \|\nabla W_{SV}\|^2 d\Omega\right)}_{I_{\nabla W_{SV}}}, \tag{187}$$

after using, first, part of the result (81) and, second, the Cauchy-Schwarz inequality for the $n_{_G} > 0$ weighted inner product. The limit process to the constrained TWKV formulation driven by this parameter is then expected to be more dominant for the RBV formulation.

Since the original TWKV is to be expected to be more stiff that any of the other two formulations given its constrained character (unrealistically over–stiff as shown in the numerical evaluations presented in Section 7), the inequality (186) point to the stiffer response predicted by the RBV formulation, again an over–stiff response when compared with full three–dimensional simulations of elastic solids presented in that section. We carry out this numerical evaluation in Section 7 for the model problem considered next.

Remark 5.5. *As discussed in Remarks 3.2 and 4.1 for the TWKV and RBV formulations, respectively, an easy way to characterize the limiting process involved for long shafts is by considering a prismatic shaft with non–varying section constants along its length, loaded at one end and fully restrained at the other, as shown in Figure 1. In this case, straightforward algebraic manipulations eliminating the field $\lambda_\varepsilon(z)$ reduce the system of equations (174) to the (high order) equation (73) with now*

$$L_T^{(MIX)} := \sqrt{\frac{\bar{E} I_{W_{SV}}}{\bar{G} J}\, \alpha^{(MIX)}}\ , \qquad \text{for} \quad \alpha^{(MIX)} := 1 + \frac{J\, I_{\nabla W_\sigma}}{\left(I_{W_{SV}}\right)^2} = 1 + \frac{1}{\kappa_t^{(MIX)}} \quad \left(> 1 = \alpha^{(TWKV)} \right)\ , \tag{188}$$

for the characteristic length of interest here; further details are omitted. Hence, the mixed formulation will recover effectively the global structural response of the shaft associated with the underlying Saint–Venant torsion for shafts of length $L \gg L_T^{(MIX)}$. Obviously, and as noted for the previous formulations too, this limit can also be materialized (trivially but unrealistically) by neglecting the section warping constant $I_{W_{SV}}$, leading to the vanishing of the characteristic length $L_T^{(MIX)}$ in (188). The connection of this characteristic length with the penalty parameter $\kappa_t^{(MIX)}$ shown by relation (188) implies that

$$L_T^{(TWKV)} < L_T^{(RBV)} \leq L_T^{(MIX)}\ , \tag{189}$$

with the later inequality following from the result (186). Because of the arguments indicated in Remark 4.1, based on the vanishing of the Saint–Venant torque at restrained supports in the TWKV formulation, the mixed formulation will produce a much more effective way to reach the Saint–Venant torsion solution for long shafts than the original constrained TWKV formulation. Numerical tests also reveal an improved performance by the current mixed formulation when compared to the RBV formulation. □

Remark 5.6. *Some more insight on the arguments behind the newly proposed mixed formulation developed in this section can be obtained by noting that the second equation in the system (174) can be rewritten as*

$$\lambda_\varepsilon(z) = \phi'(z) + \frac{\bar{E}}{\bar{G}}\, \frac{I_{\nabla W_\sigma}}{I_{W_{SV}}}\, \varepsilon'(z)\ , \tag{190}$$

assuming again, without loss of generality, constant section parameters as in the previous remark. In this way, we can see that new independent field $\lambda_\varepsilon(z)$, the amplitude of the average of the warping of the cross sections, differs from the rate of twist $\phi'(z)$ by the rate of the amplitude of the axial strain $\varepsilon'(z)$ (or, equivalently, axial stress rate $\sigma'(z)$). For a shaft fully free to warp at both ends and all along its lengths, this amplitude vanishes and we recover again the basic underlying Saint–Venant solution in this case, with $\lambda_\varepsilon(z) = \phi'(z)$ and vanishing bishear by the relation (168). □

6. A model problem

As discussed in Remarks 3.2, 4.1 and 5.5 for the three formulations under consideration, an evaluation of the features of the different formulations can be accomplished by considering a prismatic shaft of length L, with non–varying section constants along its length, subjected only to a torque T_L or, equivalently, the associated tip rotation ϕ_L at one end, free otherwise, while the other end is not allowed to rotate nor warp. This is the case depicted in Figure 1.

With $t_{ex}(z) = 0$, equation (68) for the TWKV formulation or the first equation of the systems of equations (107) and (174) for the RBV and mixed formulations, respectively, can be easily integrated once. The resulting value corresponds to the total internal torque $T(z) = T_L$, constant along the shaft. For the TWKV formulation this results already in the third order equation (73) on the twist rotation $\phi(x)$. For the RBV and mixed formulations, the respective additional independent fields $\lambda(z)$ and $\lambda_\varepsilon(z)$ can be eliminated using the second equation in those systems, arriving also a third oder ordinary differential equation in $\phi(z)$. Similarly, one may also reduce the boundary conditions for that equation to the same form for the different formulations. Further details are omitted. The resulting boundary–value problem has been summarized in Box 1, following much of the notation introduced in those remarks. To gain a better physical insight, we have reverted the problem to its full dimensional form.

6.1. The exact solution in closed–form

A look at Box 1 leads to a few observations. First, we can observe that all the three formulations result in a similar effective problem along the shaft's length for this case, a third order differential equation on $\phi(z)$ with different values of the warping constant, denoted generically by $I^{\mathit{eff}}_{W_{SV}}$ in Box

Box 1: Differential equation for a prismatic shaft: a summary.

Differential equation for a prismatic shaft of length L, with a fixed end and no warping at $x = 0$, and a free end at $x = L$ with a torque T_L applied:

$$\left.\begin{aligned} &\bar{G}J\phi'(z) - \bar{E}I^{\mathit{eff}}_{W_{SV}}\phi'''(z) = T_L \ , \\ &\phi(0) = 0 \ , \quad \phi'(0) = \phi'^{\mathit{eff}}_0 \ , \quad \phi''(L) = 0 \ , \end{aligned}\right\}$$

with the effective warping constant $I^{\mathit{eff}}_{W_{SV}} := I_{W_{SV}}\alpha^{\mathit{eff}}$ for the (non–dimensional) parameter $\alpha^{\mathit{eff}} \geq 1$ given by

$$\alpha^{\mathit{eff}} = \begin{cases} 1 \ , & \text{for the TWKV formulation,} \\ 1 + \dfrac{J}{I_{\nabla W_{SV}}} \ , & \text{for the RBV formulation,} \\ 1 + \dfrac{J}{(I^2_{W_{SV}}/I_{\nabla W_\sigma})} \ , & \text{for the mixed formulation,} \end{cases}$$

and the effective warping restraining at the shaft's root ϕ'^{eff}_0 given by

$$\phi'^{\mathit{eff}}_0 = \Theta_{T_L}\,\frac{\alpha^{\mathit{eff}} - 1}{\alpha^{\mathit{eff}}} \qquad \text{for} \qquad \Theta_{T_L} := \frac{T_L}{\bar{G}J} \ ,$$

the rate of twist in Saint-Venant's torsion.

1. Interestingly, the different formulations result in a different rate of twist $\phi'(0) = \phi'^{\mathit{eff}}_0$ at the fixed end, the different values related on the resolution of the torque anomaly discussed in the previous sections. They correspond to $\phi'(0) = 0$ for the TWKV formulation, $\lambda(0) = 0$ for the RBV formulation by equation (96), and $\lambda_\varepsilon(0) = 0$ by (170) for the newly proposed mixed formulation. Remarkably, the latter two do allow a rate of twist $\phi'(0) \neq 0$ at the shaft's root. We can observe that $\phi'^{\mathit{eff}}_0 < \widetilde{\Theta}_{T_L} = T_L/(\bar{G}J)$, the rate of twist for the Saint-Venant solution with unrestrained (uniform) warping.

As noted in (180), the effective values in the resulting problem for the RBV and mixed formulations can be obtained from each other by the con-

sideration of the section constants $I_{\nabla W_{SV}}$ and $I^2_{W_{SV}}/I_{\nabla W_\sigma}$, respectively. These values, normalized by the torsional constant J, actually define the parameter κ_t identified in equations (110) and (183) for the RBV and mixed formulations, respectively, which drive these formulations to the constrained limit defined by the TWKV formulation. In fact, the non–dimensional parameter α^{eff} in Box 1 defining the effective warping constant $I^{\mathit{eff}}_{W_{SV}}$ and effective boundary condition can be written as

$$\alpha^{\mathit{eff}} = 1 + \frac{1}{\kappa_t} \,, \tag{191}$$

for those two formulations with those particular parameters κ_t, and even for the TWKV by simply considering $\kappa_t = \infty$ in this case. Clearly, the constrained TWKV formulation is recovered by both the RBV and mixed formulation in the limit $\kappa_t \to \infty$ for its corresponding values. Recall from the result (186) that $\kappa_t^{(RBV)} \geq \kappa_t^{(MIX)}$.

The solution of the differential equation presented in Box 1 can be written in terms of non-dimensional quantities as

$$\boxed{\phi(z) = \widetilde{\Theta}_{T_L}\, \widetilde{z} + \left(\widetilde{\Theta}_0 - \widetilde{\Theta}_{T_L}\right) \frac{\tanh(\rho)}{\rho} \left(1 - \frac{\sinh(\rho(1-\widetilde{z}))}{\sinh(\rho)}\right) \,,} \tag{192}$$

for $\widetilde{z} := z/L \in [0,1]$, $\widetilde{\Theta}_{T_L} := \Theta_{T_L} L = T_L L/(\bar{G}J)$, $\widetilde{\Theta}_0 := \phi'^{\mathit{eff}}_0 L$, and

$$\rho := \frac{L}{L_T} \quad \text{for} \quad L_T := \sqrt{\frac{\bar{E} I_{W_{SV}}}{\bar{G}J}\, \alpha^{\mathit{eff}}} \,, \tag{193}$$

as some algebraic manipulations show. The length parameter L_T corresponds to the parameters identified in Remarks 3.2, 4.1 and 5.5 for the different formulations. In particular, recall the inequalities (189) relating L_T for the three formulations under consideration.

We can recognize in $\widetilde{\Theta}_{T_L}$ as the (non-dimensional) rate of twist of the underlying Saint-Venant solution with uniform warping. In fact, we can easily see that we recover that solution (the first term in (192)) when $\rho \to \infty$. This can be accomplished if the warping stiffness is neglected (i.e. $I^{\mathit{eff}}_{W_{SV}} \to 0$) or, more realistically, for long shafts $L \gg L_T$, as discussed in those remarks. In this case, the effects of the restrained warping are effectively limited locally near the fixed end of the shaft.

Similarly, the solution (192) identifies $\widetilde{\Theta}_0\widetilde{z}$ as the limit solution when the restrained warping dominates ($\rho \to 0$). Note that this implies that $\phi(\widetilde{z}) \equiv 0$ in that limit for the TWKV formulation, that is, the shaft does not twist at all. This is the response then that this formulation does predict in the limit for short shafts. This situation is one more illustration of the constrained character of this formulation as discussed in Section 3.

Remark 6.1. *We note that the three formulations under consideration involve completely different warping and stress distributions across any given cross section, despite reducing to the same formal differential equation (up to the section constants involved) summarized in Box 1 for the model problem at hand. The evaluation of these different constants through a finite element approximation of the governing problems for the different warping functions at the section level does allow to obtain, besides the final coefficients of the governing equation in Box 1 with exact closed–form solution (192) for $\phi(z)$ and other structural fields along the shaft, the full characterization of these stresses and warping over the cross sections for the different formulations, a feature that we also compare in detail in our numerical evaluations presented below.* □

6.2. The shaft flexibility

Of interest is to obtain the twist rotation $\phi(L) = \phi_L$ at the tip of the shaft $z = L$ for the given torque T_L. Equation (192) results in

$$\phi_L = f_T\, T_L \qquad \text{for} \quad f_T = \frac{L}{\bar{G}J}\left(1 - \frac{\tanh(\rho)}{\alpha^{\mathit{eff}}\,\rho}\right) , \tag{194}$$

identifying the flexibility of the shaft at hand in torsion f_T. Note that $f_T < f_T^{(SV)} = L/(\bar{G}J)$ (the flexibility of the shaft given by Saint-Venant's solution with unrestrained uniform warping), because $\alpha^{\mathit{eff}} \geq 1$ and $\tanh(\rho) < \rho$ since $\rho > 0$. This feature was expected given the stiffening character that restraining the warping has in the shaft structural response. Note that this observation applies to all three formulations considered here in modeling that warping.

In fact, a careful analysis reveals that $f_T \to f_T^{(SV)}$ in the limit $\rho \to \infty$ and, thus, recovering Saint–Venant torsion for long shafts $L \gg L_T$. As argued in previous sections, this situation is to be expected, and it is replicated by all the considered formulations. Obviously, these arguments also show that this

response is also obtained for $I_{W_{SV}} \to 0$ (so $\rho \to \infty$ too), leading effectively to no restrained warping inside the shaft at all.

More interesting is the treatment that the different formulations apply to the opposite limit $\rho \to 0$ while keeping finite the warping constant $I_{W_{SV}}$, that is, for short shafts $L \ll L_T$ keeping the cross section properties finite ($I_{W_{SV}} < \infty$). In this case, after noting that $\tanh(\rho)/\rho \to 1$ and that $\alpha^{\mathit{eff}} = 1$ for the original TWKV formulation, we obtain

$$f_T \to 0 \ , \qquad \text{for the TWKV formulation} \ , \tag{195}$$

whereas

$$f_T \to f_T^{(SV)} \cdot \begin{cases} \dfrac{1}{1 + (I_{\nabla W_{SV}}/J)} \ , & \text{for the RBV formulation} \ , \\ \dfrac{1}{1 + I_{W_{SV}}^2/(I_{\nabla W_\sigma} J)} \ , & \text{for the mixed formulation} \ , \end{cases} \tag{196}$$

both limits again smaller than the Saint-Venant flexibility $f_T^{(SV)}$, but not vanishing in contrast to the TWKV formulation in (195). In fact, given the inequality (187), we conclude that

$$0 = f_T^{(TWKV)} < f_T^{(RBV)} \leq f_T^{(MIX)} < f_T^{(SV)} \ , \tag{197}$$

in the limit $\rho \to 0$. The over constrained character of the TWKV formulation is again evident with these arguments.

6.3. The internal torque, bishear and bimoment diagrams along the shaft

The three considered formulations share the same expression for the Saint-Venant part of the internal torque $T_{SV}(z) = \bar{G}J\phi'(z)$, as pointed by equations (61), (112) and (168), for the TWKV, RBV and mixed formulations, respectively. Hence, we obtain

$$T_{SV}(z) = T_L \left(1 - \frac{\cosh(\rho(1-\widetilde{z}))}{\alpha^{\mathit{eff}} \cosh(\rho)}\right) \tag{198}$$

$$= \phi_L \frac{\bar{G}J}{L} \, \rho \, \frac{\alpha^{\mathit{eff}} \cosh(\rho) - \cosh(\rho(1-\widetilde{z}))}{\alpha^{\mathit{eff}} \rho \cosh(\rho) - \sinh(\rho)} \ , \tag{199}$$

for the problem at hand in terms of the tip torque T_L or, alternatively, the tip rotation ϕ_L, the later using the relation (194) for the shaft's flexibility. The differential equation in Box 1 corresponds to the balance of torque along the

shaft, giving a constant total internal torque $T(z) = T_L$, in the current case with no distributed external torque per unit length. Hence, the bishear is given trivially in this case by $T_W(z) = T_L - T_{SV}(z)$, leading to the distribution

$$T_W(z) = T_L \, \frac{\cosh(\rho(1-\widetilde{z}))}{\alpha^{\mathit{eff}} \cosh(\rho)} \tag{200}$$

$$= \phi_L \frac{\bar{G}J}{L} \, \rho \, \frac{\cosh(\rho(1-\widetilde{z}))}{\alpha^{\mathit{eff}} \rho \cosh(\rho) - \sinh(\rho)} \, , \tag{201}$$

given again in terms of the tip total torque T_L and, alternatively, of the tip rotation ϕ_L.

The corresponding values of these two parts of the total internal torque at the root $z = 0$ of the shaft are then given by

$$T_{SV}(0) = T_L \, \frac{\alpha^{\mathit{eff}} - 1}{\alpha^{\mathit{eff}}} \quad \text{and} \quad T_W(0) = T_L \, \frac{1}{\alpha^{\mathit{eff}}} \, , \tag{202}$$

for the Saint-Venant and bishear, respectively, in terms of the tip torque T_L. It is interesting to note that these values depend only on the total torque T_L at the opposite end of the shaft, independent of the parameter ρ and hence the shaft length L. On the other hand, at the tip of the shaft $z = L$, we obtain

$$T_{SV}(L) = T_L \, \left(1 - \frac{1}{\alpha^{\mathit{eff}} \cosh(\rho)} \right) \quad \text{and} \quad T_W(L) = T_L \, \frac{1}{\alpha^{\mathit{eff}} \cosh(\rho)} \, , \tag{203}$$

depending on the length of the shaft through the non-dimensional parameter ρ, although we recover the limit

$$T_{SV}(L) = T_L \quad \text{and} \quad T_W(L) = 0 \qquad \text{for} \quad \rho \to \infty \, , \tag{204}$$

corresponding to long shafts $L \gg L_T$, as expected. The observation made in Section 3.2 that all the torque at the root of the shaft comes from the bishear in the original TWKV formulation is confirmed by the relations (202) after noting that $\alpha^{\mathit{eff}} = 1$ for this formulation. This is not the case for the RBV and mixed formulations.

The bimoment $B_W(z)$ can be obtained by equilibrium, that is, by $T_W(z) = -dB_W/dz$, a relation holding for the three formulations under consideration.

Noting that $B_W(L) = 0$ in all cases (free warping at the tip), we obtain

$$B_W(z) = T_L L \, \frac{\sinh(\rho(1-\widetilde{z}))}{\alpha^{\mathit{eff}} \rho \cosh(\rho)} \tag{205}$$

$$= \phi_L \bar{G} J \, \frac{\sinh(\rho(1-\widetilde{z}))}{\alpha^{\mathit{eff}} \rho \cosh(\rho) - \sinh(\rho)} \, , \tag{206}$$

after integrating the bishear distribution (200)-(201). Note also that the differential equation in Box 1 corresponds to the decomposition of the constant total internal torque as $T(z) = T_{SV}(z) + T_W(z) = T_L$ for each of the terms in that equation, so we also have

$$T_W(z) = -\bar{E} I_{W_{SV}}^{\mathit{eff}} \phi'''(z) = -\bar{E} I_{W_{SV}} \alpha^{\mathit{eff}} \phi'''(z) \, , \tag{207}$$

and

$$B_W(z) = \bar{E} I_{W_{SV}} \alpha^{\mathit{eff}} \phi''(z) \, , \tag{208}$$

both results for the problem at hand, with the latter resulting from the former relation after using again the relation $T_W = -dB_W/dz$ with the boundary condition $\phi''(L) = 0$ included in Box 1 to impose $B_W(L) = 0$. These relations give an alternative way to obtain the distributions (201) and (206) directly from the closed–form solution (192) for the twist rotation $\phi(z)$. Note the relation of the non–dimensional parameter ρ in (193) with the material moduli and different torsional constants when carrying out these arguments.

The value of the bimoment at the shaft's root $z = 0$ is then given by

$$B_W(0) = T_L L_T \, \frac{\tanh(\rho)}{\alpha^{\mathit{eff}}} \, , \tag{209}$$

in terms of the value T_L of the total torque at the opposite end. In this case, this value depends on the length of the shaft, through the non-dimensional parameter ρ. However, it is interesting to observe that for long shafts $L \gg L_T$, we obtain

$$B_W(0) = T_L \, L_T \, \frac{1}{\alpha^{\mathit{eff}}} \qquad \text{for} \quad \rho \to \infty \, , \tag{210}$$

a constant finite value depending explicitly on the characteristic length L_T defined by (193) for each formulation.

6.4. The shear and normal stresses over the cross sections

The shear stresses for the TWKV and mixed formulations share the form of their distributions on a given cross section cross section, as given by equations (83) and (175)-(176), respectively. They have a Saint–Venant component $\boldsymbol{\tau}_{SV}$ proportional to $n_{G}(x,y)\,(\nabla W_{SV}+\mathbb{J})$ by the Saint-Venant torque $T_{SV}(z)/J$ and a warping component proportional to $n_{G}(x,y)\nabla W_{\sigma}$ by the bishear $T_{W}(z)/I_{W_{SV}}$. Note that these amplitudes, even if given by relations (198)-(201), will differ in actual values for each formulation. In particular, we have

$$T_{SV}(0)=0 \quad \text{for the TWKV formulation}\,, \tag{211}$$

as observed in Section 3.2 and, directly, by expression (202) with $\alpha^{\mathit{eff}}=1$, while it does not vanish for the mixed formulation.

The form of the shear stresses for the RBV formulation (117) is completely different. While they still involve the same expression for the Saint –Venant component $\boldsymbol{\tau}_{SV}$ proportional to $n_{G}(x,y)\,(\nabla W_{SV}+\mathbb{J})$ by $T_{SV}(z)/J$, the warping component $\boldsymbol{\tau}_{W}$ in (120) is now given in terms of $n_{G}(x,y)\nabla W_{SV}$ instead of $n_{G}(x,y)\nabla W_{\sigma}$, and proportional to the bishear in the combination $-T_{W}(z)/I_{\nabla W_{SV}}$. Hence, these two components directly combine. In particular, since we have

$$\frac{T_{SV}(0)}{J}-\frac{T_{W}(0)}{I_{\nabla W_{SV}}}=\frac{1}{J}\Big(T_{SV}(0)-(\alpha^{\mathit{eff}}-1)\,T_{W}(0)\Big)=0\,, \tag{212}$$

after using the result (202) and the definition of the non-dimensional parameter α^{eff} in Box 1 for the RBV formulation, the distribution of the total shear stress at the fixed end $z=0$ is given by

$$\boldsymbol{\tau}(x,y,0)=\frac{T_{SV}(0)}{J}\,\mathbb{J}=T_{L}\frac{\alpha^{\mathit{eff}}-1}{\alpha^{\mathit{eff}}\,J}\,\mathbb{J}=\frac{T_{L}}{\alpha^{\mathit{eff}}\,I_{\nabla W_{SV}}}\,\mathbb{J}\qquad\text{(RBV)}\,. \tag{213}$$

This distribution corresponds, graphically, to the stress vectors $\boldsymbol{\tau}=[\tau_{xz},\tau_{yz}]^{T}$ describing a rotation about the center of twist $\bar{\boldsymbol{x}}_{T}$, regardless of the shape of the cross section itself. The general lack of satisfaction by these stresses of equilibrium and, in particular, the proper boundary conditions along the section's boundary is clear, confirming the general analysis presented in Section 4.3 for this formulation.

The final explicit expressions of the components $\boldsymbol{\tau}_{SV}$ and $\boldsymbol{\tau}_{W}$ of the shear stresses $\boldsymbol{\tau}=\boldsymbol{\tau}_{SV}+\boldsymbol{\tau}_{W}$ can be easily obtained from the torque distributions

$T_{SV}(z)$ and $T_W(z)$ above. In particular, we have

$$\boldsymbol{\tau}_{SV}(x,y,z)/\bar{G} = \Theta_{T_L}\left(1 - \frac{\cosh(\rho(1-\widetilde{z}))}{\alpha^{\mathit{eff}}\cosh(\rho)}\right) n_{G}\left[\nabla W_{SV} + \mathbb{J}\right](x,y)\ , \quad (214)$$

for the Saint-Venant component, and

$$\boldsymbol{\tau}_{W}(x,y,z)/\bar{G} = \Theta_{T_L}\frac{\cosh(\rho(1-\widetilde{z}))}{\alpha^{\mathit{eff}}\cosh(\rho)} n_{G}\cdot\begin{cases} \dfrac{J}{I_{W_{SV}}}\ \nabla W_{\sigma}(x,y) & \begin{pmatrix}\text{TWKV}\\ \text{\& mixed}\end{pmatrix}\ , \\[2ex] -\dfrac{J}{I_{\nabla W_{SV}}}\ \nabla W_{SV}(x,y) & \text{(RBV)}\ , \end{cases} \quad (215)$$

for the warping component, where the rate of twist Θ_{T_L} can be written alternatively as

$$\Theta_{T_L} = \frac{T_L}{\bar{G}J} = \frac{\phi_L}{L}\,\frac{\alpha^{\mathit{eff}}\rho\cosh(\rho)}{\alpha^{\mathit{eff}}\rho\cosh(\rho) - \sinh(\rho)}\ , \quad (216)$$

in terms of the torque T_L at the shaft's tip or the tip rotation ϕ_L using the relation (199).

Furthermore, the developments in the previous sections (in particular, relations (76), (116) and (177)) show that the normal stress distribution $\sigma_z(x,y,z)$ in the shaft can be written in all three formulations as

$$\sigma_z(x,y,z) = \sigma(z)\ n_{E}(x,y)\ W_{SV}(x,y) \quad \text{for} \quad \sigma(z) = B_W(z)/I_{W_{SV}}\ , \quad (217)$$

thus all sharing the same distribution $n_{E}(x,y)\ W_{SV}(x,y)$ on a given cross section, with the magnitude determined by the bimoment $B_W(z)$ given by (205)-(206). Note that the units of the parameter $\sigma(z) \sim (stress)\cdot length^{-2}$, as in (152) for the mixed formulation. Using equation (208), a general expression of these stresses is given by the relation

$$\sigma_z(x,y,z)/\bar{E} = \Theta_{T_L}\,\frac{\sinh(\rho(1-\widetilde{z}))}{L_T\cosh(\rho)}\, n_{E}(x,y)\, W_{SV}(x,y)\ , \quad (218)$$

explicitly in terms of the second derivative of the closed–form solution (192).

Remark 6.2. *For later reference in the evaluation of the different formulations presented in the next section is the value of these stresses at the shaft's root $z = 0$. In this case, the distributions (214), (215) and (218) reduce to*

$$\boldsymbol{\tau}_{SV}(x,y,0)/\bar{G} = \Theta_{T_L}\,\frac{\alpha^{\mathit{eff}} - 1}{\alpha^{\mathit{eff}}}\ n_{G}(x,y)\ \left[\nabla W_{SV} + \mathbb{J}\right](x,y)\ , \quad (219)$$

$$\boldsymbol{\tau}_{W}(x,y,0)/\bar{G} = \Theta_{T_L}\, n_{G}(x,y) \cdot \begin{cases} \dfrac{J}{I_{W_{SV}}\alpha^{\mathit{eff}}}\, \nabla W_{\sigma}(x,y) & \begin{pmatrix} TWKV \\ \&\ mixed \end{pmatrix}, \\[2ex] -\dfrac{\alpha^{\mathit{eff}}-1}{\alpha^{\mathit{eff}}}\, \nabla W_{SV}(x,y) & (RBV), \end{cases} \tag{220}$$

$$\sigma_{z}(x,y,0)/\bar{E} = \Theta_{T_L}\, \frac{\tanh(\rho)}{L_T}\; n_{E}(x,y)\; W_{SV}(x,y)\,, \tag{221}$$

with the total shear stress given simply by $\boldsymbol{\tau} = \boldsymbol{\tau}_{SV} + \boldsymbol{\tau}_{W}$*, all for the rate of twist* Θ_{T_L} *given by (216) in terms of the torque* T_L *at the shaft's tip or the tip rotation* ϕ_L*, as needed. We have written these expressions in such a way that both the (incorrect) total stress* $\boldsymbol{\tau}$ *in (213) for the RBV formulation and the (unrealistic)* $\boldsymbol{\tau}_{SV} \equiv 0$ *for the TWKV formulation (with* $\alpha^{\mathit{eff}} = 1$*) are evident.* □

6.5. The warping of the cross sections

The distribution of the warping displacement for the TWKV formulation is easily obtained as

$$\begin{aligned} u_{z}(x,y,z) &= \phi'(z)\, W_{SV}(x,y) \\ &= \underbrace{\Theta_{T_L}\left(1 - \frac{\cosh(\rho(1-\widetilde{z}))}{\cosh(\rho)}\right)}_{:=\,\phi'(z)\Big|^{(TWK)}} W_{SV}(x,y) \qquad \text{(TWKV)}\,, \end{aligned} \tag{222}$$

where the rate of twist Θ_{T_L} is given by relation (216) in terms of the torque T_L or the rotation ϕ_L at the shaft's tip. Note that no α^{eff} parameter appears in this expression since $\alpha^{\mathit{eff}} = 1$ for the TWKV formulation. For the RBV and mixed formulations, the evaluation of the warping requires the additional fields $\lambda(z)$ and $\varepsilon(z)$, respectively.

The warping displacement amplitude field $\lambda(z)$ for the RBV formulation can be obtained easily by combining the two equations (104) and (208) for the bimoment, that is,

$$B_{W}(z) = \bar{E} I_{W_{SV}} \lambda'(z) = \bar{E} I_{W_{SV}} \alpha^{\mathit{eff}} \phi''(z)\,, \tag{223}$$

for the problem at hand. Hence, we obtain

$$\lambda(z) = \alpha^{\mathit{eff}} \left(\phi'(z) - \phi_0'^{\mathit{eff}} \right) = \Theta_{T_L} \left(1 - \frac{\cosh(\rho(1-\widetilde{z}))}{\cosh(\rho)} \right) , \tag{224}$$

after imposing the boundary condition $\lambda(0) = 0$, with $\phi_0'^{\mathit{eff}}$ defined in Box 1. The final warping displacement reads then, after some straightforward calculations, as

$$\begin{aligned} u_z(x,y,z) &= \lambda(z)\ W_{SV}(x,y) \\ &= \Theta_{T_L} \left(1 - \frac{\cosh(\rho(1-\widetilde{z}))}{\cosh(\rho)} \right)\ W_{SV}(x,y) \qquad \text{(RBV)} , \end{aligned} \tag{225}$$

showing then, remarkably, the same distribution (222) as for the original TWKV formulation. Note that the expressions, involving the parameter ρ, may be the same, but their values will be different in general, since ρ varies for each formulation, in particular depending on α^{eff} by the relation (193).

Finally, for the mixed formulation, the warping field $\lambda_\varepsilon(z)$ can be obtained in a similar manner, combining now relation (208) with equation (173), resulting in the relation

$$\lambda_\varepsilon(z) = \alpha^{\mathit{eff}} \left(\phi'(z) - \phi_0'^{\mathit{eff}} \right) = \Theta_{T_L} \left(1 - \frac{\cosh(\rho(1-\widetilde{z}))}{\cosh(\rho)} \right) , \tag{226}$$

exactly as we did when deriving equation (224) for the RBV formulation above. The final warping displacement reads then by (139)

$$\begin{aligned} u_z(x,y,z) &= \phi'(z)\ W_{SV}(x,y) + \frac{I_{W_{SV}}}{I_{\nabla W_\sigma}}\ (\phi'(z) - \lambda_\varepsilon(z))\ W_\sigma(x,y) \\ &= \Theta_{T_L} \left[\left(1 - \frac{\cosh(\rho(1-\widetilde{z}))}{\alpha^{\mathit{eff}} \cosh(\rho)} \right)\ W_{SV}(x,y) \right. \\ &\qquad \left. + \frac{J}{I_{W_{SV}}} \frac{\cosh(\rho(1-\widetilde{z}))}{\alpha^{\mathit{eff}} \cosh(\rho)}\ W_\sigma(x,y) \right] \qquad \text{(MIXED)} , \end{aligned} \tag{227}$$

after using the definition of the parameter α^{eff} in Box 1 for the mixed formulation in terms of the different torsional constants. We can observe that

the warping displacement (227) does not vanish pointwise at the root $z = 0$. Instead, and as discussed in Section 5.2, we have that $\lambda_\varepsilon(0) = 0$, a value that corresponds to the (weighted) average of the warping displacement (227) as shown in equation (160).

Notwithstanding the different values of the warping displacements predicted by the different formulations, we find remarkable that the actual parameter controlling the warping along the shaft for all three formulations coincides for the problem at hand, that is,

$$\phi'(z)\Big|^{(TWKV)} \triangleq \lambda(z)\Big|^{(RBV)} \triangleq \lambda_\varepsilon(z)\Big|^{(MIX)}, \tag{228}$$

all given by the expressions (222), (224) and (226), respectively. In (228), we have used the special symbol "$\triangleq$" to mean that those three fields share the same explicit expression, but that same expression will result in different values when used in combination with a particular formulation since it depends on ρ and, thus, on the α^{eff}, with a different value for each of the three formulations. Similarly, the first term in the triad (228) is to be understood as $\phi'(z)$ in the TWKV formulation, that is, precisely for $\alpha^{\mathit{eff}} = 1$ as indicated in equation (222). In this respect, $\lambda(z)$ or $\lambda_\varepsilon(z)$ are not equal to $\phi'(z)$ in the RBV and mixed formulations, but are related to this rate of twist as $\alpha^{\mathit{eff}}(\phi'(z) - \phi'^{\mathit{eff}}_0)$ by the (224) and (226), respectively. Note that this combination reduces to $\phi'(z)$ only for the TWKV formulation, where $\alpha^{\mathit{eff}} = 1$ and $\phi'^{\mathit{eff}}_0 = 0$.

In summary, the actual form of the warping distribution is the same for the TWKV and RBV (namely, (222) and (225), respectively) for the particular problem at hand, but different than the distribution (227) for the mixed formulation. All formulations will exhibit different values though, values that lead to different stresses and overall structural response of the shaft predicted by the different distributions as discussed above. We evaluate next the extent of these differences.

7. Numerical evaluation

The purpose of this section is to evaluate the different formulations considered in this work for the modeling of restrained warping in shafts in torsion, namely, the TWKV, the RBV and the mixed formulation described in the previous sections. The model problem considered in Section 6 provides an interesting context where to evaluate the common and different aspects

of these formulations, for different types of sections, together with a direct comparison with the solution obtained with a full use of three dimensional elasticity.

The three formulations require the Saint–Venant torsional constant J defined by equation (39) and the warping constant $I_{W_{SV}}$ defined by equation (64), both in terms of the Saint–Venant warping function $W_{SV}(x, y)$, solution of the (weighted) Laplace equation (33) satisfying the conditions (46) and (47). In addition, the RBV formulation involves the section constant $I_{\nabla W_{SV}}$, also defined in terms of that function in equation (102), whereas the mixed formulation considers the constant $I_{\nabla W_\sigma}$ given by equation (158) in terms of the second warping function $W_\sigma(x, y)$ solution of the (weighted) Poisson equation (79). We carry out the solution of these Laplace and Poisson problems with a 2D finite element formulation on the cross section, arriving to the evaluation of these different constants. We refer to Appendix A for some remarks of this finite element treatment, including some properties that the section constants computed this way satisfy.

We present next the results obtained for solid, open and closed (or hollow) thin–walled, and composite sections in Sections 7.1 to 7.5. The specific cross sections considered there are depicted in Figure 2. We follow the same plan of exposition for all these cases, pointing out in this way the similarities and differences among these different types of cross sections, emphasizing how the three different formulations approximate the response of the shaft for each of these possible section configurations. In all cases we also present a full three–dimensional finite element analysis of the full 3D solid shafts.

7.1. Evaluation for solid cross sections

We start considering the case of solid cross sections, through the common example provided by rectangular sections. As depicted in Figure 2, we consider a $h \times t$ rectangular section, keeping fixed the long side $h = 20\ cm$ and varying short side t in the range $0.1 \leq t/h \leq 1.0$, that is, from a relatively thin rectangle to a square section. Thin-walled cross sections, in open and closed configurations, are studied in detail in the following sections. The section is assumed made of an homogeneous linear elastic material, with a constant Young's modulus $E = 200\ GPa$ and Poisson's ratio $\nu = 0.3$, although the computations on the cross section for the warping functions $W_{SV}(x, y)$ and $W_\sigma(x, y)$ only require, trivially, the values $n_{_E} = 1.0$ and $n_{_G} = 1.0$, following the normalizations (3). In all cases, we consider regular finite element meshes of the cross sections with 20 elements per side. Without loss of generality, we

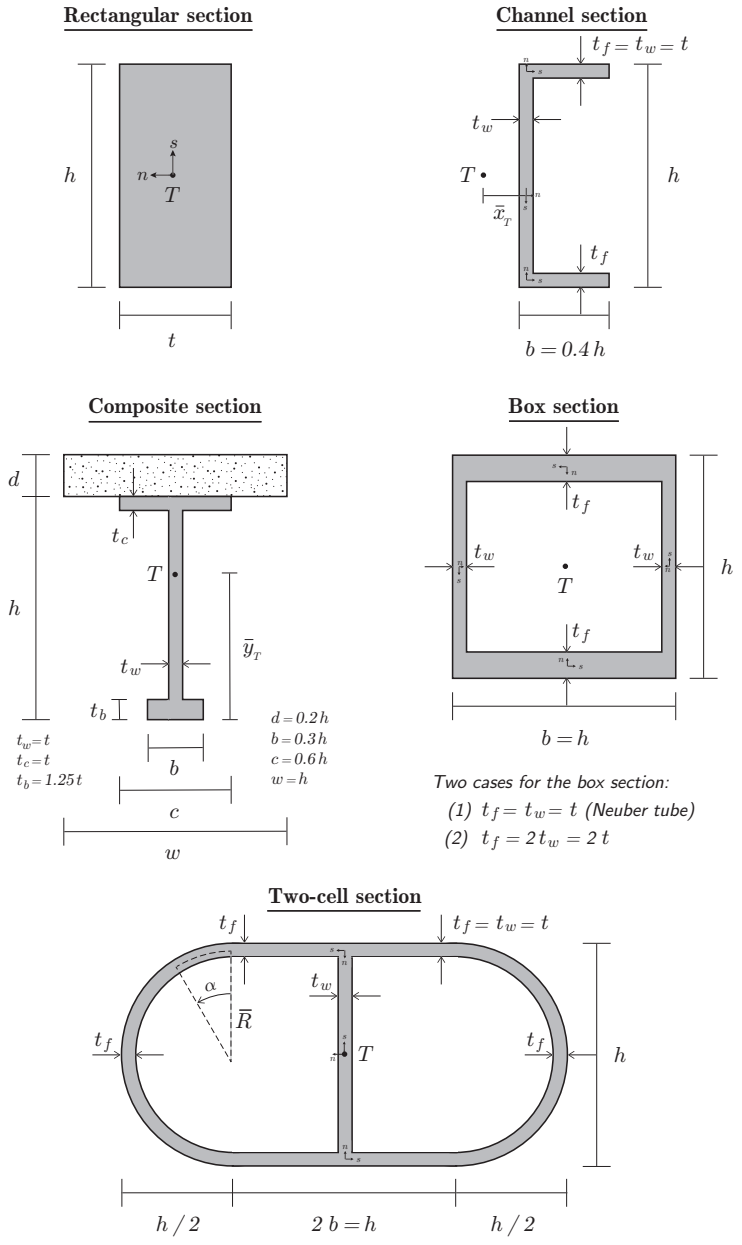

Figure 2: Numerical evaluation. Cases studied (clockwise from top left): rectangular solid section ($h = 20\ cm$, varying t), channel (open) thin–walled section ($h = 20\ cm$, varying t), hollow box thin–walled section ($h = 20\ cm$, varying t), two–cell thin–walled section ($h = 20\ cm$, varying t), and composite section ($h = 50\ cm$, $t = 2\ cm$). The centers of twist/shear T are shown, symmetrically located when not specified. The lengths h and b are defined from the outer walls.

consider 4-node bilinear elements for the interpolation of the warping functions. We note that with the double symmetry of the geometry of the cross section at hand (including the material distribution), the warping functions $W_{SV}(x, y)$ and $W_\sigma(x, y)$ solving the (Neumann) boundary-value problems (33) and (79), respectively, show (doubly) anti-symmetry.

Figure 3 depicts the computed warping functions $W_{SV}(x, y)$ (left column) and $W_\sigma(x, y)$ (right column) for the sections with aspect ratios $t/h = 1.0$, 0.5 and 0.1. Even though our implementation and different formulas in the paper do not rely on coordinate systems centered at specific points (centroid, shear center or alike) or aligned along particular directions (principal axis of inertia or related), the satisfaction of the normalizing conditions (46) and (47) is easily accomplished in this case since, due to the double symmetry of the section, both centroids $\bar{\boldsymbol{x}}_{_E} = \bar{\boldsymbol{x}}_{_G}$ and center of twist (shear center) $\bar{\boldsymbol{x}}_{_T}$ coincide trivially with the rectangle's center. The horizontal and vertical axes in Figure 2 correspond trivially to the inertia principal axes for this case.

In the same way, we compute the relevant torsional constants from the computed warping functions, using the standard 2×2 quadrature rule employed in the finite element simulations with the considered $4-$node bilinear element. Figure 4 shows the variation of J, $I_{W_{SV}}$, $I_{\nabla W_{SV}}$ and $I_{\nabla W_\sigma}$ with the section's aspect ratio t/h. The plot of the Saint–Venant torsional constant J shows also the value J_{exact} obtained by Fourier analysis[1]. A good agreement of the computed solution with this value can be observed in this figure in the whole range of considered aspect ratios t/h. For complete reference and verification, we have included in Table 1 the value of these constants for the specific section ratios $t/h = 1.0$, 0.5 and 0.1, corresponding to the specific cases presented in detail in what follows as representative cases.

The plots shown in Figure 4 also include the estimates for a thin–walled rectangle obtained in Appendix B.1 for all the different torsional constants. They indicate that the values obtained from the computed warping functions solving the exact section boundary–value problem capture well those thin–wall limit values in the lowest range of the t/h ratios considered (correct slopes). We note that the developments in this paper do not rely on these estimated limit values at all, depending on the torsional constants computed

[1] $J_{exact} = \frac{1}{3} h t^3 \left[1 - \frac{192 t}{\pi^5 h} \sum_{n \ odd} \frac{1}{n^5} \tanh\left(\frac{n\pi h}{2t}\right) \right]$; see e.g. Sokolnikoff [1956], page 132.

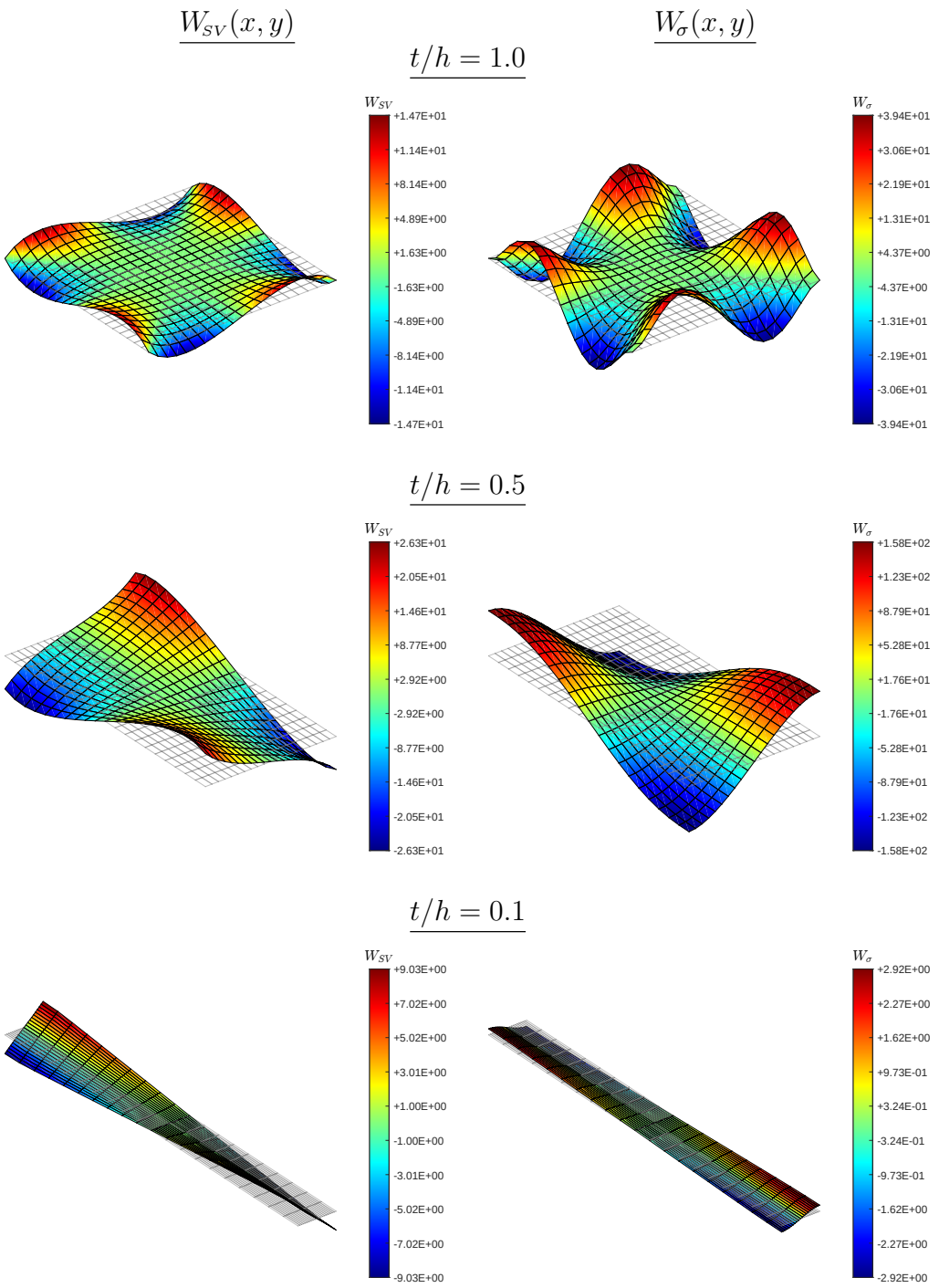

Figure 3: Rectangular cross section: warping functions. Computed warping functions $W_{SV}(x,y)$ (left) and $W_\sigma(x,y)$ (right) for sections with thickness ratios $t/h = 1.0, 0.5, 0.1$.

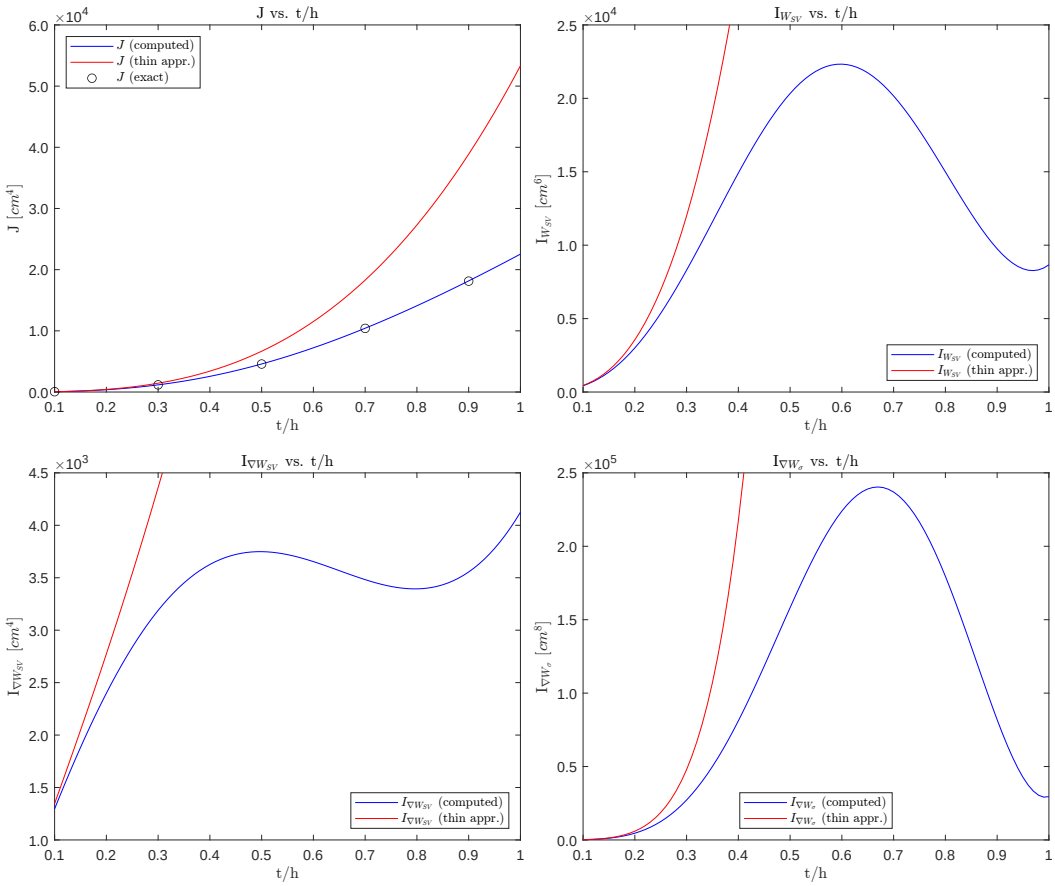

Figure 4: Rectangular cross section: torsional section properties. Values of the Saint–Venant torsional constant J, the warping constant $I_{W_{SV}}$ and the two gradient constants $I_{\nabla W_{SV}}$ and $I_{\nabla W_\sigma}$ for different t/h ratios.

Table 1: Rectangular cross section: table of torsional constants for different sections thickness ratio t/h ($h = 20\ cm$).

t/h	$J\ [cm^4]$	$I_{W_{SV}}\ [cm^6]$	$I_{\nabla W_{SV}}\ [cm^4]$	$I_{\nabla W_\sigma}\ [cm^8]$
1.0	$2.25416620{\cdot}10^4$	$8.66423278{\cdot}10^3$	$4.12500467{\cdot}10^3$	$2.94805924{\cdot}10^4$
0.5	$4.58455629{\cdot}10^3$	$2.03297383{\cdot}10^4$	$3.74877704{\cdot}10^3$	$1.58209907{\cdot}10^5$
0.1	$5.02809625{\cdot}10^1$	$4.25107929{\cdot}10^2$	$1.29638570{\cdot}10^3$	$1.67786200{\cdot}10^2$

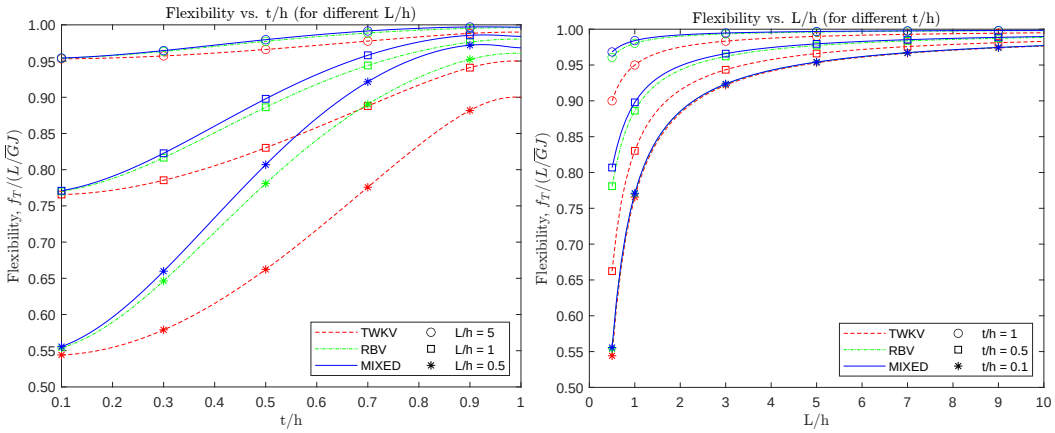

Figure 5: Rectangular cross section: shaft flexibility. Normalized torsional flexibility $f_T/(L/\bar{G}J)$ versus t/h (left) and L/h (right). All formulations tend to the Saint–Venant value ($f_T^{(SV)} = L/\bar{G}J$) for long shafts (large L/h).

by solving the associated boundary-value problems on the cross section. Still, we find interesting to report these limit values for their practical use in that thin–wall limit, if it applies for the case at hand. In addition, the solution of the problem on the cross section allows direct access to the warping functions for the particular cross section under consideration, and hence full details of the stresses acting on it.

We first compare the three different formulations of torsion with restrained warping considered in this work among themselves. To this purpose, Figure 5 depicts the non–dimensional flexibility $f_T/(L/\bar{G}J)$ in (194) for a shaft of length L, for the TWKV, RBV and mixed formulations. In particular, we include the variation of this flexibility with the section aspect ratio t/h for shafts of length $L/h = 5.0$, 1.0 and 0.5 (left plot), and its variation with the length L/h for the aspect ratios $t/h = 1.0$, 0.5 and 0.1 (right plot). We have taken the range of shaft's length starting at the, perhaps, unrealistic low value of $L/h = 0.5$ to explore the limits of the different expressions obtained in this work. Besides, we believe that these very short lengths provide a good test for the different formulations in resolving the local effects associated with retrained warping regardless of how long the shaft may be.

All the different cases considered in Figure 5 confirm the much stiffer character of the TWKV formulation, followed in order by the RBV and the mixed formulations, with the latter providing always the more flexible

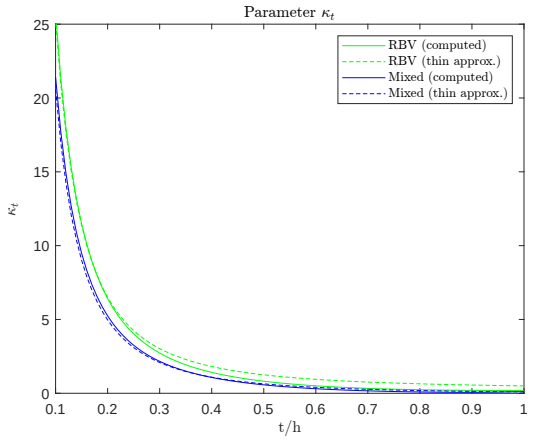

Figure 6: Rectangular cross section: parameter κ_t versus t/h. Geometric factor driving the limit process to the constrained TWKV formulation for the RBV and mixed formulations.

response, for all aspect ratios t/h and all shaft lengths L/h. The constrained character of the TWKV formulation leads physically to this stiffer response. The use of the Saint–Venant torsional constant J of the particular section t/h under consideration as normalization in the plots of Figure 5 allows to confirm the limit value of Saint–Venant torsion $f_T^{(SV)} = L/\bar{G}J$ for long shafts and the importance of constrained warping for short shafts L/h, as observed, in particular, in Sections 4.2 and 5.3 when analyzing the original TWKV formulation as the constrained limit of the RBV and mixed formulations, respectively.

In this respect, the analysis presented in those sections identified also the penalty parameter κ_t, depending only on the cross section geometry, driving that limiting process to the constrained TWKV formulation. Figure 6 depicts that parameter for both the RBV and mixed formulations (that is, relations (110) and (183), respectively) versus the section's aspect ratio t/h, the parameter controlling the section geometry for the solid sections considered here. We can first observe the monotonically increasing values with a decreasing thickness of the section. Note that as the thickness t is reduced, the solid section tends to an open thin–walled section, sections studied in detail next in Section 7.2, as opposed to the closed (hollow) thin–walled sections considered in Section 7.3.

Figure 6 also includes the penalty parameter κ_t for the different formulations based on the estimated thin–walled values of the section torsional

constants presented in Appendix B.1. The computed values show a good agreement with these estimated values, especially in that thin limit. In both cases, we emphasize the monotonic character of the dependence of the parameter κ_t on t/h (as a good penalty parameter, if we may say), especially given that the individual section constants do not share that property as seen in Figure 4. Furthermore, the result (186) by which $\kappa_t^{(RBV)} \geq \kappa_t^{(MIX)}$ is confirmed by the values depicted in Figure 6. We also refer to Remark B.2 in Appendix B.1 for an evaluation of the actual values of the parameter κ_t for the different formulations, allowing a direct comparison between them and actually quantifying their relative stiffness.

Hence, since these results show that $\kappa_t \to \infty$ as $t/h \to 0$ for the (open) simply–connected topology of the cross section under study here, the different formulations will tend to each other in the thin limit as shown in Sections 4.2 and 5.3. The differences between them become small then in the limiting range of thinner sections (e.g. $t/h = 0.1$) as opposed to thicker sections, like the square section $t/h = 1.0$. Looking at the left plot in Figure 5, this agreement occurs in the whole range of shaft lengths ($L/h = 5.0$, 1.0 and 0.5), when $t/h = 0.1$. The actual values vary for each L/h. So it is not the shaft length which, as seen above and argued in the paper, leads to responses dominated by Saint–Venant torsion for long shafts (with, hence, all different formulations dealing with the restrained warping diminishing equally their effects), but the section geometry alone. This situation leads to stronger effects of restrained warping for the thinner sections t/h with this open configuration (solid to open thin–walled), closer to the stiffer response of the TWKV formulation. In fact, looking at Figure 6, the values of the parameter κ_t for the RBV and mixed formulations are close to each other, with always $\kappa_t^{(RBV)} \geq \kappa_t^{(MIX)}$ as proven, a result that explains the stiffer response observed above for the RBV formulation when compared to the mixed formulation. This less stiff response is actually more accurate, as the comparisons of these results with full three–dimensional finite element simulations of the problem at hand presented below indicate.

First, though, we continue the comparison of the three structural theories considered in this paper by depicting in Figure 7 the distribution of the bishear $T_w(z)$ and bimoment $B_w(z)$ diagrams obtained in Section 6.3 by the different formulations. We have considered again the sections with aspect ratios $t/h = 1.0$, 0.5 and 0.1, showing for each case the diagrams for total shaft length of $L/h = 5.0$, 1.0 and 0.5. All diagrams are shown normalized by the torque T_L at the shaft's tip $z = L$ (namely, $T_w(z)/T_L$ and $B_w(z)/(T_L L)$)

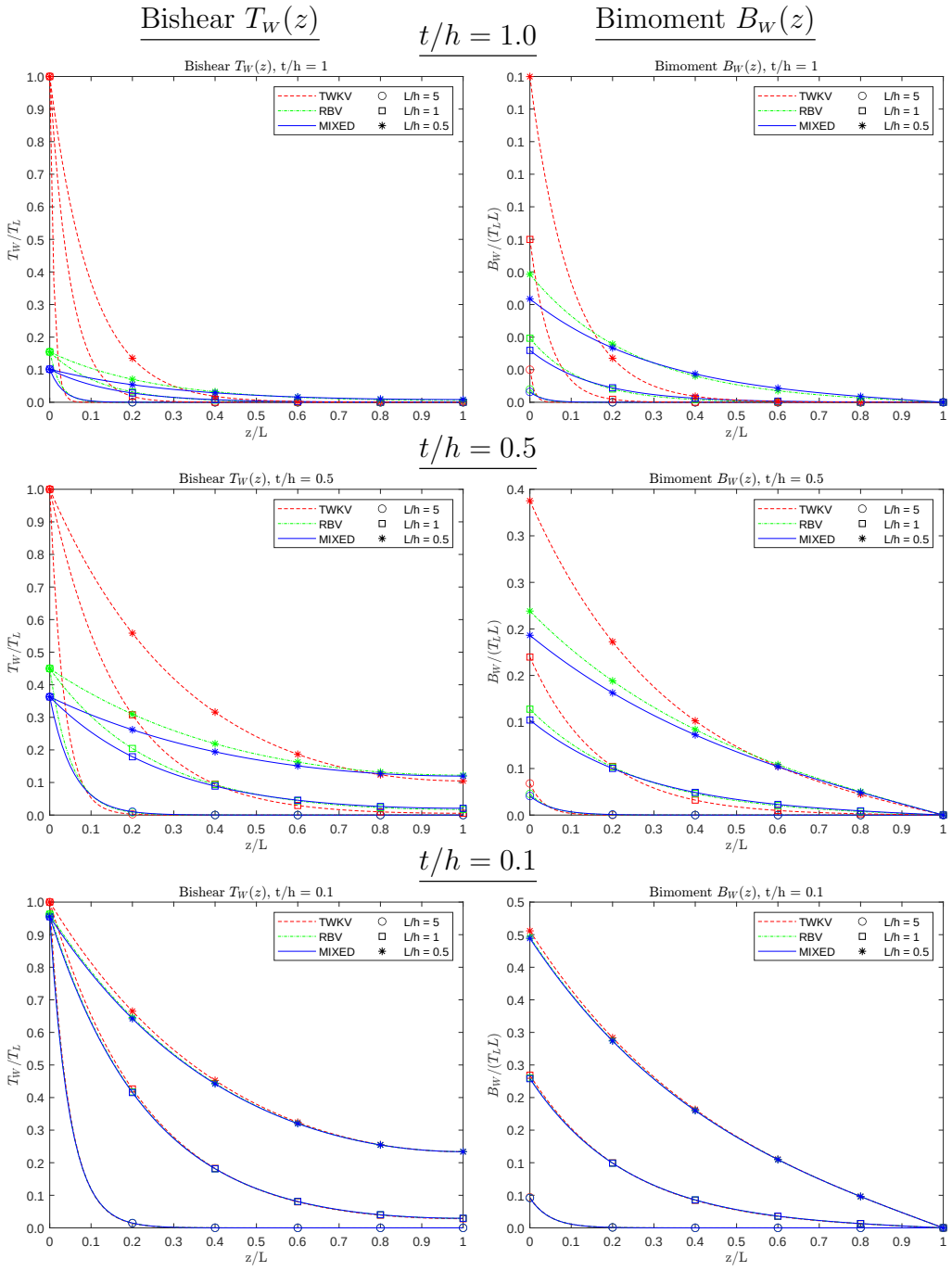

Figure 7: Rectangular cross section: moment diagrams normalized by the tip torque T_L. Distribution of the bishear $T_W(z)$ (left) and bimoment $B_W(z)$ (right) for different section aspect ratios $t/h = 1.0,\ 0.5,\ 0.1$, comparing different shaft's lengths $L/h = 5.0,\ 1.0,\ 0.5$ for each aspect ratio.

and versus the non-dimensional distance $\widetilde{z} = z/L$ from the fixed support at the shaft's root $z = 0$. They correspond to equations (200) and (205), respectively.

We first observe that the effects of the restrained warping are more significant for thinner sections (at least when looking at the RBV and mixed formulations), decreasing from that fixed end along the length of the shaft. This decrease along the shaft is relatively fast for longer shafts, nothing else but a reflection of their local character. Despite this, the original TWKV formulation is greatly affected by the unrealistic result (211) fixing the bishear at the shaft's root to $T_W(0)/T_L = 1.0$, a consequence of the way this formulation the no-warping condition $\phi'(0) = 0$ resulting on $T_{SV}(0) = 0$ for the Saint–Venant component of the torque. This situation is related to the torque anomaly; see Remark 2.3 in Section 2.2 above.

This situation also affects the bimoment diagram for the TWKV formulation, resulting in clear differences of the bishear $T_W(z)$ and bimoment $B_W(z)$ diagrams for this formulation and the other two formulations, the RBV and mixed formulations. These two formulations capture well those decreased effects of the restrained warping, especially for thicker sections $t/h = 1.0$ and 0.5, resulting on similar values. Interestingly, all three formulations agree well for the thinnest section considered $t/h = 0.1$. Still, the TWKV formulation results in higher values of both the bishear $T_W(z)$ and bimoment $B_W(z)$, confirming its stiffer character.

All these values drive the distribution of the stresses, both the shear and normal stresses, on the shaft's cross sections. In particular, Figures 8 and 9 show the shear stresses obtained by the different formulations at the shaft's root $z = 0$ for the square section $t/h = 1.0$ and rectangular section with aspect ratio $t/h = 0.5$, respectively, both for the shaft of length $L/h = 1.0$. They correspond to the relations (219)–(220). We have included the shear stress vector $\boldsymbol{\tau} = [\tau_{xz}, \tau_{yz}]^T$, shown at the points where the distribution functions gradients (i.e. ∇W_{SV} and ∇W_σ) are evaluated, the 2×2 Gauss points used in the numerical integration for the considered bilinear elements. These vectors are shown on top of the contour plots of the magnitude of these stresses $\|\boldsymbol{\tau}\| = \sqrt{\tau_{xz}^2 + \tau_{yz}^2}$. We do that for the Saint–Venant shear stress component $\boldsymbol{\tau}_{SV}$, the warping component $\boldsymbol{\tau}_W$ and the total shear stress $\boldsymbol{\tau} = \boldsymbol{\tau}_{SV} + \boldsymbol{\tau}_W$, all for each of the three considered formulations. We have normalized the stresses for a unit rotation at the shaft's tip, that is, we consider $\phi_L = 1.0$ in equation (216) defining the rate of twist Θ_{T_L} in the stress formulas (219)–(220). This option (as opposed to a unit tip torque

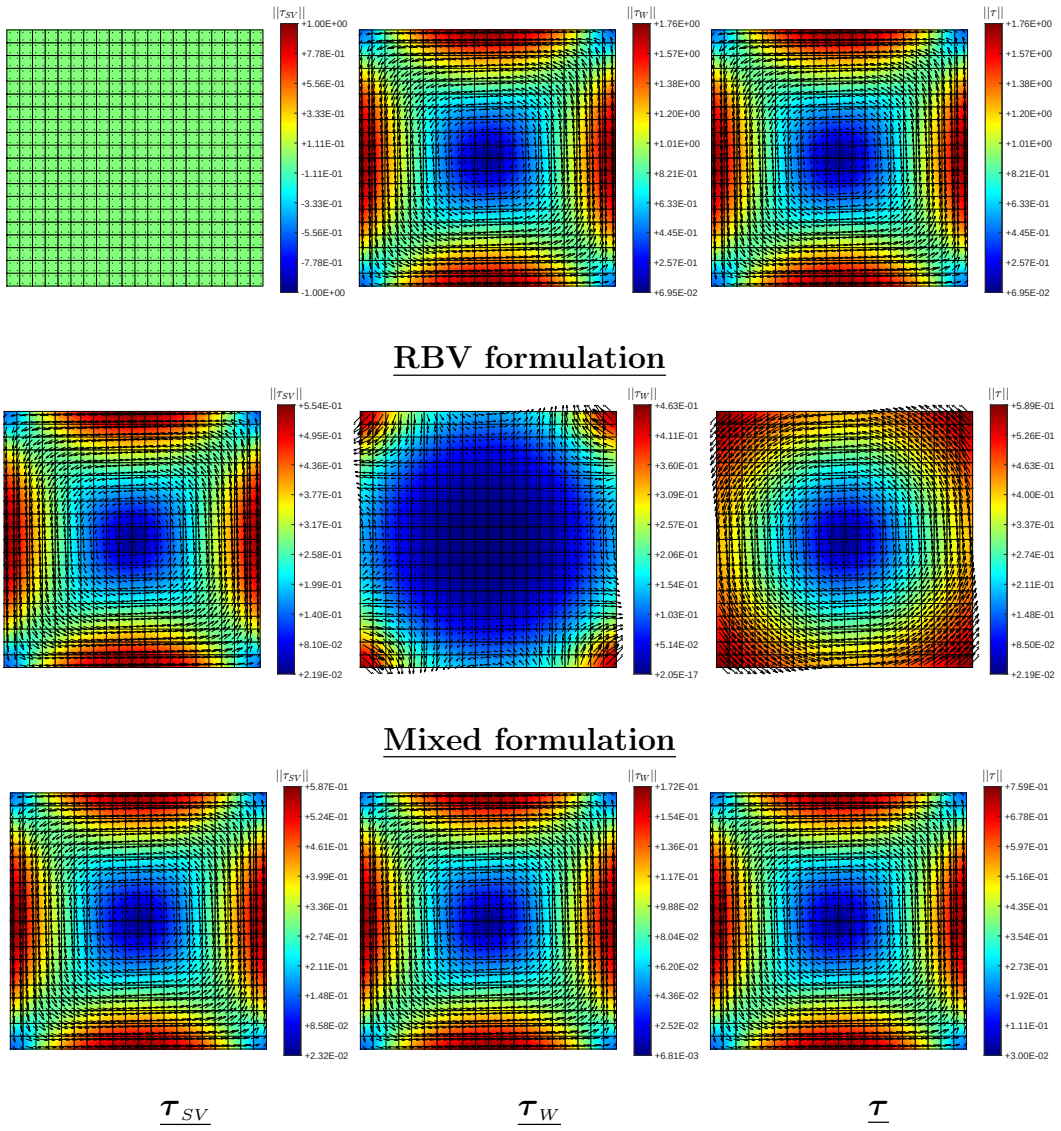

Figure 8: Rectangular cross section: shear stresses. Distributions of the Saint–Venant shear stress $\boldsymbol{\tau}_{SV}$, the warping shear stress $\boldsymbol{\tau}_{W}$ and the total shear stress $\boldsymbol{\tau}$ for the square cross section $t/h = 1.0$ and $L/h = 1.0$ at the shaft root $z = 0$. All values are normalized as $\boldsymbol{\tau}/\bar{G}$ and correspond to the case with a unit rotation $\phi_L = 1.0$ at the opposite tip of the shaft.

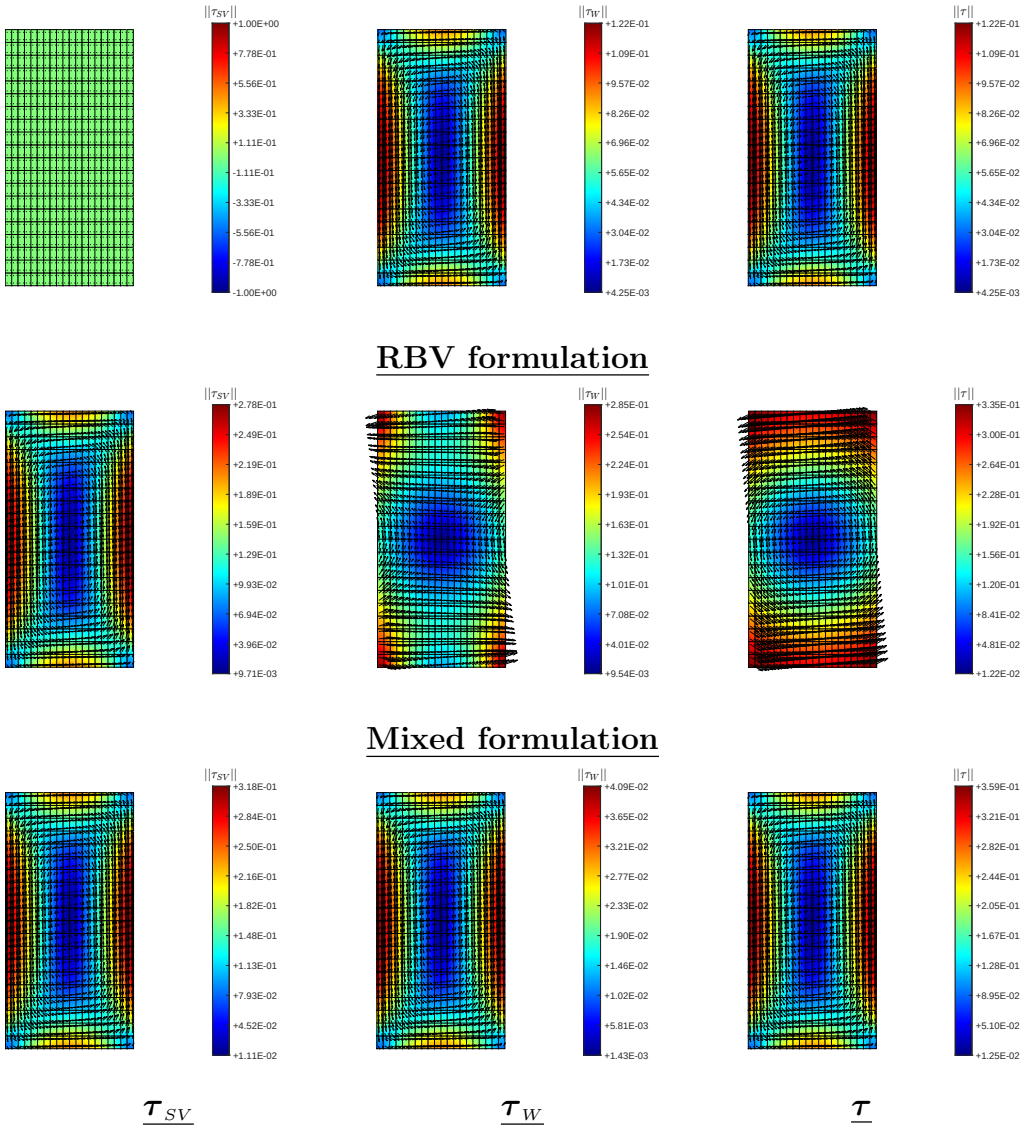

Figure 9: Rectangular cross section: shear stresses. Distributions of the Saint–Venant shear stress $\boldsymbol{\tau}_{SV}$, the warping shear stress $\boldsymbol{\tau}_{W}$ and the total shear stress $\boldsymbol{\tau}$ for the rectangular cross section $t/h = 0.50$ and $L/h = 1.0$ at the shaft root $z = 0$. All values are normalized as $\boldsymbol{\tau}/\bar{G}$ and correspond to the case with a unit rotation $\phi_L = 1.0$ at the opposite tip of the shaft.

$T_L = 1.0$) allows a simpler comparison with the full three–dimensional finite element solution considered later in this section.

The results for the original TWKV formulation show, in particular, the vanishing of the Saint–Venant part of the shear stress $\boldsymbol{\tau}_{SV}$ observed in Section 3.2, a fact associated with the direct dependence of these stresses in (83) on $\phi'(0)$, vanishing at that end of the shaft. Again, an artifact of the torque anomaly noted above. This results on the vanishing of the corresponding torque $T_{SV}(0)$, with all the reacting torque arising from the bishear $T_W(0)/T_L = 1.0$ and its corresponding shear stresses $\boldsymbol{\tau}_W$ in (77).

This situation clearly differs with the stress distributions predicted by the RBV and mixed formulations. The Saint–Venant shear stress $\boldsymbol{\tau}_{SV}$ does not vanish in these two cases, following the distribution given by the combination $[\nabla W_{SV} + \mathbb{J}]\,(x, y)$ for both, with different magnitude as observed in Figures 8 and 9, especially in the latter case for the rectangular section wit $t/h = 0.5$. The clear difference appears in the warping component of the shear stress $\boldsymbol{\tau}_W$, which follows the distributions defined by $\nabla W_{SV}(x, y)$ and $\nabla W_\sigma(x, y)$ for the RBV and mixed formulations, respectively, as given by relation (220).

It is interesting to note that the similar distributions observed for the two shear stress components $\boldsymbol{\tau}_{SV}$ and $\boldsymbol{\tau}_W$ for the mixed formulation indicate the similarity of the distributions given by $[\nabla W_{SV} + \mathbb{J}]\,(x, y)$ and $\nabla W_\sigma(x, y)$, and hence the total shear stress $\boldsymbol{\tau}$ depicted at the right column of Figures 8 and 9. This situation explains the similarities between the distribution of this total shear stress for this mixed formulation and the original TWKV formulation, even when the latter has no Saint–Venant component whatsoever. Note that, for the cases considered with, in particular, $L/h = 1.0$ at $z = 0$, the Saint–Venant component $\boldsymbol{\tau}_{SV}$ and the warping component $\boldsymbol{\tau}_W$ for the mixed formulation.

This situation is to be contrasted with the shear stress distributions obtained with the RBV formulation. The resulting "rotational" character of the final distribution of the total stress $\boldsymbol{\tau}$ obtained in Section 6.4 (see equation (213)) is blatantly apparent, including the circular pattern in the contour plots of the magnitude of this stress; see the plots in the middle row, right column in Figures 8 and 9. A consequence of this situation is the lack of satisfaction of the boundary conditions expected for these shear stresses, namely, defining shear stress vectors tangential to the section boundary. This condition is clearly not satisfied as those plots clearly illustrate. This stress distribution, observed in Section 4.3 above, is markedly incorrect as noted in that section (the RBV stresses are not in equilibrium), even when the for-

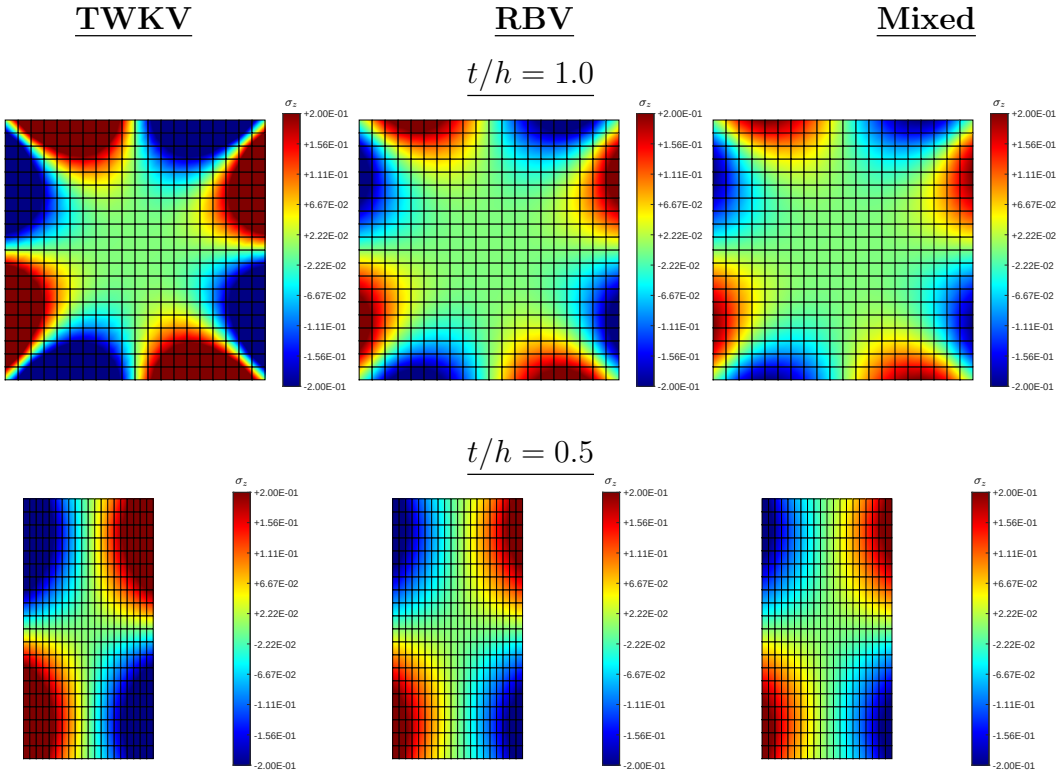

Figure 10: Rectangular cross section: axial stress. Distribution of the axial stress σ_z at the shaft root $z = 0$ for the cross sections with $t/h = 1.0$, 0.5 and shaft's length $L/h = 1.0$. All values are normalized by the material's Young modulus as $\sigma_z/\bar{E}$ and correspond to the case with a unit rotation $\phi_L = 1.0$ at the opposite tip of the shaft.

mulation may capture the overall structural response of the shaft in torsion. Again, this situation is to be contrasted with the stress distribution obtained with the mixed formulation.

The evaluation of the normal stress distribution σ_z at the shaft's root $z = 0$, a direct consequence of the restrained warping at that end of the shaft, is of particular interest. As noted in Section 6.4, all three formulations under study predict the same distribution of these stresses on a generic cross section, namely, the one given by the Saint–Venant warping function $W_{SV}(x, y)$. The actual magnitude of these stresses do vary though for each formulation, as given by formula (221), together with the actual magnitude of the rate of twist Θ_{T_L} given by equation (216). We consider again the case

of a unit rotation $\phi_L = 1.0$ at the shaft's tip $z = L$, showing the values normalized in this case by $\sigma_z/\bar{E}$. Note that the non-dimensional quantities ρ and α^{eff} appearing in all these different formulas do depend of the particular formulation considered, the latter as defined explicitly in Box 1 for the TWKV, RBV and mixed formulations.

The final obtained distributions are included in Figure 10 for the square section $t/h = 1.0$ and rectangular section with $t/h = 0.5$, both for the shaft with $L/h = 1.0$. The common distribution $W_{sv}(x, y)$ for the different formulations is apparent in those contour plots, contours that follow the perspective (elevation) view of that function shown in Figure 3 (left column). The different magnitude of these stresses among the formulations is also clear (note that the same scale of contour plots has been used in the plots of this figure), with a higher value for the TWKV formulation and similar values for the RBV and mixed formulations. This situation is a consequence of similar relations we have observed above for the distribution of the bimoment $B_w(z)$, the stress resultant driving these normal stresses; see also below for a further analysis and comparison of the specific value of the bimoment $B_w(0)$. The higher stresses σ_z at the shaft's root predicted by the original TWKV formulation is one more instance of the stiffer character of this formulation in comparison with the RBV and mixed formulations, both showing a similar overall estimation of the shaft's response.

7.1.1. Three–dimensional analysis

In an attempt to evaluate all these results and conclusions in comparison with the response not of an ideal shaft but of an actual elastic solid subjected to torsion, we consider next a full three–dimensional finite element simulation of the problem at hand. Figure 11 depicts two characteristic deformed configurations of the many cases considered in this work. In particular they correspond to the shaft with square section $t/h = 1.0$ and lengths $L/h = 1.0$ and 5.0, the former again to evaluate the appropriateness of the considered structural theories for such short shaft, if that terminology is still allowed. In fact, the results below allow to confirm these points.

As shown in Figure 11, we consider structured meshes of the three–dimensional domain, keeping the same finite element mesh topology for the cross sections, extending through 20 layers of regular 8-node brick elements along the shaft length, with a graded distribution of the elements, with thinner ones close to the fixed support, trying to catch better the more complex state of stress at the shaft's root. Enhanced strain QM1/E12 elements developed in

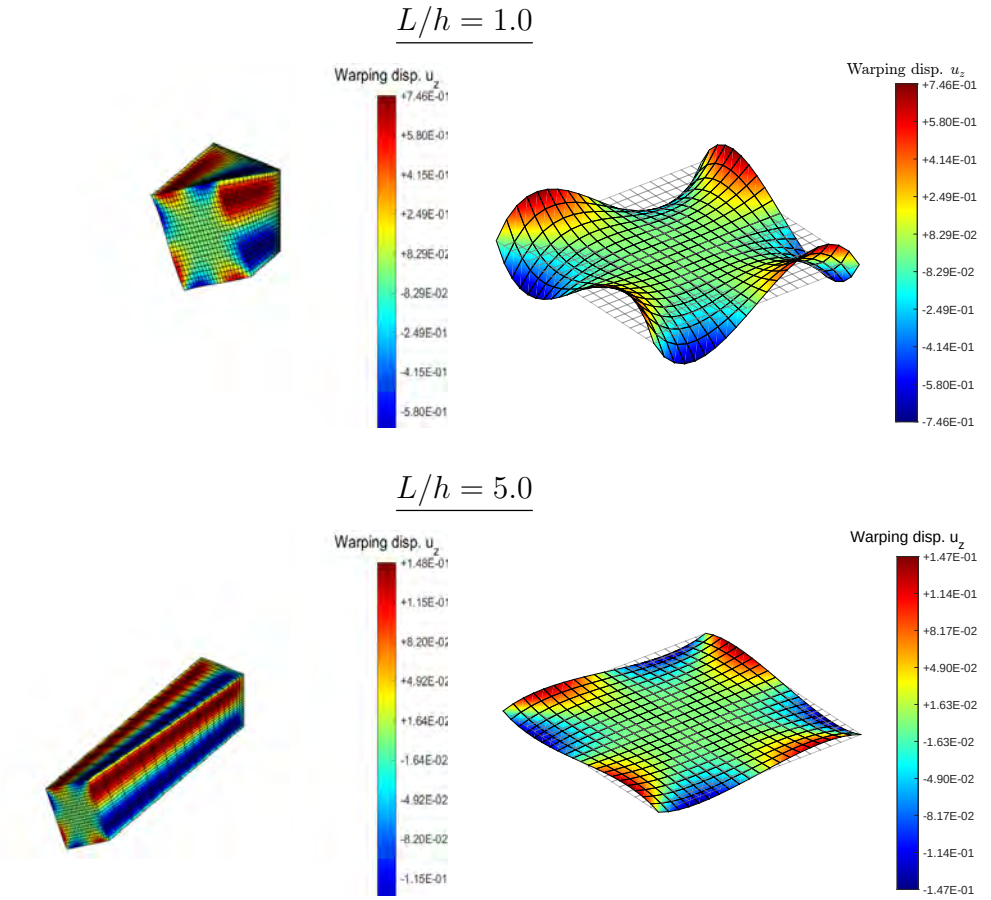

Figure 11: Rectangular cross section: 3D shaft. Three–dimensional finite element solution for shafts with $L/h = 1.0$, 5.0 and $t/h = 1.0$, showing the contours of the axial displacement u_z on top of the 3D deformed configuration of the shaft (left), and the elevation plot of the resulting warping at the shaft's tip $z = L$ (right).

Simo et al. [1993] are considered. These elements show an improved (fully locking-free) response in shear (and volume), especially when the geometry of the element involves thin configurations.

As in all the previous developments, the shaft runs along the z axis with the cross sections lying in planes parallel to the (x, y) Cartesian plane. In this way, the different problems are run by imposing the displacement components (u_x, u_y) at the tip of the shaft $z = L$ to be the ones defined by $(12)_{1,2}$ for a unit tip rotation $\phi_L = 1.0$ while the axial (warping) displacement is left free. The center of twist is taken to be the one arising from the section analysis (see

the developments in Section 2.4 above), which in this case trivially coincides with the center of the rectangular section by its double symmetry. All the three components of the displacement are set to vanish at the opposite end, the shaft's root at $z = 0$. A full three–dimensional isotropic linear elastic response is assumed for the material.

Figure 11 shows the deformed configuration obtained for the shafts with square cross section $t/h = 1.0$ of length $L/h = 1.0$ and 5.0. We have also included the contour plots of the axial displacement component u_z on top of the deformed configurations, as well as the elevation plots of the warping of the tip section at $z = L$. Those plots must be compared with the Saint –Venant warping function $W_{SV}(x, y)$ calculated for the section at hand, and shown in Figure 3, top left plot.

In order to evaluate the shear stress distributions obtained above for the different considered formulations, we have included in Figure 12 the shear and normal stress components on the cross section at the shaft's root ($z = 0$) obtained in the three–dimensional simulation for the square $t/h = 1.0$ and rectangular sections $t/h = 0.5$, both for the shaft $L/h = 1.0$. These stresses must be compared with the results shown in Figures 8 and 9 for the shear stress, and Figure 10 for the normal stress. Good agreement can be observed for the overall distributions for the normal stress σ_z and similarly for the shear stress $\boldsymbol{\tau}$ of the mixed formulation, avoiding in particular the incorrect purely "rotational" pattern of the RBV formulation (observe the expected drop of the shear stress level near the section's corners). We note that only the total stress $\boldsymbol{\tau}$ is available for the three–dimensional simulations.

Similarly, we note that the stress distributions in Figure 12 have been obtained with the usual L_2–projections of the corresponding 3D values at the quadrature points used in the 3D brick elements to the nodes, that is,

$$\bar{\boldsymbol{\sigma}}^{A}_{(3D)} := \int_{\Omega_{(3D)}} N^{A}_{(3D)}\, \boldsymbol{\sigma}_{(3D)}\, d\Omega_{(3D)} \Big/ \left(\int_{\Omega_{(3D)}} N^{A}_{(3D)}\, d\Omega_{(3D)} \right) , \tag{229}$$

for all nodes $A = 1, n^{node}_{(3D)}$ and corresponding finite element trilinear shape functions $N^{A}_{(3D)}$ of the three–dimensional simulation over the domain $\Omega_{(3D)}$ of the 3D shaft. These nodal values (and its contour plots for the magnitude of the plotted stress) are then shown for the section of interest ($z = 0$ here). Thus the different locations of the stress vectors $\boldsymbol{\tau} = [\tau_{xz}, \tau_{yz}]^T$ in Figure 12 when compared with those other figures based on the section (fully plane) analyses. The boundary values of those stress vectors and, in particular, the

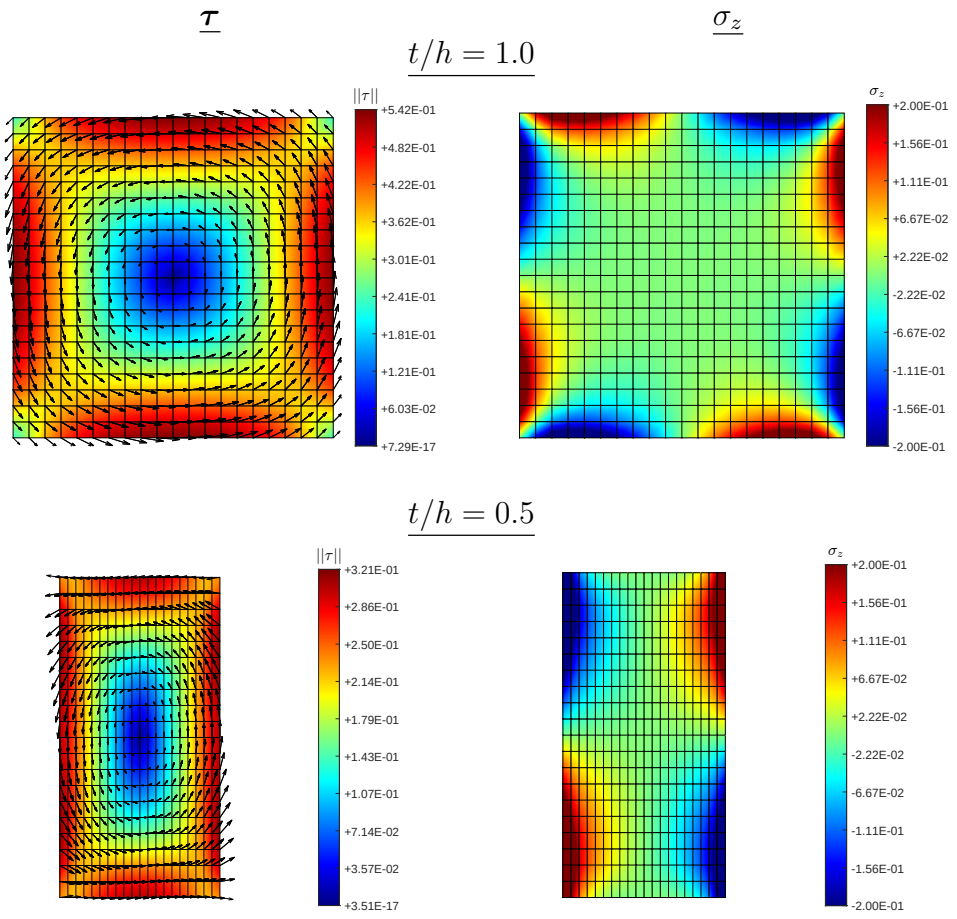

Figure 12: Rectangular cross section: stresses. Shear and normal stresses in the three–dimensional finite element solution at the shaft root $z = 0$ for $t/h = 1.0$, 0.5 and $L/h = 1.0$. Values are normalized as $\boldsymbol{\tau}/\bar{G}$ and $\sigma_z/\bar{E}$, and they correspond to the case with a unit rotation $\phi_L = 1.0$ at the opposite tip of the shaft.

values at the section's corners are to be understood in this context.

Given the direct link of the normal stress σ_z with the restrained warping under analysis, we compare further the resulting distributions and especially its magnitude. As noted above, all the considered formulations share the spatial distribution on the cross section proportional to the Saint–Venant warping function $W_{SV}(x, y)$. To this purpose, we show in Figure 13 the computed difference of the axial stress $\sigma_z - \sigma_{z(3D)}$ among the different formulations and the 3D simulations. The contour plots of this difference at the nodes (i.e. the nodal values of the projected 3D stresses (229) are compared with

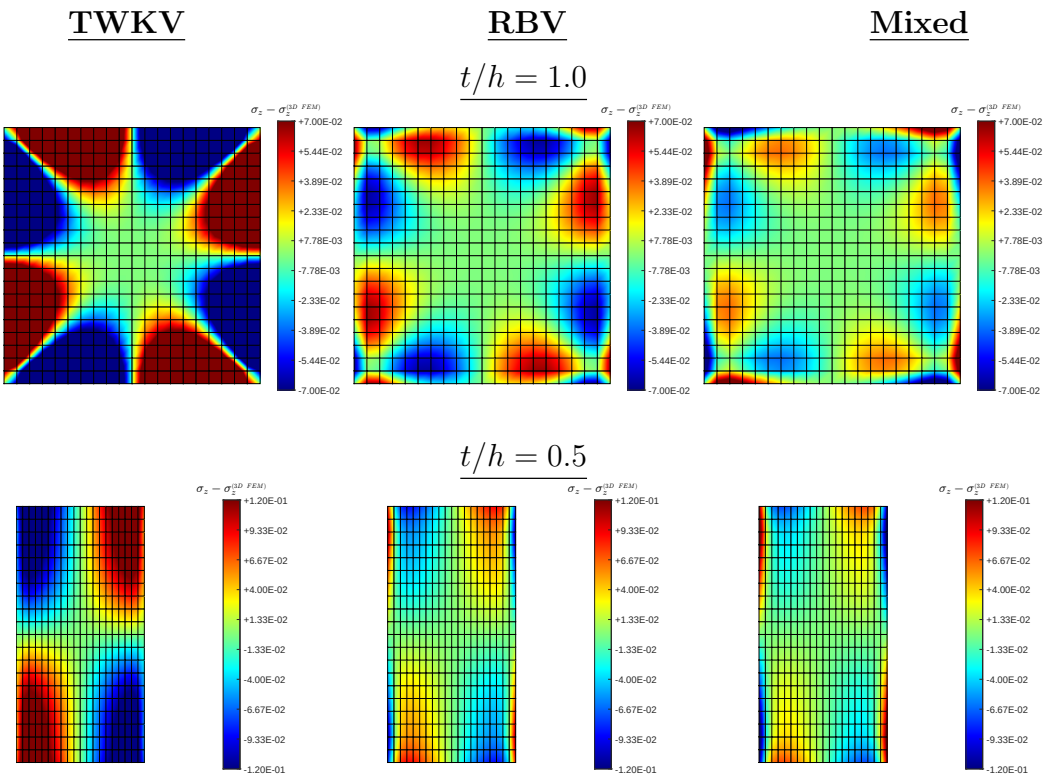

Figure 13: Rectangular cross section: axial stress difference. Comparison of the axial stress at the shaft's root $z = 0$ with the three–dimensional finite element solution $\sigma_z - \sigma_{z(3D)}$, for the sections $t/h = 1.0$, 0.5 and $L/h = 1.0$. All values normalized by the material's Young modulus as $\sigma_z/\bar{E}$ and correspond to the case with a unit rotation $\phi_L = 1.0$ at the opposite tip of the shaft.

the nodal values of the same stress for the plane analyses following a similar projection scheme on the plane section with the plane shape functions) are shown for the two sections $t/h = 1.0$ and 0.5, both for the case $L/h = 1.0$ again. We note that the mixed formulation shows the lowest values of that difference, the largest values obtained by the constrained TWKV. The overstiff response of this formulation, in comparison in this case with an "exact" three–dimensional simulation, is again concluded. The RBV formulation appears also on the stiffer side, compared to the more exact mixed formulation, but not as accused as in the TWKV formulation.

The availability of the section stresses (229) for the three–dimensional simulations allow to evaluate the associated values of the bimoment $B_W(z)$

and bishear $T_W(z)$ as defined by the relation (57) and (89), respectively. Namely, we have

$$B_W(z) = \int_\Omega \sigma_{z(3D)}(x,y,z)\ W_{SV}(x,y)\ d\Omega$$
$$= \sum_{B=1}^{n_{(2D)}^{node}} \bar{\sigma}_{z(3D)}^B \left(\int_\Omega N_{(2D)}^B(x,y)\ W_{SV}(x,y)\ d\Omega \right) , \tag{230}$$

and

$$T_W(z) = -\int_\Omega \boldsymbol{\tau}_{(3D)}(x,y,z) \cdot \nabla W_{SV}(x,y)\ d\Omega$$
$$= -\sum_{B=1}^{n_{(2D)}^{node}} \bar{\boldsymbol{\tau}}_{(3D)}^B \cdot \left(\int_\Omega N_{(2D)}^B(x,y)\ \nabla W_{SV}(x,y)\ d\Omega \right) , \tag{231}$$

for the section Ω at z involving a plane discretization with $n_{(2D)}^{node}$ nodes B and corresponding plane shape functions $N_{(2D)}^B$. For the considered finite element discretizations, these 2D shape functions are the restriction of the 3D $N_{(3D)}^B$ shape functions used in (229) to the plane of the section. Similarly, we have the Saint–Venant torque

$$T_{SV}(z) = \int_{\Omega_z} \boldsymbol{\tau}_{(3D)}(x,y,z) \cdot [\nabla W_{SV} + \mathbb{J}](x,y)\ d\Omega$$
$$= \sum_{B=1}^{n_{(2D)}^{node}} \bar{\boldsymbol{\tau}}_{(3D)}^B \cdot \left(\int_\Omega N_{(2D)}^B(x,y)\, [\nabla W_{SV} + \mathbb{J}](x,y)\ d\Omega \right) , \tag{232}$$

although we do not depict it explicitly here since we trivially have $T_{SV}(z) = T(z) - T_W(z)$ for the total torque $T(z) = \int_\Omega \boldsymbol{\tau} \cdot \mathbb{J}\ d\Omega$, constant T_L for the particular model problem under study.

Figure 14 shows the bimoment $B_W(0)$ and bishear $T_W(0)$ at the shaft's root $z = 0$ versus the section aspect ratio t/h for shaft's lengths $L/h = 5.0$, 1.0 and 0.5, and versus the shaft length itself L/h for the sections $t/h = 1.0$, 0.5 and 0.1. We have normalized these values by $T_L L$ and T_L, respectively, for the tip moment T_L at $z = L$, showing the corresponding distributions (205) and $(202)_2$, respectively, for the different formulations under study and the values computed by (230) and (231) for the three–dimensional simulations.

The plots in the top row of Figure 14 show a very good agreement between the computed values of the bimoment $B_W(0)$ in the full three–dimensional

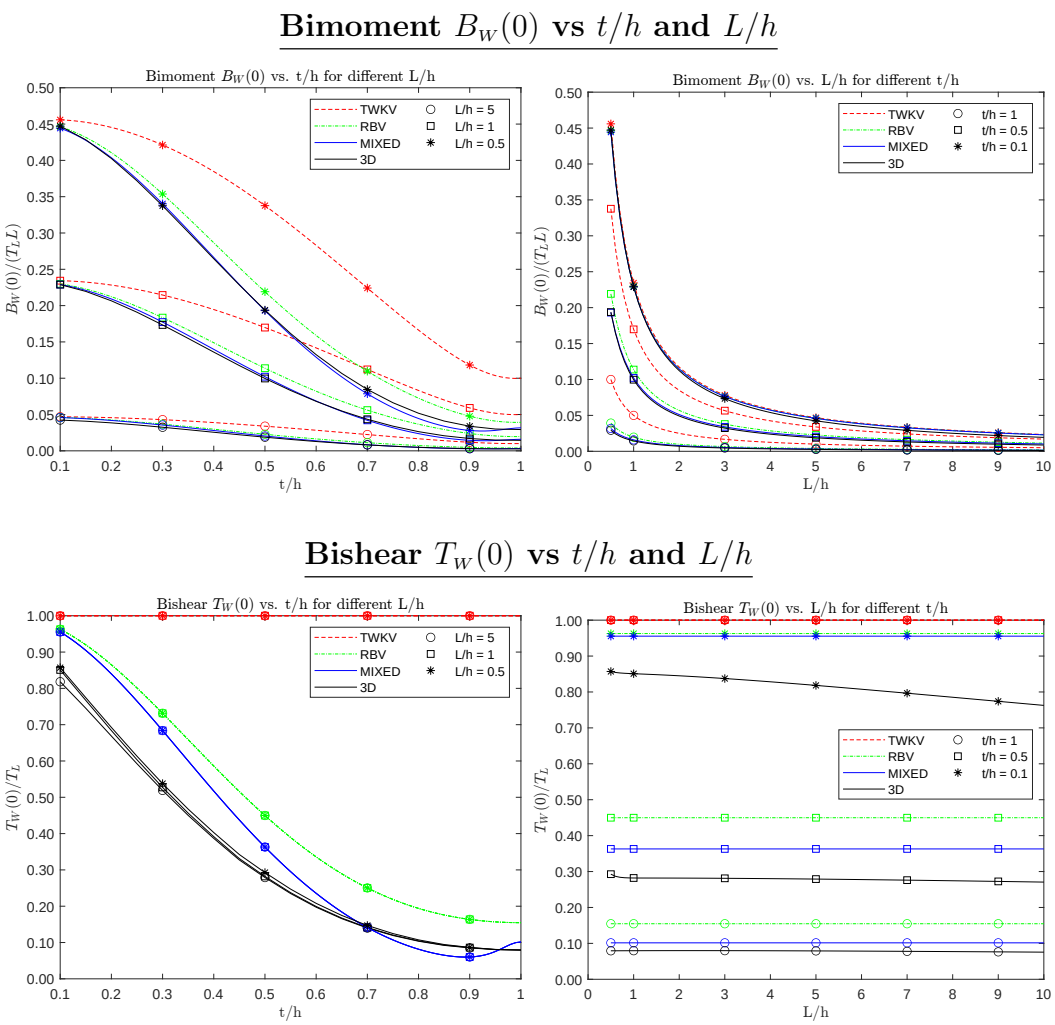

Figure 14: Rectangular cross section: bimoment and bishear at the shaft's root. Values of the bimoment $B_W(0)$ (top) and the bishear $T_W(0)$ (bottom) at $z = 0$ versus the section aspect ratio t/h (left) and shaft's length ration L/h (right) obtained by the different formulations and the 3D finite element solution.

simulations and the newly developed mixed formulation. This can be observed for the whole range t/h of solid sections under consideration and the whole range of lengths L/h considered. Remarkably, this observation includes also the range around the considered limit value of $L/h = 0.5$, despite its arguably unrealistic practicality. The effects of restrained warping are important in this range of short shafts, and especially for thinner rectangu-

lar sections. The results for the RBV formulation are consistently close to the mostly overlapping values of the mixed formulation and the full three–dimensional simulations. On the other hand, the TWKV formulation shows bigger discrepancies, especially for the thicker sections, close to the square section $t/h = 1.0$. Notably, both the RBV and, especially, the TWKV formulations show values of the bimoment $B_w(0)$ consistently larger than the solutions for the three–dimensional simulations and mixed formulation, one further proof of the excessively stiffer character of those formulations

We can draw similar conclusions for the plots of the bishear $T_w(0)$ at the bottom row of Figure 14, even though a lesser agreement can be observed with the full three–dimensional simulations. We trace part of this discrepancy to the more implied error in the evaluation of this torque with formula (231), involving the gradient of the Saint–Venant warping function $W_{sv}(x, y)$ instead of the function itself as for the bimoment $B_w(0)$ in (230). The agreement with those simulations is still much closer with the mixed formulation, followed closely by the RBV formulation, this being the case especially for thicker sections close to the square section $t/h = 1$. Actually, in these cases, the three–dimensional simulations confirm well the result obtained in $(202)_2$ giving the root's bishear normalized by the tip torque $T_w(0)/T_L$ independent of the shaft length. This result, however, does not seem to extend completely to the considered thinner sections, for $t/h = 0.1$ in particular.

Still, these results are to be contrasted with the unrealistic value $T_w(0)/T_L = 1.0$ for all section aspect ratios t/h and shaft lengths L/h predicted by the original TWKV formulation due to what we referred to as the torque anomaly. We remind the reader the origin of this anomaly, namely, the warping driven directly by the rate of twist $\phi'(z)$ which is imposed to vanish at that support, hence implying the vanishing of the Saint–Venant part of the torque $T_{sv}(0) = 0$. This formulation was seen in Section 4.2 to be the constrained limit of the RBV formulation and, by extension, the mixed formulation later proposed. This situation can be observed in the numerical results presented here, with the results of these formulations tending to that limit value given by the TWKV formulation for thinner sections. But the results for the TWKV are overly unrealistic for general (thick) solid sections, clearly now overstiff, showing that constrained character of the formulation.

Given this, it is of interest to revisit the values of the shaft's flexibility evaluated in Figure 5 for the three considered formulations and compare it with the full three–dimensional simulations. The three structural formulations rely on the torsional constant J in (39), common to all three, involving

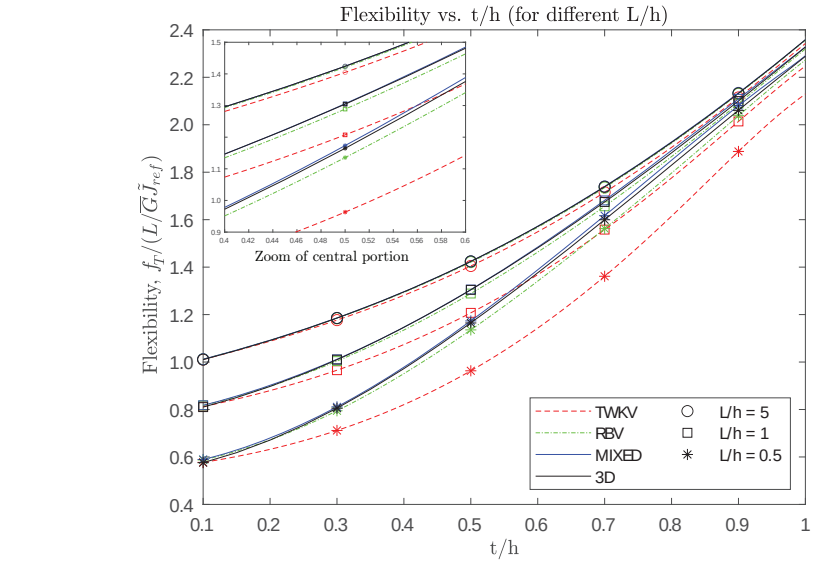

(a)

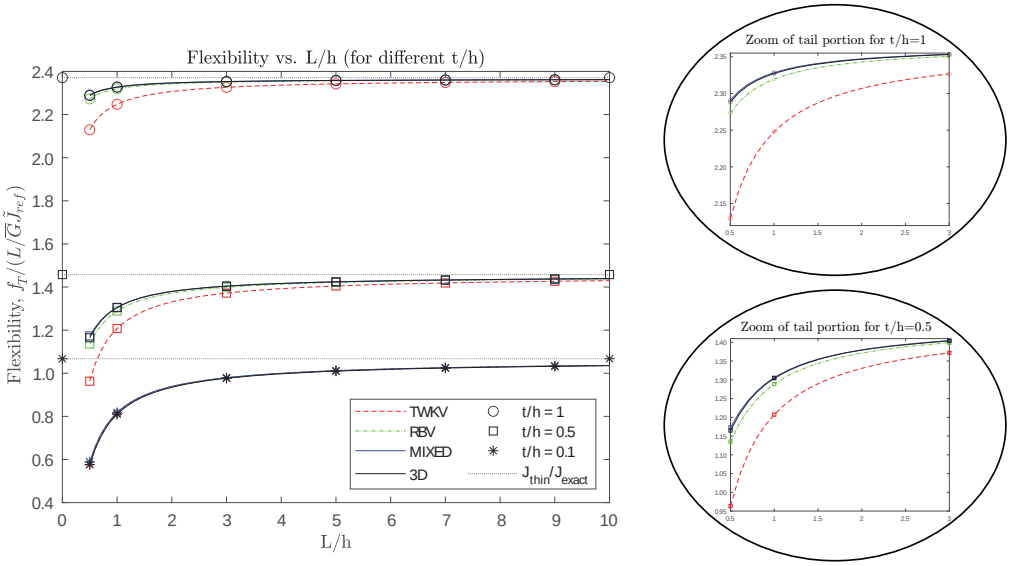

(b)

Figure 15: Rectangular cross section: shaft flexibility. Normalized torsional flexibility $f_T/(L/\bar{G}\tilde{J}_{ref})$ with a dimensional reference value ($\tilde{J}_{ref} = J^{(thin)} = ht^3/3$), allowing the incorporation of the 3D FEM solutions. Values (a) versus t/h for different L/h ratios, and (b) versus L/h for different t/h ratios.

the same Saint–Venant warping function $W_{sv}(x, y)$ giving J through that equation. See also the values of the flexibility given by (194), directly proportional to the Saint–Venant flexibility $f_T^{(SV)} = L/\bar{G}J$, hence the normalization $f_T/(L/\bar{G}J)$ employed in that figure. This choice allowed us, among other things, to evaluate the importance of the effects of restrained warping for the sections and shaft lengths under consideration, recovering easily the (ideal) response of Saint–Venant torsion in the limit of unrestrained warping for long shafts. The three–dimensional elastic models of the shafts do not rely on that function or the Saint–Venant torsional constant J. Hence, it is adequate to use a different normalization, motivated only by the dimensionality of the quantities involved.

In this way, Figure 15 depicts the flexibilities for the different formulations normalized as $f_T/(L/G\tilde{J}_{ref})$ by a reference value $\tilde{J}_{ref}$ capturing the dimensions of the section. We choose the thin–wall limit value, namely $\tilde{J}_{ref} = J^{(thin)} = ht^3/3$, and plot the flexibility both versus the section ratio geometry t/h and the shaft length L/h, in each case for different values of the other parameter. We have also included the ratio $\tilde{J}_{ref}/J_{exact}$ for the sections t/h considered in the plot versus L/h, with J_{exact} given by the value referred to in the Footnote 1. This value can be observed to be obtained asymptotically for both the structural formulations and the full three–dimensional formulations for long shafts L/h. We trace the remaining difference to the fixed finite element meshes considered in the analysis.

The results shown in this figure confirm the very good agreement between the proposed mixed formulation and the full three–dimensional simulations in all the ranges considered, including for very short shafts L/h, with the RBV formulation coming close as opposed to the TWKV formulation showing big disagreements with the full three–dimensional simulations. The differences reduce as the aspect ratio of the section geometry t/h reduces for thinner sections. These results, with all the additional aspects observed in this section (including the observed different stresses), makes us conclude the idoneity of the newly proposed mixed formulation, especially for thick solid sections, as a better alternative to the original TWKV formulation and the RBV formulation as well.

7.2. Evaluation for open thin–walled cross sections

We continue the evaluation of the different formulations of restrained warping analyzed in this work with the consideration of open thin–walled sections. As a matter of a fact, we pursue the evaluation presented in the

previous section for rectangular cross sections further, but with thickness to height ratios t/h lower than the lowest value considered there of $t/h = 0.10$. Specifically, we shall consider the range $0.01 \leq t/h \leq 0.10$ here. The results presented in this section, and in the next section for closed (hollow) thin–walled sections, show that it makes a difference to keep the simply–connected topology of the cross section (that is, the cross sections usually referred to as open thin–walled sections) for the wall thickness to control the limit process to the constrained TWKV formulation by the RBV and mixed formulations of restrained warping.

To make the comparison more interesting, we change the actual geometry of the section, from a single rectangle to the channel section depicted in Figure 2 on page 84. As shown in this figure, the two flanges has the same length $b = 0.4h$. We consider $h = 20\ cm$ so $b = 8\ cm$ in the actual simulations. This breaks the double symmetry of the section and, hence, leaves open the location of the twist/shear center (and actually the section's centroid itself), at least in its horizontal position $\bar{x}_{_T}$, as shown in Figure 2. Actually, this move of the center of twist (which defines the principal pole of the sectorial coordinate of the wall middle line) makes the section to exhibit primary warping in the thin–wall limit $t/h \to 0$; see Appendix B.2 for details on these considerations.

We note that all the developments and formulas of the paper apply to general configurations, and axes locations and orientations $\{x, y\}$ for the section, obtaining in particular the twist/shear center as part of the analysis. We continue considering a single homogeneous material, with the same values $E = 200\ GPa$ for the Young's modulus and Poisson's ratio $\nu = 0.3$, although the results below are all shown in normalized form, only requiring again the assumed homogeneous distributions $n_{_E}(x, y) = n_{_G}(x, y) = 1$ for these material parameters.

Figure 16 depicts elevation plots of the warping functions $W_{_{SV}}(x, y)$ and $W_{\sigma}(x, y)$ computed for the sections with aspect ratios $t/h = 0.10$, 0.05 and 0.01. These plots are to be contrasted with the original ones in Figure 3 for the solid rectangular sections. When computing these warping functions, we consider structured finite element discretization based on 4−node bilinear elements for the solutions of the defining boundary–value problems (33) and (79) on the cross section, with 4 equally–spaced elements through the wall thickness, and a fixed number of elements along the walls, for all values of t/h. Again, (simple) symmetry considerations apply. Actual meshes can be seen in Figure 16 and other figures below.

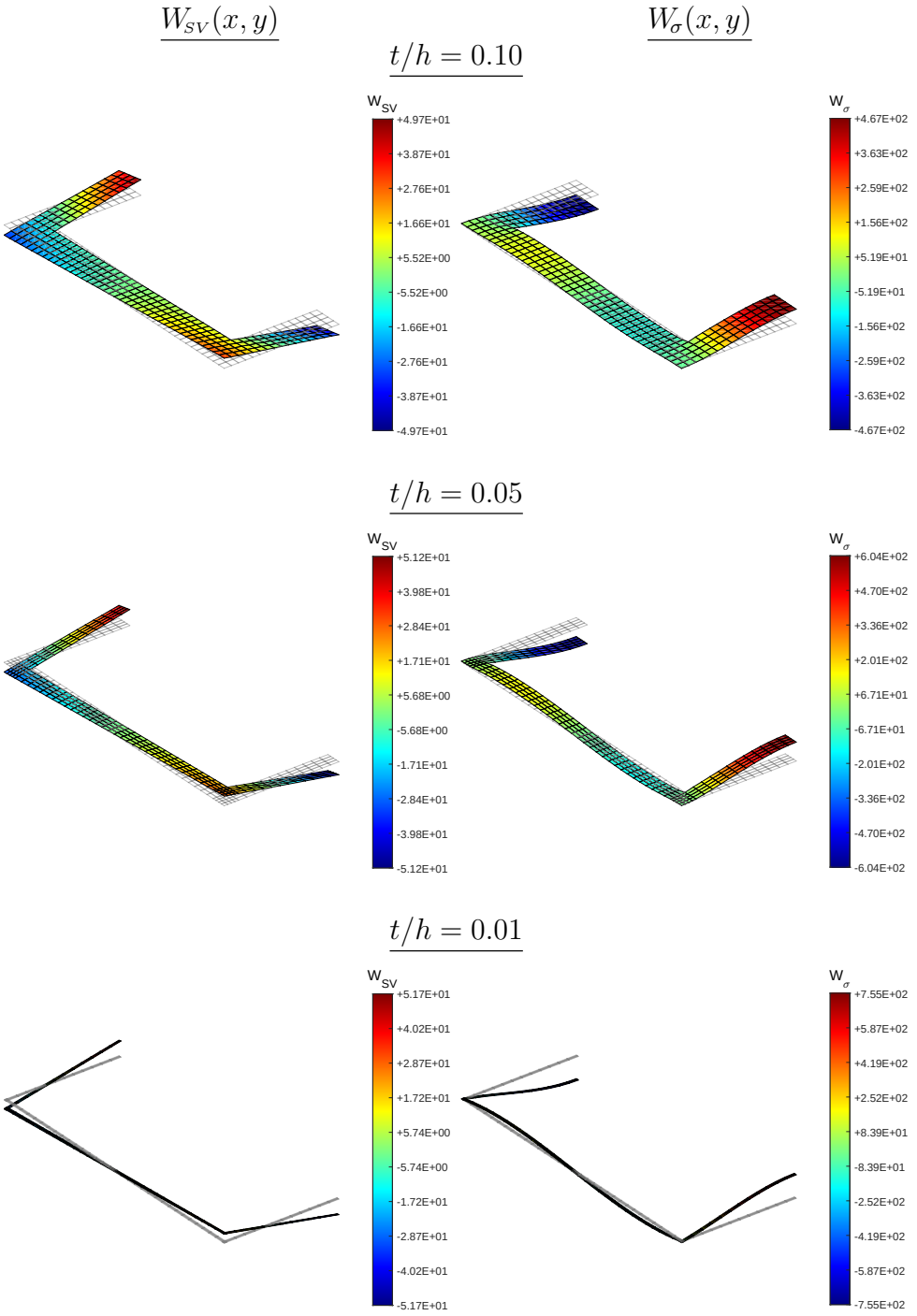

Figure 16: Channel cross section: warping functions. Computed warping functions $W_{SV}(x,y)$ (left) and $W_\sigma(x,y)$ (right) for sections with thickness ratios $t/h = 0.10,\ 0.05,\ 0.01$.

Table 2: Channel cross section: twist/shear center position $\bar{x}_{_T}$ (Figure 2). Values (left column) computed (right column) thin–wall approximation ($\bar{x}_{_T}^{(thin)} = 3\,\bar{b}^2/(\bar{h}+6\,\bar{b})$, for $\bar{h}=h-t$ and $\bar{b}=b-t/2$, being distances measured from the wall's middle line, for different t/h ratios ($h=20\ cm$).

t/h	$\bar{x}_{_T}\ [cm]$	$\bar{x}_{_T}^{(thin)}\ [cm]$
0.10	2.28811887	2.45000000
0.05	2.59689539	2.63671875
0.01	2.78436565	2.78616071

In particular, the Saint–Venant warping function $W_{_{SV}}(x,y)$ has been obtained satisfying the normalizing conditions (46) and (47). This is accomplished after evaluating the section's centroid $\bar{\boldsymbol{x}}_{_E}=\bar{\boldsymbol{x}}_{_G}$ in (6) and the center of twist $\bar{\boldsymbol{x}}_{_T}$, following the calculations (48)-(51), involving in particular the inertias (11). All these calculations are handled automatically by the finite element code, computing first the solution for an arbitrary center $\bar{\boldsymbol{x}}_{_T}^{*}$ (actually, the origin in our input setting), and then use equations (48)-(51) to determine the actual twist center $\bar{\boldsymbol{x}}_{_T}$. The second warping function $W_{\sigma}(x,y)$ is again obtained satisfying the normalizing condition (154) for the Neumann type problem (79), by shifting a first computed solution with a fixed value for an arbitrary node.

Table 2 includes the computed horizontal positions $\bar{x}_{_T}$ of the center of twist (see Figure 2) for the three cases shown in Figure 16, together with the approximate value $\bar{x}_{_T}^{(thin)}$ given by (B.10) in Appendix B.2 assuming the thin–wall limit. A good agreement is observed as the thickness t/h reduces. Similarly, the plots of the Saint–Venant warping function $W_{_{SV}}(x,y)$ in Figure 16 (left column) match well the linear distribution in the longitudinal coordinate s of the primary warping in (B.9) for the thin–wall limit $t/h\to 0$, with the bilinear distribution $s\,n$ of the secondary warping contribution in that expression being more evident as the thickness increases; see Appendix B.2 for a complete discussion of these issues.

We note again that all the developments considered in this work do not depend on the availability of those estimates for the thin–wall limit. The finite element simulations on the different sections provide the different torsional constants needed by the formulations under study. Figure 17 shows the computed values of the Saint–Venant torsional constant J in (39), the warping constant $I_{_{W_{SV}}}$ in (64), and the other two relevant constants $I_{_{\nabla W_{SV}}}$ and $I_{_{\nabla W_{\sigma}}}$ in equations (102) and (158), respectively. We have also included

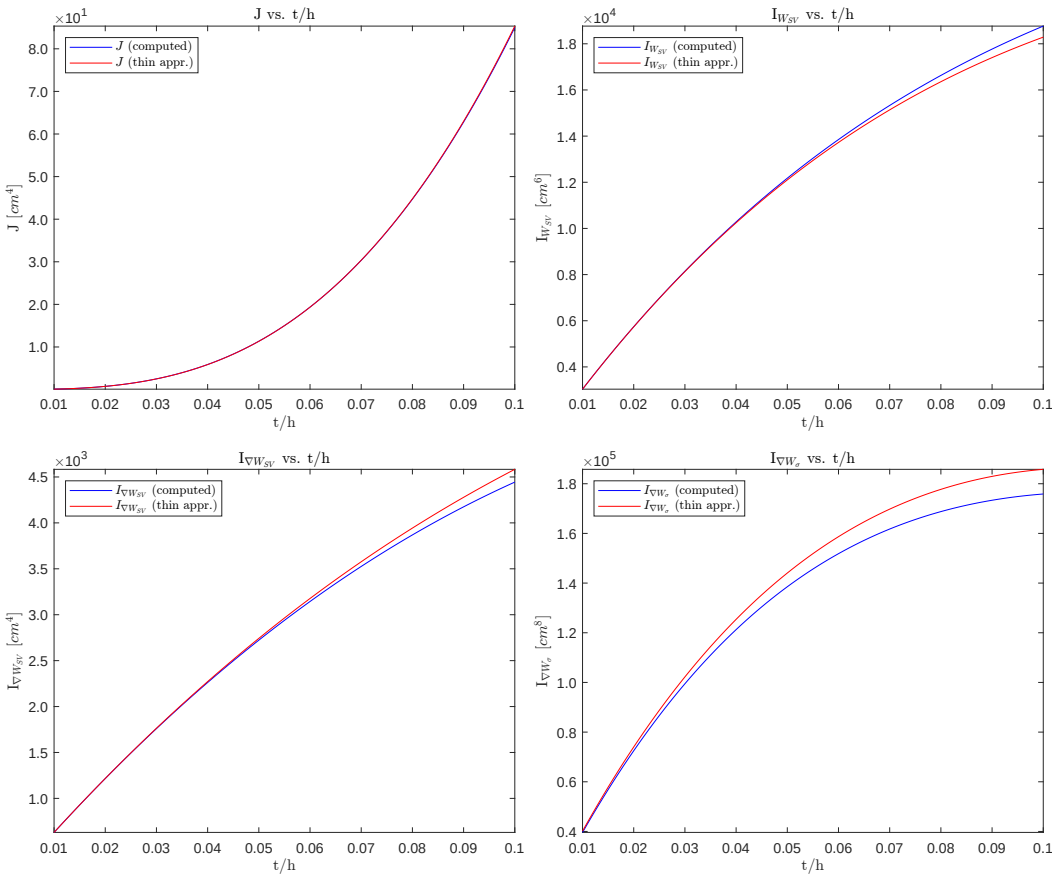

Figure 17: Channel cross section: torsional constants. Values of the Saint–Venant torsional constant J, the warping constant $I_{W_{SV}}$ and the two gradient constants $I_{\nabla W_{SV}}$ and $I_{\nabla W_\sigma}$ for different t/h ratios.

Table 3: Channel cross section: table of torsional constants for different sections thickness ratio t/h ($h = 20\ cm$).

t/h	$J\ [cm^4]$	$I_{W_{SV}}\ [cm^6]$	$I_{\nabla W_{SV}}\ [cm^4]$	$I_{\nabla W_\sigma}\ [cm^8]$
0.10	$8.50099503{\cdot}10^{+1}$	$1.87665937{\cdot}10^{4}$	$4.44404677{\cdot}10^{3}$	$1.75869485{\cdot}10^{5}$
0.05	$3.19982170{\cdot}10^{-1}$	$4.42779462{\cdot}10^{3}$	$9.28004807{\cdot}10^{2}$	$5.68392233{\cdot}10^{4}$
0.01	$9.53031691{\cdot}10^{-2}$	$3.03596030{\cdot}10^{3}$	$6.29488297{\cdot}10^{2}$	$3.96167673{\cdot}10^{4}$

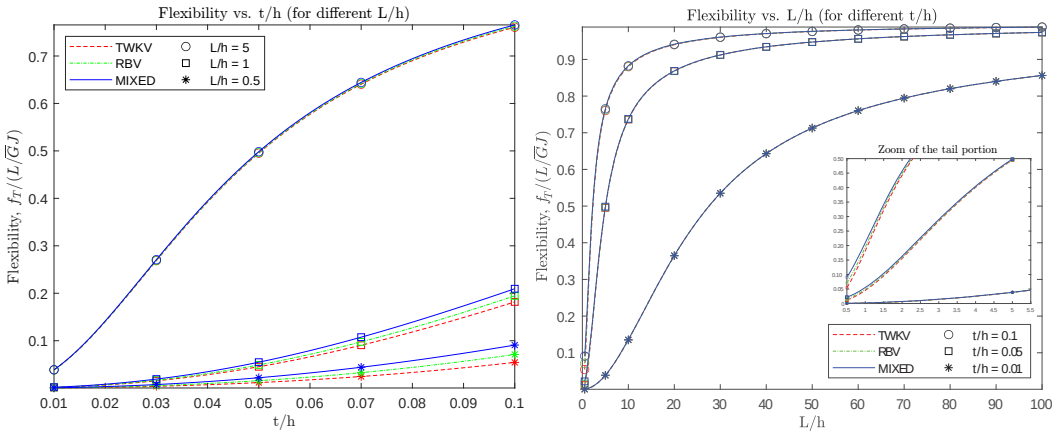

Figure 18: Channel cross section: shaft flexibility. Normalized torsional flexibility $f_T/(L/\bar{G}J)$ versus t/h (left) and L/h (right). All formulations tend to the Saint –Venant value ($f_T^{(SV)} = L/\bar{G}J$) for long shafts (large L/h).

the thin–wall approximations derived in Appendix B.2. A perfect agreement can be observed for the computed Saint–Venant torsional constant J with its thin–wall limit $J^{(thin)}$ in the considered range of thickness t/h (overlapping curves in Figure 17) whereas for the warping constant $I_{W_{SV}}$ and gradient constants $I_{\nabla W_{SV}}$ and $I_{\nabla W_\sigma}$ the matching applies to the smaller values of t/h, with a good agreement for the rest. Table 3 includes the numeric values for the particular sections t/h depicted in Figure 16 and highlighted below as representative examples.

As observed in the previous section, a quick evaluation of the three formulations under study is achieved by comparing the shaft flexibility (194). Figure 18 shows this flexibility, normalized by its Saint–Venant value with uniform warping, that is, $f_T/(L/\bar{G}J)$, for different sections t/h and different shaft lengths L/h. The plot at the left of this figure shows the effect of reducing the thickness of the walls, namely, the different formulations approach each other, with the TWKV showing always the smallest flexibility of the three, followed by the RBV formulation and the mixed formulation, the most flexible formulation of the three.

This observation is clear for the shorter shafts $L/h = 1.0$ and, again to evaluate this limit, for $L/h = 0.5$. The differences for longer shafts, like $L/h = 5.0$ as shown in the left plot of Figure 18, are minimal in the considered range of thickness ratios t/h. This situation is confirmed by the right plot in that figure, showing the normalized flexibility $f_T/(L/\bar{G}J)$ versus the shaft

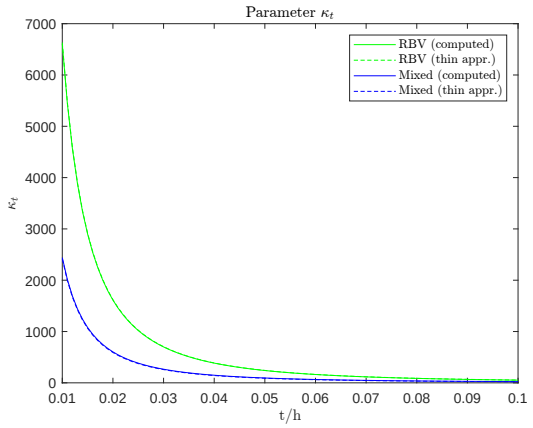

Figure 19: Channel cross section: parameter κ_t versus t/h. Geometric factor driving the limit process to the constrained TWKV formulation for the RBV and mixed formulations.

length L/h. The three formulations basically coincide for long shafts, all approaching asymptotically the value for Saint–Venant torsion (value 1.0 in that plot). Note that this approach is much slower for the thinnest section considered with $t/h = 0.01$.

These results follow the same pattern as observed in the previous section for solid sections, with the indicated effects being more prominent. This can be explained by analyzing the parameter κ_t identified in Sections 4.2 and 5.3 driving the approximation of the RBV and mixed formulations, respectively, to the constrained TWKV formulation. Figure 19 shows that parameter for those two formulations, a figure that has to be compared with Figure 6 for the solid sections studied in the previous section. We obtain again the monotonically increasing value of κ_t with decreasing thickness ratios t/h, with the stiffer RBV formulations always above the mixed formulation, confirming the result (186).

This result shows again the tendency of these two formulation to converge to the constrained TWKV formulation. One big difference of these two figures is the much bigger value of this penalty parameter for the thin–walled sections under study in this section, two orders of magnitude bigger: 6,605 vs 26 maximum values for $\kappa_t^{(RBV)}$, 2,441 vs 21 for $\kappa_t^{(MIX)}$. The bigger difference between these two formulations, with a much stiffer RBV formulation, is also noted. Figure 19 also includes the value of the penalty parameter κ_t calculated with the thin–wall estimates of the different torsional constants

involved, showing a very good agreement with the computed values in the thin range of thickness considered in this case, thus leading to the same conclusions. We refer to Remark B.3 in Appendix B.2 for a complete discussion, including the respective numerical values.

We must indicate that this tendency to converge to the constrained limit encompassed by the TWKV formulation as the thickness ratio t/h decreases is not at all obvious, even if observed for the solid and open (simply-connected) thin–walled section studied so far. We will see in the next section that this situation will not be observed for closed (multiply-connected) thin–walled sections. On the other hand, the limiting process of the overall response of the shaft to the Saint–Venant solution for long shafts is a proof of the locality of the effects of the restrained warping at the shaft's root. However, this process is slower for thin sections (small t/h), as shown by the results in the right plot of Figure 18 showing the shaft's flexibility $f_T/(L/\bar{G}J)$ versus L/h for different sections t/h.

Figure 20 shows the diagrams for the bimoment $B_W(z)$ and the bishear $T_W(z)$ along the shaft $\widetilde{z} = z/L \in [0, 1]$, given by equations (205) and (200) (normalized, again, by $T_L L$ and T_L, respectively, for the torque T_L at the shaft's tip $z = L$). We include the diagrams for the sections with $t/h = 0.10$, 0.05 and 0.01, and for the three different structural formulations under study. Each of these plots show the results for the different length ratios $L/h = 5.0$, 1.0 and 0.5. The agreement of the three formulations as the thickness ratio t/h reduces noted above for the shaft flexibility is also observed in these diagrams. Similarly, the effects of the restrained warping at the shaft's root $z = 0$ are stronger for the longer shafts, larger L/h, as seen for the larger values of both the bimoment and bishear.

Figure 20 is to be compared to Figure 7 for the solid sections, noting the stronger effects of the restrained warping in the current open channel thin–walled sections, especially as the thickness ratio t/h decreases. For solid sections, especially thicker ones like the square section, these strong effects were observed for the original TWKV formulation, partly as a consequence of the torque anomaly unrealistically fixing the value $T_W(0)/T_L = 1.0$. This fixed value also applies in this case, as given again by equation $(202)_2$, but now the values obtained by the RBV and mixed formulation fall closer. Again, the lowest values of the two stress resultants $B_W(z)$ and $T_W(z)$ are obtained by the mixed formulation, in fact all along the shaft, followed with increasing values, in order, by the RBV and TWKV formulations. This situation matches again the results observed for the shaft flexibility predicted by these

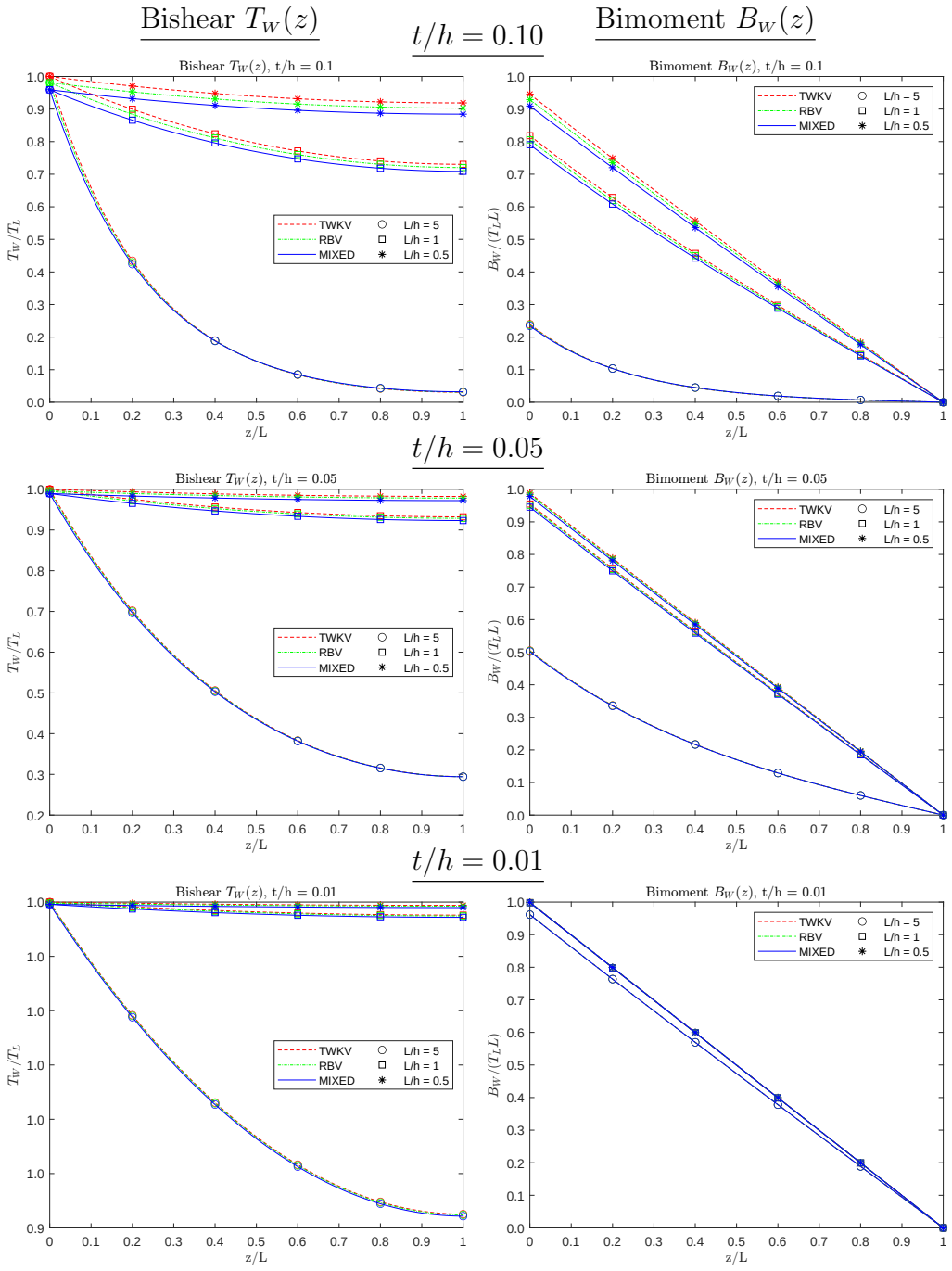

Figure 20: Channel cross section: moment diagrams normalized by the tip torque T_L. Distribution of the bishear $T_W(z)$ (left) and bimoment $B_W(z)$ (right) for different section aspect ratios $t/h = 0.10, 0.05, 0.01$, comparing different shaft's lengths $L/h = 5.0, 1.0, 0.5$ for each aspect ratio.

different formulations.

These structural stress resultants create section stresses depicted in Figures 21 to 23. In particular, Figures 21 and 22 show the shear stresses at the shaft's root for the sections $t/h = 0.10$ and 0.05, respectively, both for the shaft of length $L/h = 1.0$. We have depicted the Saint–Venant component $\boldsymbol{\tau}_{SV}$ given by (219), the warping component $\boldsymbol{\tau}_{W}$ by (220), and the total shear stress $\boldsymbol{\tau} = \boldsymbol{\tau}_{SV} + \boldsymbol{\tau}_{W}$, all as stress vectors at the quadrature points for the different elements, superposed to contour plots of their magnitude. All these values are shown again for a unit tip rotation $\phi_L = f_T T_L = 1.0$, the actual distribution not affected obviously by this normalizing choice.

The vanishing of the Saint–Venant component $\boldsymbol{\tau}_{SV}$ of the shear stress for the TWKV formulation at the shaft root (the torque anomaly) and the lack of satisfaction of the proper stress boundary conditions at the walls edge for the RBV formulation is noted again. In particular, the RBV formulation results in the unrealistic "rotational" pattern of the total stress $\boldsymbol{\tau}$ shown by equation (213). Note that in this case occurs around the center of twist $\bar{\boldsymbol{x}}_T$ as located by the values included in Table 2. In contrast, the characteristic distribution of the shear stresses under torsion can be observed for the TWKV and mixed formulations. In this respect, note that Figure 16 shows the tendency of the Saint–Venant warping function $W_{SV}(x, y)$ to become bilinear along the wall's tangent and thickness directions, with the secondary warping function $W_\sigma(x, y)$ showing a cubic variation along the direction of the middle line of the different walls, all as the thickness decreases.

Figure 23 depicts contour plots of the normal axial stress distribution σ_z at the shaft's root $z = 0$ for the sections with $t/h = 0.10$ and 0.05, and shaft's length $L/h = 1.0$, given by relation (218). Note that all three formulations follow the distribution given by the Saint–Venant warping function $W_{SV}(x, y)$, depicted at the left column of Figure 16 for the different sections. This stress is caused (or it causes, depending of personal preference) by the bimoment $B_W(0)$ and the higher value of this quantity for the TWKV formulation is clearly reflected in Figure 23, followed in order by the less stiff RBV and mixed formulations. To evaluate the adequacy of all these results, direct consequence of the approximation behind the different formulations, we undertake again a full three–dimensional elastic analysis of the shafts at hand.

7.2.1. Three–dimensional analysis

We consider finite element simulations of the shafts under study, assuming full 3D treatment of the solid with full three–dimensional linear elastic

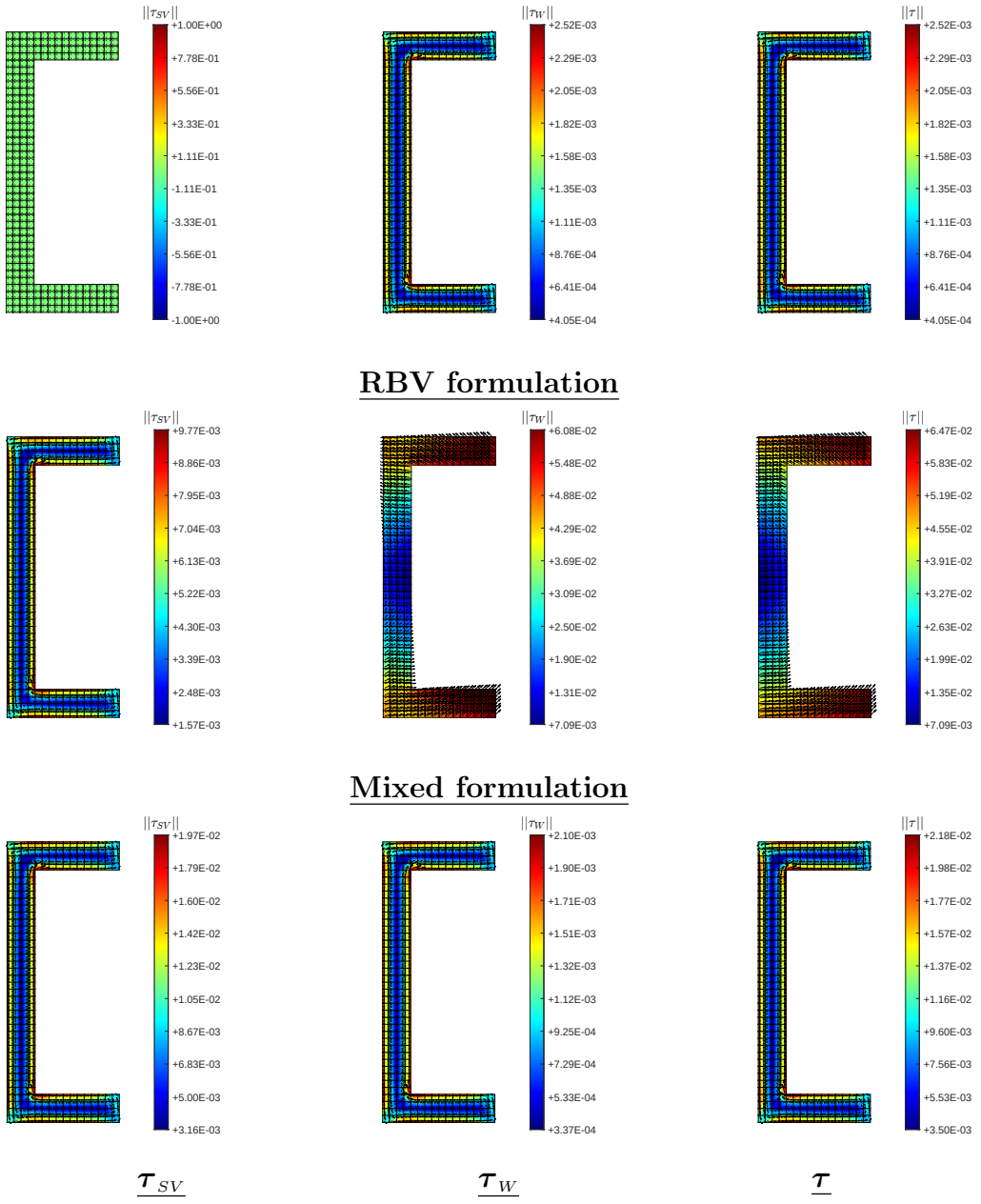

Figure 21: Channel cross section: shear stresses. Distributions of the Saint–Venant shear stress $\boldsymbol{\tau}_{SV}$, the warping shear stress $\boldsymbol{\tau}_W$ and the total shear stress $\boldsymbol{\tau}$ for the channel cross section $t/h = 0.10$ and $L/h = 1.0$ at the shaft root $z = 0$. All values are normalized as $\boldsymbol{\tau}/\bar{G}$ and correspond to the case with a unit rotation $\phi_L = 1.0$ at the opposite tip of the shaft.

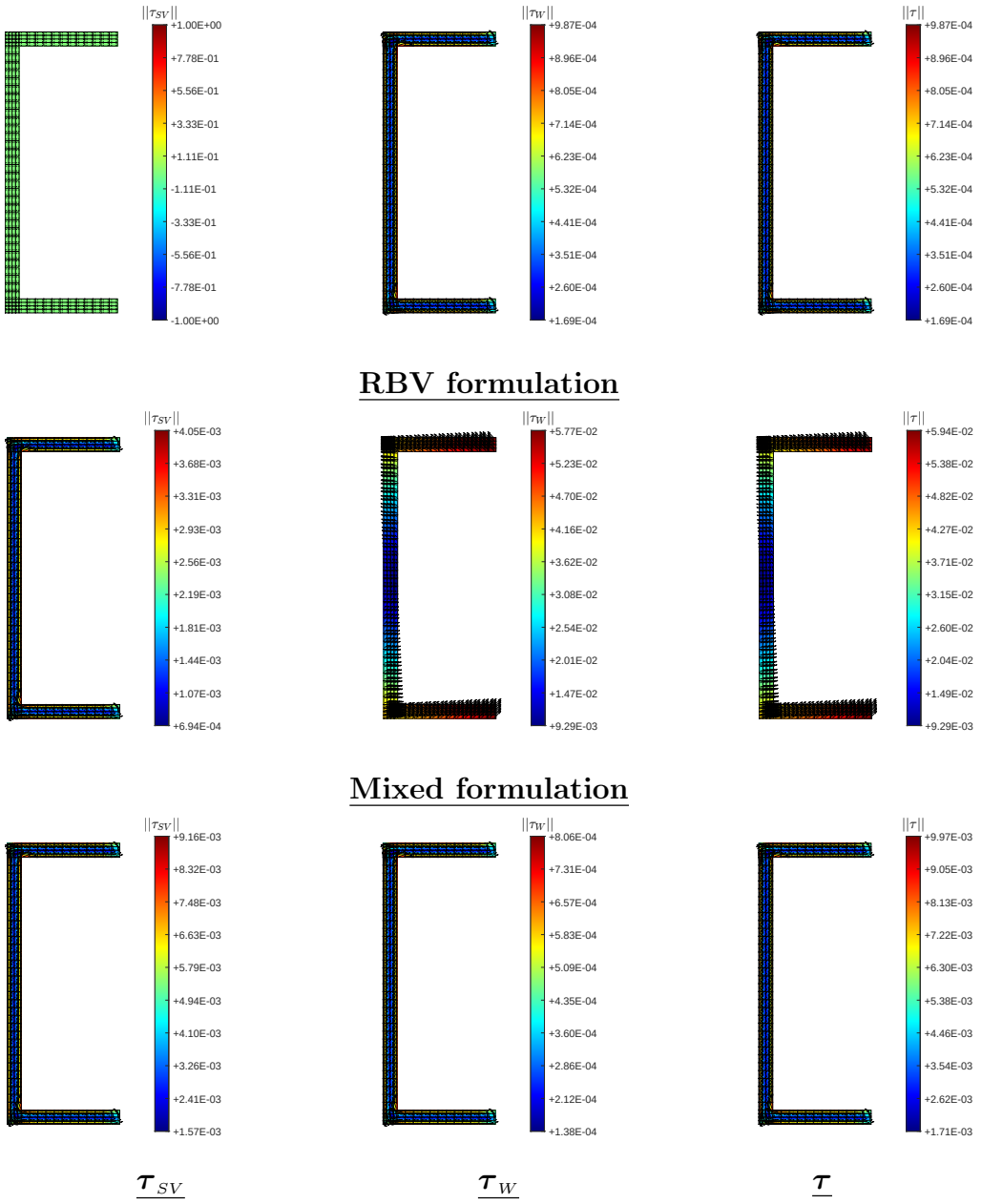

Figure 22: Channel cross section: shear stresses. Distributions of the Saint–Venant shear stress $\boldsymbol{\tau}_{SV}$, the warping shear stress $\boldsymbol{\tau}_W$ and the total shear stress $\boldsymbol{\tau}$ for the channel cross section $t/h = 0.05$ and $L/h = 1.0$ at the shaft root $z = 0$. All values are normalized as $\boldsymbol{\tau}/\bar{G}$ and correspond to the case with a unit rotation $\phi_L = 1.0$ at the opposite tip of the shaft.

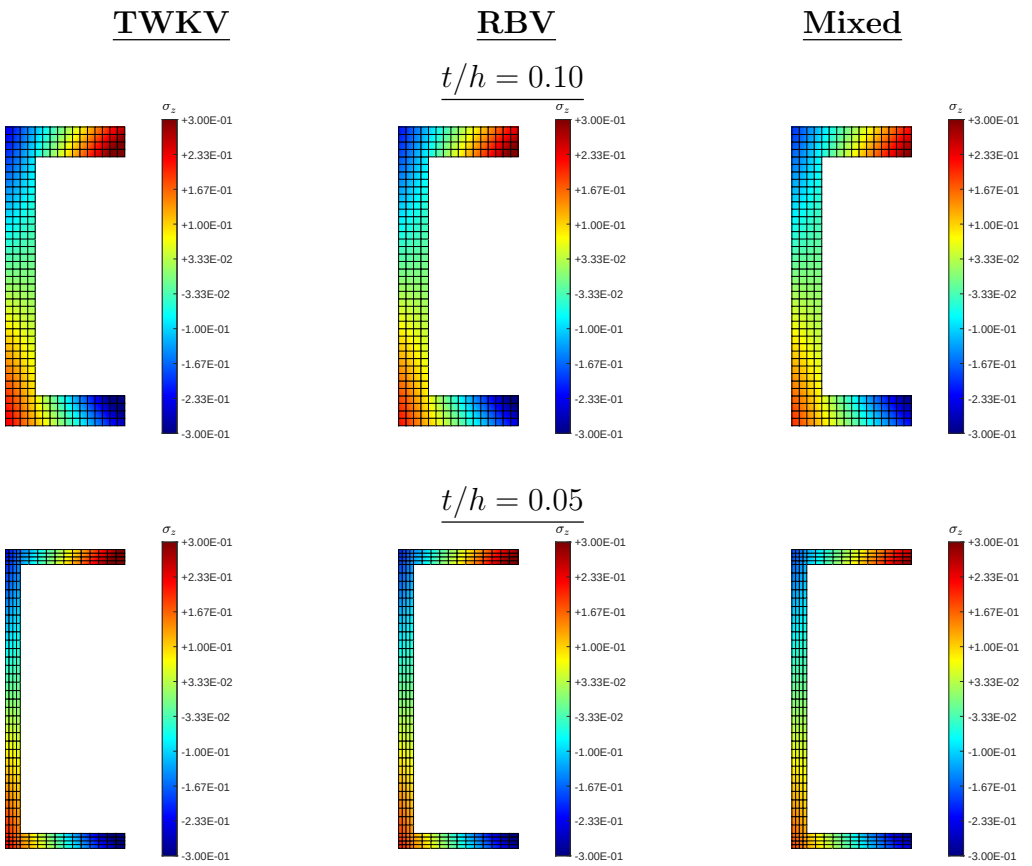

Figure 23: Channel cross section: axial stress. Distribution of the axial stress σ_z at the shaft root $z = 0$ for the cross sections with $t/h = 0.10$, 0.05 and shaft's length of $L/h = 1.0$. All values normalized by the material's Young modulus as $\sigma_z/\bar{E}$ and correspond to the case with a unit rotation $\phi_L = 1.0$ at the opposite tip of the shaft.

response of the material. We maintain the finite element discretizations of the cross sections considered above for the separate section analyses. The finite element discretization of the solid shafts consider 20 layers of three–dimensional 8−node brick elements along the length $z \in [0, L]$ graded towards the fixed root of the shaft at $z = 0$. Figure 24 shows two typical meshes for the section with thickness ratio $t/h = 0.10$. The simulations are run by imposing the displacement $(12)_{1,2}$ at the shaft's tip $z = L$ for the cross section displacements (u_x, u_y), with a unit tip rotation $\phi_L = 1.0$ and free warping displacement $u_z(x, y, L)$. The three components of the three–dimensional

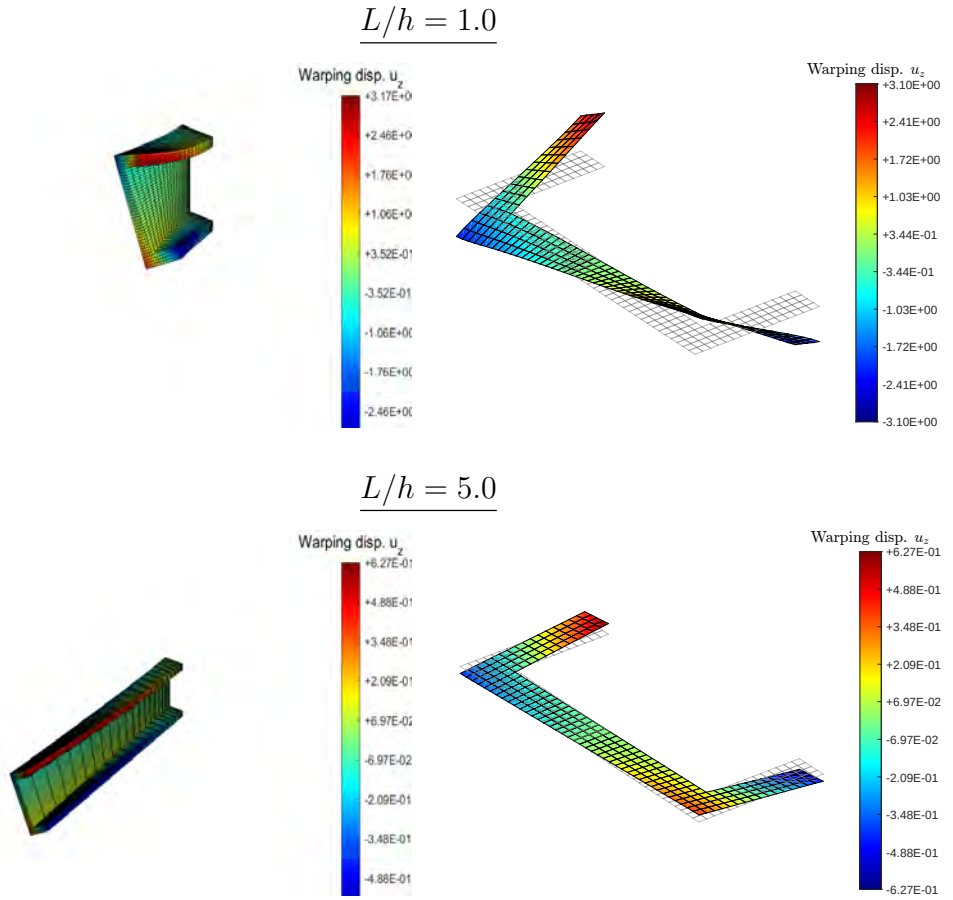

Figure 24: Channel cross section: 3D shaft. Three–dimensional finite element solution for shafts with $L/h = 1.0$, 5.0 and $t/h = 0.10$, showing the contours of the axial displacement u_z on top of the 3D deformed configuration of the shaft (left), and the elevation plot of the resulting warping at the shaft's tip $z = L$ (right).

displacements are fixed to vanish at the shaft's root $z = 0$. The QM1/E12 enhanced strain element of Simo et al. [1993] is considered in the three–dimensional finite element solutions, because of its superior performance in shear.

Figure 24 depicts the solutions obtained for the shaft lengths of $L/h = 1.0$ and 5.0, both for the channel cross section with thickness ratio $t/h = 0.10$. We show the three–dimensional deformed configuration of the shaft, with superposed contour plots of the axial (warping) displacement $u_z(x, y, z)$.

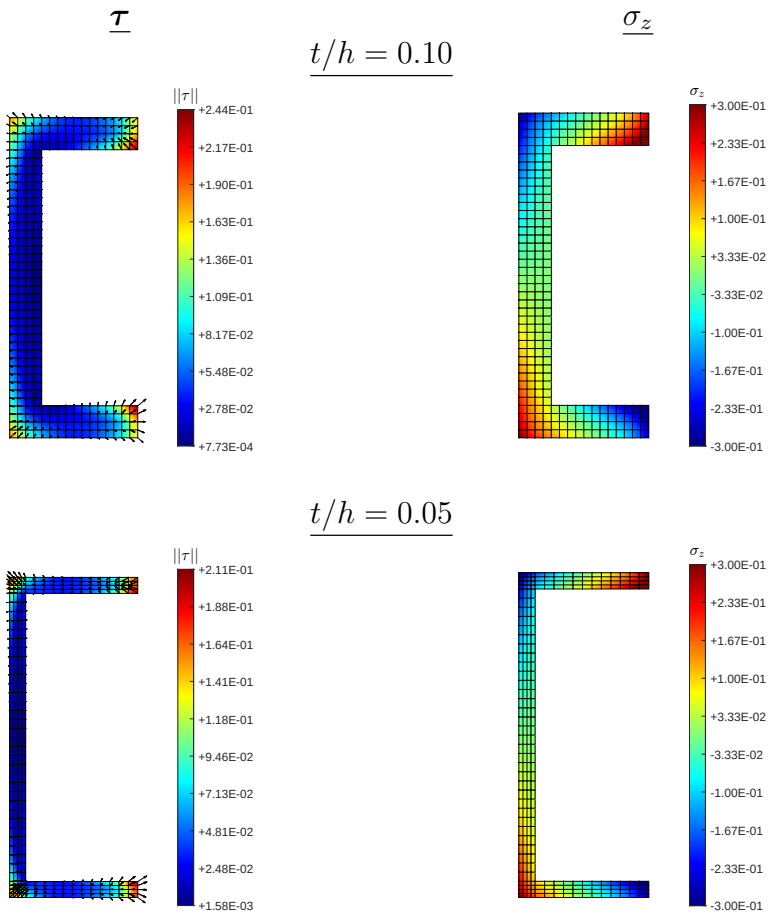

Figure 25: Channel cross section: stresses. Shear and normal stresses in the three–dimensional finite element solution at the shaft root $z = 0$ for $t/h = 0.10$, 0.05 and $L/h = 1.0$. Values are normalized as $\boldsymbol{\tau}/\bar{G}$ and $\sigma_z/\bar{E}$, and they correspond to the case with a unit rotation $\phi_L = 1.0$ at the opposite tip of the shaft.

Separately, we show elevation plots of this computed displacement component at the tip $z = L$, with free warping. These plots have to be compared with the Saint–Venant warping function $W_{SV}(x, y)$ computed for this section and shown in Figure 16 (top left corner). Good agreement is observed.

Focusing on the restrained warping caused by the fixed support, we include in Figure 25 the shear stress $\boldsymbol{\tau}$ and normal (axial) stress σ_z at the root $z = 0$ for the shafts with thickness ratios of $t/h = 0.10$ and 0.05, both for the shaft of length $L/h = 1.0$. We show contour plots of the magnitude of

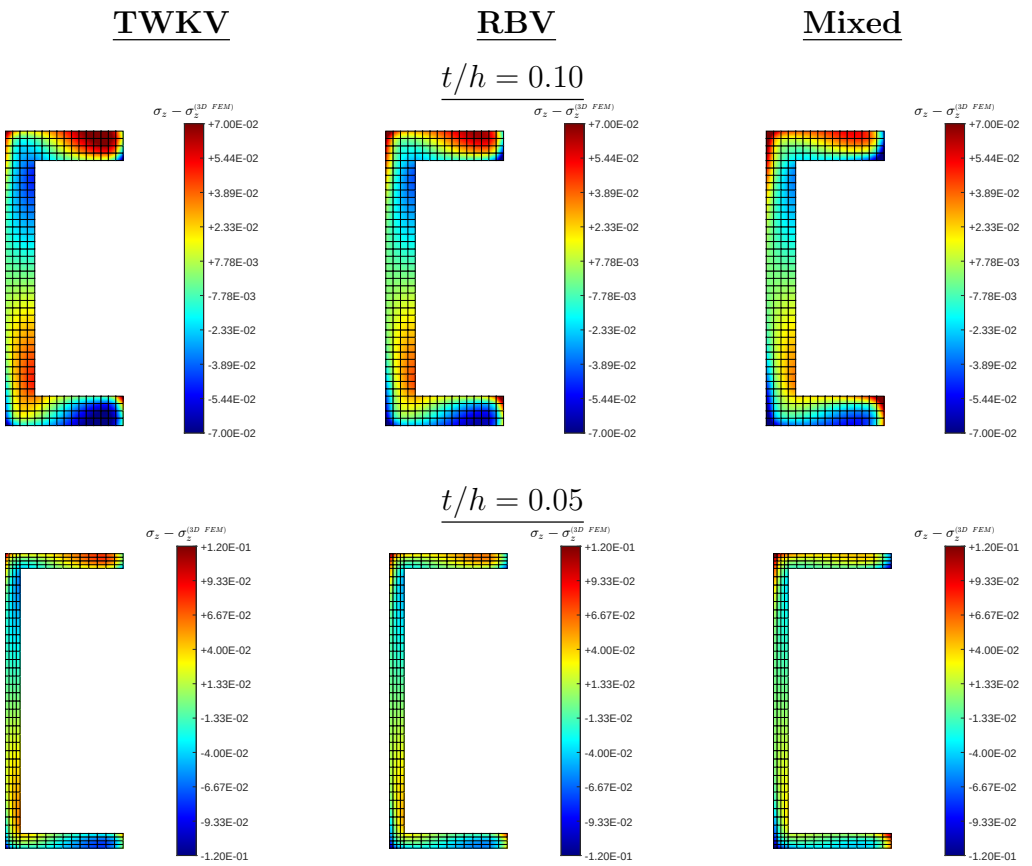

Figure 26: Channel cross section: axial stress difference. Comparison of the axial stress at the shaft's root $z = 0$ between the different considered formulations with the three–dimensional finite element solution $\sigma_z - \sigma_{z(3D)}$, for the different cross section $t/h = 0.10$, 0.05 and $L/h = 1.0$. All values are normalized by the material's Young modulus as $\sigma_z/\bar{E}$ and correspond to the case with a unit rotation $\phi_L = 1.0$ at the opposite tip of the shaft.

these quantities in this figure, including the stress vectors corresponding to the shear stress $\boldsymbol{\tau}$ as well. Note that these are the three–dimensional stresses $\bar{\boldsymbol{\sigma}}^A_{(3D)}$ in the solid volume of the shafts, projected to the nodes following the relations (229). They correspond then to a full three–dimensional state of stress, including the stress components avoiding the distortion of the cross section itself, a component not present in the structural formulations of torsional warping considered in this paper. This component shows clearly in the plots of shear stresses in Figure 25.

The normal stress $\sigma_z(x, y, 0)$ at the shaft's root is indeed a direct consequence of the restrained warping at that support, motivating then the inclusion in Figure 26 the contour plots of the difference $\sigma_z - \sigma_{z(3D)}$ of this stress for the different formulations under study with the computed three–dimensional solutions. We show contour plots of this difference for the sections with thickness ratios of $t/h = 0.10$ and 0.05, both for the shaft with $L/h = 1.0$, that is, for the same full three–dimensional solutions shown in Figure 25. As occurred for the solid sections in Figure 12 we observe a bigger discrepancy with the TWKV formulations when compared to the RBV and mixed formulations, in this order. This discrepancy/error reduces for thinner sections, smaller t/h. Still, the stress level σ_z remains higher for the RBV and, especially, the TWKV formulations, confirming the stiffer character of the approximation assumed by these formulations when contrasted to the proposed mixed formulation.

This higher stress level is also confirmed by evaluating the bimoment $B_W(0)$ at the shaft's root causing the normal stresses $\sigma_z(x, y, 0)$. Figure 27 shows this bimoment, normalized as $B_W(0)/(T_L L)$, together with the associated bishear, normalized the by tip torque as $T_W(0)/T_L$. These quantities are plotted versus the section thickness ratio t/h and the shaft's length ratio L/h, showing different curves for several of the other parameter in each case. The values of the bimoment and bishear for the three–dimensional finite element solutions are obtained using the relations (230) and (231) based on the nodally projected 3D stresses (229), while the values for the different structural theories are given by relations (209) and (202), respectively.

The plots in Figure 27 indicate a very good agreement between the three–dimensional and the three different structural theories for the bimoment $B_W(0)$, specially for the mixed formulation, always better than the RBV and TWKV formulations, in this order. The differences are small though, especially for thin (small t/h) sections and long shafts (large L/h). The bishear $T_W(0)$ exhibits, in contrast, a bigger discrepancy between the structural theories and the full three–dimensional solutions, especially again for long shafts and thinner sections. Still, we can observe the fixed value of $T_W(0)/T_L = 1$ for the bishear at the root obtained by the TWKV formulation for all sections and shaft's length (the torque anomaly, leading to the vanishing of the Saint–Venant shear stresses in Figure 21 and 22), with the other structural formulations and the 3D solutions only approaching that limit for very thin sections.

This situation reveals again the constrained character of the original

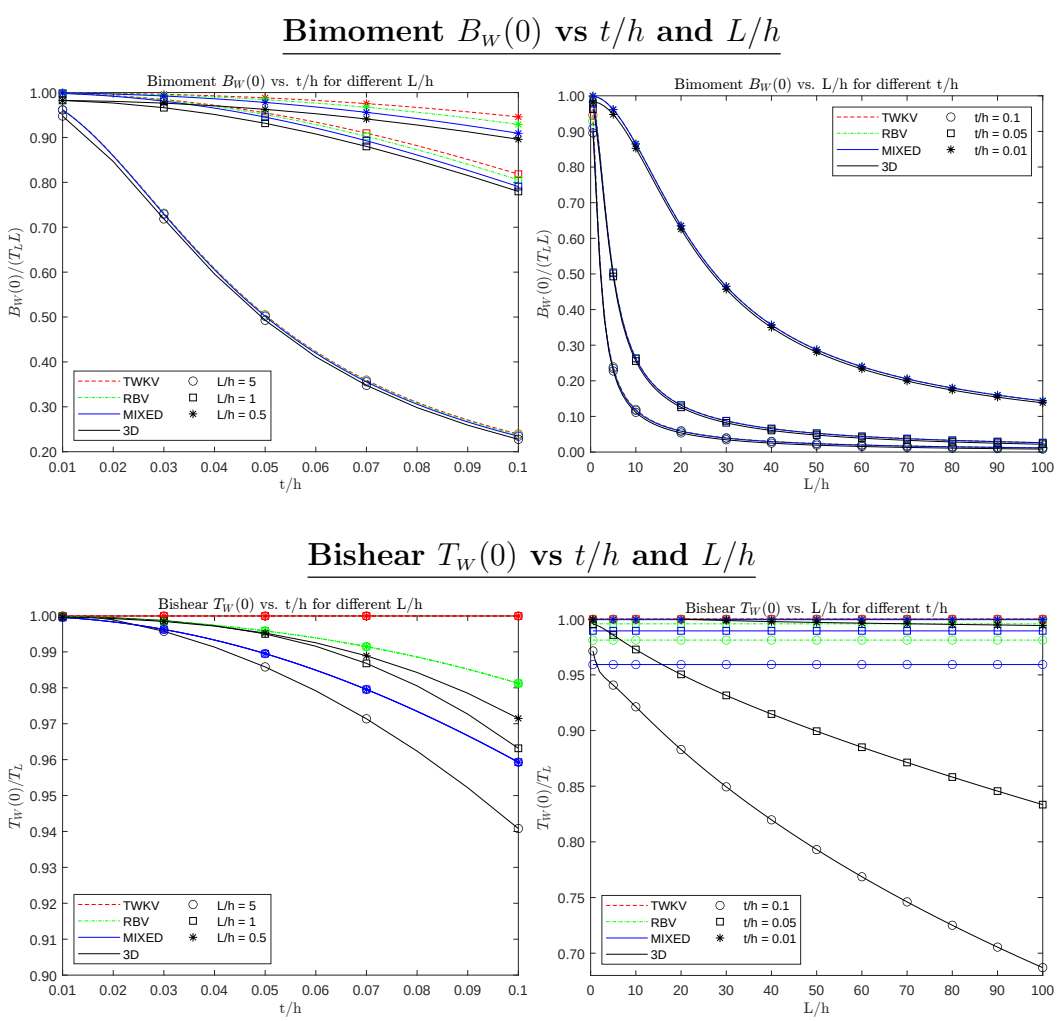

Figure 27: Channel cross section: bimoment and bishear at the shaft's root. Values of the bimoment $B_W(0)$ (top) and the bishear $T_W(0)$ (bottom) at $z = 0$ versus the section aspect ratio t/h (left) and shaft's length ration L/h (right) obtained by the different formulations and the 3D finite element solution.

TWKV formulation, leading to an over-stiff response of the shaft when compared to the full three–dimensional finite element solutions as shown in Figure 28. As occurred for the solid sections in Figure 15, we normalize the torsional flexibility as $f_T/(L/\bar{G}\tilde{J}_{ref})$ for a dimensional reference value $\tilde{J}_{ref}$, independent of the structural theories, absent in the full three–dimensional solutions. We use the thin–wall limit $J^{(thin)}$ as it can be found in equation

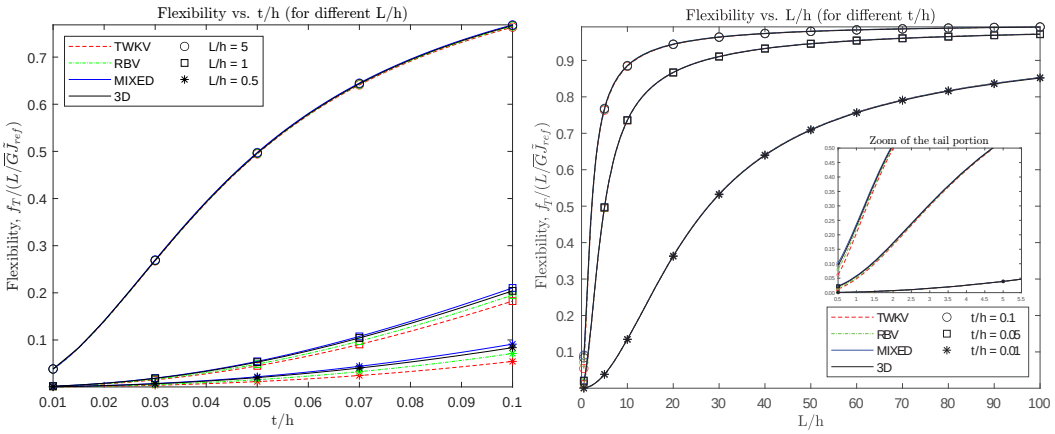

Figure 28: Channel cross section: shaft flexibility. Normalized torsional flexibility $f_T/(L/\bar{G}\tilde{J}_{ref})$ with a dimensional reference value ($\tilde{J}_{ref} = J^{(thin)}$), allowing the incorporation of the 3D FEM solutions. Values versus thickness ratio t/h (left), and shaft's length L/h (right).

(B.11) in Appendix B.2.

The stiffer response of the TWKV formulation over the RBV and mixed formulations is confirmed in the plots shown in Figure 28, although with a substantially less difference than for the solid sections as observed in Figure 15. Clearly, we are now in the range of thin to very thin sections where the limit process to warping–twist constraint encompassed by the TWKV is reached. We emphasize again that this observed response as the thickness ratio t/h reduces applies only to open (simply–supported) section topologies considered so far. The situation may, and will, change for the hollow closed thin–walled sections considered next.

7.3. Evaluation for closed (hollow) thin–walled cross sections

Next we undertake the analysis of the different formulations for closed thin–walled sections. These sections are characterized by a multiply connected topology in contrast to the simply connected open thin–walled sections of the previous section. We consider first a single cell section, in particular, the box section presented in Figure 2 on page 84, but with two thickness distributions along the wall. It consists of a square hollow section of height/width $h = 2b$, with thicknesses t_f and t_w along the opposite sides of the wall. Two cases are considered in what follows, namely, (1) a constant thickness distribution $t_f = t_w = t$ and (2) the non-uniform distribution

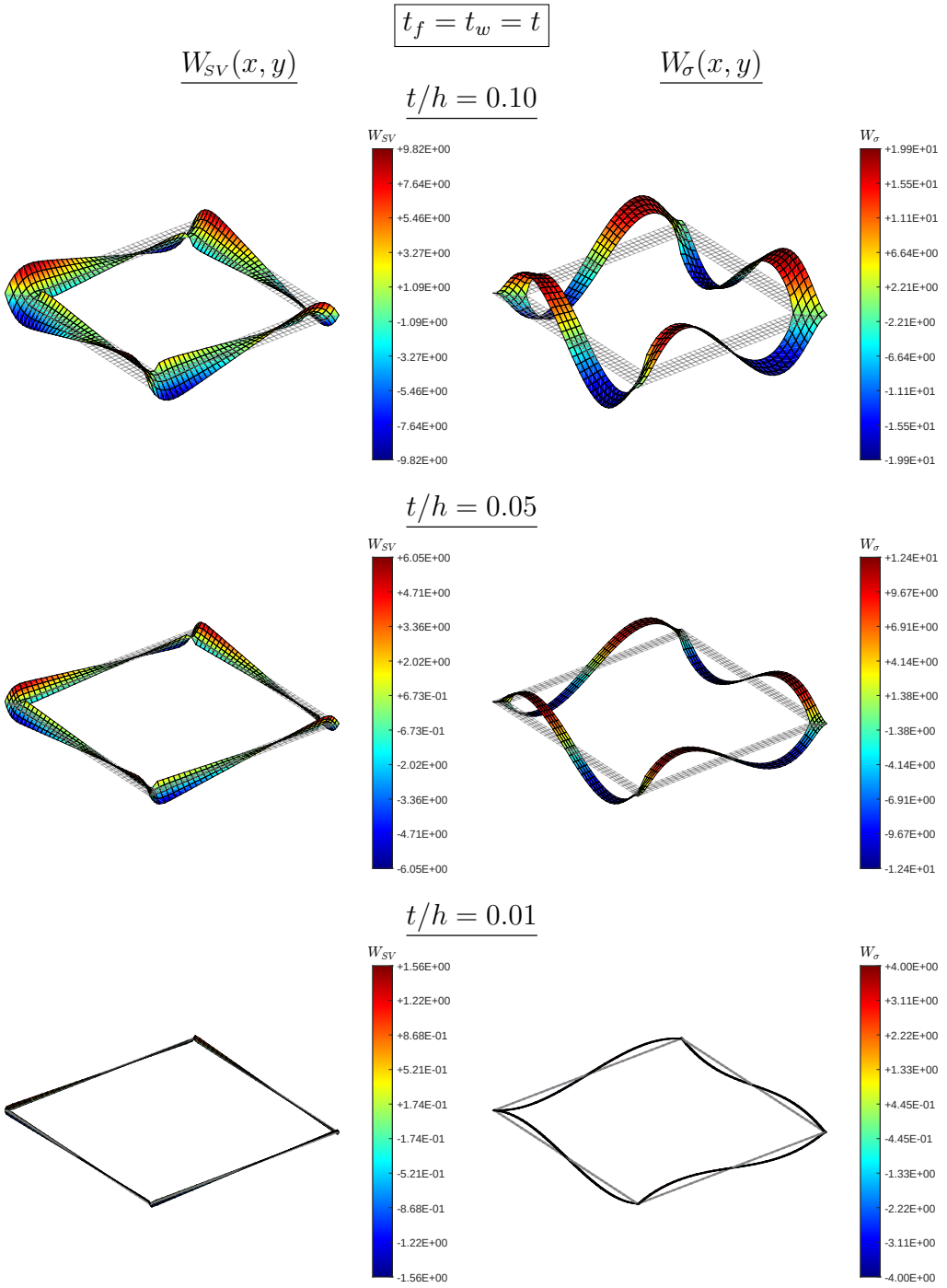

Figure 29: Box cross section ($t_f = t_w = t$, Neuber tube): warping functions. Computed warping functions $W_{SV}(x,y)$ (left) and $W_\sigma(x,y)$ (right) for sections with thickness ratios $t/h = 0.10$, 0.05, 0.01.

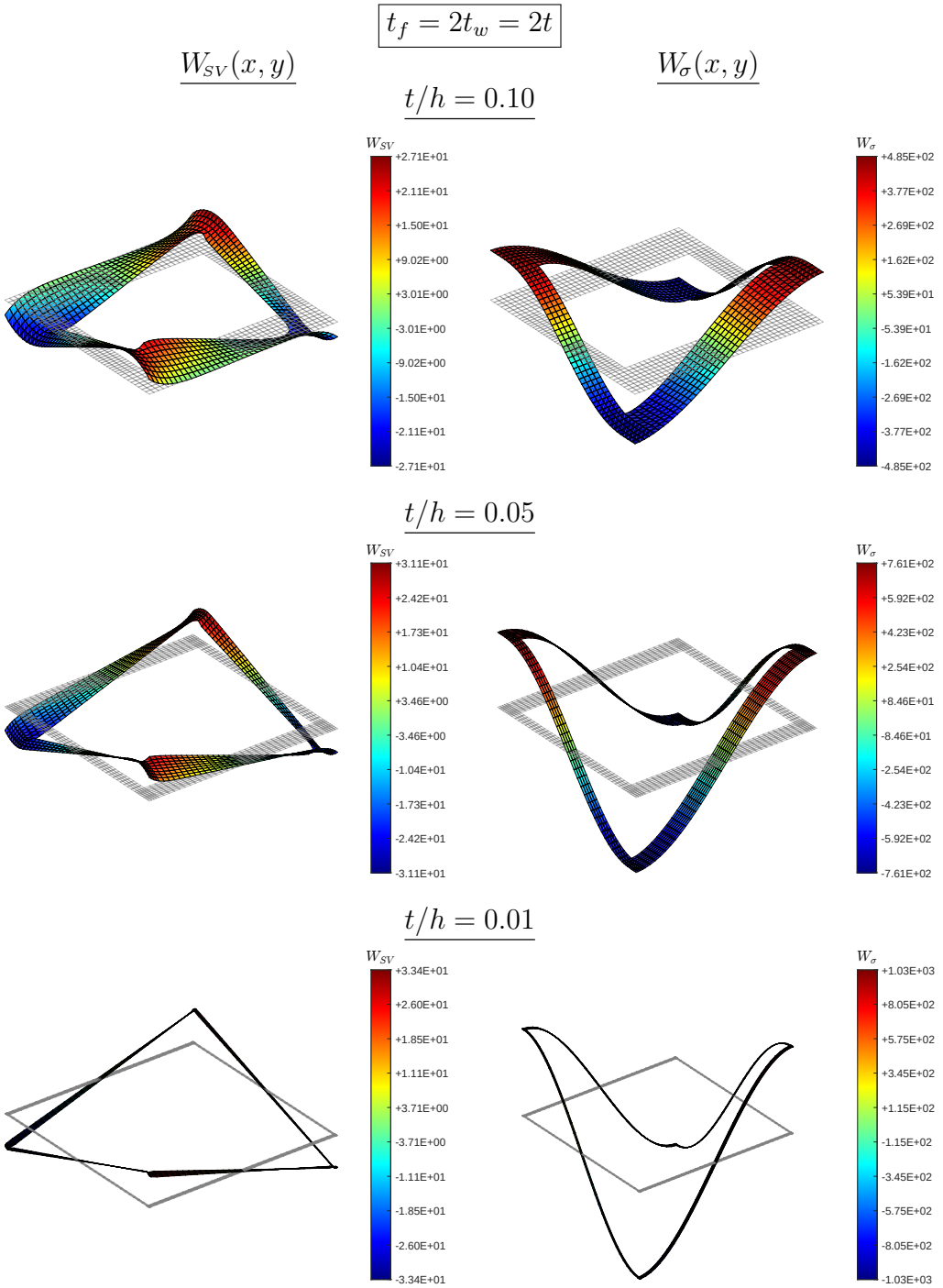

Figure 30: Box cross section ($t_f = 2t_w = 2t$): warping functions. Computed warping functions $W_{SV}(x,y)$ (left) and $W_\sigma(x,y)$ (right) for sections with thickness ratios $t/h = 0.10, 0.05, 0.01$.

$t_f = 2t_w = 2t$ for, say, the flanges and the webs; see Figure 2. The particular value of $h = 2b = 20\ cm$ is considered in the numerical simulations, with thickness ratios in the range $0.01 \leq t/h \leq 0.10$, expressed in terms of the web thickness $t_w = t$ for all cases. This is the same range considered for the open thin–walled sections of the previous section but, as we shall see, the different topology of the cross section will have significant consequences on how the three different formulations of restrained warping compare with each other.

The consideration of the two different cases is significant to the study presented here, since the case with $t_f = t_w = t$ is an example of the so-called Neuber tubes (see GJELSVIK [1981], page 128) in contrast to the second case with $t_f = 2t_w = 2t$. Neuber tubes are hollow thin-walled sections in which the primary warping, defined in terms of the sectorial coordinate along the wall middle line as described in Appendix B.3, vanishes. In that thin–wall limit, the only warping that the section suffers is then given by a bilinear distribution over the wall, the secondary warping, as occurred for the thin rectangular sections considered in Section 7.1. As noted in that appendix, this situation leads, for example, to a small warping constants $I_{W_{SV}}$ (i.e. of order t^3) as opposed to more general thin–walled closed sections (with $I_{W_{SV}}$ of order t), as it is the case for the section configuration with $t_f = 2t_w$. We emphasize that these considerations are only strictly valid in the very limit of thin–walls $t/h \to 0$. Our main purpose is to evaluate the idoneity of the different formulations of restrained warping under study for this type of sections, including the effects of these considerations. Hence, we follow a scheme in the exposition similar to the previous sections, making cross comparisons easy.

In this way, Figures 29 and 30 show the computed warping functions $W_{SV}(x,\, y)$ and $W_\sigma(x, y)$ for the two cases $t_f = t_w$ and $t_f = 2t_w$, respectively. In both cases, we present the solutions for the specific cross sections with $t/h = 0.10$, 0.05 and 0.01 as representative examples in the considered range of thickness ratios t/h. In all cases, we consider finite element discretizations of the plane section with 4 equally spaced 4−node bilinear quadrilateral elements through the web thickness and a proportional number of elements across the flanges, with a constant number of elements along the walls for all aspect ratios t/h. Double symmetry considerations apply. Due to these conditions, the centroids $\bar{\boldsymbol{x}}_{_E} = \bar{\boldsymbol{x}}_{_G}$ and the twist/shear center $\bar{\boldsymbol{x}}_{_T}$ all coincide with the geometric center of the section.

The considerations noted above regarding the warping function $W_{SV}(x, y)$

become clear by comparing the computed values shown in Figures 29 and 30, especially as the thin–wall limit is approached. The characteristic bilinear distribution, with a linear dependence through the thickness, is clearly the only dominant component present in the computed warping function $W_{SV}(x, y)$ for the Neuber tube $t_f = t_w$ in Figure 29 in that thin limit. In contrast, the characteristic limit distribution of the primary warping along the wall length dominates the alternative section with $t_f = 2t_w$ in Figure 30. We refer to Appendix B.2 for the complete characterization of these functions in the thin–wall limit. We emphasize again that all these considerations behind those limit estimates are only approximations corresponding to the thin limit. The approach presented here does not rely on any of these approximate considerations, as they are considered for typical thin–walled sections in practice. Instead, we compute the exact warping function $W_{SV}(x, y)$ for any thickness, as well as the second warping function $W_\sigma(x, y)$. In this respect, it is interesting to observe the considerable difference of this second function for the two characteristic cases under consideration. We remind the reader that this function depends directly on the Saint–Venant warping function, as it appears in the boundary-value problem (79).

Figures 31 and 32 depict the torsional constants obtained from those computed warping functions for each case under consideration. We include again the Saint–Venant torsional constant J, the warping constant $I_{W_{SV}}$ and the two additional constants $I_{\nabla W_{SV}}$ and $I_{\nabla W_\sigma}$, all shown for the considered range of the thickness ratio t/h. In all cases we include the values corresponding to the thin–wall limit presented in Appendix B.2. The computed values (evaluated directly from the computed warping function $W_{SV}(x, y)$ and not relying on any approximations for small thickness t) can be seen in Figures 31 and 32 to match well these thin–wall limits as $t/h \to 0$. Tables 4 and 5 include the actual numeric values for the three sections $t/h = 0.10$, 0.05 and 0.01 used as representative cases in what follows. These are the sections shown in the original Figures 29 and 30 in several of the figures to follow. The different orders of magnitude of some of these torsional constants for the two different section geometries, a consequence of the previous arguments, is to be noted.

It is also interesting to observe the different dependence of some of the torsional constants on the thickness ratio for the two box sections considered here. Comparing the results in Figures 31 and 32 for each of these cross sections, the most significant difference is in the nature of the distribution of the $I_{W_{SV}}$ and $I_{\nabla W_\sigma}$ section constants. The warping constant $I_{W_{SV}}$ is of order $o\left((t/h)^3\right)$ for the Neuber tube $t_f = t_w = t$, whereas it is of order $o\left((t/h)\right)$

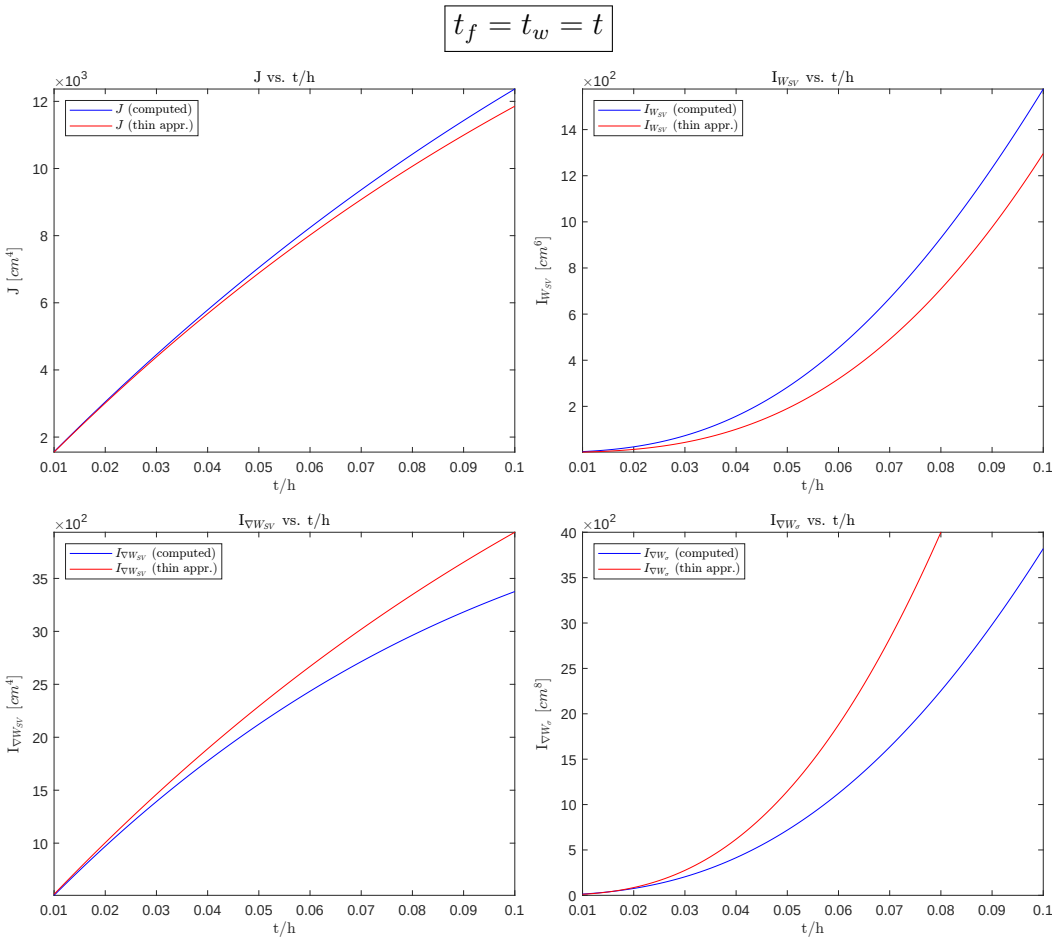

Figure 31: Box cross section ($t_f = t_w = t$, Neuber tube): torsional constants. Values of the Saint–Venant torsional constant J, the warping constant $I_{W_{SV}}$ and the two gradient constants $I_{\nabla W_{SV}}$ and $I_{\nabla W_\sigma}$ for different t/h ratios.

Table 4: Box cross section ($t_f = t_w = t$, Neuber tube): table of torsional constants for different sections thickness ratio t/h ($h = 20\ cm$).

t/h	$J\ [cm^4]$	$I_{W_{SV}}\ [cm^6]$	$I_{\nabla W_{SV}}\ [cm^4]$	$I_{\nabla W_\sigma}\ [cm^8]$
0.10	$1.23677966{\cdot}10^4$	$1.57591655{\cdot}10^3$	$3.37620344{\cdot}10^3$	$3.81971644{\cdot}10^3$
0.05	$7.04796191{\cdot}10^3$	$2.82805259{\cdot}10^2$	$2.12270476{\cdot}10^3$	$7.18179690{\cdot}10^2$
0.01	$1.56287589{\cdot}10^3$	$3.84789924{\cdot}10^0$	$5.07306512{\cdot}10^2$	$1.40319061{\cdot}10^1$

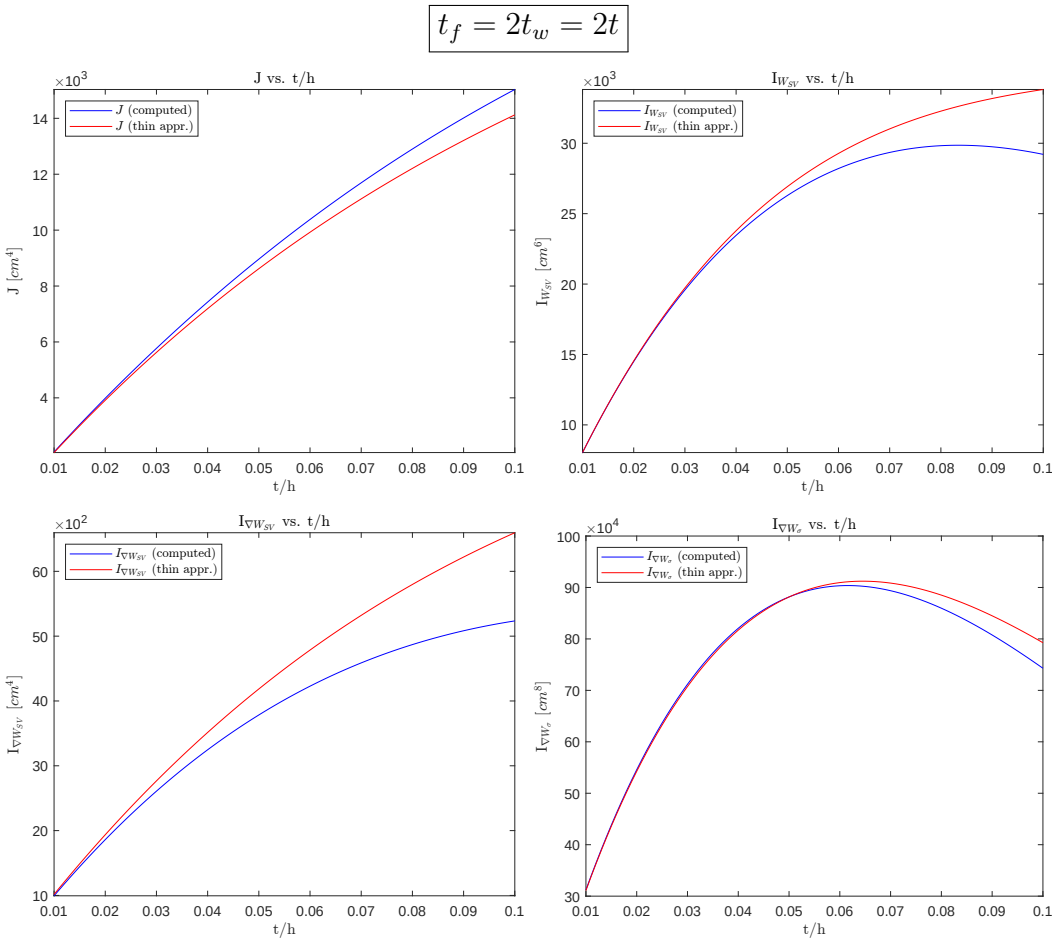

Figure 32: Box cross section ($t_f = 2t_w = 2t$): torsional constants. Values of the Saint–Venant torsional constant J, the warping constant $I_{W_{SV}}$ and the two gradient constants $I_{\nabla W_{SV}}$ and $I_{\nabla W_\sigma}$ for different t/h ratios.

Table 5: Box cross section ($t_f = 2t_w = 2t$): table of torsional constants for different sections thickness ratio t/h ($h = 20\ cm$).

t/h	$J\ [cm^4]$	$I_{W_{SV}}\ [cm^6]$	$I_{\nabla W_{SV}}\ [cm^4]$	$I_{\nabla W_\sigma}\ [cm^8]$
0.10	$1.50314876{\cdot}10^4$	$2.92100250{\cdot}10^4$	$5.23517907{\cdot}10^3$	$7.42990212{\cdot}10^5$
0.05	$8.96257119{\cdot}10^3$	$2.62850975{\cdot}10^4$	$3.78409548{\cdot}10^3$	$8.81626379{\cdot}10^5$
0.01	$2.06474176{\cdot}10^3$	$8.03505311{\cdot}10^3$	$9.94116910{\cdot}10^2$	$3.12143230{\cdot}10^5$

for the section with $t_f = 2t_w = 2t$. This mimics exactly the difference between the same constant for the rectangular section in Figure 4 and for the open channel section in Figure 17, respectively. This difference arises from the presence of (sectorial) primary warping in the latter, as noted in Appendix B.2.

Similarly, the gradient constant $I_{\nabla W_\sigma}$ shows a response of order $o\left((t/h)^3\right)$ for the Neuber tube $t_f = t_w = t$, whereas it is of order $o\left((t/h)\right)$ for the section with $t_f = 2t_w = 2t$. The former differs from the $o\left((t/h)^5\right)$ of a single thin rectangle as noted in Appendix B.3. It is interesting that the other gradient constant $I_{\nabla W_{SV}}$ shows to be of order $o\left((t/h)\right)$ for both sections. As shown by the analysis in Appendix B for the thin–wall limit estimates, this is due to the coupling of the longitudinal and transversal (through–the–thickness) wall directions in the evaluation of this constant arising from the bilinear character of the Saint–Venant function $W_{SV}^{(thin)}$ in the so–called secondary warping.

Note that the Saint–Venant torsional constants J shows the same order $o\left((t/h)\right)$ as this gradient constant $I_{\nabla W_{SV}}$ for both section configurations. All these observations are perfectly captured and, hence, confirmed by the computed values of all these constants based on the exact Poisson problems for the two warping functions $W_{SV}(x, y)$ and $W_\sigma(x, y)$.

With these constants at hand, we evaluate the shaft's flexibility (194) for the three different formulations under study and different lengths of the shaft. Figure 33 depicts the normalized values $f_T/(L/\bar{G}J)$ versus the thickness ratio t/h and the shaft length L/h, each plot for different characteristic values of the other parameter. Both cases $t_f = t_w$ and $t_f = 2t_w$ are shown in this figure in separate plots. The difference in scales for each of these two cases is to be noted, showing the lesser influence of the restrained warping for the first case (the Neuber tube), as expected. Nevertheless, we can observe a considerable difference between the values obtained by the three formulations for both cases. The differences become smaller again the thinner the section and the longer he shaft, but comparing these results with the corresponding Figure 18 for the channel open thin–walled section of the last section, the differences even for thin sections are much more significant. We remark that we are considering the same range of thickness ratios t/h. Note, though, that the difference with the Saint–Venant value $L/\bar{G}J$ is smaller. In any case, the TWKV formulation shows to be much stiffer than the RBV and mixed formulations, in this order again, for the whole range of t/h and L/h ratios. This over–stiffness is more accentuated for the case $t_f = 2t_w$ when

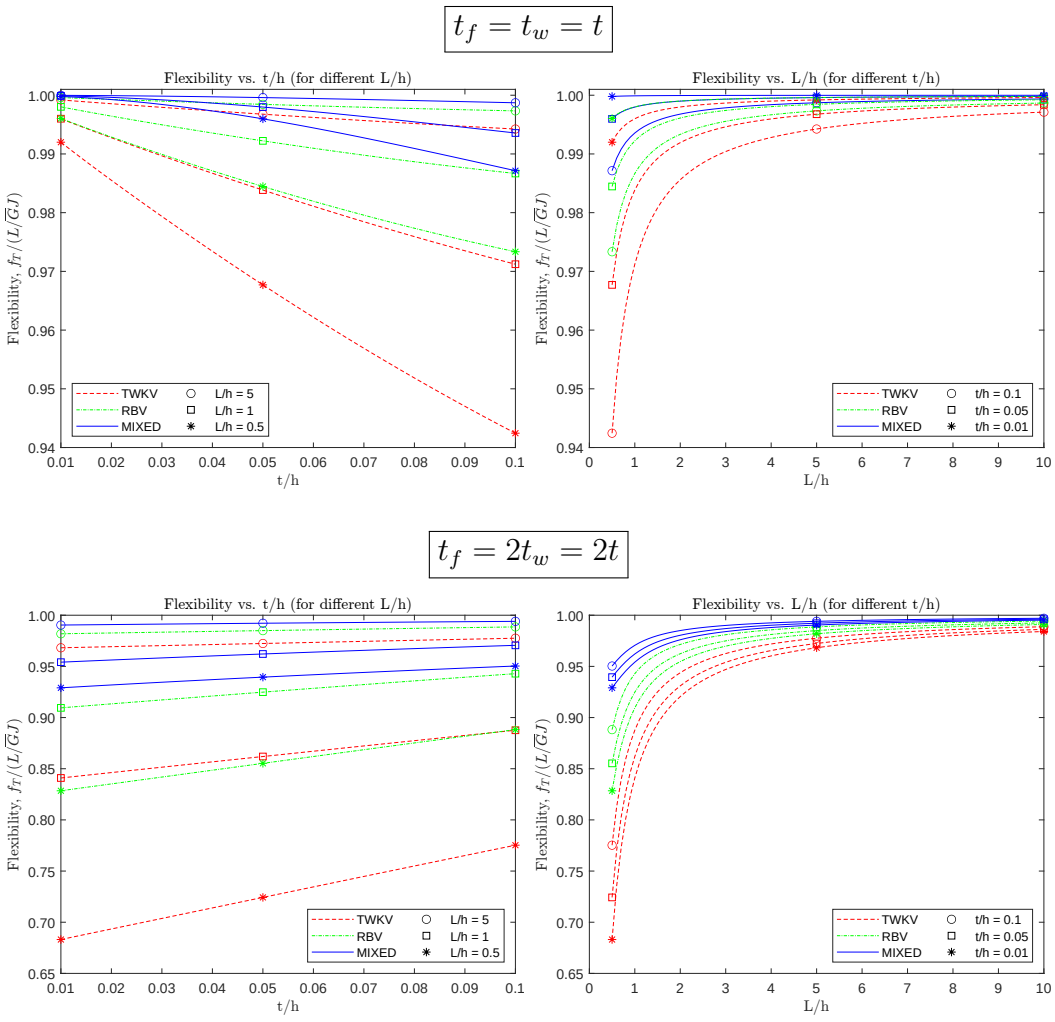

Figure 33: Box cross section: shaft flexibility. Normalized torsional flexibility $f_T/(L/\bar{G}J)$ versus t/h (left) and L/h (right), for the two considered geometries of the section $t_f = t_w$ (top) and $t_f = 2t_w$ (bottom). All formulations tend to the Saint–Venant value ($f_T^{(SV)} = L/\bar{G}J$) for long shafts (large L/h).

compared to the Neuber tube with $t_f = t_w$.

Figures 34 and 35 include the diagrams for the bishear $T_W(z)$ and bimoment $B_W(z)$ for the three representative sections $t/h = 0.10$, 0.05 and 0.01, and different shaft's lengths L/h, all for the three formulations under study and for the two cases $t_f = t_w$ and $t_f = 2t_w$, respectively. In contrast with the previous two sections, we show here these quantities normalized by the rotation ϕ_L at the tip of the shaft $z = L$ (namely, $T_W/(\phi_L \bar{G} J/L)$ and $B_W/(\phi_L \bar{G} J)$) to illustrate the relations (201) and (206), respectively. Even with this normalization, the TWKV formulation shows significant discrepancies with the other two formulations near the fixed support at the shaft's root $z = 0$. This situation is even observed for the thinnest section $t/h = 0.01$, and for all the shaft lengths. Recall that $T_W(0)/T_L = 1.0$ for this formulation due to the torque anomaly. These discrepancies extend along the length of the shaft especially for the case $t_f = 2t_w$ with a dominant primary warping, as shown in Figure 35. In all cases, the TWKV formulation overestimates both the bishear and bimoment, all along the shaft, not only near that fixed support. The full three–dimensional simulations presented below will prove this result, and specifically the big overshoot at the root, to be unrealistic, particularly when compared with the RBV formulation and, especially, with the mixed formulation.

The shear stresses on the cross section at the fixed support $z = 0$ are shown in Figures 36 and 37 for the sections with $t/h = 0.10$ and 0.05, respectively, both for the Neuber tube $t_f = t_w$ with $L/h = 1.0$. As in previous sections, we include the Saint–Venant shear stress component $\boldsymbol{\tau}_{SV}$, the warping shear stress $\boldsymbol{\tau}_W$ and the total shear stress $\boldsymbol{\tau}$, both as stress vectors at the plane section quadrature points and as contour plots of their magnitude.

Analyzing the results shown in these figures, we can observe that both the TWKV and mixed formulations capture the characteristic constant distribution through the wall thickness as the thickness t/h reduces, up to stress concentrations at the walls corners. We do not include the plots for the thinner sections with $t/h = 0.01$ because they are difficult to view at that thickness, but they confirm this well–known result for closed (hollow) thin–walled sections in torsion. We find remarkable that the original TWKV formulation accomplishes this result with a vanishing Saint–Venant component $\boldsymbol{\tau}_{SV}$ due to the torque anomaly, just with the contribution of the warping component $\boldsymbol{\tau}_W$ (and hence the associated bishear $T_W(0)/T_L = 1$ for this formulation). In contrast, the RBV formulation misses completely this characteristic shear stress distribution, leading instead to the previously noted "rotational" pat-

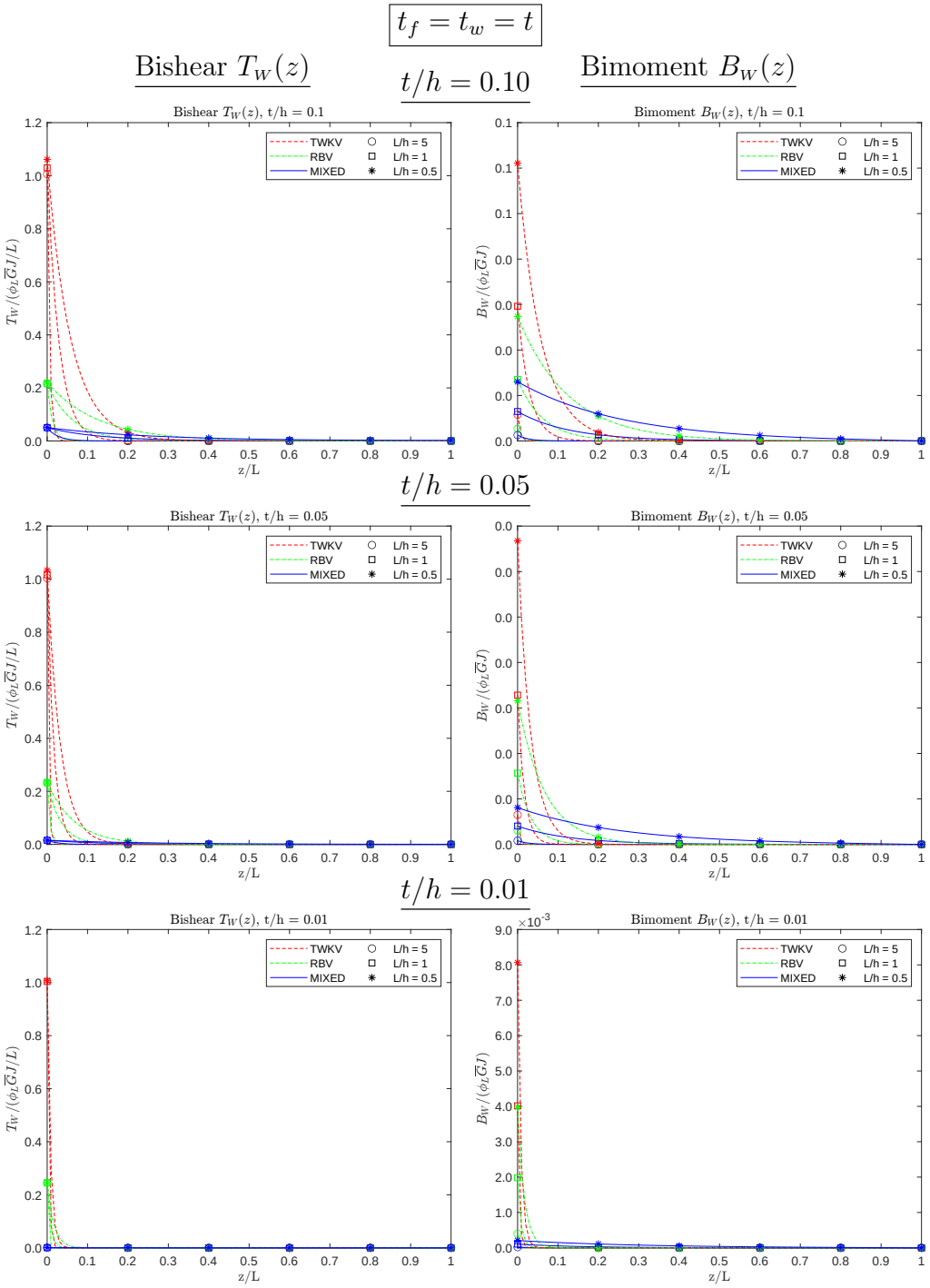

Figure 34: Box cross section ($t_f = t_w = t$, Neuber tube): moment diagrams normalized by the tip rotation ϕ_L.

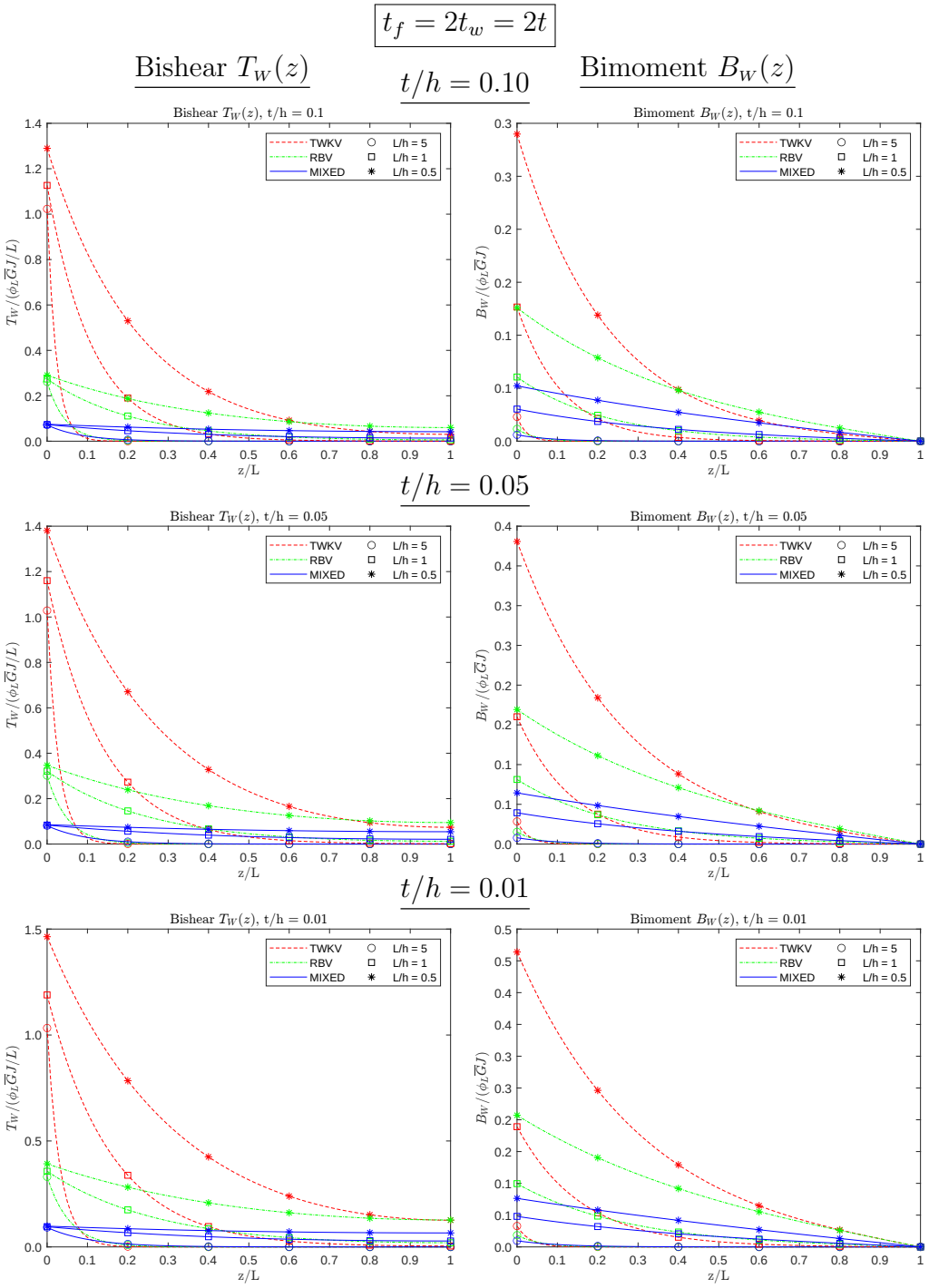

Figure 35: Box cross section ($t_f = 2t_w = 2t$): moment diagrams normalized by the tip rotation ϕ_L.

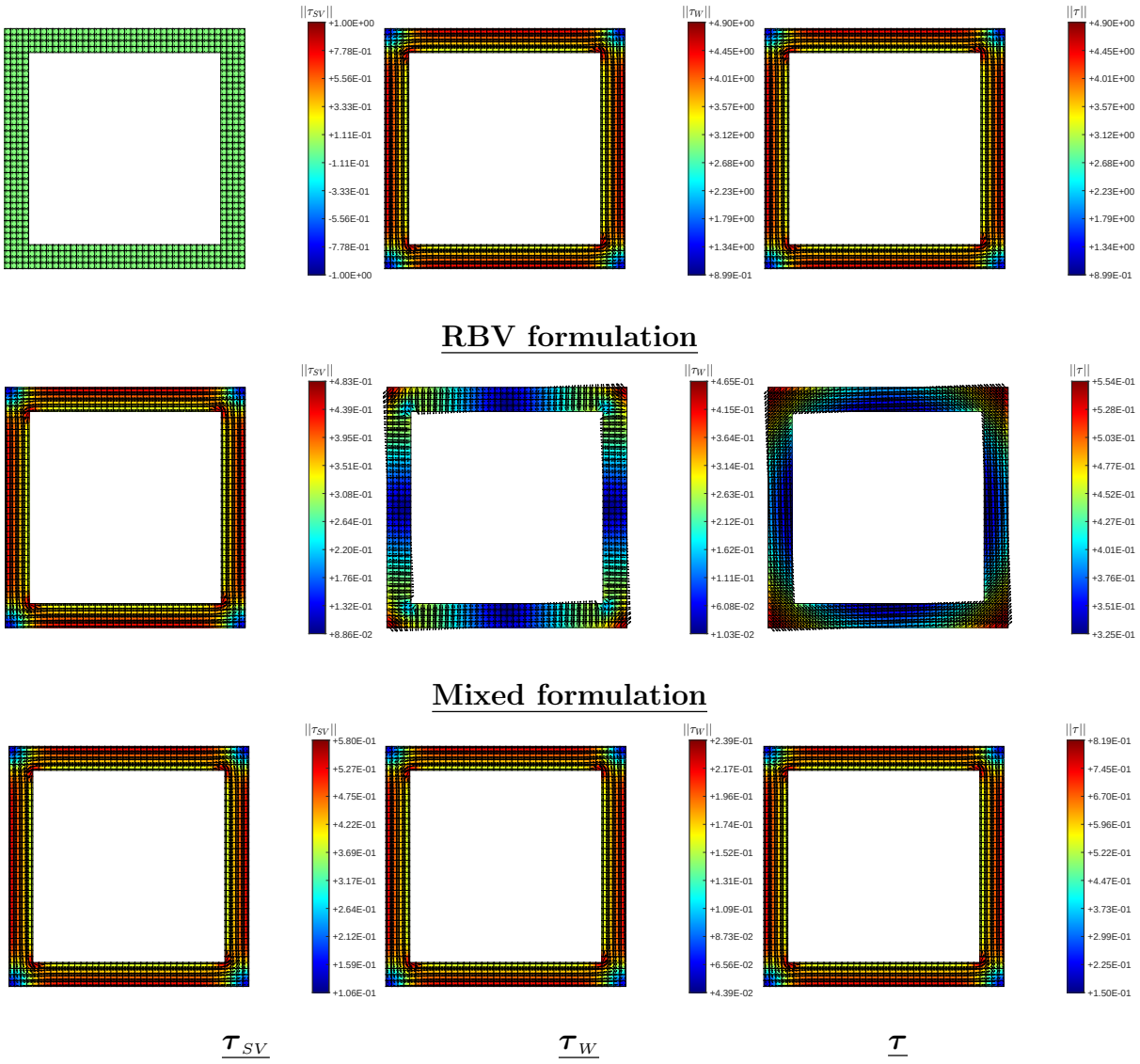

Figure 36: Box cross section ($t_f = t_w = t$, Neuber tube): shear stresses. Distributions of the Saint–Venant shear stress $\boldsymbol{\tau}_{SV}$, the warping shear stress $\boldsymbol{\tau}_W$ and the total shear stress $\boldsymbol{\tau}$ for the channel cross section $t/h = 0.10$ and $L/h = 1.0$ at the shaft root $z = 0$. All values are normalized as $\boldsymbol{\tau}/\bar{G}$ and correspond to the case with a unit rotation $\phi_L = 1.0$ at the opposite tip of the shaft.

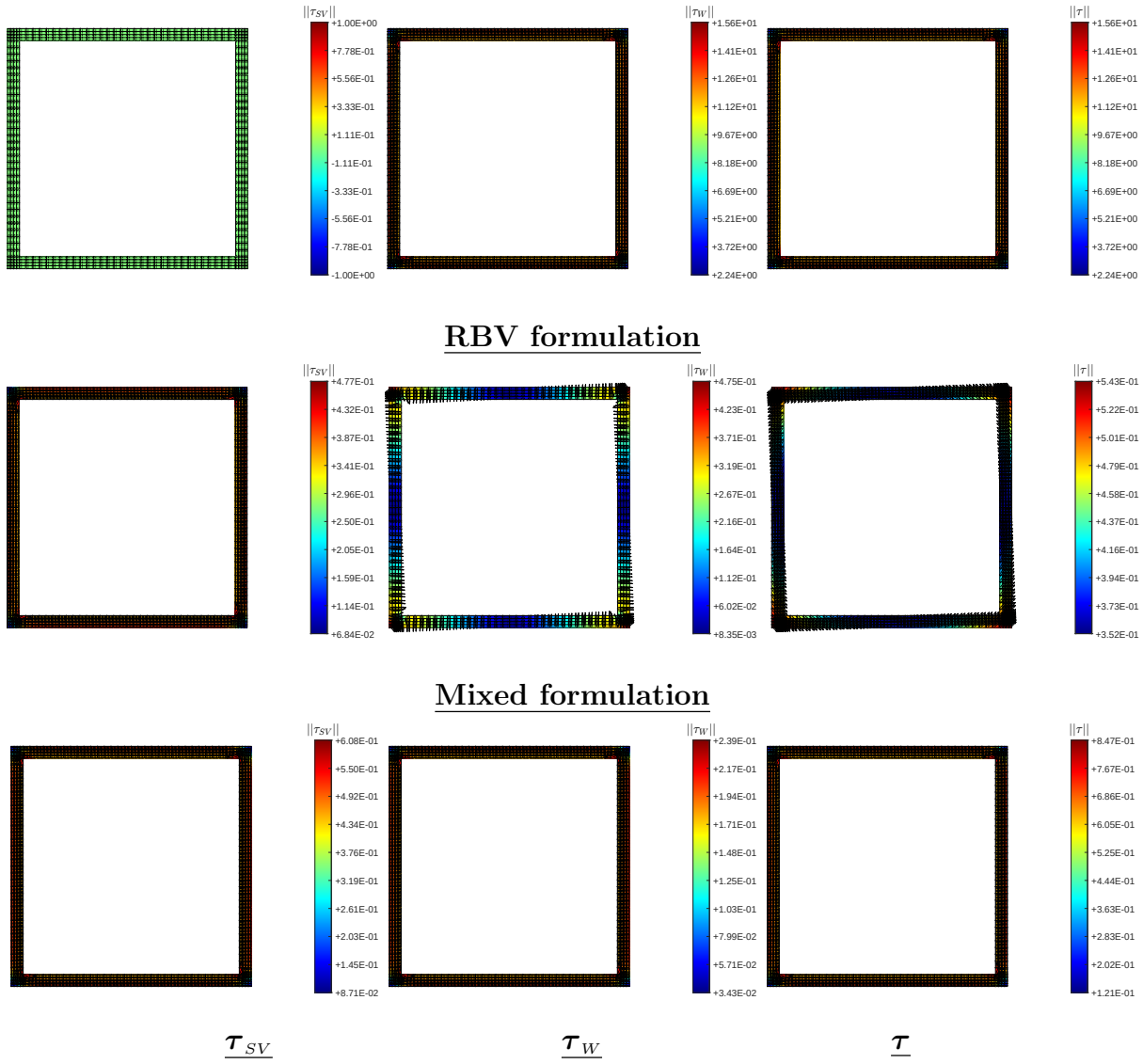

Figure 37: Box cross section ($t_f = t_w = t$, Neuber tube): shear stresses. Distributions of the Saint–Venant shear stress $\boldsymbol{\tau}_{SV}$, the warping shear stress $\boldsymbol{\tau}_W$ and the total shear stress $\boldsymbol{\tau}$ for the channel cross section $t/h = 0.05$ and $L/h = 1.0$ at the shaft root $z = 0$. All values are normalized as $\boldsymbol{\tau}/\bar{G}$ and correspond to the case with a unit rotation $\phi_L = 1.0$ at the opposite tip of the shaft.

tern (213) of the stress vectors $\boldsymbol{\tau}$ around the center of twist. We note that this distribution is incorrect in nature (in the sense that it does not satisfy the correct boundary conditions along the wall edges), even though it may capture the overall structural response of the shaft in terms of the associated bishear $T_W(0)$. The mixed formulation shows the correct stress distribution and does capture that structural response too, actually better for this type of sections as well.

The shear stresses for the section configuration with $t_f = 2t_w = 2t$ are shown in Figures 38 and 39 for the sections with $t/h = 0.10$ and 0.05, respectively. The shaft length of $L/h = 1.0$ is considered again. For the TWKV and mixed formulations, we observe the same trend to a constant stress distribution through the thickness for the thinner section, with the expected concentration along the thinner web as expected. The same deficiencies of the stress distribution predicted by the RBV can be observed in this case. It misses completely that dominance of the component tangential to the middle lines of the walls, constant through the thickness. The concentration along the webs is lost, with the main contribution to the torque taken by the section concentrated at the section's corners.

Figures 40 and 41 show the distribution of the axial stress σ_z at the fixed support of the shaft for, again, the two sections $t/h = 0.10$ and 0.05, both for the shaft $L/h = 1.0$, and for the Number tube $t_f = t_w$ and the case $t_f = 2t_w$, respectively. The distribution of this stress is proportional to the Saint–Venant warping function $W_{SV}(x, y)$ for all the three formulations considered here, and hence those two section configurations show completely different distributions, with the absence of the primary warping for the Neuber tube, at least for the thinner section. Still, we can observe again the much higher level of stress obtained with the TWKV formulation followed in order by the RBV and mixed formulations, for both cases $t_f = t_w$ and $t_f = 2t_w$. This situation agrees with the distributions observed for the solid and open thin–walled sections in the previous section. It also confirms the stiffer character of the TWKV and RBV formulations in comparison with the mixed formulation, even for entirely different warping distributions. To finally decide on the adequacy of these formulations for this type of sections, we consider full three–dimensional finite element analyses as presented next.

7.3.1. Three–dimensional analysis

We continue with the full three–dimensional of the shafts at hand, considering a graded distribution of 8−node enhanced QM1/E12 brick elements

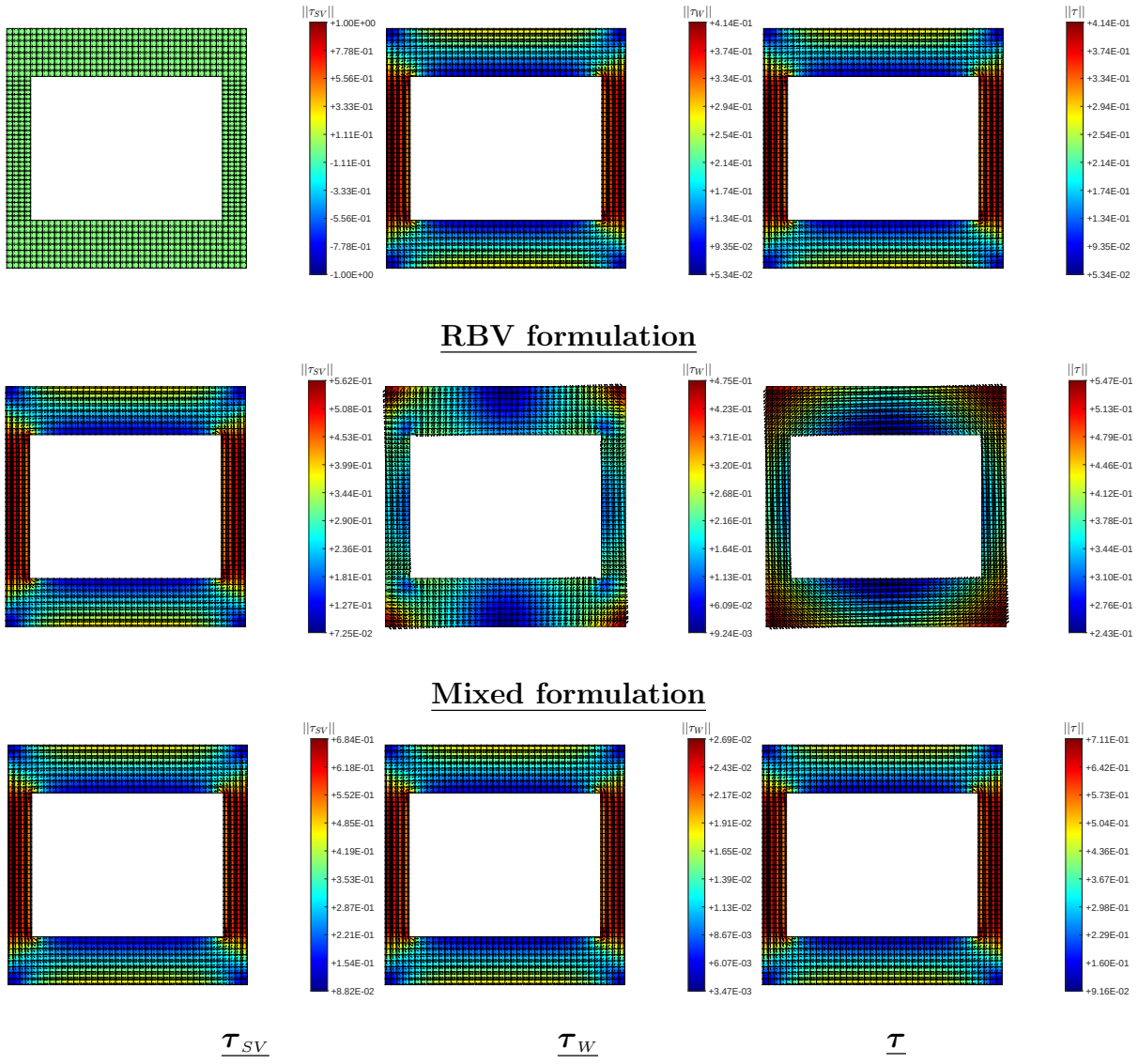

Figure 38: Box cross section ($t_f = 2t_w = 2t$): shear stress. Distributions of the Saint–Venant shear stresses $\boldsymbol{\tau}_{SV}$, warping stresses $\boldsymbol{\tau}_{W}$ and total stresses $\boldsymbol{\tau}$ for the channel cross section $t/h = 0.10$ and $L/h = 1.0$ at the shaft root $z = 0$. All values are normalized as $\boldsymbol{\tau}/\bar{G}$ and correspond to the case with a unit rotation $\phi_L = 1.0$ at the opposite tip of the shaft.

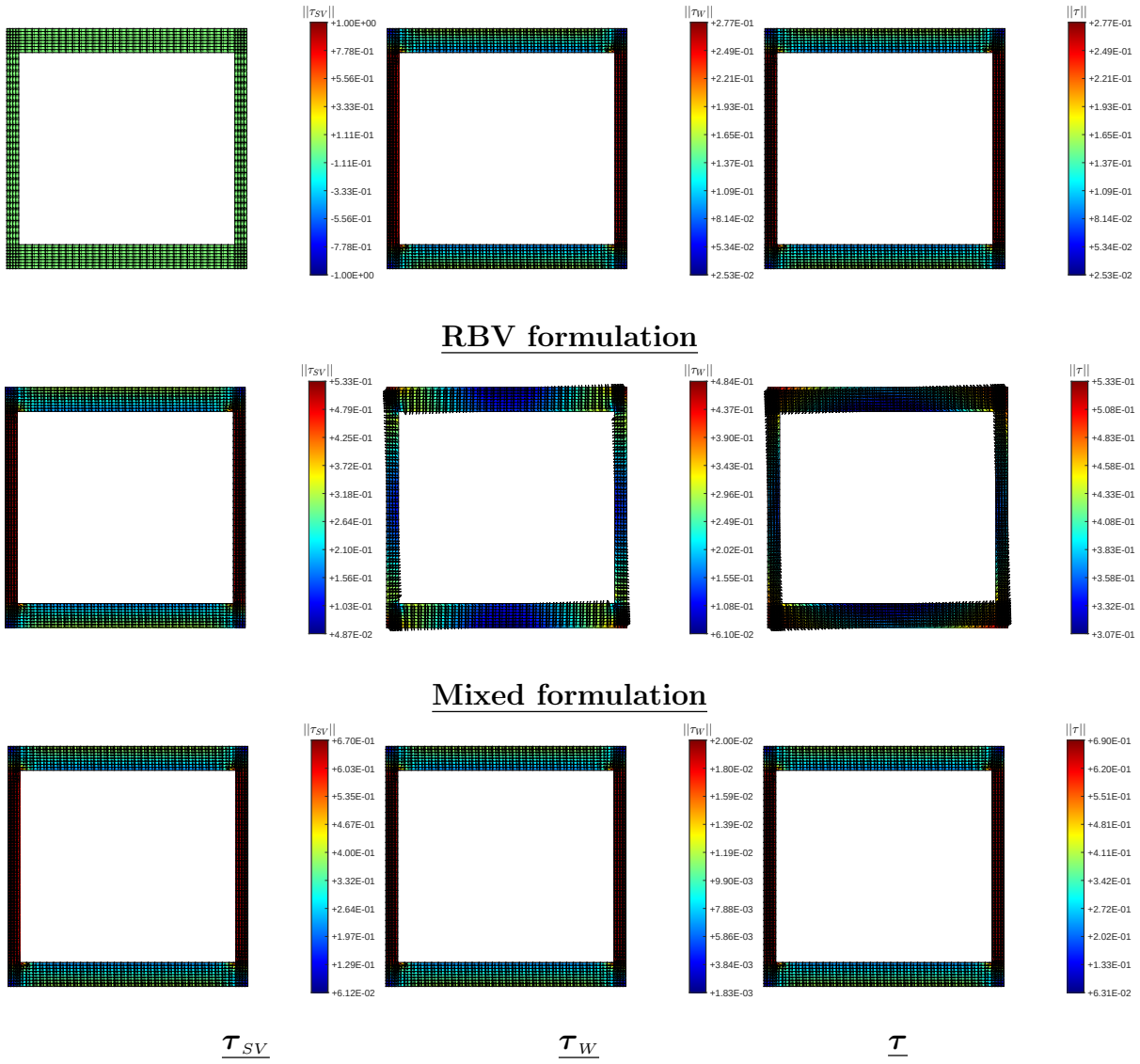

Figure 39: Box cross section ($t_f = 2t_w = 2t$): shear stress. Distributions of the Saint–Venant shear stresses $\boldsymbol{\tau}_{SV}$, warping stresses $\boldsymbol{\tau}_W$ and total stresses $\boldsymbol{\tau}$ for the channel cross section $t/h = 0.05$ and $L/h = 1.0$ at the shaft root $z = 0$. All values are normalized as $\boldsymbol{\tau}/\bar{G}$ and correspond to the case with a unit rotation $\phi_L = 1.0$ at the opposite tip of the shaft.

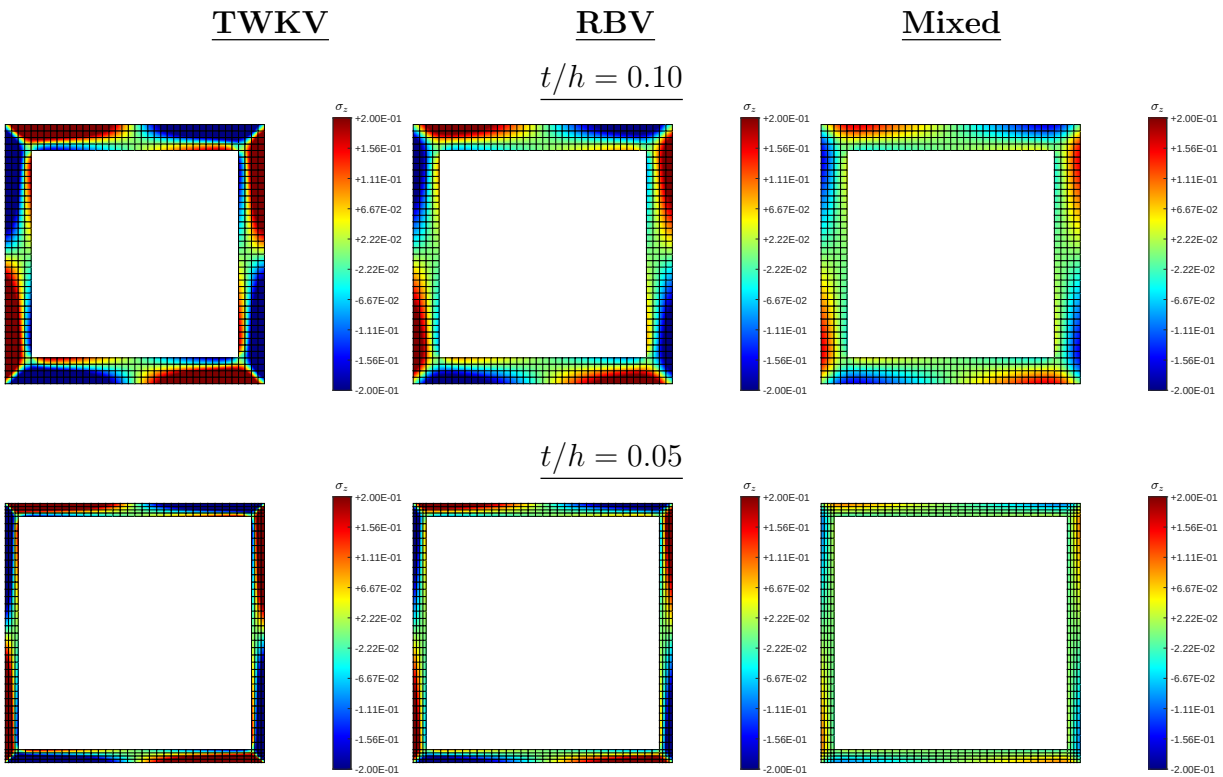

Figure 40: Box cross section ($t_f = t_w = t$, Neuber tube): axial stress. Distribution obtained by the different formulations of the end axial stress σ_z at the shaft root $z = 0$ for the cross section with $t/h = 0.10$, 0.05 and shaft's length $L/h = 1.0$. All values are normalized by the material's Young modulus as $\sigma_z/\bar{E}$ and correspond to the case with a unit rotation $\phi_L = 1.0$ at the opposite tip of the shaft.

along the shaft length. We consider again 20 layers of such elements. We impose the plane (u_x, u_y) displacements $(12)_{1,2}$ with a unit rotation $\phi_L = 1$, leaving the axial displacement u_z free at the shaft's tip $z = L$. We fix all these 3D displacement components at the opposite end $z = 0$.

The plots in Figure 42 illustrate the assumed 3D finite element discretization. It includes the deformed configurations for the section with $t/h = 0.10$ and shaft length $L/h = 1.0$ for the two cases considered here, the Neuber tube $t_f = t_w = t$ and the section with varying thickness $t_f = 2t_w = 2t$. Superposed to these deformations we show contour plots of the axial (warping) displacement u_z, including separate elevation plots of this displacement on the section at the shaft tip. This distribution must be compared with the the-

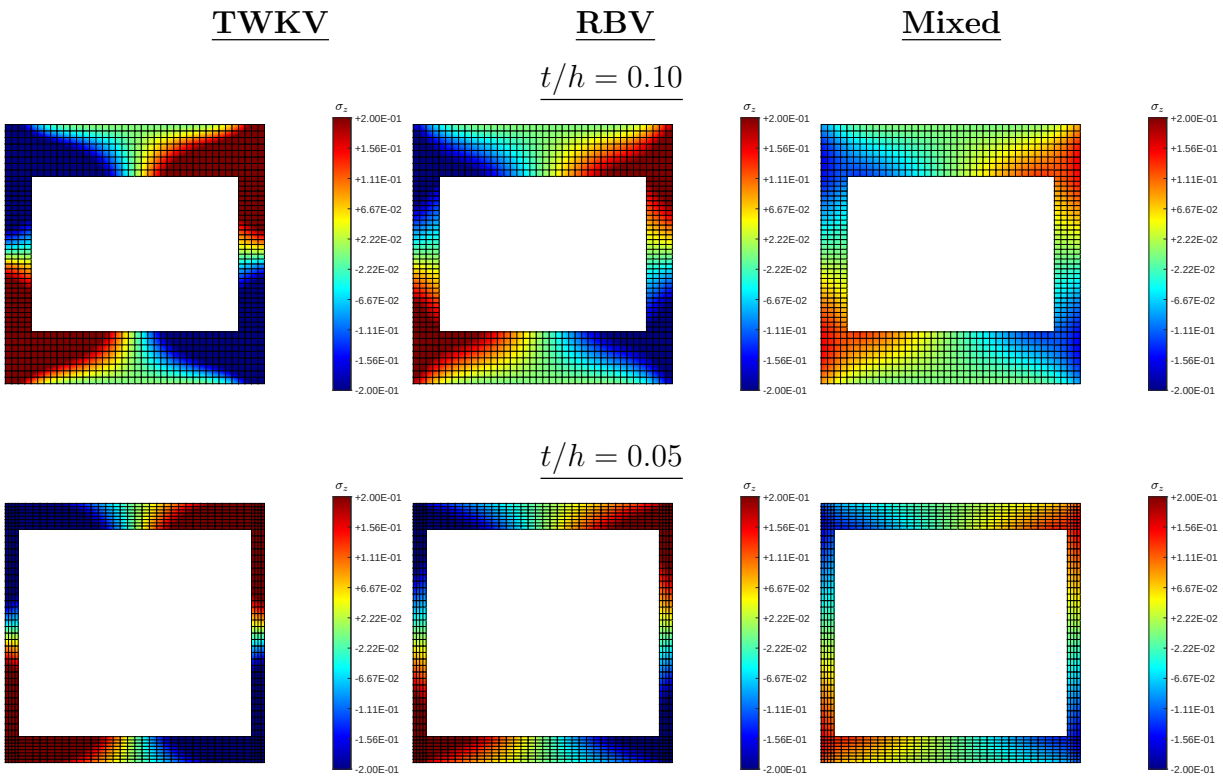

Figure 41: Box cross section ($t_f = 2t_w = 2t$): axial stress. Distribution obtained by the different formulations of the end axial stress σ_z at the shaft root $z = 0$ for the cross section with $t/h = 0.10$, 0.05 and shaft's length $L/h = 1.0$. All values are normalized by the material's Young modulus as $\sigma_z/\bar{E}$ and correspond to the case with a unit rotation $\phi_L = 1.0$ at the opposite tip of the shaft.

oretical distribution given by the Saint–Venant warping function $W_{SV}(x, y)$ shown in Figures 29 and 30 for that particular section in those two respective cases. The same scaling is used for the two cases, allowing a direct comparison of the warping between the two. In this way, the three–dimensional simulations confirm the higher amount of warping for the case $t_f = 2t_w$ over the Neuber tube $t_f = t_w$.

The three–dimensional shear and normal stress at the root of the shaft are included in Figures 43 and 44 for sections $t/h = 0.10$ and 0.05, both for $L/h = 1.0$, so they can be compared with the same stresses obtained by the different structural formulations presented in Figures 36 to 40, and Figures 38 to 41 for each case. The stresses shown are the nodally projected values

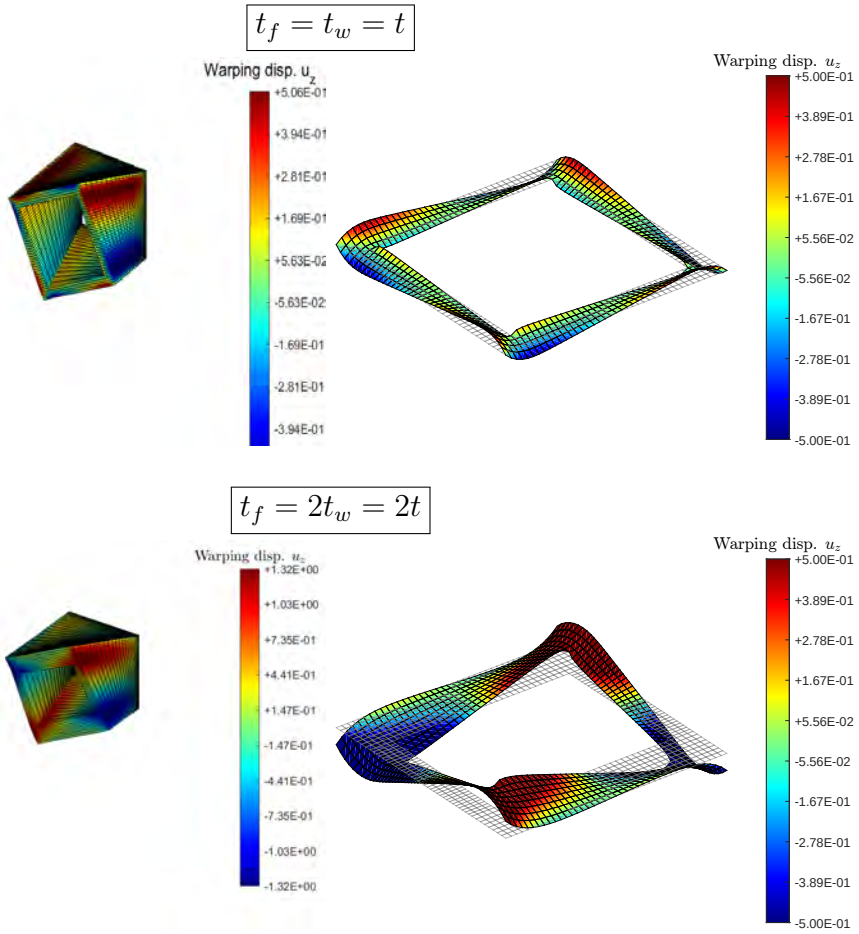

Figure 42: Box cross section: 3D shaft. Three–dimensional finite element solution for shafts with $L/h = 1.0$, 5.0 and $t/h = 0.10$, showing the contours of the axial displacement u_z on top of the 3D deformed configuration of the shaft (left), and the elevation plot of the resulting warping at the shaft's tip $z = L$ (right).

given by equation (229). The characteristic constant distribution through the thickness, tangential to the wall middle line, of the shear stress $\boldsymbol{\tau}$ noted above as the thickness t/h decreases is clearly recovered in the simulations as a full 3D elastic solid. The stress distribution obtained by the RBV formulation of Figures 36-37 and 38-39 are confirmed to be completely unrealistic.

To evaluate better the level of the normal stresses σ_z we have included in Figures 45 and 46 the difference of this stress in the 3D simulations with the one predicted by the different structural theories given by equation (221),

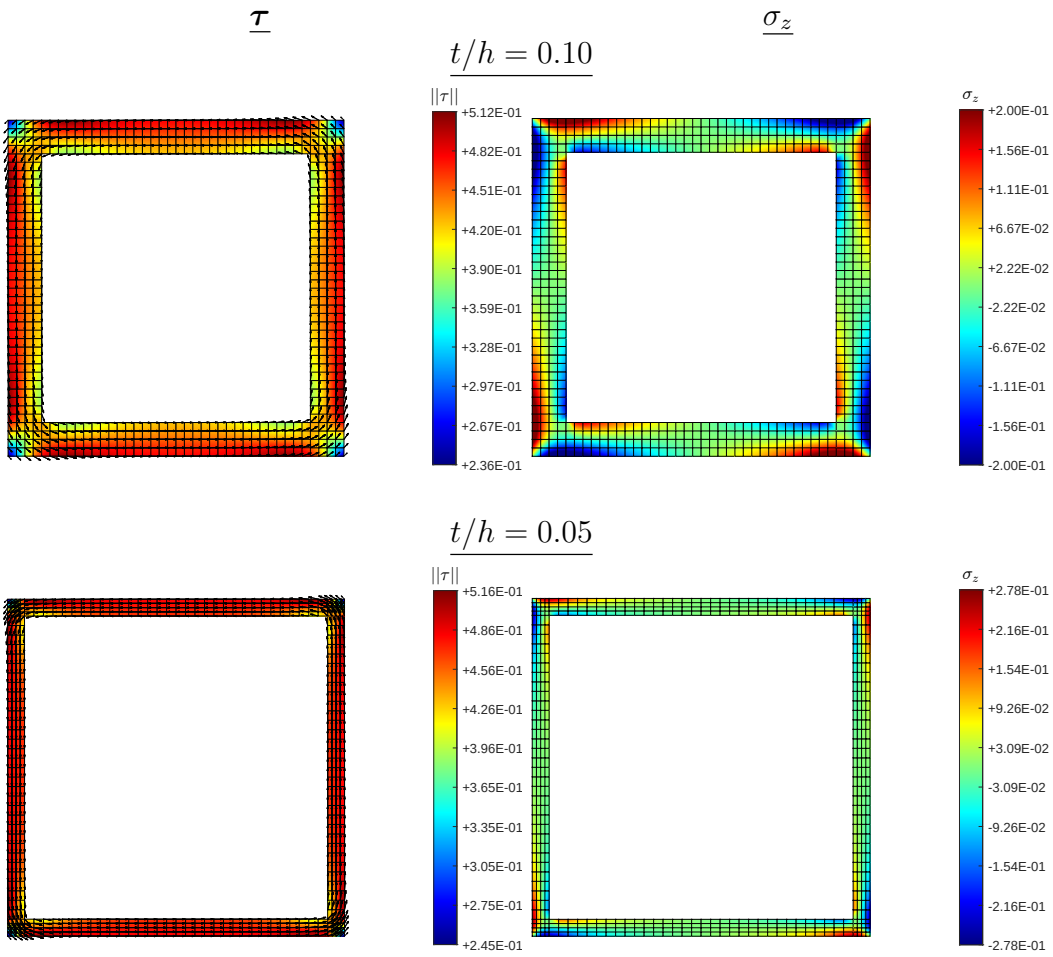

Figure 43: Box cross section ($t_f = t_w = t$, Neuber tube): stresses. Shear and normal stresses in the three–dimensional finite element solution at the shaft root $z = 0$ for $t/h = 0.10$, 0.05 and $L/h = 1.0$. Values are normalized as $\boldsymbol{\tau}/\bar{G}$ and $\sigma_z/\bar{E}$, and they correspond to the case with a unit rotation $\phi_L = 1.0$ at the opposite tip of the shaft.

all projected to the nodes. As occurred for the solid and open thin–walled sections, we can observe a higher level of error for the TWKV formulation, followed in order by the RBV and mixed formulation. This error is much bigger for the case $t_f = 2t_w$ in Figure 46 where the primary warping dominates. We have kept constant the color scale of the contour plots in these figures among the three formulations to observe these differences, a significant difference for the original TWKV constrained formulation. Remember

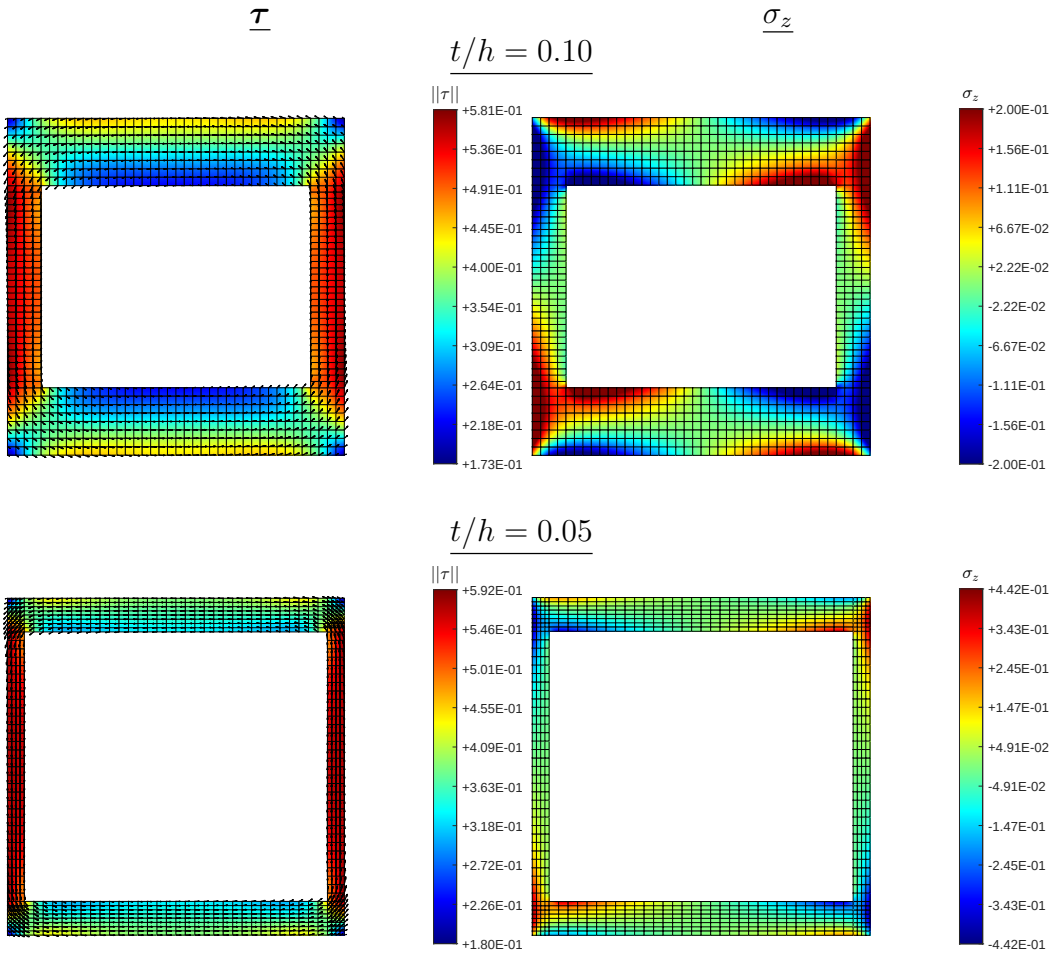

Figure 44: Box cross section ($t_f = 2t_w = 2t$): stresses. Shear and normal stresses in the three–dimensional finite element solution at the shaft root $z = 0$ for $t/h = 0.10$, 0.05 and $L/h = 1.0$. Values are normalized as $\boldsymbol{\tau}/\bar{G}$ and $\sigma_z/\bar{E}$, and they correspond to the case with a unit rotation $\phi_L = 1.0$ at the opposite tip of the shaft.

that this axial normal stress shows a spatial distribution on the cross section given by the Saint–Venant warping function for all structural formulations.

The structural stress resultant driving this normal stress is the bimoment $B_W(0)$ at the fixed support $z = 0$. Figures 47 and 48 include this quantity as well as the bishear $T_W(0)$ for the sections with $t_f = t_w$ and $t_f = 2t_w$, respectively. They show the dependence of these stress resultants on the section aspect ratio t/h and the shaft length L/h for the three structural

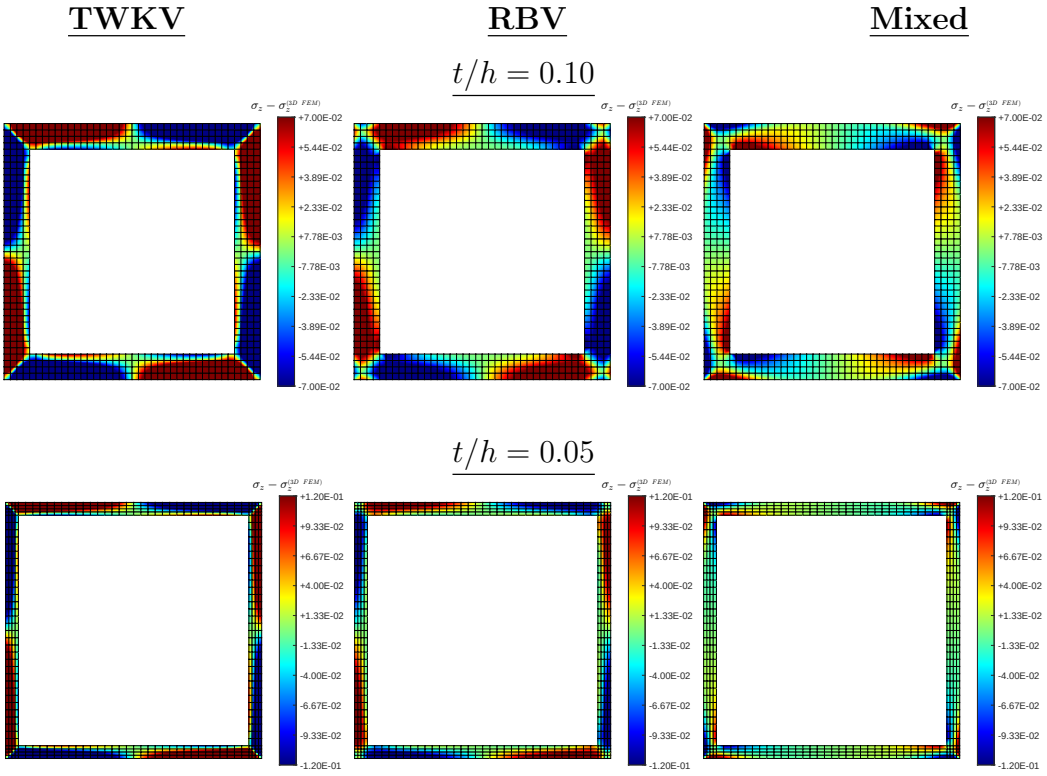

Figure 45: Box cross section ($t_f = t_w = t$, Neuber tube): axial stress difference. Comparison of the axial stress at the shaft's root $z = 0$ between the different considered formulations with the three–dimensional finite element solution $\sigma_z - \sigma_{z(3D)}$, for the different cross section $t/h = 0.10$, 0.05 and $L/h = 1.0$. All values normalized by the material's Young modulus as $\sigma_z/\bar{E}$ and correspond to the case with a unit rotation $\phi_L = 1.0$ at the opposite tip of the shaft.

theories under study as well as the three–dimensional finite element solutions. The values for the 3D solutions are obtained using the postprocessing given by relations (230) and (231) for the bimoment and bishear, respectively, in terms of the nodally projected 3D stresses in (229). In contrast to the similar results in previous sections, and to illustrate the results (201) and (206) evaluated at $z = 0$ in terms of the tip rotation ϕ_L, we have used the normalization $B_W(0)/(\phi_L \bar{G} \tilde{J}_{ref})$ and $T_W(0)/(\phi_L \bar{G} \tilde{J}_{ref}/L)$ in terms of the dimensional factor $\tilde{J}_{ref} = J^{(thin)}$ in equation (B.24).

The plots in these figures show a very good agreement for the values of both the root bimoment $B_W(0)$ and bishear $T_W(0)$ with the 3D results for the newly proposed mixed formulation when compared to the other two

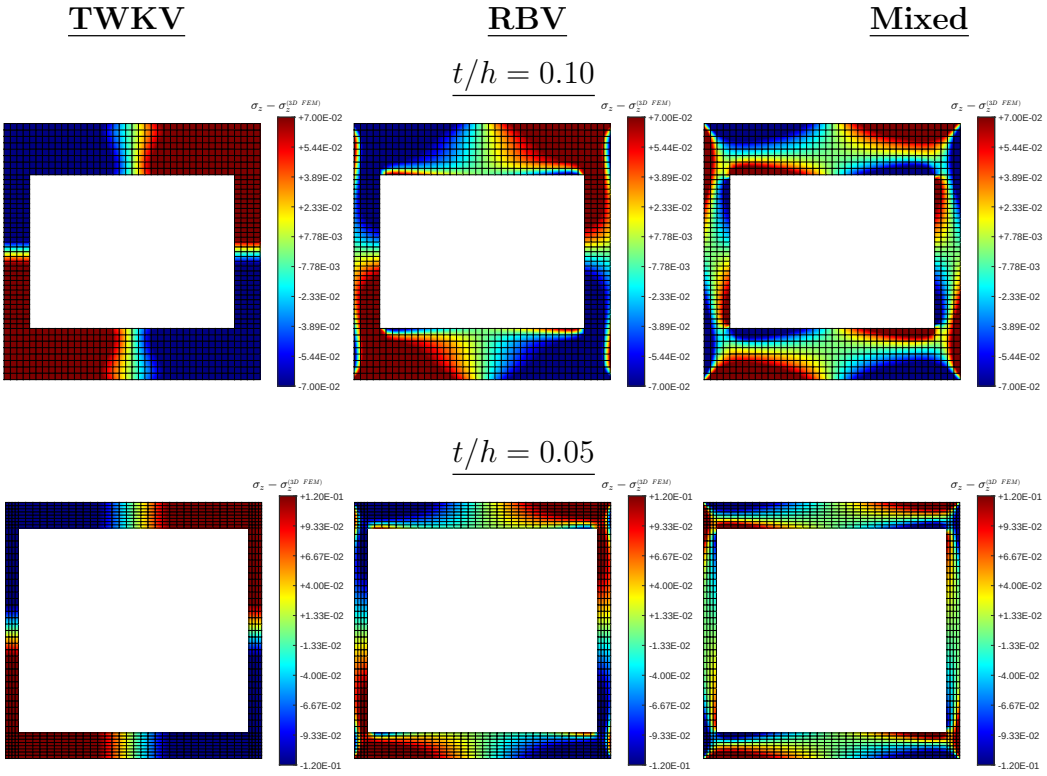

Figure 46: Box cross section ($t_f = 2t_w = 2t$): axial stress difference. Comparison of the axial stress at the shaft's root $z = 0$ between the different considered formulations with the three–dimensional finite element solution $\sigma_z - \sigma_{z(3D)}$, for the different cross section $t/h = 0.10$, 0.05 and $L/h = 1.0$. All values normalized by the material's Young modulus as $\sigma_z/\bar{E}$ and correspond to the case with a unit rotation $\phi_L = 1.0$ at the opposite tip of the shaft.

structural formulations, especially the TWKV formulation that clearly overestimates these stress resultants. This agreement is good in the whole range of section thickness t/h and shaft lengths L/h, and better for the Neuber tube $t_f = t_w$ in Figure 47. We can also observe the completely different response of the closed (hollow) thin–walled sections considered in the current section with that of the open thin–walled sections studied in the previous section. In particular, comparing the results in this figure with the similar plots in Figure 27 for the (open) channel section, showing a much closer agreement among the three structural theories, confirm that the basic warping–twist constraint underlying the original TWKV formulation (that is, warping magnitude given by the rate of twist $\phi'(z)$) only dominates the thin–walled

$$\boxed{t_f = t_w = t}$$

Bimoment $B_W(0)$ vs t/h and L/h

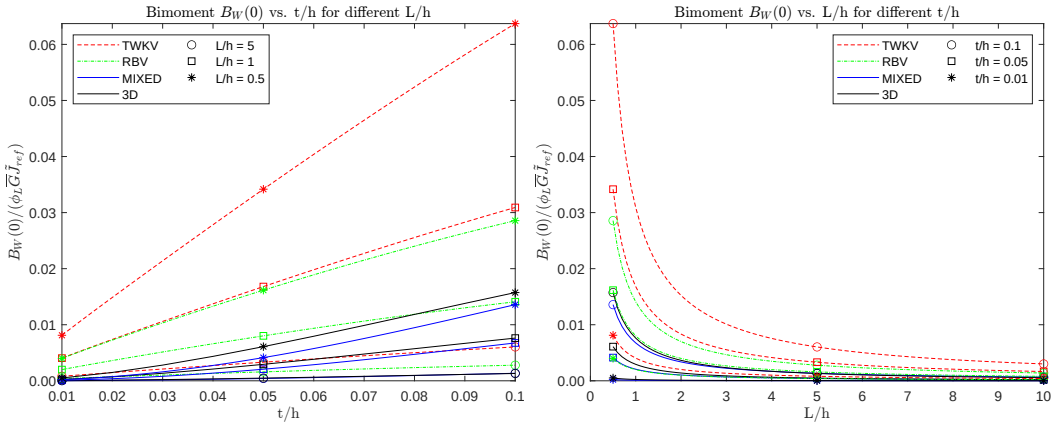

Bishear $T_W(0)$ vs t/h and L/h

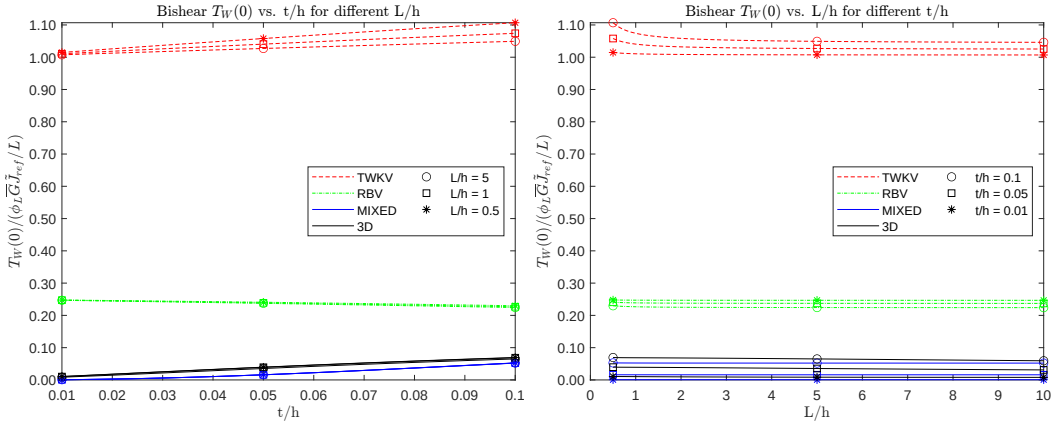

Figure 47: Box cross section ($t_f = t_w = t$, Neuber tube): bimoment and bishear at the shaft's root. Values of the bimoment $B_W(0)$ (top) and the bishear $T_W(0)$ (bottom) at $z = 0$ versus the section aspect ratio t/h (left) and shaft's length ration L/h (right) obtained by the different formulations and the 3D finite element solution.

sections when they have a simply connected topology. This conclusion applies to both the cases of thickness distributions, that is, when the primary warping dominates or not in the thin–wall limit.

$$\boxed{t_f = 2t_w = 2t}$$

Bimoment $B_W(0)$ vs t/h and L/h

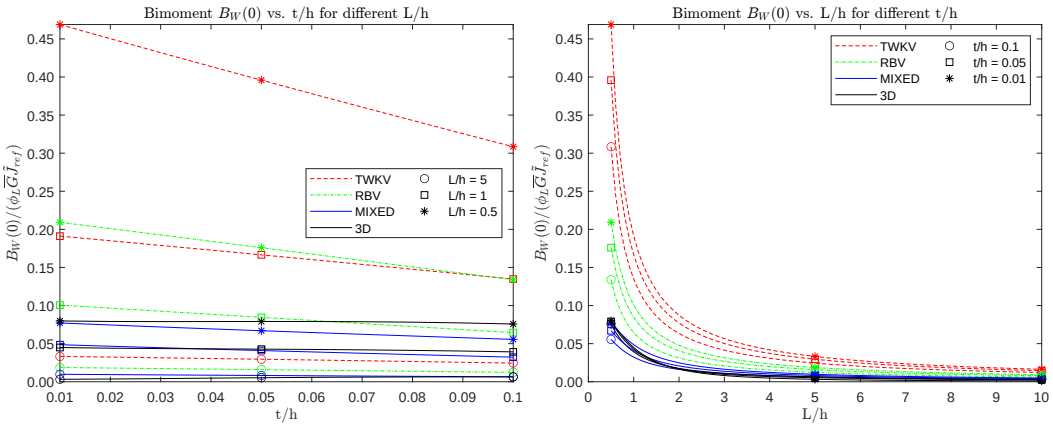

Bishear $T_W(0)$ vs t/h and L/h

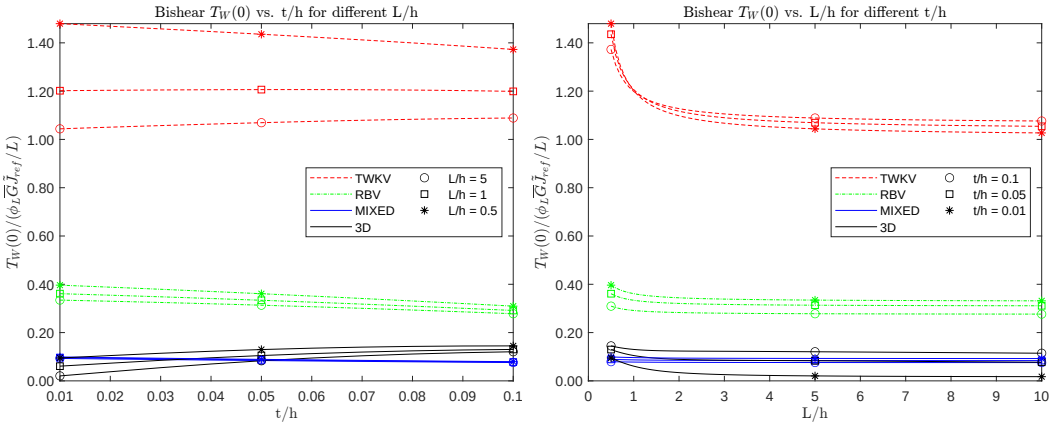

Figure 48: Box cross section ($t_f = 2t_w = 2t$): bimoment and bishear at the shaft's root. Values of the bimoment $B_W(0)$ (top) and the bishear $T_W(0)$ (bottom) at $z = 0$ versus the section aspect ratio t/h (left) and shaft's length ration L/h (right) obtained by the different formulations and the 3D finite element solution.

This situation is confirmed by evaluating the parameter κ_t identified in this work for both the RBV and mixed formulations as controlling the limit process to the constrained limit given by the TWKV formulation. Figure 49 shows this parameter versus the thickness ratio t/h for those two formula-

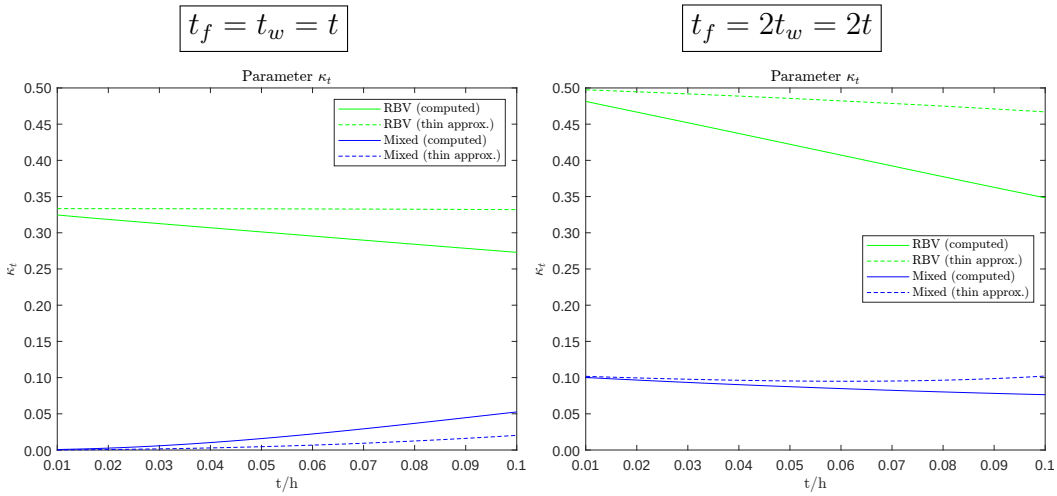

Figure 49: Box cross section: parameter κ_t versus t/h. Geometric factor identified to drive the limit process to the constrained TWKV formulation for the RBV and mixed formulations if $\kappa_t \to \infty$. No such trend is observed for the current box section in either configuration: $t_f = t_w$, Neuber tube (left), or $t_f = 2t_w$ (right).

tions, and for each of the considered cases $t_f = t_w$ and $t_f = 2t_w$. The plots in this figure are to be compared with Figure 19 for open thin–walled sections. Not only the actual values of this parameter are much smaller for both closed thin–walled sections than for that case, but the monotonic increasing character of κ_t as the thickness decreases observed for open thin–walled sections is lost. This result is a clear proof that reducing the thickness ratio t/h does not define a penalty process approaching the constrained TWKV formulations for closed (hollow) thin–walled sections. This observation also explains the differences observed above in all the aspects of the solutions obtained by the different structural formulations for this section topology. This conclusion applies to both examined configurations of the cross section, with and without primary warping in the thin–wall limit.

These conclusions are also confirmed when the parameter κ_t is calculated with the thin–wall estimates of the different torsional constants, as presented in Appendix B.3. The plots in Figure 49 also include the distributions $\kappa_t(t/h)$ using those estimated constants for the different formulations. They show a good agreement, especially in the thin–wall limit, as expected; see Remark B.4, in particular, where we have included detailed numerical comparisons. Notably that agreement is not as good as for the open channel cross section

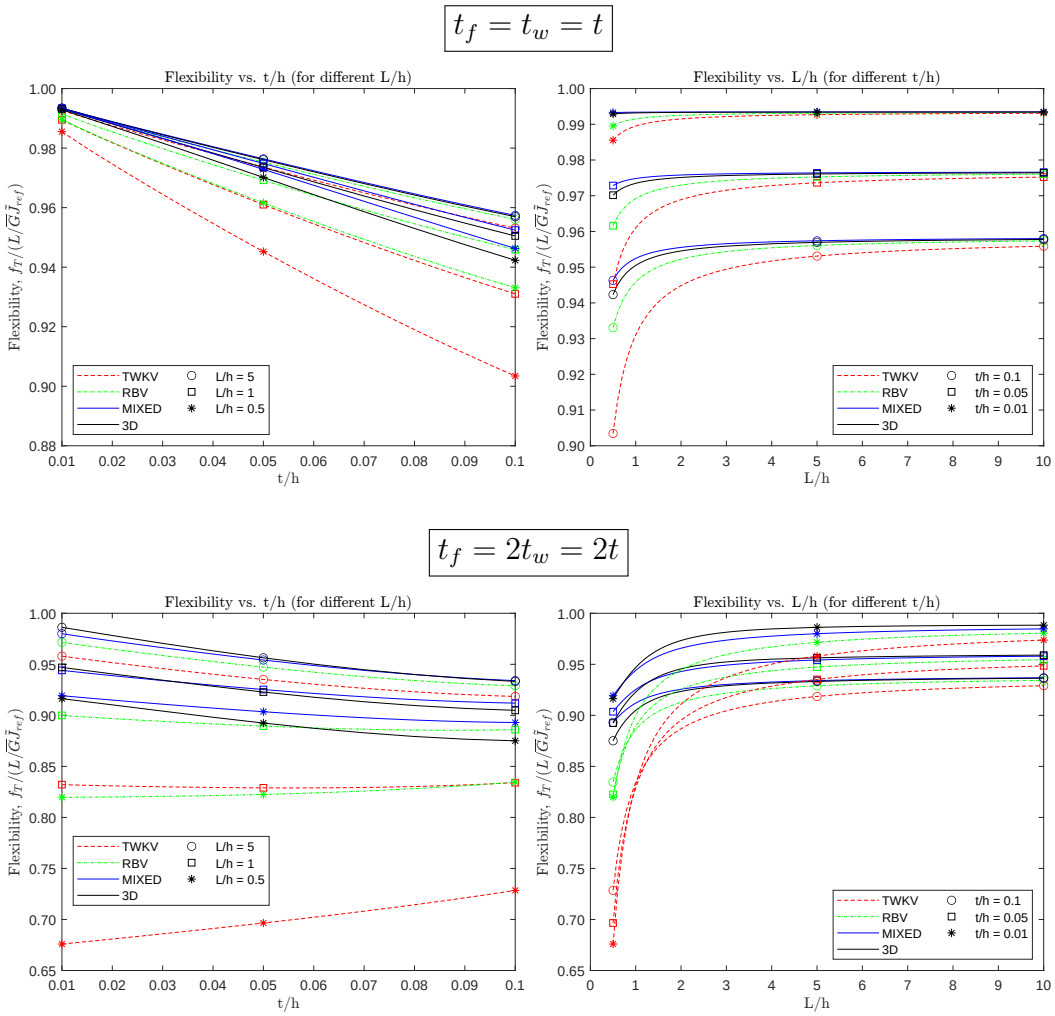

Figure 50: Box cross section: shaft flexibility. Normalized torsional flexibility $f_T/(L/\bar{G}\tilde{J}_{ref})$ with a dimensional reference value ($\tilde{J}_{ref} = J^{(thin)}$), allowing the incorporation of the 3D FEM solutions. Values versus thickness ratio t/h (left) and shaft's length L/h (right), for the section configuration $t_f = t_w$, Neuber tube (top) and $t_f = 2t_w$ (bottom).

of Section 7.2, another clear indication of the completely different nature of the warping in these two type of thin–walled sections.

To finish this section, we emphasize the over–stiff response of the whole shaft with the TWKV formulation, when compared not only to the RBV and mixed formulations, but also to the full three–dimensional elastic solutions; in fact, with a much marked difference. Figure 50 allows this comparison by considering the normalized shaft flexibility $f_T/(L/\bar{G}\tilde{J}_{ref})$ for the common dimensionally normalizing factor $\tilde{J}_{ref} = J^{(thin)}$, showing the results both versus the section thickness ratio t/h and shaft lengths L/h. We have included separate plots for the two different thickness distributions. In all cases, and along the whole range of the defining ratios t/h and L/h, the observed over–stiff response of the TWKV and, to a lesser degree, the RBV is to be noted. The scale in the plots in this figure indicate also that this less accurate response of these formulations is especially significant when the (primary) warping dominates like in the section configuration with $t_f = 2t_w$ when compared to the Neuber tube $t_f = t_w$. These plots are to be compared to Figure 28 for the channel open thin–walled sections with its much closer agreement among the different solutions in that case. The appropriateness of the proposed mixed formulation of restrained warping, especially for these closed thin–walled sections, is concluded.

7.4. Evaluation for multi–cell thin–walled cross sections

Next we consider the evaluation of the different formulations for multi–cell closed sections, exploring also the thin–wall limit. In particular, we study the two–cell section shown in Figure 2 on page 84. The double symmetry of the section makes the middle web to exhibit only secondary warping in the thin–wall limit, that is, its primary (sectorial) warping vanishes, making it efficiently equivalent a single cell only in that very limit. It is of interest though to view its effects for finite thicknesses, as consider here. The semicircular wings makes also the section of interest in the evaluation of those thin–wall approximate estimates, as undertaken in Appendix B.4.

The center boxed part is defined by a square $h = 2b$ box, divided in two by the web of thickness $t_w = t$. The outer top and bottom walls are connected by the two semicircular segments, all with the same thickness $t_f = t$. We fix h (the section height from the outer walls) and vary t in the range $0.01 \leq t/h \leq 0.10$, the same as in the previous sections when studying thin–walled sections. Similarly, we consider a homogeneous material distribution, so $n_{_E}(x, y) = n_{_G}(x, y) = 1.0$. The double symmetry leads easily

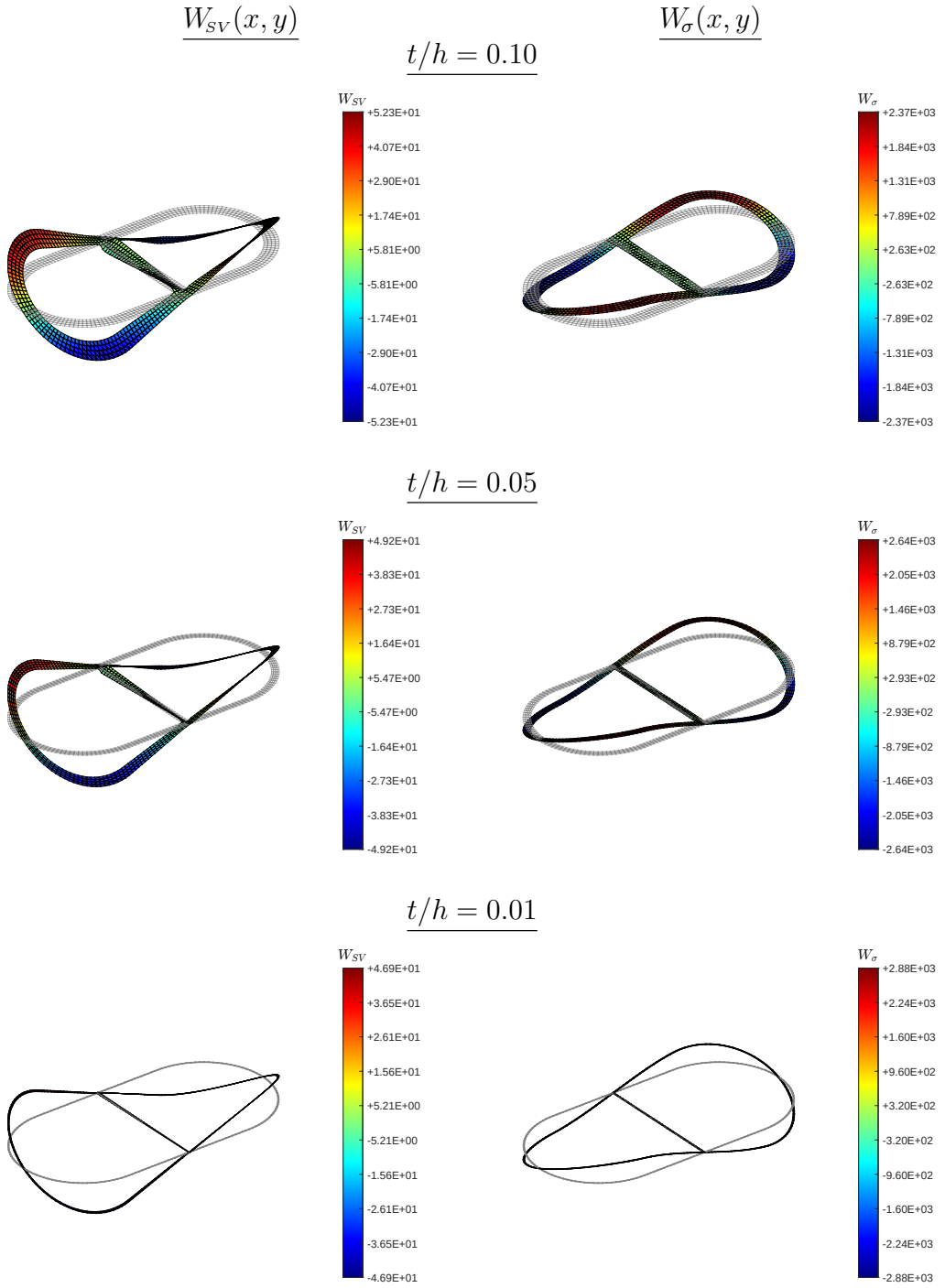

Figure 51: Two–cell cross section: warping functions. Computed warping functions $W_{SV}(x,y)$ (left) and $W_\sigma(x,y)$ (right) for sections with thickness ratios $t/h = 0.10, 0.05, 0.01$.

to the coincidence of the centroids and shear/twist center $\bar{\boldsymbol{x}}_{_E} = \bar{\boldsymbol{x}}_{_G} = \bar{\boldsymbol{x}}_{_T}$ with the geometric center of the section; see Figure 2. The actual numerical simulations consider $h = 2b = 20\ cm$, with $E = 200\ GPa$ and $\nu = 0.3$ for the Young modulus and Poisson ratio, respectively, in the 3D simulations below.

For now, we focus on the two–dimensional numerical solution of the warping functions on the plane cross section. To that purpose, we consider structured finite element discretization of the section geometry with 4−node bilinear elements. We consider 4 elements uniformly distributed through the thickness of the walls, with proportional number of elements along the length of each wall. Double symmetry considerations apply. Figure 51 shows representatives cases of the considered meshes, together with elevation plots of the computed warping functions $W_{_{SV}}9x, y)$ and $W_\sigma(x, y)$. Specifically, we consider the cross sections with $t/h = 0.10$, 0.05 and 0.01 as in the previous example, thus allowing more direct comparisons.

The availability of the warping functions allows the evaluation of the different torsional constant of interest for the considered sections. Figure 52 depicts them as they vary with the thickness ratio t/h in the considered range. We show again the Saint–Venant torsional constant J, the warping constant $I_{_{W_{SV}}}$ and the two gradient constants $I_{_{\nabla W_{SV}}}$ and $I_{_{\nabla W_\sigma}}$, all shown for the considered range of the thickness ratio t/h. We have also included the thin–wall limit estimate obtained in Appendix B.4, observing a good agreement especially in the low range of thicknesses t/h as expected. Table 6 includes the numeric values for the three representative sections $t/h = 0.10$, 0.05 and 0.01 shown in Figure 51 and other figures below in this section.

The availability of these torsional constants allow us to evaluate the exact solutions of the model problem outlined in Box 1 for the different formulations, as developed in Section 6 for different thickness ratios t/h and shaft lengths L/h. We start again with the normalized shaft flexibility $f_T/(L/\bar{G}J)$, as given by equation (194). Figure 53 depicts the variation of these values versus both the thickness ratio t/h and the shaft length L/h, each plot including different representative values of the other parameter. The plots show significant differences of the values computed by the different formulations, especially for thicker sections and longer shafts. Interestingly, and in contrast with the single cell box cross sections considered in Section 7.3, the curves versus L/h (right plot in Figure 53) obtained for the different section geometries t/h match each other well for a given formulation, all converging to the pure Saint–Venant solution $f_T/(L/\bar{G}J) = 1$ for long shafts (large L/h). This convergence is clearly slower for the TWKV formulation when

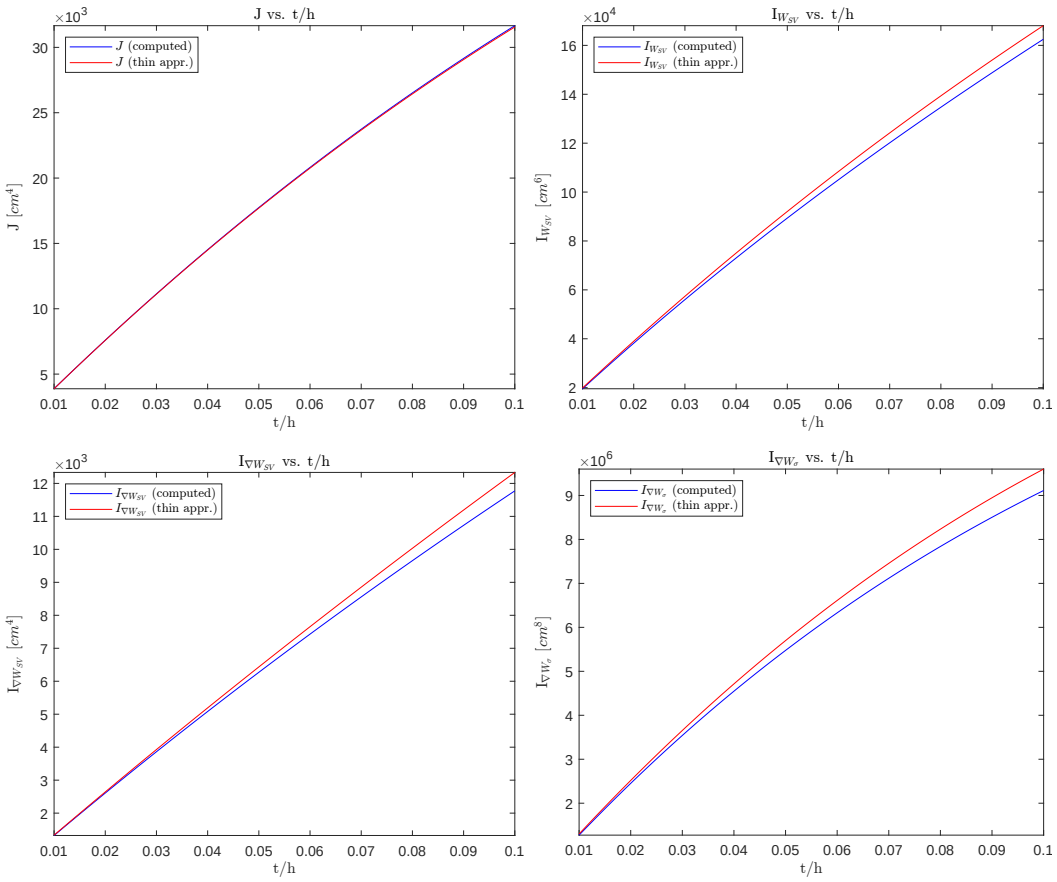

Figure 52: Two–cell cross section: torsional constants. Values of the Saint–Venant torsional constant J, the warping constant $I_{W_{SV}}$ and the two gradient constants $I_{\nabla W_{SV}}$ and $I_{\nabla W_\sigma}$ for different t/h ratios.

Table 6: Two–cell cross section: table of torsional constants for different sections thickness ratio t/h ($h = 20\ cm$).

t/h	$J\ [cm^4]$	$I_{W_{SV}}\ [cm^6]$	$I_{\nabla W_{SV}}\ [cm^4]$	$I_{\nabla W_\sigma}\ [cm^8]$
0.10	$3.16599435{\cdot}10^4$	$1.62488850{\cdot}10^5$	$1.17737445{\cdot}10^4$	$9.11281099{\cdot}10^6$
0.05	$1.77438378{\cdot}10^4$	$8.93618602{\cdot}10^4$	$6.27119852{\cdot}10^3$	$5.47580817{\cdot}10^6$
0.01	$3.88215938{\cdot}10^3$	$1.95546204{\cdot}10^4$	$1.32217133{\cdot}10^3$	$1.27403112{\cdot}10^6$

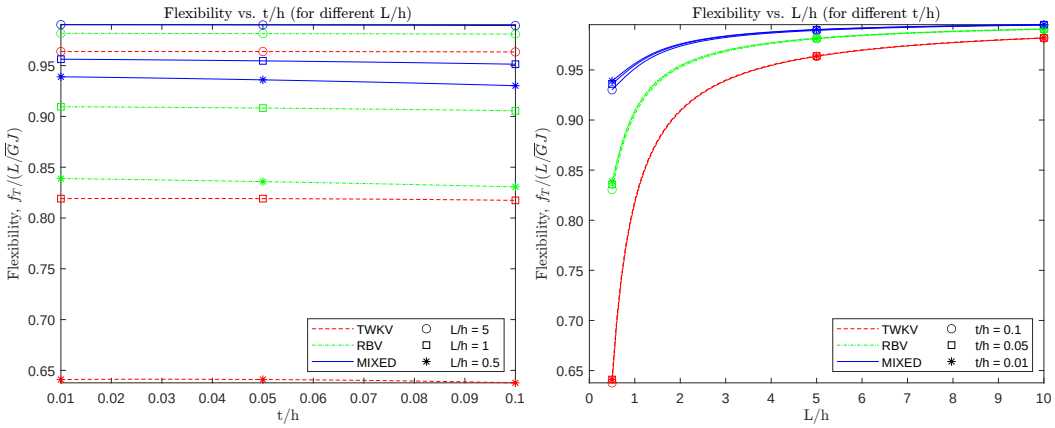

Figure 53: Two–cell cross section: shaft flexibility. Normalized torsional flexibility $f_T/(L/\bar{G}J)$ versus t/h (left) and L/h (right). All formulations tend to the Saint–Venant value ($f_T^{(SV)} = L/\bar{G}J$) for long shafts (large L/h).

compared with the other two formulations, a sign of the stiffer response of this (constrained) direct formulation for the current cross section topology as well. As in previous cases, the lowest flexibility always corresponds to the TWKV formulation, followed in order by the RBV and mixed formulations.

Similarly, Figure 54 allows to compare the diagrams of the bishear $T_W(z)$ and bimoment $B_W(z)$ along the shaft length with the same diagrams obtained in previous section, in particular the single cell box cross sections as shown in Figure 34 and 35 for the different thickness distributions. Again, we include the diagrams for the three representative values $t/h = 0.10$, 0.05 and 0.01, and different shaft's lengths L/h, all for the three formulations under study. Clearly, the diagrams obtained for the two–cell section considered here compares well with the latter in Figure 35, corresponding to the box section with $t_f = 2t_w$, in contrast with the former in Figure 34, corresponding to the Neuber tube $t_f = t_w$. We conclude that the source of the widely distributed stress resultants $T_W(z)$ and $B_W(z)$ along the shaft, quantities characteristic of the restrained warping caused by the end support at $z = 0$, is the stronger warping characteristic of the primary warping that appears in these cross sections, as opposed to that Neuber case only showing the smaller secondary warping across the thickness of the wall.

Comparing the different formulations, we observe again the overall higher values of the bishear $T_W(z)$ and the bimoment $B_W(z)$ predicted by the TWKV formulation, followed in order by the RBV and mixed formulations. The 3D

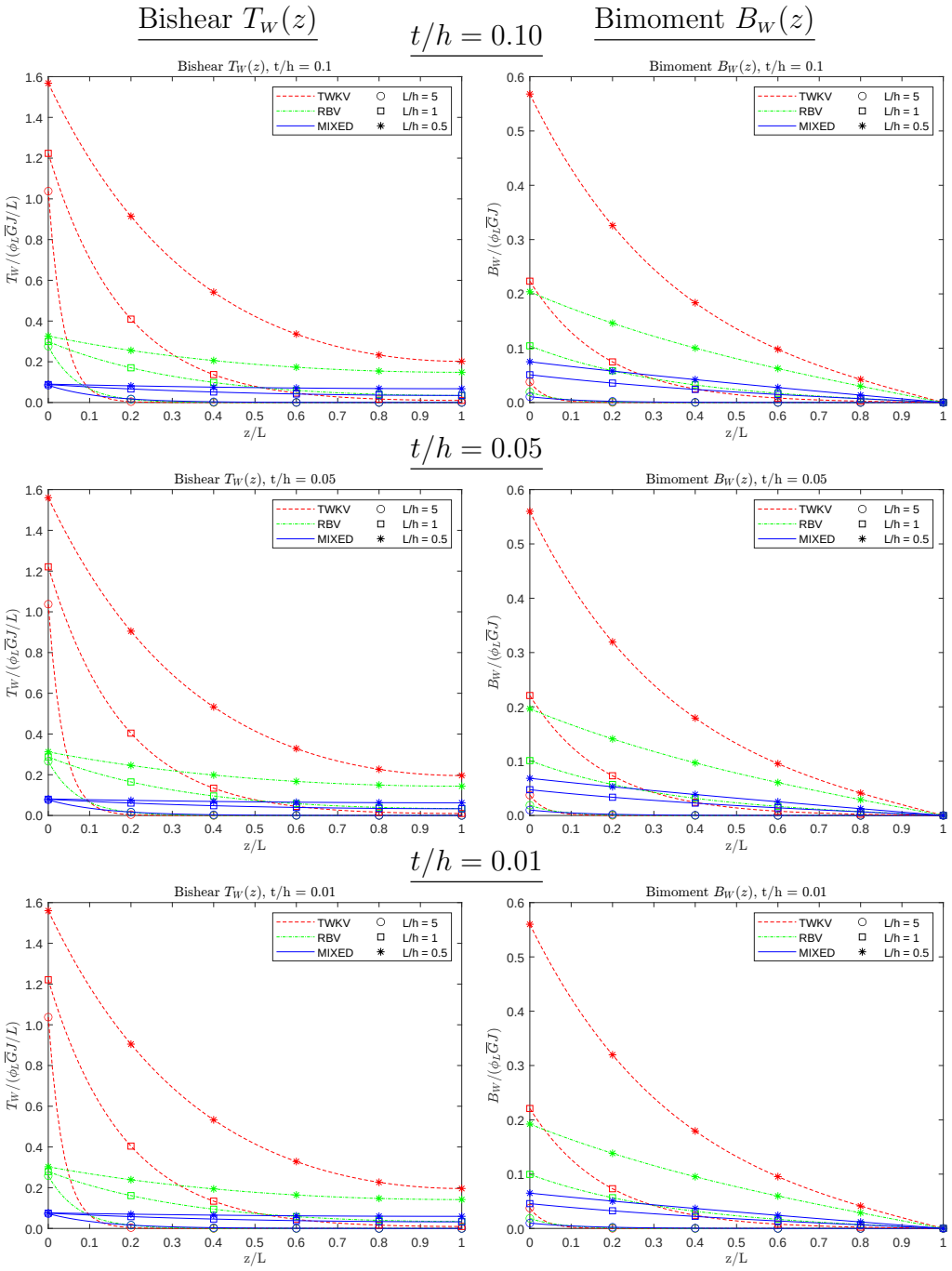

Figure 54: Two–cell cross section: moment diagrams normalized by the tip rotation ϕ_L. Distribution of the bishear $T_W(z)$ (left) and bimoment $B_W(z)$ (right) for different section aspect ratios $t/h = 0.10, 0.05, 0.01$, comparing different shaft's lengths $L/h = 5.0, 1.0, 0.5$ for each aspect ratio.

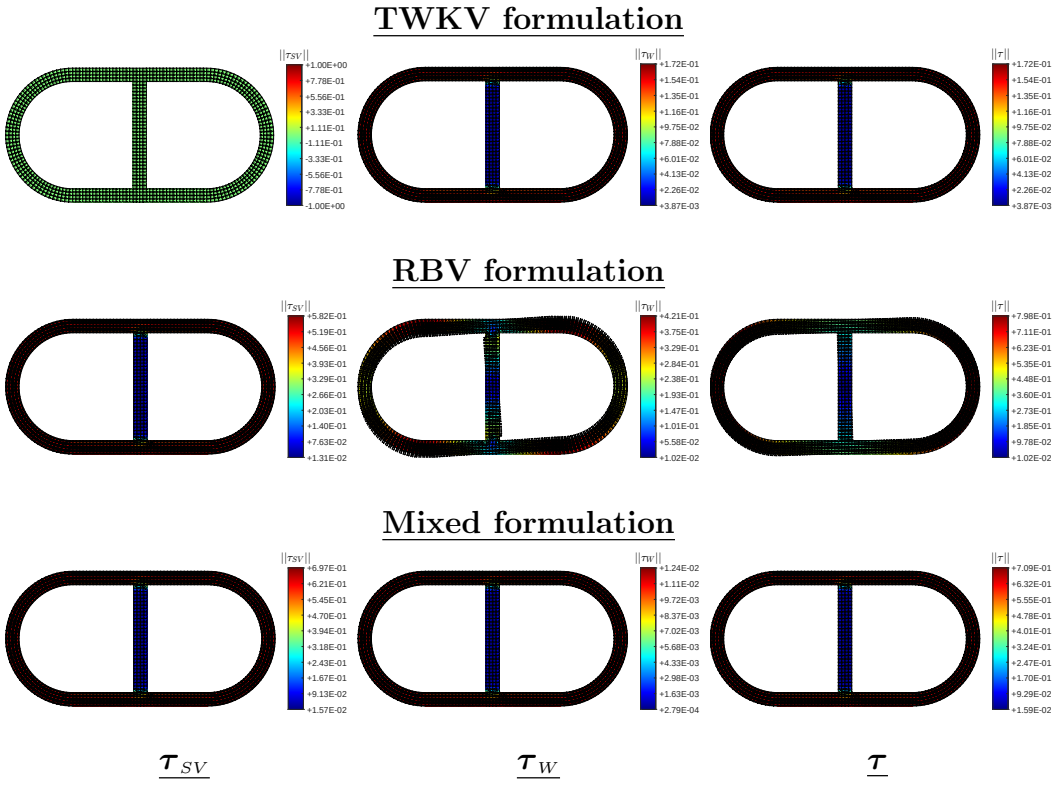

Figure 55: Two–cell cross section: shear stresses. Distributions of the Saint–Venant shear stress $\boldsymbol{\tau}_{SV}$, the warping shear stress $\boldsymbol{\tau}_{W}$ and the total shear stress $\boldsymbol{\tau}$ for the channel cross section $t/h = 0.10$ and $L/h = 1.0$ at the shaft root $z = 0$. All values are normalized as $\boldsymbol{\tau}/\bar{G}$ and correspond to the case with a unit rotation $\phi_L = 1.0$ at the opposite tip of the shaft.

results presented below will confirm that those values corresponds to an over–estimation of the more realistic value obtained by the mixed formulation. This is especially the case near the fixed support restraining the warping at $z = 0$. Recall that the TWKV formulation unrealistically makes the Saint–Venant torque to vanish at that end, forcing the bishear (or warping torque) to have the fixed value $T_W(0) = T_L$, the torque acting at the opposite tip of the shaft $z = L$ by equilibrium. The values shown in Figure 54 at the shaft's root vary because we show the normalized values for a fixed tip rotation ϕ_L, that is, $T_W/(\phi_L \bar{G} J/L)$ and $B_W/(\phi_L \bar{G} J)$. Still, the much higher values predicted by the TWKV formulation, and thus its stiffer response of the shaft, is clear.

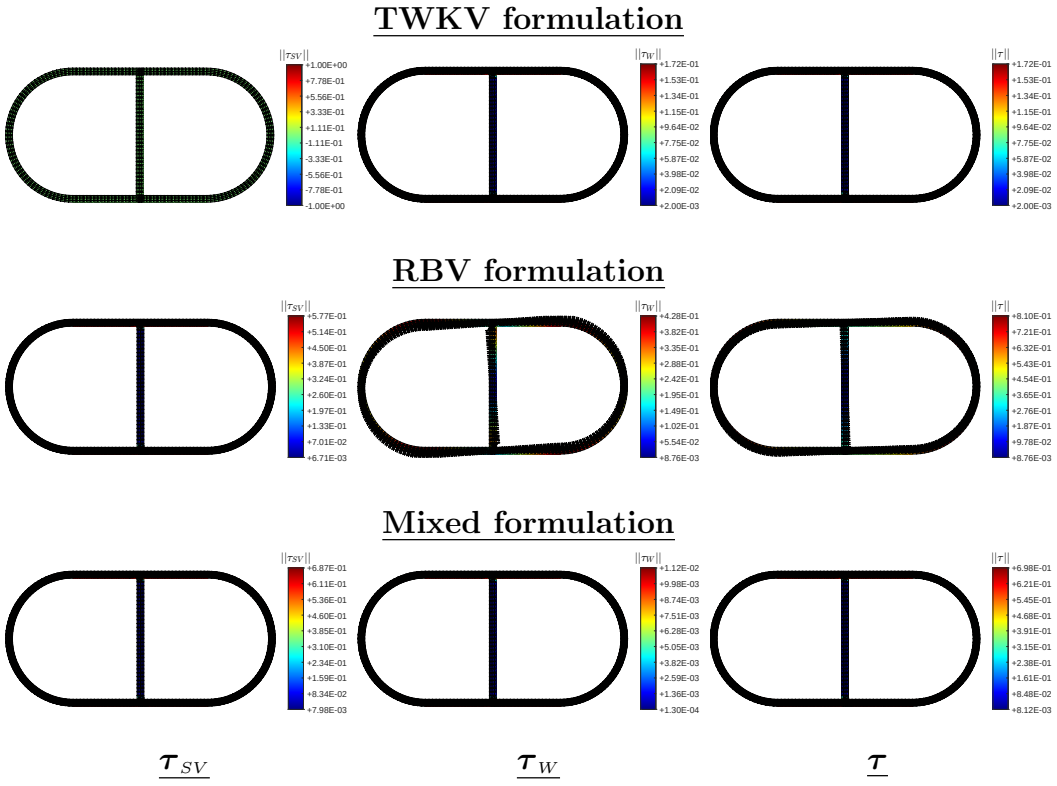

Figure 56: Two–cell cross section: shear stresses. Distributions of the Saint–Venant shear stress $\boldsymbol{\tau}_{SV}$, the warping shear stress $\boldsymbol{\tau}_{W}$ and the total shear stress $\boldsymbol{\tau}$ for the channel cross section $t/h = 0.05$ and $L/h = 1.0$ at the shaft root $z = 0$. All values are normalized as $\boldsymbol{\tau}/\bar{G}$ and correspond to the case with a unit rotation $\phi_L = 1.0$ at the opposite tip of the shaft.

The shear stresses on the cross section associated with the different formulations, in their Saint–Venant $\boldsymbol{\tau}_{SV}$ and warping $\boldsymbol{\tau}_{W}$ components, are given by equations (219)-(220) at the shaft's root. Their values depend on the computed warping functions $W_{SV}(x, y)$ and $W_{\sigma}(x, y)$, through the non–dimensional parameter α^{eff} given by in Box 1 for the different formulations in terms of the different torsional constants. Figures 55 and 56 show these stresses, together with the total shear stress $\boldsymbol{\tau} = \boldsymbol{\tau}_{SV} + \boldsymbol{\tau}_{W}$, for the sections with $t/h = 0.10$ and 0.05, respectively, both for the shaft with $L/h = 1.0$. The completely unrealistic nature of these stresses for the direct RBV formulation is clearly depicted again by the rotational pattern shown by the shear stress vectors $\boldsymbol{\tau}$. The anomaly of the vanishing of the Saint–Venant compo-

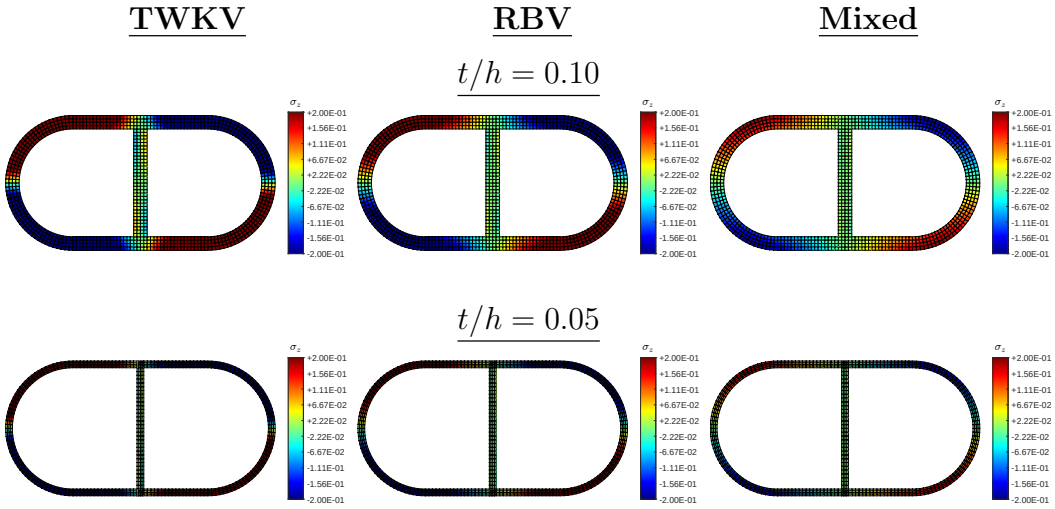

Figure 57: Two–cell cross section: axial stress. Distribution obtained by the different formulations of the end axial stress σ_z at the shaft root $z = 0$ for the cross section with $t/h = 0.10$, 0.05 and shaft's length $L/h = 1.0$. All values are normalized by the material's Young modulus as $\sigma_z/\bar{E}$ and correspond to the case with a unit rotation $\phi_L = 1.0$ at the opposite tip of the shaft.

nent $\boldsymbol{\tau}_{SV}$ for the original TWKV formulation is to be noted again, although the total shear stresses $\boldsymbol{\tau}$ show the correct pattern. In fact, as shown by the relation (220), the mixed formulation follows the same distribution, given by the (weighted) gradient $n_{_G}\,\nabla W_\sigma$ of the second warping function $W_\sigma(x, y)$, although with a different magnitude.

For the axial stress σ_z on a cross section, given by equation (221) at the shaft's root, all three formulations share the same distribution $n_{_E}\,W_{SV}(x, y)$, with again a different magnitude. Figure 57 shows this axial stress for, again, the two sections $t/h = 0.10$ and 0.05, both for the shaft $L/h = 1.0$. We use the same scale range in all plots, thus showing the much higher stress level predicted by the TWKV formulation followed in order by the RBV and mixed formulations, a new indication of the over–stiff response of the first two formulations. Note that the direct source of this stress is the bimoment $B_{_W}(0)$, with the higher value for those formulations.

7.4.1. Three–dimensional analysis

We contrast the previous conclusions with full three–dimensional simulations of the different shafts as full three–dimensional solids. To that purpose we consider again finite element discretizations of the problems at hand with

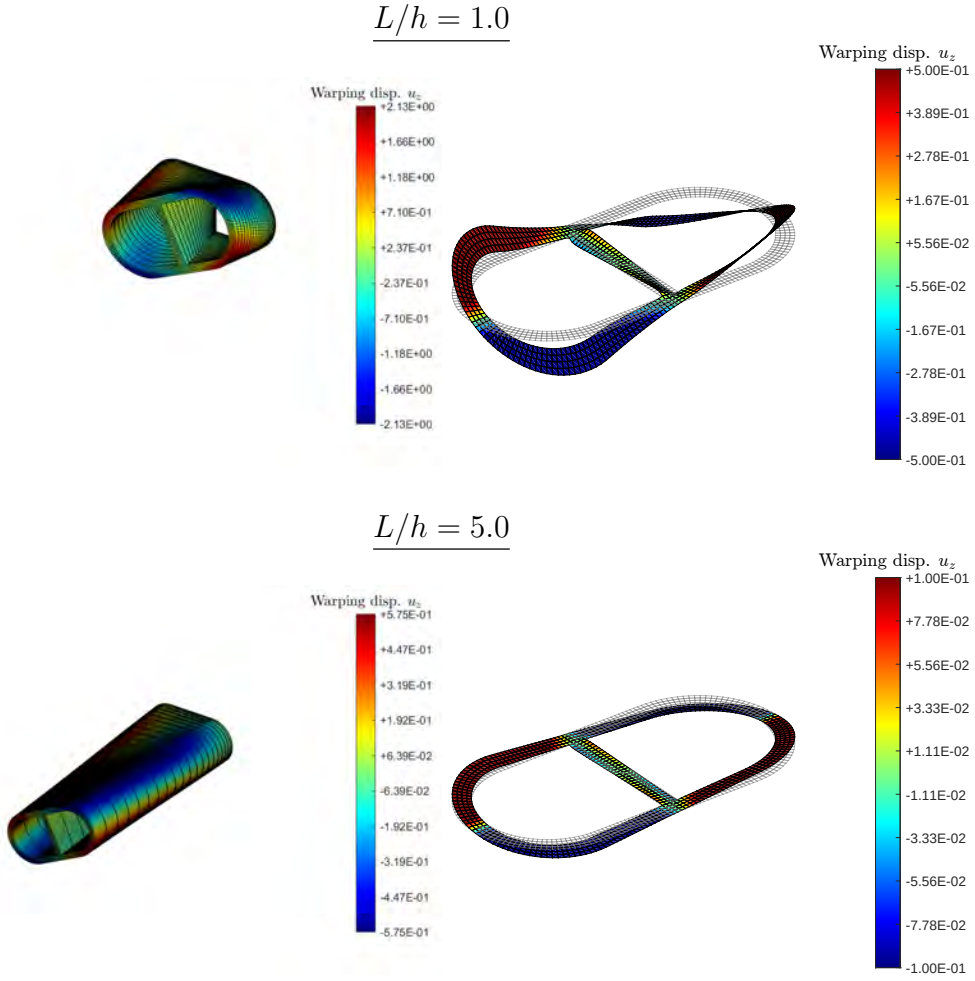

Figure 58: Two–cell cross section: 3D shaft. Three–dimensional finite element solution for shafts with $L/h = 1.0$, 5.0 and $t/h = 0.10$, showing the contours of the axial displacement u_z on top of the 3D deformed configuration of the shaft (left), and the elevation plot of the resulting warping at the shaft's tip $z = L$ (right).

8−node enhanced QM1/E12 brick elements, again 20 layers of the elements along the axis direction of the shaft z, with a graded distribution towards the root of the shaft at $z = 0$. We impose the plane (u_x, u_y) displacements $(12)_{1,2}$ with a unit rotation $\phi_L = 1$, leaving the axial displacement u_z free at the shaft's tip $z = L$. All 3D displacement components are imposed to vanish at the opposite tip of the shaft $z = L$.

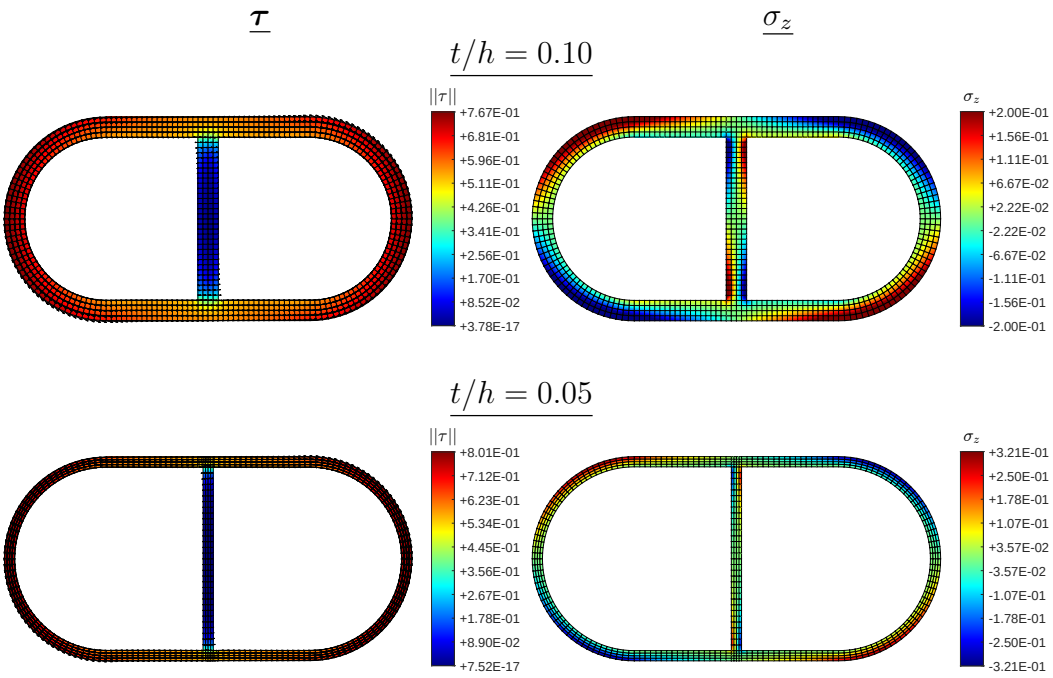

Figure 59: Two–cell cross section: stresses. Shear and normal stresses in the three–dimensional finite element solution at the shaft root $z = 0$ for $t/h = 0.10$, 0.05 and $L/h = 1.0$. Values are normalized as $\boldsymbol{\tau}/\bar{G}$ and $\sigma_z/\bar{E}$, and they correspond to the case with a unit rotation $\phi_L = 1.0$ at the opposite tip of the shaft.

The considered finite element meshes can be seen in Figure 58 for the shafts with lengths $L/h = 1.0$, 5.0 and the section with $t/h = 0.1$. We have included the deformed configuration of the twisted shafts with superposed contours of the level of the axial (warping) displacement u_z. Separate elevation plots of this warping displacement at the end tip of the shaft $z = L$ is also shown separately. The resulting distribution matches well the Saint–Venant warping function $W_{SV}(x, y)$ shown in the top left corner of Figure 51, its theoretical value.

Figure 59 shows the distribution of total shear stress $\boldsymbol{\tau}$ and normal axial stress σ_z for the section at the shaft's root $z = 0$ obtained in the three–dimensional simulation for the shafts with $t/h = 0.1$ and 0.05, both for the length of $L/h = 1.0$. As occurred in the previous sections, these stresses correspond to the nodally projected values (229) from their values evaluated at the quadrature points of the three–dimensional brick elements. The the-

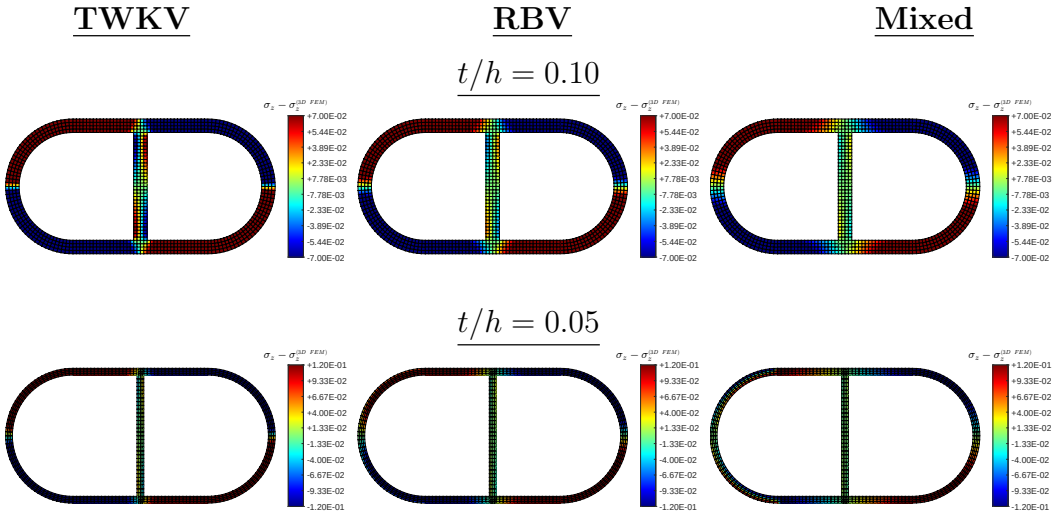

Figure 60: Two–cell cross section: axial stress difference. Comparison of the axial stress at the shaft's root $z = 0$ between the different considered formulations with the three–dimensional finite element solution $\sigma_z - \sigma_{z(3D)}$, for the different cross section $t/h = 0.10$, 0.05 and $L/h = 1.0$. All values normalized by the material's Young modulus as $\sigma_z/\bar{E}$ and correspond to the case with a unit rotation $\phi_L = 1.0$ at the opposite tip of the shaft.

oretical constant through–the–thickness of the shear stresses, with the shear stress vectors $\boldsymbol{\tau}$ following the direction of the wall, can be easily observed, with the web showing no shear stress to all practical purposes. Interestingly, that same web shows a high level of normal stress σ_z.

The difference between the axial stress resulting from the full three–dimensional elastic simulations with the same stress predicted by the different formulations is shown in Figure 60. As occurred in previous sections, this modeling error is much higher for the TWKV formulation followed by the RBV and mixed formulation. In particular, the latter shows a good resolution of that axial stress σ_z along the central web, while some error can be appreciated for the two direct formulations. This comparisons basically refer to the level of the stress since all formulations predict the same distribution, given by the weighted Saint–Venant warping function $n_{_E}\, W_{SV}(x, y)$ as noted above.

This difference in the level of axial stress is directly linked to the discrepancy of the bimoment $B_{_W}(0)$ at the shaft's root predicted by the different formulations. Figure 61 compares this value as well as the bishear $T_{_W}(0)$ at that same section among the different formulations for different geometries of

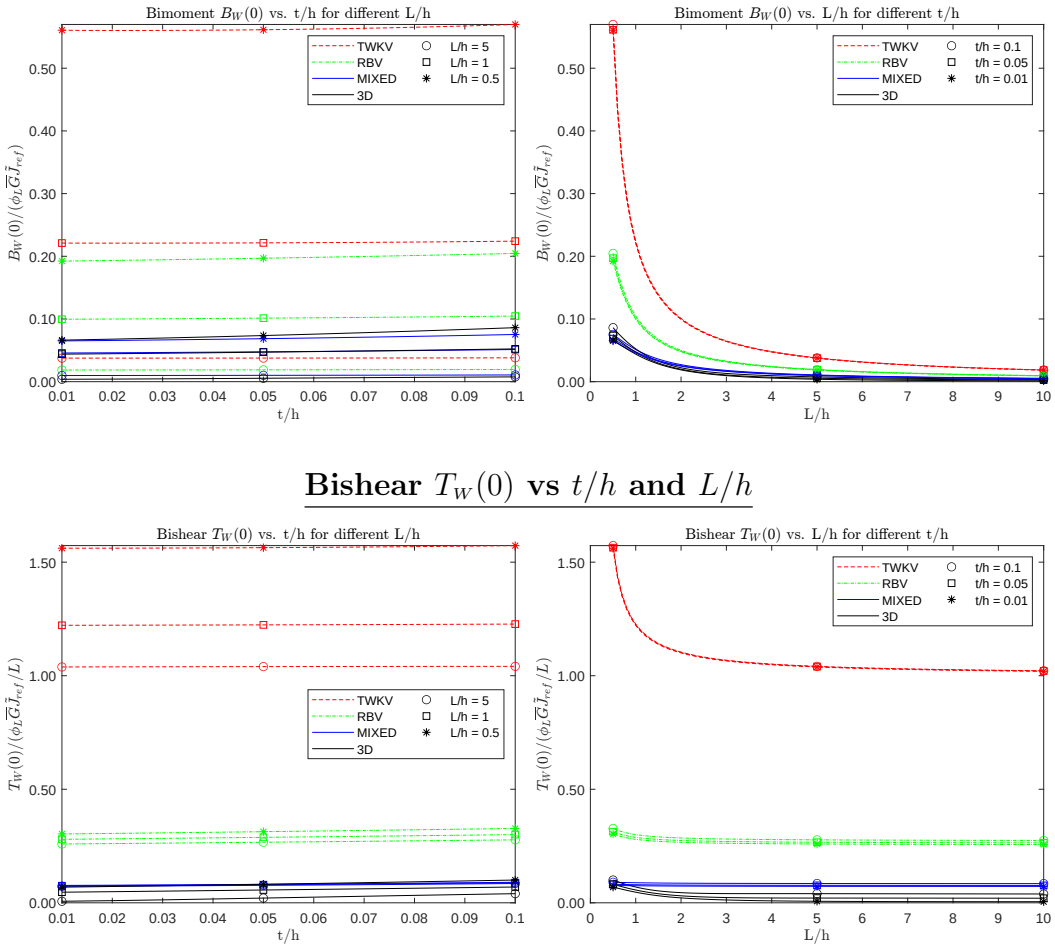

Figure 61: Two–cell cross section: bimoment and bishear at the shaft's root. Values of the bimoment $B_W(0)$ (top) and the bishear $T_W(0)$ (bottom) at $z = 0$ versus the section aspect ratio t/h (left) and shaft's length ration L/h (right) obtained by the different formulations and the 3D finite element solution.

the shaft's cross section as determined by the thickness ratio t/h and the shaft length L/h, all with the values obtained from the stresses obtained in the three–dimensional simulations (and their nodal projections (229)) through the postprocessing formulas (230) and (231) for the bimoment and bishear, respectively. The resulting values have been normalized in terms of the tip rotation ϕ_L. In all cases, the very good agreement of the 3D solutions with

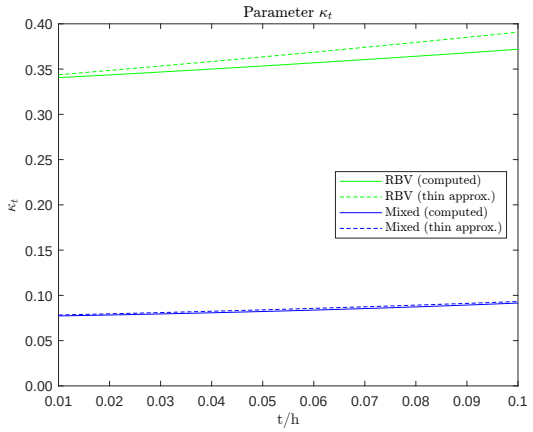

Figure 62: Two–cell cross section: parameter κ_t versus t/h. Geometric factor identified to drive the limiting process to the constrained TWKV formulation for the RBV and mixed formulations if $\kappa_t \to \infty$. No such process is observed for the current two–cell section.

the values obtained with the proposed mixed formulations can be clearly observed, noting the much over–stiff response of the original TWKV formulation. The RBV formulation, releasing the warping–twist constraint of that original formulation, falls in between, but still on the stiff side, this conclusion arising from the always higher values of these two quantities $B_W(0)$ and $T_W(0)$.

These results agree well with the same observations made for the single–cell closed section reported in Figures 47 and 48, especially with the latter corresponding to that section with a significant primary warping, as it is the case for the current two–cell section. In fact, we see a far more matching of the values obtained with different aspect ration t/h for a given formulation. In both cases though, the results are quite different to the ones obtained for the open channel section presented in Figure 27, also developing primary warping along the wall.

In that case of an open thin–walled section, the three structural formulations were quite close, especially in the thin–wall limit. As discussed in Section 7.2, this is due to the penalization that this limit imposes for the warping–twist constraint encompassed by the TWKV formulations. This was not the case for thin closed single–cell sections and continues not being the case for the two–cell section under consideration here. This situation is again illustrated by the evaluation of the parameter κ_t identified in this work

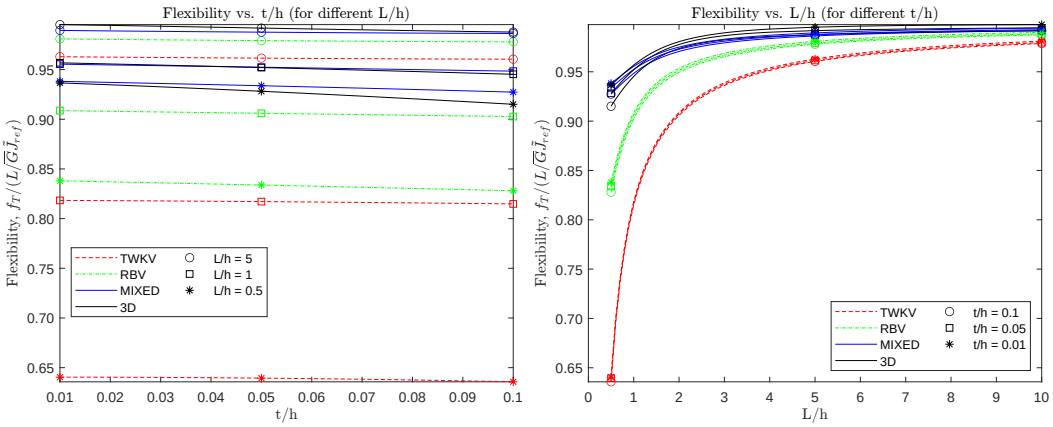

Figure 63: Two–cell cross section: shaft flexibility. Normalized torsional flexibility $f_T/(L/\bar{G}\tilde{J}_{ref})$ with a dimensional reference value ($\tilde{J}_{ref} = J^{(thin)}$), allowing the incorporation of the 3D FEM solutions. Values versus thickness ratio t/h (left), and shaft's length L/h (right).

for both the RBV and mixed formulations. The variation of this parameter with the thickness ratio t/h is shown in Figure 62 for those two formulations. The low value of this parameter, with no monotonic increase as the thickness ratio t/h is reduced in contrast with what occurred for the open channel thin–walled section in Figure 19, is a clear proof of this situation. We have included the evolution of this parameter κ_t evaluated with both the actual torsional constants for the section and with the thin–wall estimated formulae obtained in Appendix B.4. In particular, we refer to Remark B.5 for a detailed consideration of the actual numerical values involved for this parameter κ_t for both of these formulations.

As we did the previous sections, we conclude the evaluation for the two–cell closed thin–walled section by comparing directly the shaft flexibility predicted by the three structural formulations under study with the three–dimensional simulations of the full 3D elastic solid. To this purpose, we normalize these values as $f_T/(L/\bar{G}\tilde{J}_{ref})$ with the formulation–independent dimensional factor $\tilde{J}_{ref} = J^{(thin)}$, the thin–wall limit estimate for a given section t/h. The resulting values are shown in Figure 63 for both different thickness ratios t/h and shaft lengths L/h. The good agreement obtained with the mixed formulation with the full three–dimensional simulations is to be contrasted with the stiffer responses obtained with the RBV and TWKV formulations, especially the latter. The appropriateness of the proposed mixed formulation

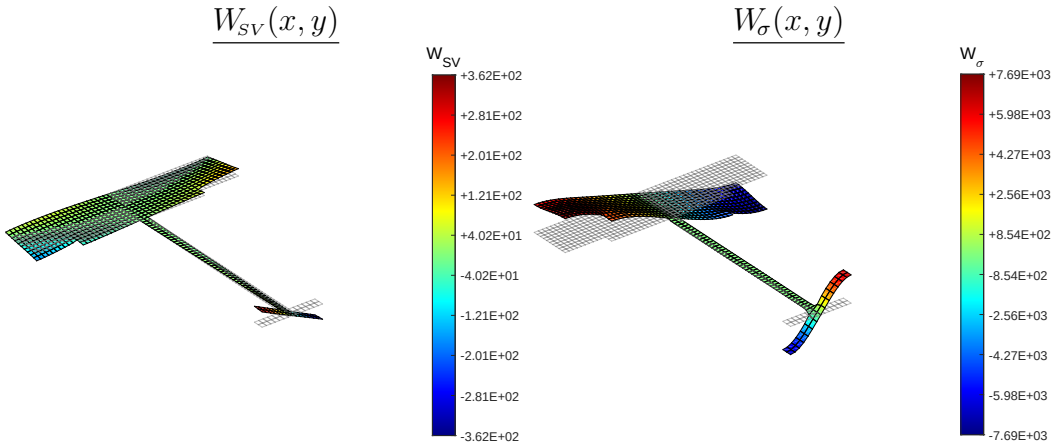

Figure 64: Composite cross section: warping functions. Computed warping functions $W_{SV}(x,y)$ (left) and $W_{\sigma}(x,y)$ (right) for the considered composite section ($t/h = 0.04$).

is also concluded for the multi–cell cross sections considered here.

7.5. Evaluation for composite cross sections

To illustrate the generality of the results presented here as it refers to general distributions of the material for inhomogeneous shafts, we consider briefly the composite cross section depicted in Figure 2 on page 84. It consist an I-beam made of a linear elastic material with Young modulus $E_1 = \bar{E} = 200\ GPa$ and Poisson's ration $\nu_1 = 0.3$ (so $G_1 = \bar{G} = 76.92\ GPa$), with a rectangular slab on its top with a linear elastic material with $E_2 = \bar{E}/10 = 20\ GPa$ and $\nu_2 = 0.20$, say, steel and concrete, respectively. Perfect bond is assumed between the two parts. As indicated in referring to these values, we take the values for the steel profile as the reference values $\bar{E}$ and $\bar{G}$ for the elastic parameters, leading to the distributions $n_{_{E_1}} = n_{_{G_1}} = 1.0$ for the thin–walled part of the section and $n_{_{E_2}} = 0.10$ and $n_{_{G_2}} = 0.108\bar{3}$ for the slab at the top of the composite section.

The dimensions of the different parts of the assumed cross section are indicated in Figure 2, keeping the height $h = 50\ cm$ of the I-profile as the reference value in the normalizations below. Note also than a different thickness is considered along the walls of this profile, taking as reference in our normalizations the value $t = t_w = t_c$ of the web and top flange. The cross section is kept constant in the arguments to follow, varying only the length of the shaft (i.e. the ratios L/h). The resulting value $t/h = 0.04$ for the

Table 7: Composite cross section: table of torsional constants for the section under consideration ($h = 50\ cm$, $t = 2\ cm$).

t/h	$J\ [cm^4]$	$I_{W_{SV}}\ [cm^6]$	$I_{\nabla W_{SV}}\ [cm^4]$	$I_{\nabla W_\sigma}\ [cm^8]$
0.04	$4.23488407{\cdot}10^3$	$1.75506164{\cdot}10^6$	$1.63767657{\cdot}10^5$	$4.53999995{\cdot}10^7$

Table 8: Composite cross section: table of section centers. Vertical positions (from the bottom) of the torsional center and the Young's and shear centroids ($h = 50\ cm$, $t = 2\ cm$).

t/h	$\bar{y}_T\ [cm]$	$\bar{y}_E\ [cm]$	$\bar{y}_G\ [cm]$
0.04	$4.84813375{\cdot}10^1$	$3.36881551{\cdot}10^1$	$3.40540865{\cdot}10^1$

thickness ratio locates the I-profile part of the section at the middle of the range of open thin–walled sections studied in Section 7.2, whereas the concrete slab at the top, with an aspect ratio of $d/w = 0.2$ (in the notation shown in Figure 2) puts that part in the range of solid rectangular sections analyzed in Section 7.1 above.

Figure 64 depicts the computed warping functions $W_{SV}(x, y)$ and $W_\sigma(x, y)$ for the considered composite cross section. It also depicts the assumed plane finite element mesh for the analysis of this fixed section. It consists of a structured mesh with 2 equally spaced 4−node bilinear quadrilateral elements through the thickness for the thin–walled part of the section, 10 elements through the thickness of the top slab, and proportional elements along the other different lengths. Symmetry considerations apply.

The plot of the Saint–Venant warping function $W_{SV}(x, y)$ in Figure 64 (left plot) shows the dominance of that thin–walled part in the overall warping of the section, at least at the tip of the shaft. This function with the second warping function $W_\sigma(x, y)$ (right plot in that figure) lead to the torsional constants of interest in the analysis below, namely, the Saint–Venant torsional constant J, the warping constant $I_{W_{SV}}$ and the two gradient constants $I_{\nabla W_{SV}}$ and $I_{\nabla W_\sigma}$. We have included all the computed values in Table 7. The calculation of the warping functions and the section constants also provides the location of the twist/shear center $\bar{\boldsymbol{x}}_T$ following the arguments presented in Section 2.4. Table 8 shows the coordinate $\bar{y}_T$ of this center along the vertical axis of symmetry of the section, measured from the bottom of the section. We have also included the vertical position of the centroid of the Young modulus distribution $\bar{y}_E$ and the centroid of the shear modulus

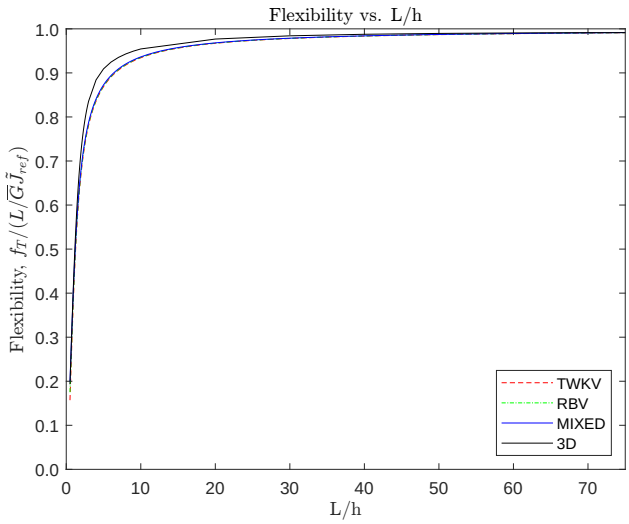

Figure 65: Composite cross section: shaft flexibility. Normalized torsional flexibility $f/(L/\bar{G}\tilde{J}_{ref})$ with the reference value $\tilde{J}_{ref} = J$, the numerically computed value for the fixed section. Convergence to the Saint–Venant theory for long shafts can be observed.

distribution $\bar{y}_G$, both centroids located along that vertical axis of symmetry of the section.

Figure 65 shows the value of the shaft flexibility $f_T/(L/\bar{G}\tilde{J}_{ref})$ (for $\tilde{J}_{ref} = J$, the computed Saint–Venant torsional constant for the fixed cross section under study), for different lengths L/h as given by the result (194) in terms of those different section constants for the problem at hand. The three different formulations of restrained warping show basically the same value for all L/h's, basically indicating the dominance of the thin–walled part of the section and, in this case too, the stiffer part. This result conforms with the results for open thin–walled cross sections presented in Section 7.1, where the warping–twist constraint underlying the TWKV formulation is reached for small wall thickness in this type of sections. The situation would be different if the thin–walled part of the section was multiply connected, as observed in Section 7.3, an analysis we do not undertake here for the sake of brevity.

In Figure 65 we have also included the result obtained with a full three–dimensional simulation of the solid shaft, showing a good overall matching with the values predicted by the different structural theories under study. It is significant that this occurs again for low values of the ratio L/h, as low a $L/h = 0.5$. As in previous sections, the 3D finite element simulations

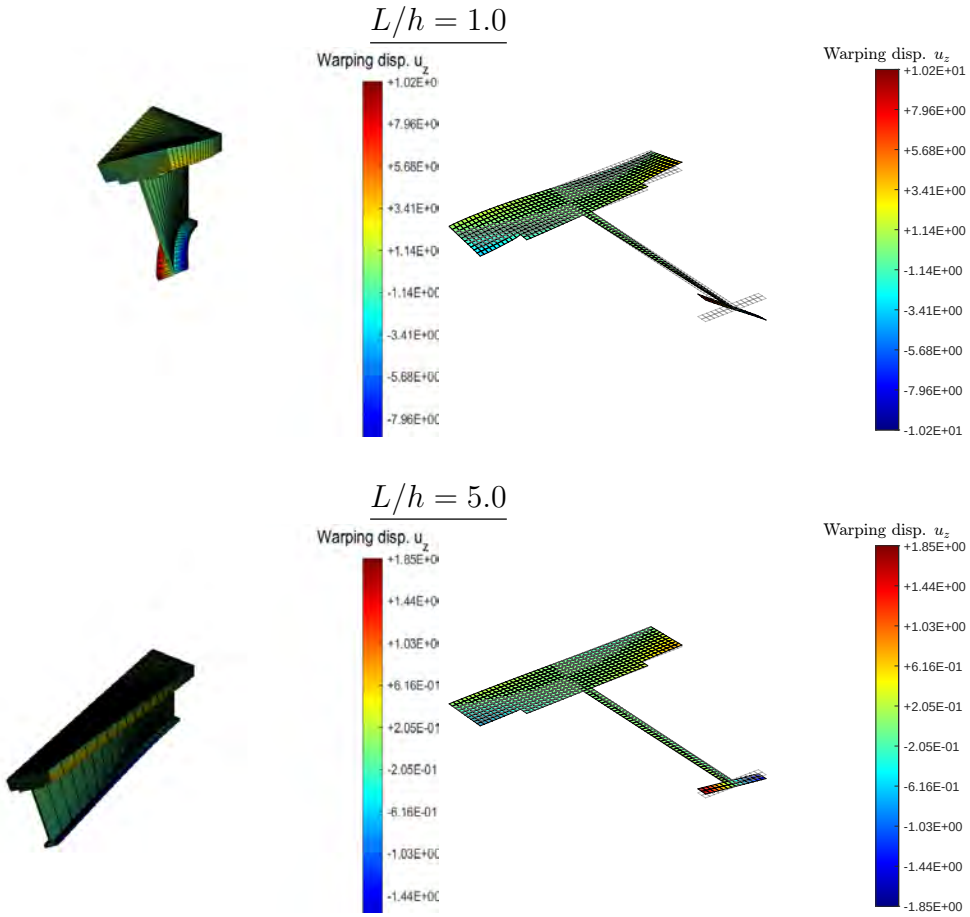

Figure 66: Composite cross section: 3D shaft. Three–dimensional finite element solution for shafts with $L/h = 1.0$, 5.0, showing the contours of the axial displacement u_z on top of the 3D deformed configuration of the shaft (left), and the elevation plot of the resulting warping at the shaft's tip $z = L$ (right).

consider 20 layers of QM1/E12 enhanced brick elements along the length of the shaft, smoothly graded as the fixed support at $z = 0$ is approached. Typical meshes can be seen in Figure 66.

As in previous sections, the three–dimensional simulations are run imposing a unit rotation $\phi_L = 1$ with the imposed plane displacements $(12)_{1,2}$ at the shaft tip $z = L$, fixing all displacement components at the opposite fixed support $z = 0$. Figure 66 shows the deformed configuration for the shaft lengths $L/h = 1.0$ and 5.0, depicting the contour plots of the warping displacement u_z. We have included separate elevation plots of the computed

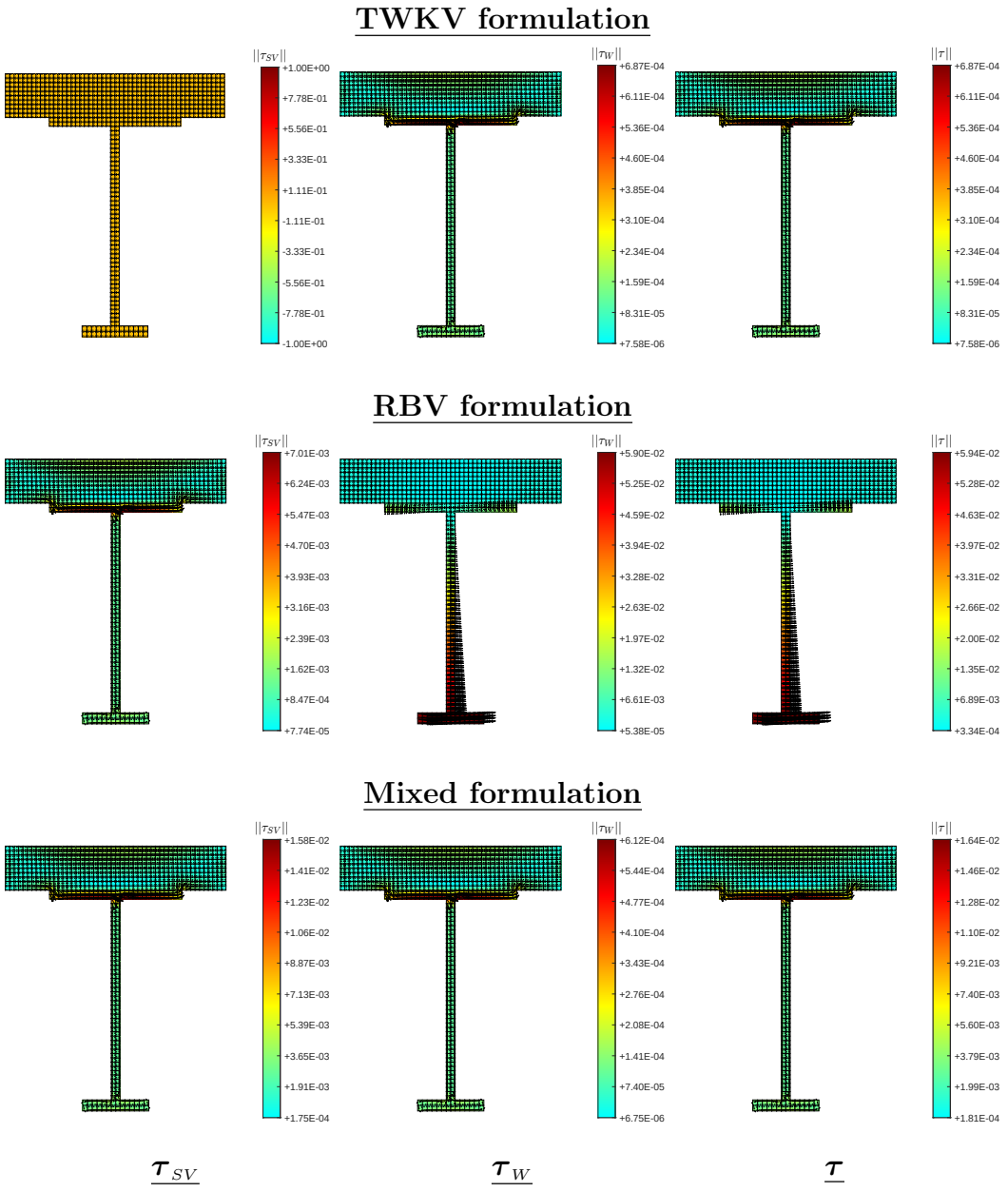

Figure 67: Composite cross section: shear stresses. Distributions of the Saint–Venant shear stress $\boldsymbol{\tau}_{SV}$, the warping shear stress $\boldsymbol{\tau}_W$ and the total shear stress $\boldsymbol{\tau}$, all at the shaft root $z = 0$, for the considered cross section ($t/h = 0.04$) and shaft's length $L/h = 1.0$. All values are normalized as $\boldsymbol{\tau}/\bar{G}$ and correspond to the case with a unit rotation $\phi_L = 1.0$ at the opposite tip of the shaft.

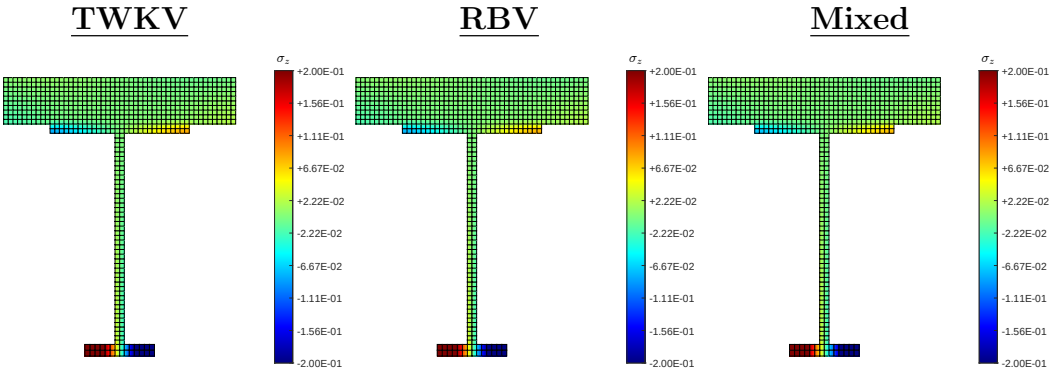

Figure 68: Composite cross section: axial stress. Distribution obtained by the different formulations of the end axial stress σ_z at the shaft root $z = 0$ for the considered cross section ($t/h = 0.04$) and shaft's length $L/h = 1.0$. All values are normalized by the reference Young modulus as $\sigma_z/\bar{E}$ and correspond to the case with a unit rotation $\phi_L = 1.0$ at the opposite tip of the shaft.

warping of the section at the tip of the shaft in the 3D simulations, with the distribution to be compared with the Saint–Venant warping function $W_{SV}(x, y)$ in Figure 64 (left plot).

Figure 67 shows the shear stresses at the shaft's root $z = 0$ for the shaft of length $L/h = 1.0$, obtained with the TWKV, RBV and mixed formulations. As in previous sections, we include the Saint–Venant component $\boldsymbol{\tau}_{SV}$ in (219) the warping component $\boldsymbol{\tau}_W$ in (219) and the total shear stress $\boldsymbol{\tau} = \boldsymbol{\tau}_{SV} + \boldsymbol{\tau}_W$. We note the similar distributions obtained by the TWKV and mixed formulations for the total stress $\boldsymbol{\tau}$ (not its components due to the torque anomaly of the former formulation), with the bigger stresses occurring at the top flange of the (stiffer) I-profile, whereas the RBV formulation gives again the observed rotational pattern (213) around the center of twist, loading then especially the lower flange instead.

The normal stress σ_z at the fixed root of the shaft corresponding to that same case is shown in Figure 68 for the TWKV, RBV and mixed formulations. The three formulations result in a stress proportional to the weighted Saint –Venant warping function $n_E(x, y)W_{SV}(x, y)$ given by formula (221). The plots in this figure indicate that the two flanges of the I-profile, the stiffer part of the composite section, take the main part of the normal stress σ_z in a basically linear and symmetric manner along each individual flange, especially the bottom one; see the warping function $W_{SV}(x, y)$ in the left plot of Figure 64. As noted in Section 3.2, this situation clearly illustrates the

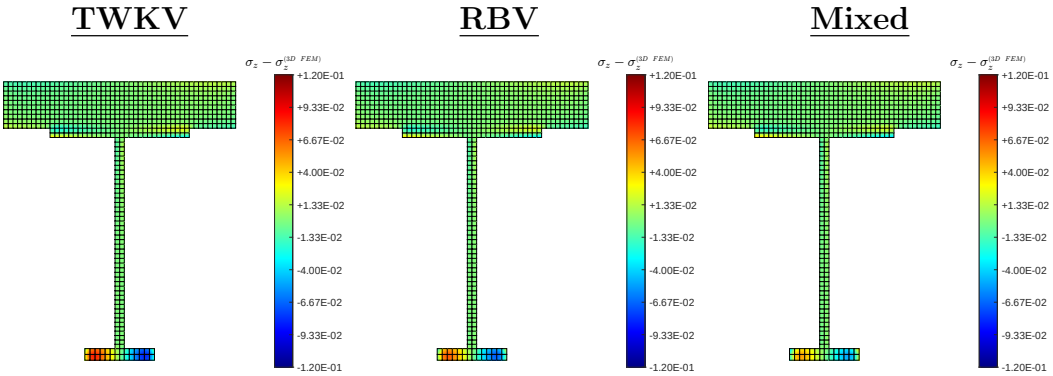

Figure 69: Composite cross section: axial stress difference. Comparison of the axial stress at the shaft's root $z = 0$ between the different considered formulations with the three–dimensional finite element solution $\sigma_z - \sigma_{z(3D)}$, for the shaft with $L/h = 1.0$ ($t/h = 0.04$). Values are normalized as $\sigma_z/\bar{E}$, and they correspond to the case with a unit rotation $\phi_L = 1.0$ at the opposite tip of the shaft.

popular representation of the bimoment $B_W(0)$ causing these stresses and the associated bishear $T_W(0)$ as two equal and opposite bending moments and associated shear forces acting on the flanges; see e.g. Oden & Ripperger [1981], page 226. As noted in the introduction presented in Section 1, it was precisely this observation that motivated the original developments by Timoshenko in Timoshenko [1905, 1906, 1910] for thin–walled sections; see Timoshenko & Gere [1961], page 213.

We compare these normal stresses for the different formulations with the ones obtained in the full three–dimensional finite element simulations, projected to the nodes of the section at the shaft's root using equation (229). This results in the plots shown in Figure 69. We observe the bigger difference occurring again in the solution of the TWKV formulation followed, in order, by the RBV and mixed formulations.

The higher stresses in the TWKV formulation confirms the overstiff response obtained with this formulation also for composite cross sections of the type considered in this section. This situation is also apparent when looking at the resulting bishear $T_W(z)$ and bimoment $B_W(z)$ diagrams shown in Figure 70. These diagrams are normalized by the tip torque T_L for shafts of length $L/h = 0.5$, 1.0 and 5.0. In all cases, the TWKV formulation falls above the diagrams for the RBV and mixed formulations, always in this order monotonically, especially for shorter shafts. As the length of the shaft increases, the overall effects of the restrained warping at the root $z = 0$ re-

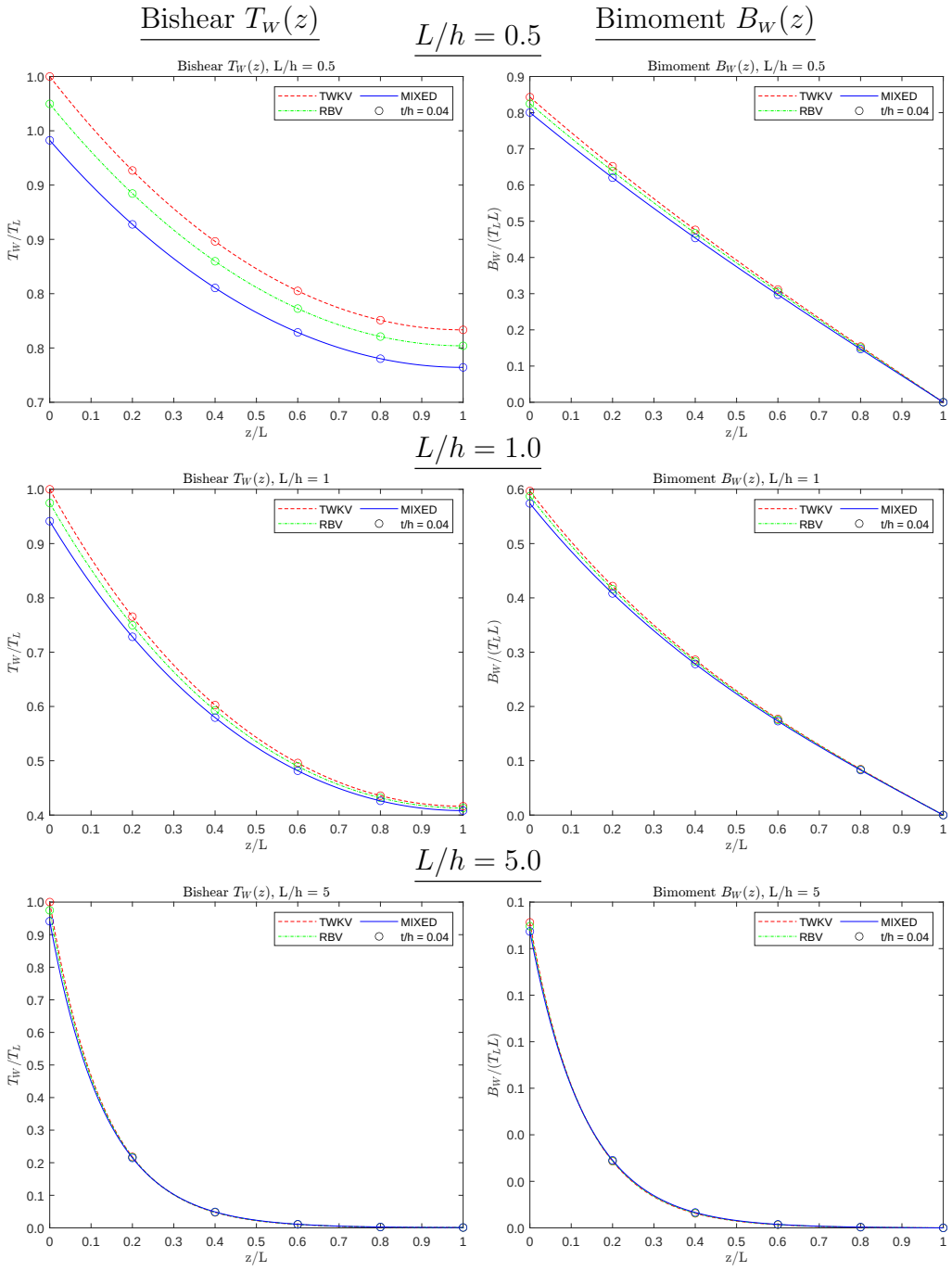

Figure 70: Composite cross section: moment diagrams normalized by the tip torque T_L. Distribution of the bishear $T_W(z)$ (left) and bimoment $B_W(z)$ (right) for different shaft lengths $L/h = 0.5$, 1.0, 5.0.

duces, as it can be verified by the lower overall values of both bishear and bimoment, including the values of these quantities for the fixed support at that end. However, note that the TWKV formulation forces $T_W(0)/T_L = 1.0$ in an unrealistic manner, a consequence of the vanishing of the Saint–Venant torque and stresses at that end with no warping and $\phi'(0) = 0$, that is, a consequence of the torque anomaly discussed in Remark 2.3 in combination with the warping–twist constraint (93). The only way to resolve this anomaly and maintain balance of moments with the applied torque T_L is the appearance of the unrealistically high bishear at that support, regardless of the type of cross section involved (like in all the ones studied above in this paper) or the length of the shaft.

The better resolution of these issues by the mixed formulation is to be noted again. It leads also to more accurate distributions of the stresses on the cross sections, especially when compared with the incorrect distributions obtained with the RBV formulation. These results indicate the appropriateness of the newly proposed mixed formulation for composite cross sections too.

8. Concluding remarks

We have presented in this paper an analysis of different treatments of restrained warping in elastic shafts. Specifically, we have considered the original TWKV formulation of Timoshenko-Wagner-Kappus-Vlasov, the RBV formulation of Reissner-Benscoter-Vlasov, and a newly developed mixed formulation of the problem at hand, the latter motivated on ideas originally considered by Reissner in general terms from an alternative framework. The different formulations have been developed in detail, together with their analysis and comparative evaluation in the context of the model problem of a prismatic shaft under a tip torque/twist rotation while having a restrained warping at its opposite end. The evaluations include both the computation of the involved warping functions via finite element discretizations of the considered cross sections in order to evaluate the torsional section constants and stress distributions, as well as full three–dimensional solid finite element simulations of the elastic shaft to assess the accuracy of the different formulations. These comparisons include not only the overall structural response of the shaft, in the form of the shaft's flexibility in torsion and the diagrams of the additional stress resultants created by restraining of the warping (namely, bishear and bimoment), all obtained exactly and in closed–form for the model

problem, but also the distribution of the shear and normal stresses on the shaft's cross sections predicted by the different formulations based on the computed warping functions for different cross section topologies.

Based on these analyses and evaluations, we can draw the following concluding remarks:

1. The original TWKV formulation encompasses a kinematic constraint by which the rate of twist $\phi'(z)$ along the shaft in z drives directly the amplitude of the warping of the different cross sections. We refer to this condition as the *warping–twist constraint.* The distribution of that warping displacement on the cross section is given by the original Saint –Venant warping function $W_{SV}(x, y)$, uniformly along the shaft.

2. The RBV formulation relaxes that constraint considering a general field $\lambda(z)$ along the shaft to define the amplitude of the warping displacement besides the twist rotation $\phi(z)$ itself, still keeping the basic distribution $W_{SV}(x, y)$ over all cross sections and, consequently, still uniformly along the shaft.

3. In a first mixed treatment of the problem at hand, both the axial strain and stress normal to the cross section are given general assumed distributions over it while being uniform along the shaft, crucially in combination of a completely general distribution of the warping displacement creating that normal strain in the whole shaft. This generality allows to identify an alternative distribution on this warping displacement over the cross section, involving two different components defined in terms of two separate warping functions: the original Saint–Venant warping function $W_{SV}(x, y)$ and a second warping function $W_\sigma(x, y)$. For the linear elastic problem considered herein, the first function is given by the classical (weighted) Laplacian problem of the Neumann type on the cross section domain, while the second warping function satisfies a (weighted) Poisson problem also of the Neumann type driven by the first function as its source.

4. This insight allows the development of a new fully structural mixed formulation to model restrained warping in torsion, introducing an independent field $\lambda_\varepsilon(z)$ along the shaft's length, defining with the twist rotation $\phi(z)$ the amplitude of each of those two components of the warping displacement, a combination that varies along the shaft. The

independent field $\lambda_\varepsilon(z)$ is introduced so it corresponds physically to the average warping displacement of the particular cross section at z, leaving free the twist rotation and, hence, releasing the warping–twist constraint of the original TWKV formulation.

5. Perhaps, the key aspect behind the new mixed formulation, in some sense the distinctive feature of this formulation, is the non–uniform character of the shape of the distribution of the warping over the cross sections along the shaft. The two driving fields, the twist rotation $\phi(z)$ and the warping field $\lambda_\varepsilon(z)$, define the warping of the cross section, in both shape and amplitude, through the combinations of the two different components identified in Item 3 above. This situation takes full advantage of having two independent driving fields at the structural level when compared to the RBV formulation. A major consequence of this new warping kinematics is that it results in the proper stress distributions discussed below.

6. A clear indication of the constrained character of the TWKV formulation is given by the fourth order differential equation on the twist rotation $\phi(z)$ governing this formulation, in contrast to the second order system of differential equations on the twist $\phi(z)$ and either the field $\lambda(z)$ or $\lambda_\varepsilon(z)$ governing the RBV or mixed formulations, respectively.

7. Particular combinations of the section constants identified here act effectively as "penalty" parameters driving the RBV and mixed formulations to the constrained TWKV formulation in a limit process. The explicit bounds obtained analytically for these parameters points to the stiffer response of the RBV formulation when compared to the mixed formulation in approaching the constrained TWKV formulation, a much stiffer model of the structural response of the shaft given precisely its constrained character.

8. Having developed all three formulations from fully kinematic considerations of the idealized shaft (axis with cross sections attached), the stresses predicted by each of them are readily available for analysis and evaluation. In particular, all three formulations result in the same form of the distribution for the normal stresses acting on the cross sections, namely, the Saint–Venant warping function $W_{SV}(x, y)$ for the particular cross section with their magnitude given directly by the aforementioned

bimoment. Similarly, each formulation identifies two components of the total shear stress on a cross section, the Saint–Venant and warping components depending, respectively, on the Saint–Venant and bishear parts of the total internal torque acting on the cross section. The three formulations differ considerably on the origin and final form of the warping component of the shear stress.

9. In particular, the prediction of the warping shear stress by the RBV formulation is physically incorrect, in the sense that it results in total stresses that do not satisfy equilibrium equations, in contrast with the equilibrated stresses involved in both the TWKV and mixed formulations. The RBV formulation considers incorrectly warping shear strains and stresses proportional to the gradient of the Saint–Venant warping function $W_{SV}(x, y)$ alone, leading to unrealistic situations as the numerical evaluations illustrate.

10. Despite this completely different warping shear strains and stresses at the cross section level, the RBV and mixed formulations have been shown to lead to similar governing problems at the structural level along the shaft. In fact, for both cases, we recover a system of second order differential equations in the corresponding driving fields but with differing coefficients, involving different combinations of the section torsional constants.

11. Remarkably, the distributions of the warping shear stresses for the TWKV and mixed formulations exhibit the same distribution form on a given cross section, namely, the (weighted) gradient of that second warping function $W_\sigma(x, y)$, as opposed to $W_{SV}(x, y)$ in the RBV formulation. For the mixed formulation, this component follows naturally from the shear strain associated to that new independent field $\lambda_\varepsilon(z)$, whereas it arises as a Lagrange multiplier–type response enforcing the warping–twist constraint in the TWKV formulation (that is, by static equilibrium considerations solely, with no associated strains involved). The new mixed formulation accomplishes this correct modeling of the warping stresses without the need of the warping–twist constraint, resulting in an overall improved modeling as the numerical results presented here show. This is a clear consequence of the assumed two component warping distribution indicated in Item 5.

12. The complete restrainment of the warping at a support forces the TWKV formulation to eliminate the rate of twist at that end due to the warping–twist constraint and, thus, the Saint–Venant component of the shear stress and its resultant Saint–Venant torque altogether. Therefore, the TWKV formulation must rely entirely on the bishear at that end to balance any applied torque when trying to model such a fixed support. We refer to this situation as a torque anomaly. As shown in the numerical evaluations presented here, this situation leads, in general, to unrealistic diagrams of the bishear and bimoment along the shaft, contributing to that over–stiff response associated with the TWKV formulation. Both the RBV and mixed formulations are not affected by this anomaly, since they do not involve the warping–twist constraint.

13. The analyses and evaluations presented here, including the closed–form exact solutions of a typical model problem, show that the original TWKV formulation leads to an overstiff response of the shaft, followed in order by the RBV formulation and mixed formulation, in all type of cross sections cases considered (solid, open and closed thin–walled, and composite sections). In particular, the mixed formulation has been shown to lead to more accurate results when compared with full three–dimensional finite element simulation of the elastic solids at hand. This situation has been observed for all type of sections and for the whole range of thickness ratios t/h of the cross sections and shaft length L/h, for the section height h.

14. This more accurate modeling of the mixed formulation applies even as the effects of restrained warping are local in nature, concentrated near the restrained sections (usually by fixed supports, stiffeners or similar). For this reason, the overall structural response of the shaft tends to the basic Saint–Venant torsion for long shafts $L \gg L_T$, with the the analyses presented here identifying explicitly the characteristic length scale L_T associated with the different formulations in terms of the section constants that they involve. All formulations recover this limit response in that case, but on the overstiff side by the both the TWKV and RBV direct formulations due to their limited resolution of those local effects.

15. However, we note that the recovery of the Saint–Venant torsion should

be understood for the overall structural response of the shaft (e.g. its flexibility), with still the need to model correctly the local effects associated with the restrained warping associated with a fixed support, stiffener or similar. The aforementioned relevance in obtaining the local stresses correctly, specially in combination with more general inelastic material models as noted above, is of clear practical importance. In this respect, we note the good agreement observed between the solutions obtained with the newly proposed mixed formulation and full three–dimensional finite element simulations even for unrealistically very short shafts, as considered for the range of the length ration L/h for all section topologies.

16. The warping–twist constraint behind the TWKV is effectively reached by the other two formulations (and full three–dimensional simulations for that matter, that is, physically) for open (simply–connected) thin–walled sections as the thickness/height ratio t/h of the cross section is reduced. Hence, the three formulations lead to similar results in the thin limit for this type of sections. Precisely because of that constraint, the effects of restrained warping become important for this type of sections relative to solid sections.

17. On the other hand, for thin–walled sections involving a multiply–connected topology that limit is not attained as the thickness ratio t/h of the cross section reduces. Hence, closed (hollow) thin–walled sections, as well as general solid sections, are modeled much better by the proposed mixed formulation. This distinct limit behavior for the different types of cross sections has been clearly observed in the numerical evaluations presented in this paper, and confirmed by the analytical estimates obtained for thin–walled sections presented in Appendix B.

18. Interestingly, the conclusions in the previous two items on the different performance of open and closed sections applies when the section exhibits the so–called primary warping given by the sectorial coordinate along the cross section's wall or only the higher order secondary warping through the thin wall thickness. The numerical results presented here for different particular cross sections, with open or close topologies, involving one or the other warping, corroborate this conclusion, as it does the thin–wall estimates obtained in the analyses included in

Appendix B. All these results and conclusions apply to both single and multiple cell hollow sections, as the developments in this work show.

All these conclusions point to the adequacy of the newly proposed mixed formulation in modeling torsion with restrained warping. Along them, we have identified the extension of the formulation to nonlinear models as being of major interest, including the consideration of inelastic material responses. In fact, this is one of our motivations in considering general distributions of the elastic parameters in this work, besides its inherent interest when analyzing composite elastic shafts as also evaluated here.

Similarly, we are considering the extension of the new mixed formulation to general geometrically nonlinear formulations, including it in a general model of curved rods twisting with restrained warping. This includes both its theoretical characterization as well as its computationally implementation, along the lines presented in e.g. Simo & Vu-Quoc [1991], Gruttmann et al. [2000], both based on a RBV treatment of the warping, two representative examples of a widely used option in this nonlinear setting despite the limitations found in this paper. In this respect, both the reduced order of the governing problem noted in Item 6 (thus requiring simpler interpolations of the fields involved) and the noted generality in terms of the distribution of the material properties in all the developments presented here (thus allowing the treatment of more general material models noted above) will help in this endeavor. We plan to present these extensions in future publications.

Appendix A. Some remarks on the finite element approximation of the section constants

The three structural formulations considered in this work involve different warping functions that are the solution of particular boundary–value problems defined on the cross section domain, leading to explicit expressions of the different torsional constants involved for a particular formulation at the structural level as well as to a complete description of the distribution of several quantities on the cross section itself, including the different stresses and warping displacement. We have undertaken the numerical solution of these boundary–value problems through finite element analysis on the plane domains for different types of cross sections, leading to approximations of those warping functions and the resulting torsional constants derived from them. We want to understand better this approximation in this appendix.

Specifically, the direct formulations TWKV and RBV presented in Sections 3 and 4, respectively, require only the Saint–Venant warping function $W_{SV}(x,y)$ solution of the boundary-value problem (33). The mixed formulation in the final form presented in Section 5.2 requires in addition the function $W_\sigma(x,y)$ solution of the boundary–value problem (140) with, in particular, the stress function $\Sigma_\sigma(x,y)$ given by $(149)_2$, thus recovering the Poisson problem (79) in terms of the Saint–Venant warping function $W_{SV}(x,y)$. Note that the original TWKV formulation only requires the second warping function $W_\sigma(x,y)$ to recover the warping shear stresses $\boldsymbol{\tau}_W$ as a post–processing with none of the torsional constants involved in this formulation (namely, J and $I_{W_{SV}}$) depending on this function. The mixed formulation requires instead the evaluation of the torsional constant $I_{\nabla W_\sigma}$ directly related to this warping function by its definition (158), besides those other two section constants. On the other hand, the RBV formulation requires, instead, the gradient section constant $I_{\nabla W_{SV}}$ given by (102).

We approximate the boundary-value problem (33) using the weak form

$$\int_\Omega n_{_G}(x,y)\left(\nabla W_{SV}^h + \mathbb{J}\right)\cdot\nabla(\delta W_{SV}^h)\,d\Omega = 0 \qquad \forall \delta W_{SV}^h \in \mathcal{V}^h\,, \tag{A.1}$$

the space of (finite element) admissible variations $\mathcal{V}^h \subset \mathcal{V} = H^1(\Omega)/\mathbb{R}$, accounting for solutions of the original problem up to a constant. To accomplish this in practice, we fix the value of the function $W_{SV}^h(x,y)$ at one node of the finite element mesh while solving the problem (A.1) for an arbitrary point as center of twist in $\mathbb{J}$, and then obtain the final function and the actual center of twist using relations (48)-(51), and thus imposing the conditions (46) and (47).

We approximate the second boundary-value problem (79) in a similar way, with the weak form

$$\int_\Omega \left[n_{_G}(x,y)\nabla W_\sigma^h\cdot\nabla(\delta W_\sigma^h) + n_{_E}(x,y)\; W_{SV}^h\;\delta W_\sigma^h\right]d\Omega = 0 \quad \forall \delta W_\sigma^h \in \mathcal{V}^h\,, \tag{A.2}$$

for the same finite element approximation $\mathcal{V}^h \subset \mathcal{V} = H^1(\Omega)/\mathbb{R}$. As for the problem (A.1), we solve the finite element problem (A.2) in practice by fixing first the value of the function $W_\sigma^h(x,y)$ at one node of the finite element mesh and then shifting all the computed nodal values by imposing the normalizing condition (154).

Different arguments presented in the paper are based on particular relations between the two warping functions $W_{SV}(x,y)$ and $W_\sigma(x,y)$ that also

apply for their finite element approximations as defined above. In particular, we have:

i. The orthogonality relation (38) follows directly from the weak equation (A.1) by choosing $W^h_{SV}(x,y)$ as variation, a valid choice after having normalized it to have a zero (weighted) average.

ii. The property (159) of the constant $I_{\nabla W_\sigma}$, critical in the argument (160) motivating the warping field $\lambda_\varepsilon(z)$ in the mixed formulation, follows directly for the finite element warping functions in the same way by simply considering $W^h_\sigma(x,y)$ as variation in the weak equation (A.2).

iii. Finally, equation (81) also holds for the discrete functions after combining the weak equations (A.1) and (A.2) with $W^h_\sigma(x,y)$ and $W^h_{SV}(x,y)$ as variations, respectively. Hence, the estimate (187) applies, with the Cauchy–Schwarz part of the argument still applying for the finite element functions, and so are its consequences on the relative strength (186) penalty parameters for the RBV and mixed formulations, on the orderings of the characteristic lengths (189), and the limit flexibilities (197) for all three formulations under study. All these results apply when the section constants obtained in with the considered finite element approximations are involved.

With these results, the final formulations based on the considered finite element approximation of the section problems share the same properties of their continuum forms as elaborated in the main paper. For example, theTWKV and mixed formulations involve section stresses in equilibrium understood in the (finite element) weak sense. Typical considerations in finite element approximations (e.g. the use of full quadratures, approximate domain geometry and so on) apply to all these arguments.

Remark A.1. *It is interesting to observe that the weak form (A.1) corresponds to a finite element approximation of the variational problem consisting in minimizing the functional*

$$J(W) := \int_\Omega n_{_G}(x,y)\,\|\nabla W + \mathbb{J}\|^2\,d\Omega\,, \tag{A.3}$$

among all functions $W(x,y) \in \mathcal{V} = H^1(\Omega)/\mathbb{R}$. Given than the functional (A.3) corresponds to the Saint–Venant torsional constant J as given by (39)

(hence the name employed in (A.3) for the functional), we conclude that the approximate torsional constant $J(W_{SV}^h) := J^h \geq J = J(W_{SV})$ *that is, the considered finite element approximation of the Saint–Venant constant* J^h *is an upper bound of its exact value* J*, a result that can be found in* Washizu *[1982], page 188, for the case of homogeneous sections. This reference also discusses complementary formulations, based on the the well-known Prandtl stress function for the shear stresses on the cross section (*Prandtl *[1903]), obtaining lower bounds of the torsional constant.* □

Remark A.2. *Similarly, the problem (A.2) is the finite element approximation of the minimization of the functional*

$$I_\sigma(W) := \int_\Omega \left[n_{_G}(x,y)\, \|\nabla W\|^2 + 2\; n_{_E}(x,y)\; W_{SV}\; W \right] d\Omega \,, \tag{A.4}$$

among all functions $W(x,y) \in \mathcal{V} = H^1(\Omega)/\mathbb{R}$*. For the actual solution of the continuum problem* $W_\sigma(x,y)$*, we actually have*

$$I_\sigma(W_\sigma) = -\int_\Omega n_{_G}(x,y)\;\; \|\nabla W_\sigma\|^2 \, d\Omega = -I_{\nabla W_\sigma} \tag{A.5}$$

and similarly $I_\sigma(W_\sigma^h) = -I_{\nabla W_\sigma}^h$*, involving now the discrete approximation* $W_{SV}^h(x,y)$ *in its definition. Neglecting this approximation (and, again, typical finite element approximations like the domain geometry and numerical integration), we conclude that* $I_{\nabla W_\sigma}^h \leq I_{\nabla W_\sigma}$*, i.e., a lower bound in this case.* □

Appendix B. Estimates of the torsional constants for thin–walled sections

The developments presented in this work do not rely on explicit formulas for the different torsional constant describing the response of the particular cross section under consideration. Instead, we calculate them from the warping functions $W_{SV}(x,y)$ and $W_\sigma(x,y)$ obtained by solving the corresponding boundary–value problems on the given cross section. The generality and added accuracy of this approach makes it interesting in our opinion. Furthermore, the availability of those functions allow a complete evaluation of the stresses and warping distributions on the cross sections.

Still, it is convenient to have estimates of those constants in particular cases, for their practical use and for the evaluation of the considerations presented in this work. A typical example is the case of thin–walled sections, in

the different configurations considered in the paper. Estimates for the Saint –Venant torsional constant $J^{(thin)}$ and the warping constant $I_{W_{SV}}^{(thin)}$ in that thin–wall limit can be broadly found in the literature; see e.g. the monographs Oden & Ripperger [1981] and Gjelsvik [1981], or handbooks like Young et al. [2012], among many others.

Notwithstanding, the section constants $I_{\nabla W_{SV}}$ and $I_{\nabla W_\sigma}$ that appear in our developments are new to the best of our knowledge, so having similar estimates $I_{\nabla W_{SV}}^{(thin)}$ and $I_{\nabla W_\sigma}^{(thin)}$ in the thin–wall limit is of practical interest too. We present next these estimates for the different cross sections studied in the main paper. We consider homogeneous sections (i.e. $n_{_E}(x,y) = n_{_G}(x,y) = 1$) in all cases.

Appendix B.1. Estimates for a thin rectangular section

Even though we do not explore the full thin–wall limit in the results presented in Section 7.1 for a solid rectangular section, estimates for the different torsional constants are still of interest given their use in the analysis of other sections presented below. In particular, we have the well–known, broadly–used values

$$J^{(thin)} = \frac{1}{3} h\, t^3 \,, \qquad \text{and} \qquad I_{W_{SV}}^{(thin)} = \frac{h^3\, t^3}{144} \,, \tag{B.1}$$

for the Saint–Venant torsional constant and warping constant, respectively. Referring to Figure 2, the thickness parameter corresponds to the length t, so $t \ll h$ is assumed in these values and all the formulas to follow.

In the thin–wall limit behind the formulas (B.1), an estimate for the Saint –Venant warping function solving the boundary–value problem (33) is given by the bilinear function

$$W_{SV}^{(thin)}(s,n) = s\, n \,, \tag{B.2}$$

for the Cartesian coordinates (s,n) corresponding to the distance s along the middle line for the long side of the rectangle and the perpendicular thickness direction n, both measured from the center of the rectangle; see Figure 2. The function (B.2) is a common consideration for thin rectangles; see e.g. Gjelsvik [1981], page 69, among others. It can be easily seen to satisfy exactly the differential equation and the Neumann boundary conditions along the long side of the rectangle for the problem (33), but only approximately to order $o(t/h)$ for the same boundary conditions along the short side of the rectangle, including its corners. In this respect, see Remark B.1 below. We

note that the bilinear function (B.2) can indeed be guessed when observing the computed Saint–Venant warping functions in Figure 3.

Given the function (B.2), we easily obtain

$$I_{\nabla W_{SV}}^{(thin)} = \frac{h^3\, t}{12} \left[1.0 + \left(\frac{t}{h} \right)^2 \right] , \tag{B.3}$$

for the gradient constant $I_{\nabla W_{SV}} = \int_\Omega n_{_G} \|\nabla W_{SV}\|^2 d\Omega$ in (102). Note that, as opposed to the traditional torsional constants (B.1) of order $o((t/h)^3)$, the new constant (B.3) is of order $o(t/h)$. As developed in the following sections, this observation has important consequences in the estimation of this constant in more general sections, as different contributions to the warping displacement of the cross section will lead to terms of the same order.

The second gradient constant $I_{\nabla W_\sigma} = \int_\Omega n_{_G} \|\nabla W_\sigma\|^2 d\Omega$ in (158) can be written as

$$I_{\nabla W_\sigma}^{(thin)} = \frac{h^3\, t^5}{1440} \left[1.0 + \frac{51}{42} \left(\frac{t}{h} \right)^2 \right] , \tag{B.4}$$

after estimating the second warping function as

$$W_\sigma^{(thin)}(s,n) = \frac{s\, n}{8} \left(\frac{4}{3} n^2 - t^2 \right) , \tag{B.5}$$

in the thin limit $t \ll h$. This function is motivated by considering the thickness direction n as dominant in the thin–wall limit of the Poisson problem (79) with the source function (B.2). The cubic dependence n^3 through the thickness can clearly be observed in the actual computed solution of the exact Poisson problem in Figure 3 for small t/h aspect ratios.

Remark B.1. *As noted above, the limit function (B.2) only satisfies approximately the boundary conditions along the short sides of the rectangle. It leads to the classical approximation of linear shear stresses through the thickness in the direction along the now wall. It is well–known that these shear stresses only account for half the torque acting on the section, a result that goes back to Kelvin and Tait (see* Thompson & Tait *[1903], page 267), so it requires the consideration of additional transversal point loads at those ends of the rectangular cross section in the thin limit. It also requires the introduction of an additional constant shear flow through–the–thickness, of lower order $o(t^2)$, for a more general curved open thin–walled section; see* Popov *[1970] for details, and to* Davini et al. *[2008] for a modern treatment in the context of*

$\Gamma-$*convergence. In fact, these considerations apply not only to the wall ends but also to wall junctions, as they occur in the other sections considered below, where the considered limit estimates for the warping functions will show discontinuities. This level of detail has no direct consequence in this work and, hence, avoided in this appendix; recall also that the estimates presented here only provide an added verification of the values obtained from solving the exact problems. Nevertheless, we refer to the monograph by* Gjelsvik *[1981] were these considerations are nicely accounted by treating the thin walls as plates/shells with junctions. One consequence of these arguments worth noting, though, for our purposes here is that the limit function (B.2) does not lead to the torsional constant estimate* $J^{(thin)}$ *in* $(B.1)_1$ *when combined with formula* $(39)_1$ *for the Saint–Venant torsional constant* J*, namely,* $J = \int_\Omega n_{_G}(\nabla W_{_{SV}} + \mathbb{J}) \cdot \mathbb{J}\, d\Omega$*. This formula just leads to half the value* $(B.1)_1$ *if used with the approximate Saint–Venant function (B.2), since the formula is a direct moment balance of those linear shear stresses in the thin–wall limit, missing those end contributions . Interestingly, the alternative expression* $(39)_2$*, that is,* $J = \int_\Omega n_{_G} \|\nabla W_{_{SV}} + \mathbb{J}\|^2 d\Omega$*, does lead to the correct value* $(B.1)_1$ *for the Saint–Venant torsional constant estimate* $J^{(thin)}$*. Not surprisingly, the equality in equation (39) relies crucially on* $W_{_{SV}}(x, y)$ *being an exact solution of the problem (33). The correct warping constant is obtained correctly by the formula (64), that is,* $I^{(thin)}_{W_{SV}} = \int_\Omega n_{_E} (W^{(thin)}_{SV})^2 d\Omega$*.* □

Remark B.2. *The availability of the thin–wall estimates presented in this section allows to estimate the relative stiffness of the RBV and mixed formulations in imposing the kinematic warping–twist constraint behind the TWKV formulation. Namely, we can estimate the penalty parameters*

$$\left(\kappa_t^{(RBV)}\right)^{(thin)} = \frac{I^{(thin)}_{\nabla W_{SV}}}{J^{(thin)}} = \frac{1}{4}\left(\frac{t}{h}\right)^{-2}\left[1 + \left(\frac{t}{h}\right)^2\right] , \tag{B.6}$$

for the RBV formulation, confirming that $\kappa_t^{(RBV)} \to \infty$ *as* $t/h \to 0$*, and*

$$\left(\kappa_t^{(MIX)}\right)^{(thin)} = \frac{\left(I_{W_{SV}}\right)^2}{J^{(thin)}\, I^{(thin)}_{\nabla W_\sigma}} = \frac{5}{24}\left(\frac{t}{h}\right)^{-2}\left[1 + \frac{51}{42}\left(\frac{t}{h}\right)^2\right]^{-1} , \tag{B.7}$$

for the mixed formulation, so $\kappa_t^{(MIX)} \to \infty$ *as* $t/h \to 0$ *too. With these*

results, we conclude that

$$\frac{\left(\kappa_t^{(RBV)}\right)^{(thin)}}{\left(\kappa_t^{(MIX)}\right)^{(thin)}} \longrightarrow \frac{1/4}{5/24} = \frac{6}{5} = 1.20 \qquad as \quad t/h \longrightarrow 0\ , \tag{B.8}$$

confirming the stiffer response of the RBV formulation when compared with the mixed formulation as observed in the numerical evaluations presented in Section 7.1. In fact, given (B.8), we could say that the RBV formulation is 20% *stiffer than the mixed formulation for thin rectangular sections when approaching the constrained TWKV formulation, an over–stiff formulation for finite thickness ratios* t/h *as observed in the main paper.* □

Appendix B.2. Estimates for an open thin–walled channel section

Open thin–walled sections are characterized for showing a large amount of warping in general. This is due to the appearance of the so–called primary warping, characterized by a constant through–the–thickness distribution and a general variation along the middle line of the section's thin wall. Actually, in the thin limit, this variation is given by the sectorial coordinate along the middle line of the section's wall, as originally denoted by Vlasov [1961]. This coordinate corresponds to double the area swept along this line from the center of shear/twist of the section. In fact, the three normalizing conditions (46)-(47) allow to determine that center (the principal pole of the sectorial coordinate) and its principal origin. We refer to Oden & Ripperger [1981] or Gjelsvik [1981], among others, for complete details on these considerations.

In contrast, the warping defined by the limit function (B.2) for the rectangular section is a typical example to the so–called secondary warping, characterized by a linear variation along the thin through–the–thickness direction n. For the rectangular section of the previous section, with the center of twist (principal pole) located along the (straight) axis of the thin rectangle, the primary warping vanishes. This situation resulted, in particular, in the warping constant $I_{W_{SV}}^{(thin)}$ in $(B.1)_2$ of order $o((t/h)^3)$, and the gradient constant $I_{\nabla W_\sigma}^{(thin)}$ in (B.4) of order $o((t/h)^5)$. The cubic order $o((t/h)^3)$ of the Saint–Venant torsional constant $J^{(thin)}$ in $(B.1)_1$ can be seen to be characteristic of open thin–walled sections (as opposed to the closed hollow sections considered in the following sections). We note once more the first order $o(t/h)$ of the first gradient constant $I_{\nabla W_{SV}}^{(thin)}$ in (B.3), despite the fact that the original

rectangular section only shows secondary warping. As a consequence, it is crucial to consider both the primary and secondary warpings in the limit warping functions when estimating this constant $I^{(thin)}_{\nabla W_{SV}}$.

The channel section depicted in Figure 2 exhibits primary warping because, in contrast to the rectangular cross section previously considered, the center of shear/twist is now located out of the wall's middle line and the sectorial coordinate does not vanish identically as in that case. With the help of all these considerations, we can identify the thin limit function

$$W^{(thin)}_{SV}(s,n) = \begin{cases} \bar{x}^{(thin)}_{T}\, s - s\, n & \text{for the web ,} \\ \\ \pm\frac{\bar{h}}{2}\, s - (\bar{x}^{(thin)}_{T} + s)\, n & \text{for the flanges ,} \end{cases} \tag{B.9}$$

with $(+)$ for the top flange, $(-)$ for the bottom flange, all in terms of the wall length coordinate s along the different parts of the wall, normal through–the–thickness coordinate n, and the position of the shear/twist center given by the (positive) distance $\bar{x}^{(thin)}_{T}$ measured from the middle line of the web, all as shown in Figure 2. The normalizing conditions (46) and (47) are satisfied by the function (B.9) if

$$\bar{x}^{(thin)}_{T} = \frac{3\,\bar{b}^2\,t_f}{6\,\bar{b}\,t_f + \bar{h}\,t_w}\ , \tag{B.10}$$

after imposing, in particular, equation $(47)_2$, where we have introduced the lengths $\bar{h} := h - t_f$ and $\bar{b} = b - t_w/2$ along the wall middle line. This result locates the center of shear/twist.

Similarly, the function (B.9) leads to

$$J^{(thin)} = \frac{1}{3}\bar{h}\,t_w^3 + \frac{2}{3}\,\bar{b}\,t_f^3\ , \tag{B.11}$$

and

$$\begin{aligned} I^{(thin)}_{W_{SV}} = {} & \frac{\bar{h}^2\,\bar{b}^3\,t_f}{12}\,\frac{2\,\bar{h}\,t_w + 3\,\bar{b}\,t_f}{\bar{h}\,t_w + 6\,\bar{b}\,t_f} \\ & + \frac{t_f^3}{18}\left[\left(\bar{x}^{(thin)}_{T} + \bar{b}\right)^3 - \left(\bar{x}^{(thin)}_{T}\right)^3\right] + \frac{\bar{h}^3\,t_w^3}{144}\ , \end{aligned} \tag{B.12}$$

for the Saint–Venant torsional constant and the warping constant, respectively, in the thin–wall limit $t/h \to 0$ as it can be found in the literature,

at least for the principal part of the latter; see e.g. YOUNG ET AL. [2012] (page 430). The limit warping function (B.9) considers both the primary and secondary warping contributions, the latter given by the terms linear in the thickness coordinate n resulting in the two last contributions to the warping constant $I_{W_{SV}}^{(thin)}$ in (B.12). Note the higher order $o((t/h)^3)$ nature of these terms, similar to the term obtained for the rectangular section in (B.1), but opposed to the $o(t/h)$ contribution of the primary sectorial coordinate, now the leading contribution to the warping constant. We have included the thin–wall estimates (B.11) and (B.12) in the plots of the computed torsional constants in Figure 17, observing a very good agreement with those computed value based on the exact governing problem. We consider the case $t_f = t_w = t$ in the main paper.

As justified above, the reason for considering both the primary and secondary warpings in the limit function (B.9) is the evaluation of the thin–wall estimate of the new gradient torsional constant $I_{\nabla W_{SV}}$, not found in the literature. Proceeding with the gradient of that function and some straightforward manipulations, we obtain

$$
\begin{aligned}
I_{\nabla W_{SV}}^{(thin)} = & \frac{\bar{h}^3\, t_w}{12} + \frac{\bar{h}}{3}\left[\left(\bar{x}_{_T}^{(thin)} + \frac{t_w}{2}\right)^3 - \left(\bar{x}_{_T}^{(thin)} - \frac{t_w}{2}\right)^3\right] \\
& + \frac{\bar{b}}{12}\left[\left(\bar{h} + t_f\right)^3 - \left(\bar{h} - t_f\right)^3\right] \\
& + \frac{2\, t_f}{3}\left[\left(\bar{x}_{_T}^{(thin)} + \bar{b}\right)^3 - \left(\bar{x}_{_T}^{(thin)}\right)^3\right] \,. \qquad \text{(B.13)}
\end{aligned}
$$

If one only considers the primary sectorial contribution to the limit warping function (B.9), a simple calculation shows that this gradient constant would reduce to

$$
I_{\nabla W_{SV}}^{(thin^P)} = \left(\bar{x}_{_T}^{(thin)}\right)^2 \bar{h}\, t_w + \frac{1}{2}\bar{h}^2\, \bar{b}\, t_f \,, \qquad \text{(B.14)}
$$

which provides a poor thin–wall estimate. The secondary warping leads to contributions of order $o(t/h)$, missing in (B.14). We have seen this discrepancy when comparing these estimated values with the exactly computed values. Indeed, we have included the full thin–wall estimate (B.13) in the plot for that constant in Figure 17. The good agreement of the full estimate $I_{\nabla W_{SV}}^{(thin)}$ in (B.13) with the computed values of $I_{\nabla W_{SV}}$ is apparent in the whole range of aspect ratios t/h considered.

Finally, based on the warping function (B.9) as the source term in the Poisson problem (79) we can estimate the second warping function $W_\sigma^{(thin)}(s,n)$, with the linear terms in s of $W_{SV}^{(thin)}(s,n)$ leading to cubic s^3 distributions along the different parts of the wall, matched at the junctions; further details are omitted. This allows to obtain the thin–wall estimate of the second gradient torsional constant

$$I_{\nabla W_\sigma} = \frac{\bar{b}\,t_w}{4}\left[\frac{\bar{b}^4}{80}\left(\bar{x}_{_T}^{(thin)}\right)^2 + 4\,C_{_1}^2 + \frac{\bar{x}_{_T}^{(thin)}\,\bar{b}^2}{3}C_{_1}\right] + \frac{\bar{h}^2\,\bar{b}^3}{24}\left[\frac{8}{5}\bar{b}^2 + 4\left(\bar{x}_{_T}^{(thin)}\right)^2 - 5\bar{b}\bar{x}_{_T}^{(thin)}\right] , \tag{B.15}$$

for

$$C_{_1} := \frac{\bar{h}}{4}\left[\bar{b}^2 - 2\,\bar{b}\,\bar{x}_{_T}^{(thin)} - \frac{1}{2}\,\bar{h}\,\bar{x}_{_T}^{(thin)}\right] , \tag{B.16}$$

with $\bar{x}_{_T}^{(thin)}$ given in turn by formula (B.10). Here, we have neglected the secondary warping in the estimated thin–wall limit for the Saint–Venant warping function in (B.9) (the bilinear term $s\,n$). It results in high–order terms in the thickness in this case. As illustrated in the corresponding plot in Figure 17, the estimate (B.15) shows a good agreement with the computed values based on the finite element solution of the exact boundary–value problem (with the finite element solution of the exact Saint–Venant warping function $W_{SV}(x,y)$ as well).

Remark B.3. *Evaluating the penalty parameter κ_t as in Remark B.2 but for the channel cross section considered in the main paper (with $b = 0.4h$ and $t_f = t_w = t$), we obtain*

$$\left(\kappa_t^{(RBV)}\right)^{(thin)} \sim 0.67842\left(\frac{t}{h}\right)^{-2} \qquad as \quad t/h \longrightarrow 0\,, \tag{B.17}$$

and

$$\left(\kappa_t^{(MIX)}\right)^{(thin)} \sim 0.24702\left(\frac{t}{h}\right)^{-2} \qquad as \quad t/h \longrightarrow 0\,. \tag{B.18}$$

Note that we have the same order for the penalty parameter $\kappa_t \sim (t/h)^{-2} \to \infty$ as $t/h \to 0$ as for the rectangular cross section in Remark B.2 even though

the order of several of the sections constants in (t/h) *differs. Given the results (B.17)-(B.18), we conclude that*

$$\left(\kappa_t^{(RBV)}\right)^{(thin)} \Big/ \left(\kappa_t^{(MIX)}\right)^{(thin)} \longrightarrow 2.7464 \qquad as \quad t/h \longrightarrow 0 \,, \tag{B.19}$$

that is, the RBV formulation is close to three times stiffer than the mixed formulation in approaching the constrained TWKV formulation for the considered open channel section, a cross section with dominant primary warping. These estimates agree well with the computed values for the exact problem reported in Figure 19. Indeed, for the lowest thickness ratio considered in that figure, $t/h = 10^{-2}$*, we obtain*

$$\kappa_t^{(RBV)} = 0.66051 \cdot 10^4 \,, \qquad and \qquad \kappa_t^{(MIX)} = 0.24412 \cdot 10^4 \,, \tag{B.20}$$

so

$$\kappa_t^{(RBV)} \Big/ \kappa_t^{(MIX)} = 2.7056 \,, \tag{B.21}$$

computed values that show a very good agreement with the estimated values (B.17) to (B.19). The high order of magnitude of the values (B.20) indicates the role of the parameter κ_t *as a penalty parameter imposing the warping–twist constraint for this type of sections as shown in the paper, in contrast of the closed thin–walled sections considered next.* □

Appendix B.3. Estimates for a closed thin–walled box section

The thin–wall limit approximation of the Saint–Venant warping function for closed hollow sections involves a correction of the middle line's sectorial coordinate accounting for the now constant shear flow across the thickness of the wall in that limit; see e.g. Gjelsvik [1981], page 100. For the single–cell box cross sections considered in Section 7.3, the final limit function can be written as

$$W_{SV}^{(thin)}(s,n) = \begin{cases} \frac{\bar{b}}{2}\,\beta\, s - s\, n & \text{for the left/right webs} \,, \\ \\ -\frac{\bar{h}}{2}\,\beta\, s - s\, n & \text{for the top/bottom flanges} \,, \end{cases} \tag{B.22}$$

referring to the sketch of the section in Figure 2, including the definition of the (s,n) coordinates along the middle line of each wall, and corresponding lengths $\bar{h} := b - t_f$ and $\bar{b} := b - t_w$. The coordinate n refers again to the thickness direction, with s being measured along the wall. In (B.22) we

have considered both that primary (sectorial) warping and the secondary (thickness) warping of the section, corresponding to the first and second terms in $W_{SV}^{(thin)}(s,n)$, respectively.

In particular, the primary warping contribution is proportional to the non–dimensional factor β given by

$$\beta := \frac{\bar{h}\ t_f - \bar{b}\ t_w}{\bar{h}\ t_f + \bar{b}\ t_w}\ . \tag{B.23}$$

In this way, for the first considered cross section in Section 7.3 with $b = h$ and $t_f = t_w$, we have $\beta = 0$, that is, the section develops no primary warping, a Neuber tube as referred to in the main paper. We can observe that the computed exact functions $W_{SV}(x,y)$ matches these considerations for the thin cross sections considered in Section 7.3. Note how the elevation plots of this function shown in Figure 29 for the Neuber tube $t_f = t_w$ (with $b = h$) converges to the characteristic bilinear distribution of the secondary warping $\beta = 0$ in (B.22). This situation is to be contrasted with the corresponding plots in Figure 30 for the section with $t_f = 2t_w$, showing clearly the computed warping functions $W_{SV}(x,y)$ having a thin–wall limit with a linear distribution along the walls strongly dominating the whole distribution, the primary warping $\beta \neq 0$ in (B.22).

Based on the function (B.22), we can directly obtain the thin–wall limit estimates

$$J^{(thin)} = \frac{2\,\bar{b}^2\,\bar{h}^2}{\bar{b}/t_f + \bar{h}/t_w} + \frac{2}{3}\,\bar{h}\,t_w^3 + \frac{2}{3}\,\bar{b}\,t_f^3\ , \tag{B.24}$$

for the Saint–Venant torsional constant ($J^{(thin)} = \int_\Omega n_{_G}\,\|\nabla W_{SV}^{(thin)} + \mathbb{J}\|^2 d\Omega$),

$$I_{W_{SV}}^{(thin)} = \frac{1}{24}\,\beta^2\,\bar{b}^2\,\bar{h}^2\,\left(\bar{h}\,t_w + \bar{b}\,t_f\right) + \frac{1}{72}\,\left(\bar{h}^3\,t_w^3 + \bar{b}^3\,t_f^3\right)\ , \tag{B.25}$$

for the warping constant ($I_{W_{SV}}^{(thin)} = \int_\Omega n_{_E}\,(W_{SV}^{(thin)})^2 d\Omega$), and

$$\begin{aligned} I_{\nabla W_{SV}}^{(thin)} &= \frac{1}{2}\,\beta^2\,\bar{h}\,\bar{b}\,\left(\bar{h}\,t_f + \bar{b}^2\,t_w\right) \qquad \text{(primary warping contrib.)} \\ &+ \frac{1}{6}\,\left(\bar{h}^3\,t_w + \bar{b}^3 t_f\right) + \frac{1}{6}\,\bar{h}\,t_w^3 + \frac{1}{6}\,\bar{b}\,t_f^3\ , \end{aligned} \tag{B.26}$$

for the first gradient constant ($I_{\nabla W_{SV}}^{(thin)} = \int_\Omega n_{_E}\,|\nabla W_{SV}^{(thin)}\|^2 d\Omega$). In particular, we recognize the well–known (second) Bredt's formula (Bredt [1896])

$$J_{Bredt}^{(thin)} = \frac{4\text{Ⓐ}^2}{\oint ds/t(s)}\ , \tag{B.27}$$

(with Ⓐ = area enclosed by the middle line loop) for the Saint–Venant torsional constant of closed single–cell sections in the first term of the estimate (B.24). It captures the leading linear order $o(t/h)$ in the thickness as $t/h \to 0$ for closed hollow sections. The last two terms in the estimate (B.24) for $J^{(thin)}$ are higher order $o((t/h)^3)$ corrections arising from the considered secondary thickness warping, terms which are usually neglected in practice. Note that they simply correspond to the contributions of the thin rectangle defining each wall following the estimate $(B.1)_1$ for a single thin rectangle. The plots of the Saint–Venant torsional constant in Figures 31 and 32 incorporate these higher–order terms for the thin–wall estimate $J^{(thin)}$, leading to a slightly better matching with the computed values based on the exact problem for the larger values in the considered range of t/h thickness ratios.

The thin–wall estimate (B.25) for the warping constant $I_{W_{SV}}^{(thin)}$ has a similar structure. Its first term, depending on the non–dimensional the parameter β, corresponds to the primary warping and it leads to an order $o(t/h)$ warping constant, whereas the last two terms in that estimate are the higher order $o((t/h)^3)$ contributions of the secondary thickness warping, mimicking again the contributions $(B.1)_2$ for the rectangular portions of the walls. This different nature of the contribution to the limit of the warping constant becomes apparent for the Neuber tubes with vanishing primary warping $\beta = 0$, a situation clearly evident when comparing the values of the computed exact warping constants depicted in Figures 31 and 32 for the sections with $t_f = t_w$ (Neuber) and $t_f = 2t_w$ (non Neuber), respectively.

The main reason why we engage in a discussion of these details is to point out the different nature of the new torsional constant $I_{\nabla W_{SV}}$. As occurred for the cross sections topologies considered in the previous two sections, the secondary warping results in contributions of leading order to this section constant. The first term in the second line of estimate (B.26) is of order $o(t/h)$, the same order as the contributions of the primary warping to that constant in the first line, proportional to the parameter β^2. This explains the response of that constant obtained when solving for its exact values and reflected in Figures 31 and 32. While the plots for the warping constant $I_{W_{SV}}$ and the, next explored, warping gradient constant $I_{\nabla W_\sigma}$ change completely its response as the ratio t/h changes for the two cases considered in those figures (the Neuber case $t_f = t_w$ and $t_f = 2t_w$ respectively), as opposed to the similar response obtained for the gradient formula $I_{\nabla W_{SV}}$ and, for that matter, the Saint–Venant torsional J itself, due to the Bredt's contribution

noted above.

We proceed with the evaluation of the second warping function $W_\sigma^{(thin)}(s,n)$ as before, approximating the Poisson problem (79) by its particularization to the longitudinal s direction, resulting in a cubic variation s^3 along the walls after matching the solution at the different corners. This approach produces the estimate of the second gradient torsional constant $I_{\nabla W_\sigma}$

$$I_{\nabla W_\sigma}^{(thin)} = \frac{\bar{b}^2\,\bar{h}^2}{1440}\,\beta^2\left(\bar{h}\,t_w\,\left(\bar{h}^2\,+5\,\bar{b}^2\right)+\bar{b}\,t_f\,\left(\bar{b}^2\,+5\,\bar{h}^2\right)\right), \tag{B.28}$$

when primary warping is present, that is, when $\beta \neq 0$ in (B.22). We have neglected the secondary warping (second term in this last equation) in the thin estimate (B.28). It agrees well with the computed solutions of the exact problem as shown in Figure 32 for the section with $t_f = 2t_w$ experiencing that primary warping ($\beta \neq 0$).

We treat the Neuber tube $t_f = t_w = t$, $b = h$ (so $\beta = 0$) separately, accounting for the secondary warping in (B.22) (the bilinear ($s\,n$ term), the only one present in the thin–wall limit for this cross section. Note that this is a discontinuous function, exhibiting jumps at the corners ranging in value as $[\![W_{SV}]\!] = \pm\bar{h}\,t/2$. Restricting the problem again along the dominant longitudinal direction along the walls, we obtain the estimate

$$I_{\nabla W_\sigma}^{(thin)} = \frac{\bar{h}^5\,t^3}{2160} \qquad \text{for} \quad t_f = t_w = t\ ,\ b = h \quad (\text{so } \beta = 0)\ , \tag{B.29}$$

which we have also included in the corresponding plot of Figure 31. As it can be observed in this figure, it shows a good agreement with the values computed from the exact problems. Note that this estimate is of order $o((t/h)^3)$ so it does not affect the leading term of order $o(t/h)$ for the predicted value (B.28) when primary warping is present (i.e. $\beta \neq 0$), as seen in the good matching with the computed value in the corresponding plot of Figure 32, and so it happens in Figure 17 for the channel section which also involves a discontinuous secondary warping in (B.9) at the wall corners.

Remark B.4. *The numerical results presented in Section 7.3 for the closed box section of interest here have shown that the thin–wall limit does not make neither the RBV nor the mixed formulations approach the constrained TWKV. As depicted in Figure 49, the parameter κ_t driving this limiting process remains finite for all t/h, small values in particular, for both formulations. It even vanishes as $t/h \to 0$ for the mixed formulation in the case of*

a Neuber tube. All these observations are confirmed by the estimates derived above. In particular, we have:

i. *The two section constants driving the RBV, with* $\kappa_t^{(RBV)} = I_{\nabla W_{SV}}/J$, *remain of the same order (*$\sim h^3 t$ *so* $\kappa_t^{(RBV)} \sim$ *finite), in the presence or not of primary warping. Even when no warping occurs, the Saint–Venant constant* J *is dominated by the twisting itself (the* $\mathbb{J}$ *term alone in its definition* $J = \int n_G \|\nabla W_{SV} + \mathbb{J}\|^2 d\Omega$*), as it happens with the basic circular sections exhibiting no warping whatsoever. Remarkably, the new constant* $I_{\nabla W_{SV}}$ *is affected by the secondary thickness warping in its leading terms so it exhibits the same order. In this way, the estimates obtained above show that*

$$\left.\begin{aligned} \left(\kappa_t^{(RBV)}\right)^{(thin)} &\sim \frac{1}{3} \qquad as\ t/h \to 0 \quad (case\ t_f = t_w = t)\ , \\ \left(\kappa_t^{(RBV)}\right)^{(thin)} &\sim \frac{1}{2} \qquad as\ t/h \to 0 \quad (case\ t_f = 2t_w = 2t)\ , \end{aligned}\right\} \tag{B.30}$$

both being finite values ($b = h$ *in both cases).*

ii. *The response of the mixed formulation, driven by the parameter* $\kappa_t^{(MIX)} = I_{W_{SV}}^2/(J I_{\nabla W_\sigma})$ *is more involved, and it depends on the presence of primary warping or not. A similar calculation with the thin–wall estimates derived above lead to*

$$\left.\begin{aligned} \left(\kappa_t^{(MIX)}\right)^{(thin)} &\sim \frac{5}{3}\left(\frac{t}{h}\right)^2 \qquad as\ t/h \to 0 \quad (case\ t_f = t_w = t)\ , \\ \left(\kappa_t^{(MIX)}\right)^{(thin)} &\sim \frac{5}{48} \qquad\qquad as\ t/h \to 0 \quad (case\ t_f = 2t_w = 2t)\ , \end{aligned}\right\} \tag{B.31}$$

hence vanishing in the limit for the first case (Neuber tube).

iii. *The values (B.30) and (B.31) are to be compared with the values (B.20) for the open channel cross section, confirming the lack of enforcing the warping–twist constraint for the current closed box sections as opposed to the open one. All these estimated limit values agree well with the computed values with the exact problem as shown in Figure 49. Note*

that the RBV always comes stiffer than the mixed formulation with, in particular,

$$\left(\kappa_t^{(RBV)}\right)^{(thin)} \Big/ \left(\kappa_t^{(MIX)}\right)^{(thin)} \longrightarrow 24/5 = 4.80 \qquad as \quad t/h \longrightarrow 0 \ , \tag{B.32}$$

for the case $t_f = 2t_w = 2t$, a value that compares well with the value

$$\kappa_t^{(RBV)} \Big/ \kappa_t^{(MIX)} = 4.8064 \ , \tag{B.33}$$

obtained with the values of the torsional constants computed from the exact problem. □

Appendix B.4. Estimates for a two–cell thin–walled section

The main characteristic of the two–cell section depicted in Figure 2 for the estimates evaluated here is the presence of the semicircular arcs at its sides, thus involving varying arms for their in-plane rotation. The final estimate that we consider for the Saint–Venant warping function in the thin–wall limit can be written as

$$W_{SV}^{(thin)} = \begin{cases} (\hat{F} - \bar{R})\, s - n\, s & \text{for the top/bottom flanges} \ , \\ -\bar{R}\,(\hat{F} - \bar{R})\,\left(\frac{\pi}{2} - \alpha\right) & \\ \quad +b\,\bar{R}\,\cos\alpha - n\,b\,\cos\alpha & \text{for the semicircular wings} \ , \\ -n\, s & \text{for the middle web} \ , \end{cases} \tag{B.34}$$

with

$$\bar{R} := \bar{h}/2 \qquad \text{and} \qquad \hat{F} := \bar{R}\,\frac{4\,b + \pi\,\bar{R}}{2\,b + \pi\,\bar{R}} \ , \tag{B.35}$$

for and the angle α and the coordinates (s, n) along the walls as shown in Figure 2. These expressions involve the lengths measured along the middle line, namely, $\bar{h} = h - t_f$, with R in equation (B.35) corresponding to the radius of the semicircular ends, and $b = h$ for the section under consideration; see Figure 2. The contributions involving the factor $\hat{F}$ in the expressions (B.34)-(B.35) correspond to the aforementioned correction of the sectorial coordinate along the middle line accounting for the constant shear flow through–the–thickness of the wall; see again Gjelsvik [1981] for details.

The limit warping function (B.34) includes the secondary warping given by the terms depending on the thickness direction n, with the remaining terms corresponding to the primary warping. Based on this function, we obtain the thin–wall estimate

$$J^{(thin)} = \frac{2\,\left(2\,b\,\bar{h} + \pi\,\bar{R}^2\right)^2\,t_f}{2\,\bar{b} + \pi\,\bar{R}} + \frac{1}{3}\bar{h}_w\,t_w^3 + \frac{2}{3}\left(2\,b + \pi\,\bar{R}\right)\,t_f^3 - \frac{2}{3}b\,\left(1 - \frac{\pi}{8}\,\frac{b}{\bar{R}}\right)\,t_f^3\,, \tag{B.36}$$

for the Saint–Venant torsional constant,

$$I_{W_{SV}}^{(thin)} = \frac{16}{3}C_2^2\,b^5\,t_f + b^2\,\bar{R}^3\,t_f\,\left(\pi + \frac{2}{3}\pi^3 C_2^2 - 16\,C_2\right) + \frac{b^3\,t_f^3}{9} + \frac{\pi\,b^2\,\bar{R}\,t_f^3}{12} + \frac{\bar{h}^3\,t_w^3}{144}\,, \tag{B.37}$$

where $C_2 := \bar{R}/2\,b + \pi\,\bar{R}$,

$$I_{\nabla W_{SV}}^{(thin)} = \bar{R}^2\,b^2\,\left[\pi + 8\,\pi\,C_3^2 - 16\,C_3\right]\ln\left(\frac{R + t_f/2}{R - t_f/2}\right) + 16\,b^3\,t_f\,C_3^2 + \pi\,b^2\,\bar{R}\,t_f\,\left[1 + \frac{1}{12}\,\left(\frac{t_f}{\bar{R}}\right)^2\right] + \frac{4\,b^3\,t_f}{3}\,\left[1 + \frac{1}{4}\left(\frac{t_f}{b}\right)^2\right] + \frac{\bar{h}_w^3\,t_w}{12}\,\left[1 + \left(\frac{t_w}{\bar{h}_w}\right)^2\right]\,, \tag{B.38}$$

for the first gradient constant, and

$$I_{\nabla W_\sigma}^{(thin)} = 4\,C_4^2\,b^3\,t_f + \frac{4}{5}C_3^2\,b^7\,t_f + \frac{8}{3}\,C_4\,C_3\,b^5\,t_f + \bar{R}^3\,b^2\,t_f\,\left[\frac{\pi^5}{40}\,C_3^2\bar{R}^2 + \pi\,\bar{R}^2 + \frac{2\,\pi}{\bar{R}^2}\,C_5^2 - \frac{\pi^3}{3}\,C_3\,C_5 - 8\,C_5 + 2\,\left(\pi^2 - 8\right)\,C_3\,\bar{R}^2\right]\,, \tag{B.39}$$

with

$$C_4 := \left[\frac{C_3}{3}\,\left(-2\,b^3 - 3\pi\,b^2\,\bar{R} + \frac{\pi^3}{2}\,\bar{R}^3\right) - 2\bar{R}^3\right]\Big/\left(\pi\bar{R} + 2b\right)\,, \tag{B.40}$$

and

$$C_5 := \left[\frac{C_3}{3}\left(-4\,b^3 + \frac{3\pi^2}{2} b\,\bar{R}^2 + \frac{\pi^3}{4}\,\bar{R}^3\right) + 2\bar{R}^3\right] \Big/ \left(\pi\bar{R} + 2b\right) , \qquad \text{(B.41)}$$

for the second gradient constant.

As in the previous cases, we have accounted for both the primary and secondary warpings in the estimates (B.24)-(B.26), and only the primary warping in the estimate (B.28) for $I^{(thin)}_{\nabla W_\sigma}$. The resulting higher order contributions to this estimate follow the same pattern of the estimate (B.3) for a thin rectangle, like the web at the center of the current two–cell hollow section. In all cases, we can observe a very good agreement with the computed values based on the exact problem; see the common plots in Figure 52.

In particular, the estimate $J^{(thin)}$ of the Saint–Venant torsional constant in (B.36) includes in its first and leading term of order $o(t/h)$ the Bredt's theory (extended to multi–cell sections) as in (B.27). The other terms in (B.36) are higher–order corrections (order $o((t/h)^3)$) introduced by the secondary warping. As occurred with the single–cell section cross of the previous section, the first two terms of these high–order corrections can be identified with the usual open (simply–connected) section contribution of the different walls (including the web at the center of the section, which only exhibits this thickness warping by symmetry). Interestingly, we now obtain an additional correcting term due to the curvature of the side walls; note the appearance of $1/\bar{R}$ in the estimate (B.36). All of these correcting terms are of order $(o((t/h)^3)$ in front of the leading Bredt's term of order $o(t/h)$. These terms are neglected in practice and, indeed, make no significant difference in the low range of values t/h considered in Section 7.4. However, we have noticed an improvement when compared with the exact computed values for the larger values of t/h, as it can be verified by the good matching of the two curves in the corresponding plot of Figure 52. Similarly, the contributions of the secondary thickness warping to the warping constant $I^{(thin)}_{W_{SV}}$ can be easily identified with the last three terms of order $o((t/h)^3)$ versus the first ones of order $o(t/h)$.

However, and as occurred for the previous cross sections, the correct estimation of the section constant $I_{\nabla W_{SV}}$ requires the consideration of both primary and secondary warpings. Hence, our consideration of the latter from the beginning even if it may lead to higher order contributions for other constants. Of the five terms of order $o(t/h)$ in the expression (B.38) for $I^{(thin)}_{\nabla W_{SV}}$, only the first two (the first line of this expression) can be traced

to the primary warping alone. Note that the logarithmic term in this last expression can approximated as

$$\int_{R-tt_f/2}^{R-tt_f/2} \frac{dr}{r} = \ln\left(\frac{R+t_f/2}{R-t_f/2}\right) \approx \frac{t_f}{\bar{R}} \tag{B.42}$$

that is, of leading order $o(t/h)$, giving the contribution of the primary warping along the semicircular ends of the cross section. Here, we have used the radial coordinate $r := R - n \in [R - t_f/2, R + t_f/2]$ in those ends, and we have neglected higher–order terms using the similar approximations $\int n/r \; dr \approx 0$ and $\int n^2/r \; dr \approx t_f^3/(12\,R)$ in the evaluation of expression (B.38) for the estimate $I^{(thin)}_{\nabla W_{SV}}$. Again, a good agreement with the values computed with the exact problem can be observed in the plot corresponding to this torsional constant in Figure 52.

The remaining order $o(t/h)$ terms in the estimate (B.38) (lines two and three in this expression) can be traced to the secondary warping in the evaluation of the gradient torsional constant $I_{\nabla W_{SV}}$. Note that this includes a leading order contribution of the web at the center of the section (line three in that estimate), as occurred with the single thin rectangle of Appendix B.1, when it only adds higher order contributions to the other constants, by symmetry. Hence, our interest of considering this two–cell cross section as different to the single–cell cross section of the previous section.

Finally, the estimate of the second gradient constant $I_{\nabla W_\sigma}$ in (B.39) have been obtained after reducing the Poisson problem (79) to the longitudinal direction s, accounting only for the primary terms (terms not dependent in n) in the limit Saint–Venant function (B.34) as we did for the previous cross sections above. A good agreement with the computed values from the exact value reported in Figure 52 can be observed.

Remark B.5. *Given the thin–wall estimates (B.36)-(B.39) for the different torsional constants of the two–cell hollow section under consideration, we obtain the ratio of the κ_t parameters for the RBV and mixed formulations*

$$\frac{\left(\kappa_t^{(RBV)}\right)^{(thin)}}{\left(\kappa_t^{(RBV)}\right)^{(thin)}} = \frac{I^{(thin)}_{\nabla W_{SV}}/J^{(thin)}}{\left(I^{(thin)}_{W_{SV}}\right)^2/(J^{(thin)} I^{(thin)}_{\nabla W_\sigma})} \sim \frac{0.33909}{0.07068} = 4.3999\,, \tag{B.43}$$

as $t/h \to 0$. In both cases, the orders of the different torsional constants involved in their definition match so the individual values of the κ_t remain

finite (and non-zero), indicating again that these formulations do not impose the warping–twist constraint behind the original TWKV formulation. The full three–dimensional simulations presented in the paper indicate that this unconstrained situation is a more realistic modeling for this type of sections. The limit thin–wall estimates agree well with the corresponding values calculated from the sections constants obtained by the FEM solution of the exact problem on the cross section. In particular, we have

$$\frac{\kappa_t^{(RBV)}}{\kappa_t^{(MIX)}} = \frac{0.34058}{0.07312} = 4.4052 \qquad for \quad t/h = 0.01 \ , \tag{B.44}$$

combining the values for the different constants for that low thickness ratio t/h as it can be found in the Table 6. These values give also an estimation of the stiffer response of the RBV formulation over the proposed mixed formulation, not reaching the over–stiff response predicted by the constrained TWKV formulation, an unrealistic situation as indicated above. □

Appendix C. Summary of the theoretical developments

As a quick reference, we present in this appendix a self–contained summary of the main theoretical developments presented in this report. After presenting in Appendix C.1 a brief summary of the basic solution of Saint–Venant torsion with uniform warping underlying all the different formulations considered in this work for restrained working, we include in Appendix C.2 a summary of these formulations in a bullet–list style. In particular, the main equations for the TWKV, RBV and mixed formulations are condensed to three different boxes. Finally, the relation among these three formulations, especially as it refers to the underlying warping–twist constraint, is taken briefly in Appendix C.3. The setup and notation introduced in the main report is considered throughout all the expressions in this appendix including, in particular the Cartesian system with the shaft's axis along the z direction and cross sections Ω in the $x - y$ plane.

Appendix C.1. The Saint–Venant problem in torsion and its basic solution

The first fundamental assumption reducing the three–dimensional problem defined by the prismatic elastic shafts to the structural models of interest here is the consideration of the cross sections Ω infinitesimally rotating rigidly in their planes about the shaft's axis z by the amount $\phi(z)$ the twist rotation.

This implies that the in–plane coordinates of the infinitesimal displacements $\boldsymbol{u}_{(x,y)} = [u_x, u_y]^T$ can be written as

$$\boldsymbol{u}_{(x,y)} = \phi(z)\,\mathbb{J}(x,y) \qquad \text{where} \quad \mathbb{J}(x,y) := \begin{bmatrix} -(y-\bar{y}_{_T}) \\ (x-\bar{x}_{_T}) \end{bmatrix} , \tag{C.1}$$

for the center of twist $\bar{\boldsymbol{x}}_{_T} = (\bar{x}_{_T}, \bar{y}_{_T})$ defined by the relations in Remark C.1 below. As in the main report, here and in all what follows we consider the common assumption of small infinitesimal displacements and strains.

Clearly, it remains to define third component of the displacement $u_z(x, y, z)$, the warping displacement. Basic Saint–Venant torsion, involving a uniform warping along the shaft, is recovered by considering

$$u_z(x,y,z) = \overline{\phi'}\; W_{_{SV}}(x,y)\;, \qquad \phi'(z) = \overline{\phi'} = \text{constant rate of twist}, \tag{C.2}$$

independent of the axial coordinate z (here $(\cdot)' := d(\cdot)/dz$), where we have introduced the Saint–Venant function $W_{_{SV}}(x,y)$ defined on the cross section by the (weighted) Laplacian problem

$$\left.\begin{aligned} \nabla\cdot\big(n_{_G}(x,y)\;\big(\nabla W_{_{SV}} + \mathbb{J}\big)\big) = 0 \quad \text{in } \Omega\;, \\ \big(\nabla W_{_{SV}} + \mathbb{J}\big)\cdot\boldsymbol{\nu} = 0 \quad \text{along } \partial\Omega\;, \end{aligned}\right\} \tag{C.3}$$

with the characteristic Neumann boundary condition along the boundary $\partial\Omega$ of the cross section with unit outward normal $\boldsymbol{\nu}$. Here, as in the main preport, $\nabla(\circ)$ denotes the plane gradient operator $\nabla(\cdot)$ in the plane of the cross section Ω, and so is the Euclidean dot product " $\cdot$ " and associated Euclidean norm $\|(\cdot)\|$, as used in what follows.

The solution (C.2) with the particular problem (C.3) defining the shape of the warping distribution given by $W_{_{SV}}(x,y)$ follows from well–known arguments based on the equilibrium of the shear stresses

$$\boldsymbol{\tau}_{_{SV}} = G\,\phi'(z)\;(\nabla W_{_{SV}} + \mathbb{J}) = n_{_G}(x,y)\,\frac{T_{_{SV}}(z)\;(\nabla W_{_{SV}} + \mathbb{J})}{J}\;, \tag{C.4}$$

where $\phi'(z) = \overline{\phi'}$ for the basic Saint–Venant solution so far, only involving these stresses too. The last expression in this equation introduces the resultant torque of these stresses, the Saint–Venant torque $T_{_{SV}}(z)$ (again all the internal torque $T(z)$ so far), given by

$$T_{_{SV}}(z) = \int_\Omega \boldsymbol{\tau}_{_{SV}}\cdot\mathbb{J}\,d\Omega = \int_\Omega \boldsymbol{\tau}_{_{SV}}\cdot(\nabla W_{_{SV}} + \mathbb{J})\;d\Omega = \bar{G}\;J\;\phi'(z)\;, \tag{C.5}$$

for the Saint–Venant torsional constant

$$J := \int_\Omega n_{_G}\,(\nabla W_{_{SV}} + \mathbb{J}) \cdot \mathbb{J}\; d\Omega = \int_\Omega n_{_G} \|\nabla W_{_{SV}} + \mathbb{J}\|^2\; d\Omega > 0\;. \tag{C.6}$$

The equality between these two expressions of J, as it does for the second equality in (C.4), follows from the orthogonality relation $\int_\Omega n_{_G}\,(\nabla W_{_{SV}} + \mathbb{J}) \cdot \nabla W_{_{SV}}\, d\Omega = 0$, a direct consequence of the relations (C.3) defining the Saint–Venant function $W_{_{SV}}(x,y)$. We have kept a general dependence on z in the expressions (C.4) and (C.6), even though the quantities involved are constant along the shaft in this basic Saint–Venant solution, because the same expressions apply in this general form in all three formulations of restrained warping considered next.

Remark C.1. *The Neumann problem (C.3) defines the Saint–Venant function $W_{_{SV}}(x,y)$ up to an additive constant and up to the values of the two coordinates of the center of twist $\bar{\boldsymbol{x}}_{_T} = [\bar{x}_{_T}, \bar{y}_{_T}]^T$. In fact, none of these three values are relevant to the basic Saint–Venant solution considered so far, but need to be specified in the solution with restrained warping discussed next. As motivated below, we need to impose the relations*

$$\int_\Omega n_{_E}(x,y)\, W_{_{SV}}(x,y)\, d\Omega = 0\;, \tag{C.7}$$

and

$$\int_\Omega x_{_E}\, n_{_E}(x,y)\, W_{_{SV}}(x,y)\, d\Omega = \int_\Omega y_{_E}\, n_{_E}(x,y)\, W_{_{SV}}(x,y)\, d\Omega = 0\;, \tag{C.8}$$

where we use, without loss of generality here, the shifted coordinates $\boldsymbol{x}_{_E} := [x_{_E}, y_{_E}]^T := [x - \bar{x}_{_E}, y - \bar{y}_{_E}]^T$ for the centroid of the Young modulus distribution $\bar{\boldsymbol{x}}_{_E} = (\int n_{_E} \boldsymbol{x}\, d\Omega)/A_{n_{_E}}$, for the weighted area $A_{n_{_E}} := \int_\Omega n_{_E}(x,y)\; d\Omega$. The center of twist can then be found by imposing the relations (C.8), resulting in

$$\bar{\boldsymbol{x}}_{_T} := \bar{\boldsymbol{x}}^*_{_T} + \begin{bmatrix} 0 & -1 \\ 1 & 0 \end{bmatrix} \tilde{\boldsymbol{I}}^{-1} \tilde{\boldsymbol{Q}}\;, \tag{C.9}$$

with

$$\tilde{\boldsymbol{I}} := \int_\Omega \boldsymbol{x}_{_E} \boldsymbol{x}_{_E}^T\, n_{_E}(x,y)\, d\Omega\;,\;\; \textit{and} \quad \tilde{\boldsymbol{Q}} := \int_\Omega \boldsymbol{x}_{_E}\, n_{_E}(x,y)\, W^*_{_{SV}}(x,y)\, d\Omega\;, \tag{C.10}$$

for the solution $W^*_{_{SV}}(x,y)$ of the problem (C.3) with an arbitrary point $\bar{\boldsymbol{x}}^*_{_T}$. As noted in Section 2.4 of the main report, the particular point given by the relations (C.9) corresponds to the shear center of the section Ω too. □

Appendix C.2. Three models of restrained warping in torsion: a summary

The Saint–Venant solution (C.2) assumes a constant rate of twist $\phi'(z) = \overline{\phi'}$ and, consequently, a uniform warping displacement $u_z(x, y, z)$. This is obviously not the general situation. Non–uniform warping occurs when it is restrained by a support as in Figure 1 in page 14, or a stiffener or other mechanism, or simply when a general distributed torque $t_{ex}(z)$ is applied along the shaft. The consideration of a varying warping along the shaft requires an alternative approximation of the axial displacement $u_z(x, y, z)$ and of the associated axial normal strain ε_z ($= u_z'$ or its approximation) and the resulting normal stress σ_z. Different approximations lead to specific structural formulations of restrained warping in torsion.

With the normal stress σ_z, a new component of the total shear stress $\boldsymbol{\tau}$ and corresponding stress resultants appear as direct consequence of the restrained warping. The best way to introduce these new quantities is to observe the algebraic decomposition

$$T(z) = \int_\Omega \boldsymbol{\tau} \cdot \mathbb{J}\, d\Omega = \underbrace{\int_\Omega \boldsymbol{\tau} \cdot (\nabla W_{SV} + \mathbb{J})\, d\Omega}_{=:T_{SV}(z)} \underbrace{- \int_\Omega \boldsymbol{\tau} \cdot \nabla W_{SV}\, d\Omega}_{=:T_W(z)} , \qquad \text{(C.11)}$$

of the total internal torque $T(z)$ in the Saint–Venant torque already introduced in the previous section, and the new *bishear* $T_W(z)$ (sometimes also referred as the warping torque), together with the *bimoment* $B_W(z)$ defined as

$$B_W(z) := \int_\Omega \sigma_z\, W_{SV}\, d\Omega , \qquad \text{(C.12)}$$

both for the cross section at z. Denoting the warping component of the shear stress by $\boldsymbol{\tau}_W := \boldsymbol{\tau} - \boldsymbol{\tau}_{SV}$ for the Saint–Venant shear stress component $\boldsymbol{\tau}_{SV}$ in (C.4), the definition (C.11) of the bishear $T_W(z)$ leads also to

$$T_W(z) = T(z) - T_{SV}(z) = \int_\Omega \boldsymbol{\tau} \cdot \mathbb{J}\, d\Omega - \int_\Omega \boldsymbol{\tau}_{SV} \cdot \mathbb{J}\, d\Omega = \int_\Omega \boldsymbol{\tau}_W \cdot \mathbb{J}\, d\Omega , \qquad \text{(C.13)}$$

after using the relations $(C.5)_1$ and $(C.11)_1$, that is, the bishear $T_W(z)$ is the resultant torque of the warping shear stresses $\boldsymbol{\tau}_W$.

With the bishear $T_W(z)$ and bimoment $B_W(z)$ now available, the balance between these two new stress resultants is then characterized (and, in general, postulated) at the structural level by the relation

$$T_W(z) = -\frac{d}{dz} B_W(z) , \qquad \text{(C.14)}$$

along the shaft $z \in [0, L]$. This relation follows directly from section stresses satisfying the 3D equilibrium relation

$$\nabla \cdot \boldsymbol{\tau} + \sigma'_z = 0 \quad \text{in } \Omega\,, \quad \text{with} \quad \boldsymbol{\tau} \cdot \boldsymbol{\nu} = 0 \quad \text{along } \partial\Omega\,, \tag{C.15}$$

as a simple use of integration by parts shows together with the definitions (C.11) and (C.12) of $T_W(z)$ and $B_W(z)$, respectively. Note that the three–dimensional equilibrium relations (C.15) do imply the structural equilibrium relation (C.14), but not the other way around, as observed for the stresses in the RBV formulation below. Similarly, we note that we may simply have the warping shear stress $\boldsymbol{\tau}_W$ in (C.15) instead of the total stress $\boldsymbol{\tau}$, since the Saint–Venant component $\boldsymbol{\tau}_{SV}$ is in equilibrium by itself, without any normal stress σ_z. Similarly, $\boldsymbol{\tau}_{SV}$ leads to no bishear $T_W(z)$ given the relation (C.13)

With these general considerations at hand, we have summarized in Boxes C.1, C.2 and C.3 the significant relations associated to the TWKV, RBV and mixed formulations, respectively, the three formulations of interest in this work. Each box starts by identifying the structural fields involved in each formulation, the fundamental assumption in the treatment of the warping displacement $u_z(x, y, z)$ and its relation with the axial strain/stress (the assumed axial strain compatibility), to arrive at the governing equations defining those fields. We also include the resulting expressions for the bimoment and bishear distributions along the shaft (or, simply, their diagrams) as well as the section warping stresses involved, both normal σ_z and shear $\boldsymbol{\tau}_W$. All three formulations share the expressions (C.4) and (C.5) for the Saint–Venant shear stress component $\boldsymbol{\tau}_{SV}$ and its resultant torque $T_{SV}(z)$, respectively. We add the following remarks:

C.1. The TWKV formulation. Box C.1 in page 206 reveals:

C.1.1. The TWKV formulation relies on a single structural field, the twist rotation $\phi(z)$, which defines the warping displacement $u_z(x, y, z)$ as in the basic Saint–Venant solution (C.2), even with a non–constant rate of twist $\phi'(z)$. That is, one assumes equation (Box C.1-1), the *Wagner assumption.*

C.1.2. The only governing equation for the single unknown field $\phi(z)$ is given by equation (Box C.1-3), which is nothing else but the balance of moment equation ($dT/dz + t_{ex}(z) = 0$ for the total torque $T(z) = T_{SV}(z) + T_W(z)$.

Box C.1: Summary of the TWKV formulation

- *Independent structural fields:* $\phi(z)$.
- *Assumed warping displacement:*

$$u_z(x,y,z) = \phi'(z)\, W_{SV}(x,y)\ . \qquad \text{(Box C.1-1)}$$

- *Axial strain/stress:* Strong (pointwise) strain compatibility

$$\varepsilon_z = u'_z = \phi''(z)\, W_{SV}(x,y)\ , \qquad \text{and} \qquad \sigma_z = E\varepsilon_z\ . \qquad \text{(Box C.1-2)}$$

- *Governing equations:* Fourth order differential equation

$$\frac{d}{dz}\left[\bar{G}J\phi'(z) - \frac{d}{dz}\Big(\bar{E}I_{W_{SV}}\phi''(z)\Big)\right] + t_{ex}(z) = 0\ , \qquad \text{(Box C.1-3)}$$

  for the warping constant

$$I_{W_{SV}} := \int_\Omega n_{_E}(x,y)\left(W_{SV}(x,y)\right)^2 d\Omega\ . \qquad \text{(Box C.1-4)}$$

- *Restraining warping boundary condition:* $\phi'(0) = 0$.
- *Stress resultants:* $T_{SV}(z) = \bar{G}\, J\phi'(z)$, and warping resultants

$$B_W(z) = \bar{E}\, I_{W_{SV}}\, \phi''(z) \quad \text{and} \quad T_W(z) = -\frac{d}{dz}B_W(z)\ . \qquad \text{(Box C.1-5)}$$

- *Stresses:* $\boldsymbol{\tau} = \boldsymbol{\tau}_{SV} + \boldsymbol{\tau}_W$, with $\boldsymbol{\tau}_{SV}$ given by (C.4) and

$$\boldsymbol{\tau}_W = n_{_G}(x,y)\,\frac{T_W(z)\,\nabla W_\sigma(x,y)}{I_{W_{SV}}}\ , \qquad \text{(Box C.1-6)}$$

$$\sigma_z = E\,\phi''(z)\,W_{SV}(x,y) = n_{_E}(x,y)\,\frac{B_W(z)\ W_{SV}(x,y)}{I_{W_{SV}}}\ , \qquad \text{(Box C.1-7)}$$

  with $W_\sigma(x,y)$ defined by the Poisson problem

$$\left.\begin{aligned} \nabla\cdot(n_{_G}(x,y)\ \nabla W_\sigma) = n_{_E}(x,y)\ W_{SV}(x,y) \quad &\text{in } \Omega\ , \\ \nabla W_\sigma\cdot\boldsymbol{\nu} = 0 \quad &\text{along } \partial\Omega\ , \end{aligned}\right\} \qquad \text{(Box C.1-8)}$$

  with again $\int_\Omega n_{_E}\, W_\sigma\, d\Omega = 0$ imposed for a unique function.

Box C.2: Summary of the RBV formulation

- *Independent structural fields:* $\phi(z)$, $\lambda(z)$.
- *Assumed warping displacement:*

$$u_z(x,y,z) = \lambda(z)\, W_{SV}(x,y)\ . \qquad \text{(Box C.2-1)}$$

- *Axial strain/stress:* Strong (pointwise) strain compatibility

$$\varepsilon_z = u_z' = \lambda'(z) W_{SV}(x,y)\ , \qquad \text{and} \qquad \sigma_z = E\varepsilon_z\ . \qquad \text{(Box C.2-2)}$$

- *Governing equations:* Second order system of differential equations

$$\left.\begin{aligned} \frac{d}{dz}\left[\bar{G}J\left(\phi'(z) + \frac{I_{\nabla W_{SV}}}{J}\big(\phi'(z)-\lambda(z)\big)\right)\right] + t_{ex}(z) = 0 \\ \frac{d}{dz}\left[\bar{E} I_{W_{SV}} \lambda'(z)\right] + \bar{G} I_{\nabla W_{SV}}\big(\phi'(z)-\lambda(z)\big) = 0 \end{aligned}\right\} \qquad \text{(Box C.2-3)}$$

  for the first gradient section constant

$$I_{\nabla W_{SV}} := \int_\Omega n_{_G}(x,y)\, \|\nabla W_{SV}\|^2 d\Omega > 0\ . \qquad \text{(Box C.2-4)}$$

- *Restraining warping boundary condition:* $\lambda(0) = 0$.
- *Stress resultants:* $T_{SV}(z) = \bar{G}\, J\phi'(z)$, and warping resultants

$$B_W(z) = \bar{E} I_{W_{SV}} \lambda'(z) \quad \text{and} \quad T_W(z) = \bar{G} I_{\nabla W_{SV}}\big(\phi' - \lambda\big)\ . \qquad \text{(Box C.2-5)}$$

- *Stresses:* $\boldsymbol{\tau} = \boldsymbol{\tau}_{SV} + \boldsymbol{\tau}_W$, with $\boldsymbol{\tau}_{SV}$ given by (C.4) and

$$\boldsymbol{\tau}_W = -G\left(\phi' - \lambda\right)\nabla W_{SV} = -n_{_G}(x,y)\,\frac{T_W(z)\nabla W_{SV}(x,y)}{I_{\nabla W_{SV}}}\ , \qquad \text{(Box C.2-6)}$$

$$\sigma_z = E\,\lambda'(z)\, W_{SV}(x,y) = n_{_E}(x,y)\,\frac{B_W(z)\, W_{SV}(x,y)}{I_{W_{SV}}}\ . \qquad \text{(Box C.2-7)}$$

Box C.3: Summary of the mixed formulation

- *Independent structural fields:* $\phi(z)$, $\lambda_\varepsilon(z)$
  and mixed fields $\varepsilon(z)$ and $\sigma(z)$ eliminated locally.

- *Assumed warping displacement:*

$$u_z(x,y,z) = \phi'(z) W_{SV}(x,y) + \frac{I_{W_{SV}}}{I_{\nabla W_\sigma}} \big(\phi'(z) - \lambda_\varepsilon(z)\big) W_\sigma(x,y)\,. \quad \text{(Box C.3-1)}$$

- *Axial strain/stress:* Given by the assumed distributions

$$\varepsilon_z = \varepsilon(z)\, W_{SV}(x,y) \quad \text{and} \quad \sigma_z = \sigma(z)\, n_{_E}(x,y)\, W_{SV}(x,y)\,, \quad \text{(Box C.3-2)}$$

  for the mixed parameters given by $\sigma(z) = \bar{E}\varepsilon(z)$ and by the weak (average) compatibility relation $\varepsilon(z) = \lambda'_\varepsilon(z)$.

- *Governing equations:* Second order system of differential equations

$$\left.\begin{aligned} \frac{d}{dz}\left[\bar{G}J\left(\phi'(z) + \frac{\big(I_{W_{SV}}\big)^2}{J\, I_{\nabla W_\sigma}}\big(\phi'(z) - \lambda(z)\big)\right)\right] + t_{ex}(z) = 0 \\ \frac{d}{dz}\left[\bar{E} I_{W_{SV}} \lambda'_\varepsilon(z)\right] + \bar{G}\frac{\big(I_{W_{SV}}\big)^2}{I_{\nabla W_\sigma}}\,(\phi' - \lambda_\varepsilon) = 0 \end{aligned}\right\} \quad \text{(Box C.3-3)}$$

  for the second gradient section constant

$$I_{\nabla W_\sigma} := \int_\Omega n_{_G}(x,y)\, \|\nabla W_\sigma\|^2 d\Omega > 0\,. \quad \text{(Box C.3-4)}$$

- *Restraining warping boundary condition:* $\lambda_\varepsilon(0) = 0$.

- *Stress resultants:* $T_{SV}(z) = \bar{G}\, J\phi'(z)$, and warping resultants

$$B_W(z) = \bar{E} I_{W_{SV}} \lambda'_\varepsilon(z)\,, \text{ and } T_W(z) = \bar{G}\frac{\big(I_{W_{SV}}\big)^2}{I_{\nabla W_\sigma}}\,(\phi' - \lambda_\varepsilon)\,. \quad \text{(Box C.3-5)}$$

- *Stresses:* $\boldsymbol{\tau} = \boldsymbol{\tau}_{SV} + \boldsymbol{\tau}_W$, with $\boldsymbol{\tau}_{SV}$ given by (C.4) and

$$\boldsymbol{\tau}_W = G\,\frac{I_{W_{SV}}}{I_{\nabla W_\sigma}}\,(\phi' - \lambda_\varepsilon)\,\nabla W_\sigma = n_{_G}(x,y)\,\frac{T_W(z)\nabla W_\sigma(x,y)}{I_{W_{SV}}}\,, \quad \text{(Box C.3-6)}$$

$$\sigma_z = E\,\lambda'_\varepsilon(z)\, W_{SV}(x,y) = n_{_E}(x,y)\,\frac{B_W(z)\, W_{SV}(x,y)}{I_{W_{SV}}}\,. \quad \text{(Box C.3-7)}$$

C.1.3. Besides the Saint–Venant torsion constant J in (C.6), the TWKV formulation (and the remaining two formulations as well) uses the warping constant $I_{W_{SV}}$ defined in (Box C.1-4).

C.1.4. The boundary condition restraining the warping at the shaft's root $z = 0$ is give by $\phi'(0) = 0$, restraining the rate of twist too. As a consequence, the Saint–Venant shear stress component $\boldsymbol{\tau}_{SV}$ in (C.4) vanishes entirely and so is its resultant torque $T_{SV}(0) = 0$, a partial "torque anomaly", in the sense that it is partially resolved by $T_W(0) \neq 0$ (so $T(0) \neq 0$), in general, although it distorts the stress resultants diagrams along the shaft.

C.1.5. The bishear $T_W(z)$ is only defined from the bimoment $B_W(z)$ by the structural equilibrium relation (C.14); see Appendix C.3 below.

C.1.6. Similarly, the associated warping component $\boldsymbol{\tau}_W$ of the shear stresses in (Box C.1-6) are obtained by using the 3D equilibrium relation (C.15) from the normal stress (Box C.1-7). Hence, they are in equilibrium by construction. The explicit expression of the warping shear stress $\boldsymbol{\tau}_W$ uses the new warping function $W_\sigma(x, y)$ defined by the Poisson problem (Box C.1-8).

C.1.7. For the TWKV formulation, the second warping function $W_\sigma(x, y)$ only appears in a post–processing step, in the sense that it is not involved in the governing equation (Box C.1-3) driving the unknown field $\phi(z)$, but only in the evaluation of the full distribution of the warping shear stress component $\boldsymbol{\tau}_W$ in (Box C.1-6). This is not the case for the mixed formulation below where it plays a crucial role at the structural level too. The function $W_\sigma(x, y)$ is not involved in any form in the RBV formulation discussed next.

C.2. The RBV formulation. Box C.2 in page 207 reveals:

C.2.1. The RBV involves an additional independent field $\lambda(z)$besides the twist rotation $\phi(z)$. The new field gives the amplitude of the warping of the cross section by (Box C.2-1), instead of $\phi'(z)$, with still a uniform shape of the distribution on the cross sections along the shaft defined by the Saint–Venant warping function $W_{SV}(z)$. Note that we can associate the new field with the weighted average $\lambda(z) = \left(\int_\Omega u_z W_{SV} d\Omega\right) / I_{W_{SV}}$ too.

C.2.2. The axial strain is still defined strongly (pointwise) by the three–dimensional compatibility relation $\varepsilon_z = u'_z$.

C.2.3. The two governing equations (Box C.2-3) define a second order system of ordinary equations in the fields $\phi(z)$ and $\lambda(z)$). The first of these equations corresponds to the balance of moments along the shaft ($dT/dz + t_{ex}(z) = 0$), while the second equation corresponds to the equilibrium relation $dB_W/dz + T_W(z) = 0$ in (C.14). In contrast to the TWKV formulation, the enforcement of these relations is done separately, with the help of the additional field $\lambda(z)$, reducing the original fourth order differential equation (Box C.1-3) to a second order system of differential equations.

C.2.4. These arguments identify the relations bimoment $B_W(z)$ and bishear $T_W(z)$ in (Box C.2-5), both defined directly in terms of the driving fields $\phi(z)$ and $\lambda(z)$.

C.2.5. In particular, the bishear $T_W(z)$ involves the new gradient torsional constant $I_{\nabla W_{SV}}$ in (Box C.2-4). The formulation still uses the Saint–Venant torsional constant J and the warping constant $I_{W_{SV}}$, given by the original equations (C.6) and (Box C.1-4), respectively.

C.2.6. Restraining the warping at the fixed support at $z = 0$ is accomplished by imposing the boundary condition $\lambda(0) = 0$, independent of the twist rotation $\phi'(z)$ or its rate. This also frees the Saint–Venant shear stress component $\boldsymbol{\tau}_{SV}$ in (C.4) and its resultant torque $T_{SV}(0)$ in (C.5), avoiding altogether the "torque anomaly" pointed in Item C.1.4 for the TWKV formulation.

C.2.7. The warping stresses (Box C.2-6) and (Box C.2-7) are not in equilibrium, in the sense that they not satisfy the 3D equilibrium equation (C.15), but the stress resultants (Box C.2-5) do satisfy the structural balance equation (C.14); see Section 4.3 in the main report for an extended discussion.

C.3. The mixed formulation. Box C.3 in page 208 reveals:

C.3.1. The mixed formulation also considers two basic (displacement–like) structural fields, the twist rotation $\phi(z)$ and an independent warping field $\lambda_\varepsilon(z)$, besides two mixed fields $\varepsilon(z)$ and $\sigma(z)$ defining the axial strain and stress distribution.

C.3.2. Distinctively, the assumed distribution for the warping displacement (Box C.3-1) involves now two separate components, the first one defined in terms of the original Saint–Venant function $W_{SV}(x,y)$ and driven by the twist rotation, while the second depends on the second warping function $W_\sigma(x,y)$ through the new structural independent field $\lambda_\varepsilon(z)$ along the shaft. Different combinations of these components lead to a non–uniform warping displacement along the shaft in form on individual cross sections too.

C.3.3. The specific expression (Box C.3-1) of the warping displacement involves the new section constant $I_{\nabla W_\sigma}$ defined by (Box C.3-4) in terms of the second warping function $W_\sigma(x,y)$ determined by the Poisson problem (Box C.1-8). Given the defining relations in this problem, we obtain $I_{\nabla W_\sigma} = -\int_\Omega n_{_E} W_{SV} W_\sigma d\Omega$ after some straightforward manipulations and integration by parts, assuring that

$$\lambda_\varepsilon(z) = \frac{1}{I_{W_{SV}}} \int_\Omega n_{_E}(x,y) W_{SV}(x,y) u_z(x,y,z) d\Omega \,, \qquad \text{(C.16)}$$

given the combination of torsional section constants in (Box C.3-1). That is, the new field $\lambda_\varepsilon(z)$ corresponds to the weighted average of the warping of the cross section. The average relation (C.16) is similar to the one noted in Item C.2.1 for the field $\lambda(z)$ in the RBV formulation, but in that case this field controls entirely (pointwise) the warping displacement (Box C.2-1) in its only $W_{SV}(x,y)$ component.

C.3.4. In addition, the mixed formulation considers the assumed distributions (Box C.3-2) of the axial strain $\varepsilon_z(x,y,z)$ and stress $\sigma_z(x,y,z)$ in terms of the mixed structural fields $\varepsilon(z)$ and $\sigma(z)$, respectively. Both distributions are of uniform shape along the shaft, given by the Saint–Venant function $W_{SV}(x,y)$. This setting allows the mixed treatment of the axial strain compatibility, which reduces to $\varepsilon(z) = \lambda'_\varepsilon(z)$, thus holding in average since we also have $\varepsilon(z) = (\int_\Omega n_{_E} W_{SV} \varepsilon_z d\Omega)/I_{W_{SV}}$ as in equation (C.16) for $\lambda_\varepsilon(z)$.

C.3.5. The mixed formulation involves again a second order system of ordinary equations (Box C.3-3) in terms of the two fields $\phi(z)$

and $\lambda_\varepsilon(z)$ alone, after eliminating the mixed fields $\varepsilon(z)$ and $\sigma(z)$. The two equations in the system (Box C.3-3) correspond again to the balance of torque and balance of warping stress resultants, respectively, as in Item C.2.3 for the previous RBV formulation.

C.3.6. Similarly, the restrainment of the warping at the fixed support $z = 0$ is accomplished by the boundary condition $\lambda_\varepsilon(0) = 0$. This is consistent with the (average) mixed treatment of the strain compatibility in the axial direction indicated in Item C.3.3 rather than the similar condition in Item C.2.6 for the RBV formulation that leads to a pointwise enforcement in that case. The rate of twist $\phi'(0)$ is again not involved in the restraining, avoiding altogether the "torque anomaly" of the TWKV formulation in Item C.1.4 so we do not have zero Saint–Venant stresses $\boldsymbol{\tau}_{SV}$ nor torque $T_{SV}(0)$, necessarily.

C.3.7. The warping shear and normal stresses in equations (Box C.3-6) and (Box C.3-7) are in equilibrium in the sense that they satisfy the three–dimensional equilibrium equation (C.15).

To conclude this summary list, we note that the normal stress σ_z predicted by each formulation will, in general, show different values (magnitude), but all three formulations share the same distribution shape over a cross section, namely, proportional to $n_E(x, y)\, W_{SV}(x, y)$, as given by equations (Box C.1-7), (Box C.2-7) and (Box C.3-7), respectively. The conditions (C.7) and (C.8) on this particular combination of functions assure then that no axial force and bending moments are associated to the normal axial stress σ_z, keeping all the arguments presented in this paper to the torsion problem of interest here. By the way, the condition (C.7) also assures the well–posedness of the Poisson problem (Box C.1-8) with pure Neumann boundary conditions.

Appendix C.3. The warping–twist constraint

The developments in the previous section identify the constrained character of the original TWKV formulation in two key ways. First, the resulting governing equation (Box C.1-3) for this formulation is a high order differential equation (fourth order to be specific) for the single driving field $\phi(z)$ in contrast to the second order system of differential equations (Box C.2-3) and (Box C.3-3) for that field $\phi(z)$ and an additional independent field, $\lambda(z)$ or $\lambda_\varepsilon(z)$, for the RBV and mixed formulations, respectively.

Secondly, and perhaps more revealing, the warping shear stresses $\boldsymbol{\tau}_{W}$ in (Box C.1-6) for the TWKV formulation arises solely from static considerations based on the equilibrium equation (C.15) with no explicit dependence on the driving field $\phi(z)$. Similarly, the bishear $T_{W}(z)$ in $(\text{Box C.1-5})_2$ is again given directly by the structural balance equation (C.14), with no explicit expression relating this stress resultant wit the driving field in a structural constitutive form involving the material and section parameters. This situation is to be contrasted again with the expressions of the warping stress $\boldsymbol{\tau}_{W}$ in (Box C.2-6) and (Box C.3-7) or of the bishear $T_{W}(z)$ in $(\text{Box C.2-5})_2$ and $(\text{Box C.3-5})_2$, all for the RBV and mixed formulations, respectively.

Pursuing further this last aspect, we can identify the absence of a warping shear strain associated to the basic kinematic assumption (Box C.1-1) of the TWKV formulation. Indeed, denoting the total shear strain by $\boldsymbol{\gamma} := \nabla u_z + \phi' \mathbb{J}$ and its Saint–Venant component by $\boldsymbol{\gamma}_{_{SV}} := \phi' \left(\nabla W_{_{SV}} + \mathbb{J} \right)$, the warping component $\boldsymbol{\gamma}_{_{W}}$ reads

$$\boldsymbol{\gamma}_{_{W}} := \boldsymbol{\gamma} - \boldsymbol{\gamma}_{_{SV}} = \begin{cases} 0 & (TWKV) \, , \\ -\left(\phi' - \lambda_{\varepsilon} \right) \nabla W_{_{SV}} & (RBV) \, , \\ \frac{I_{W_{SV}}}{I_{\nabla W_{\sigma}}} \left(\phi' - \lambda_{\varepsilon} \right) \nabla W_{\sigma} & (MIXED) \, . \end{cases} \tag{C.17}$$

This expression also indicates that the RBV and mixed formulations recovers that constrained situation when

$$\left\{ \, \lambda(z) \text{ or } \lambda_{\varepsilon}(z) \, \right\} = \phi'(z) \, , \tag{C.18}$$

for the RBV or mixed formulations, respectively. The statement (C.18) identifies what we referred to as the *warping–twist constraint*.

In order to characterize how the RBV and mixed formulations enforce the warping–twist constraint (C.18) in a limit process (or processes), we summarize here the variational principles behind each formulation, starting with the TWKV formulation whose governing equation (Box C.1-3) corresponds to the Euler–Lagrange equation of the functional

$$\Pi^{(TWKV)}(\phi) = \int_0^L \left[\frac{1}{2} \bar{G} J \left(\phi' \right)^2 + \frac{1}{2} \bar{E} I_{_{W_{SV}}} \left(\phi'' \right)^2 \right] dz + \Pi_{ext}(\phi) \, , \tag{C.19}$$

for the potential energy of the external loading $\Pi_{ext}(\phi) = -\int_0^L t_{ex}(z) dz - T_L \phi(L)$. Without loss of generality, we assume here a conservative loading

given by a distributed torque $t_{ex}(z)$ and tip torque T_L. The potential (C.19) is to be compared with the functionals

$$\Pi^{(RBV)}(\lambda,\phi) = \int_0^L \left[\frac{1}{2}\bar{G}J\big(\phi'\big)^2 + \frac{1}{2}\bar{G}I_{\nabla W_{SV}}\big(\phi'-\lambda\big)^2 + \frac{1}{2}\bar{E}I_{W_{SV}}\big(\lambda'\big)^2 \right] dz + \Pi_{ext}(\phi)\ , \qquad \text{(C.20)}$$

and

$$\Pi^{(MIX)}_{HW}(\phi,\lambda_\varepsilon,\varepsilon,\sigma) = \int_0^L \left[\frac{1}{2}\bar{G}J\big(\phi'\big)^2 + \frac{1}{2}\bar{G}\frac{\big(I_{W_{SV}}\big)^2}{I_{\nabla W_\sigma}}\big(\phi'-\lambda_\varepsilon\big)^2 + \frac{1}{2}\bar{E}I_{W_{SV}}\varepsilon^2 + I_{W_{SV}}\sigma\big(\lambda'_\varepsilon-\varepsilon\big) \right] dz + \Pi_{ext}(\phi)\ , \qquad \text{(C.21)}$$

behind the governing equations (Box C.2-3) and (Box C.3-3) for the RBV and mixed formulations, respectively. For the latter, the functional (C.21) is of the Hu–Washizu form, revealing the mixed treatment behind the assumed distributions (Box C.3-2) for the axial strain and stress, as well as the resulting weak compatibility relation for the axial strain parameter $\varepsilon(z) = \lambda'_\varepsilon(z)$. See Section 5.1 in the main report for a complete derivation motivated by the full three–dimensional mixed treatment.

Clearly now, we recover the original functional (C.19) of the TWKV formulation from the functionals (C.20) and (C.21) when the parameters

$$\kappa_t^{(RBV)} := \frac{I_{\nabla W_{SV}}}{J} \qquad \text{or} \qquad \kappa_t^{(MIX)} := \frac{\big(I_{W_{SV}}\big)^2}{J\ I_{\nabla W_\sigma}} \qquad \text{(C.22)}$$

for either the RBV or the mixed formulations approach the limit $\kappa_t \to \infty$, that is, they act as penalty parameters. As noted in Remarks 4.1 and 5.5, the three formulations will also meet in the limit for long shafts, where the first factor in all the three functionals (C.19), (C.20) and (C.21) dominates, producing effectively the Saint–Venant solution (with $\phi'(z) = \lambda(z) = \lambda_\varepsilon(z) =$ constant) for most of the shaft away from the local effects restraining the warping.

A look at the parameters (C.22) indicate their dependence on the geometry of the cross section (including the material distribution given by

the distributions $n_{_E}(x,y)$ and $n_{_G}(x,y)$ for composite sections) through the different combinations of the torsional constants for each of these two formulations. In fact, we can observe that we recover the mixed formulation from the RBV formulation by replacing $I_{\nabla W_{SV}}$ by $(I_{W_{SV}})^2/I_{\nabla W_\sigma}$, an argument that also applies to the functionals (C.20) and (C.21), and governing equations in (Box C.2-3) and (Box C.3-3). Note, however, that this direct relation between these two formulations is only at the structural level, with each formulation producing completely different warping and stress distributions at the cross section level, with even the stresses being physically incorrect for the RBV formulation as noted above.

Furthermore, even at the structural level the RBV and mixed formulations are expected to produce different results despite the relation (C.23), especially given the result

$$\kappa_t^{(RBV)} \geq \kappa_t^{(MIX)} \ , \tag{C.23}$$

given that $(I_{W_{SV}})^2 \leq I_{\nabla W_{SV}} I_{\nabla W_\sigma}$, a result obtained in equation (187) of the main report from the Cauchy–Schwarz inequality.

Given the result (C.23), the RBV formulation predicts a stiffer structural response of the shaft when compared to the mixed formulation, with both of these formulations being overshadow in that respect by the original TWKV formulation given its constrained character. It is precisely one of the main objectives of the current work to evaluate these features of the three formulations under study, confirming and quantifying these results for different cross sections topologies, especially in the thin–wall limit (hence the notation employed for the parameter κ_t for a thickness t).

In particular, the numerical evaluations presented in this report show that the limit process $\kappa_t \to \infty$ is indeed obtained for open (simply–connected) in the thin–wall limit $t/h \to 0$, but not in closed (multiply–connected) sections. Hence, the discrepancy among the different formulations can quite significant for solid/closed sections. Complete details for the different section configurations can be found in the main report.

Acknowledgments

I would like to thank Sanjay Govindjee for enlightening discussions on the general topic of torsion and, specifically, for his help in digging out the original German literature on the subject.

References

Benscoter, S. U. [1954], "A Theory of Torsion Bending for Multi-Cell Beams", *J. Appl. Mech.*, **20**, 25–34.

Bredt, R. [1896], "Kritische Bemerkungen zur Drehunfselasticität", *Zeitschrift des Vereins deutscher Ingenieure*, **40**, 785–790, 813–817, (in German).

Burgoyne, C. J. & Brown, E. H. [1994], "Nonuniform Elastic Torsion", *Int. J. Mech. Sci.*, **36**, 23–38.

Connor, J. J. [1976], *Analysis of Structural Member Systems*, The Ronald Press Company, New York.

Coulomb, C. A. [1784], "Recherches Théoriques et Expérimentales sur la Force de Torsion et sur l'Élasticité des fils de métal", *Mém. Acad. Sci.*, 229–269, (in French).

Davini, C.; Paroni, R. & Puntel, E. [2008], "An Asymptotic Approach to the Torsion Problem in Thin Walled Beams", *J. Elasticity*, **93**, 149–176.

Epstein, M. & Segev, R. [2019], "Vlasov's Beam Paradigm and Multivector Grassmann Statics", *Math. Mech. Solids*, **24**, 3167–3179.

Föppl, A. [1917], "Der Drillungswiderstand von Walzeisenträgern", *Zeitschrift des Vereins deutscher Ingenieure*, **60**, 694–695, (in German).

Gjelsvik, A. [1981], *The Theory of Thin Walled Bars*, John Wiley and Sons, New York.

Goodier, J. N. [1942], "Torsional and Flexural Buckling of Bars of Thin-Walled Open Section Under Compressive and Bending Loads", *J. Appl. Mech., Trans. ASME*, **9**, A103–107.

Gruttmann, F.; Sauer, R. & Wagner, W. [2000], "Theory and Numerics of Three-Dimensional Beams with Elastoplastic Material Behavior", *Int. J. Num. Meth. Engr.*, **48**, 1675–1702.

Kappus, R. [1938], "Twisting Failure of Centrally Loaded Open-Section Columns in the Elastic Range", Technical Memorandum no. 851, National Advisory Committee for Aeronautics, Washington, D.C.

Kármán, T. v. & Christensen, N. B. [1944], "Methods of Analysis for Torsion with Variable Twist", *J. Aero. Sci.*, **11**, 110–124.

Oden, J. T. & Ripperger, A. E. [1981], *Mechanics of Elastic Structures*, Hemisphere, Washington, D.C., 2nd edition.

Pilkey, W. D. [2002], *Analysis and Design of Elastic Beams*, John Wiley and Sons, New York.

Popov, E. P. [1970], "Kelvin's Solution of Torsion Problem", *ASCE J. Eng. Mech.*, **96**, 1005–1012.

Prandtl, L. [1903], "Zur Torsion von Prismatischen Stäben", *Phys. Zeitschr.*, **4**, 758–770.

Reissner, E. [1952], "On Non-Uniform Torsion of Cylindrical Rods", *Journal of Mathematics and Physics*, **31**, 214–221.

Reissner, E. [1983], "On a Simple Variational Analysis of Small Finite Deformations of Prismatical Beams", *Journal of Applied Mathematics and Physics (ZAMP)*, **34**, 642–648.

Saint-Venant, B. [1855], *Mémoire sur la Torsion des Prismes*, Mém. Savants Étrangers, Paris, (in French).

Salmon, C. G.; Johnson, J. E. & Malhas, F. A. [2009], *Steel Structures, Design and Behavior*, Prentice Hall, Upper Saddle River, NJ, 5th edition.

Seaburg, P. A. & Carter, C. J. [1997], *Torsional Analysis of Structural Steel Members*, Steel Design Guide Series 9, American Institute of Steel Construction, 2nd printing 2003.

Simo, J. C.; Armero, F. & Taylor, R. L. [1993], "Improved Tri-Linear Versions of Assumed Enhanced Strain Elements for 3D Finite Deformation Problems", *Comp. Meth. Appl. Mech. Engr.*, **110**, 359–386.

Simo, J. C. & Vu-Quoc, L. [1991], "A Geometricall-Exact Rod Model Incorporating Shear and Torsion-Warping Deformation", *Int. J. Solids Struct.*, **27**, 371–393.

Sokolnikoff, I. S. [1956], *Mathematical Theory of Elasticity*, McGraw-Hill, New York, 2nd edition.

Thompson, W. L. K. & Tait, P. G. [1903], *Tretatise on Natural Philosophy, Part II*, Cambridge University Press, London.

Timoshenko, S. P. [1905], "Torsional Vibrations of Shafts", *Proc. St. Petersburg Polytechnical Institute*, **3**, 397–406, (in Russian).

Timoshenko, S. P. [1906], "Lateral Buckling of I-beams under the Influence of Forces Acting in the Plane of largest Rigidity", *Proc. St. Petersburg Polytechnical Institute*, **4-5**, 151–219, 3–34, 262–292, (in Russian).

Timoshenko, S. P. [1910], "Einige Stabilitätsprobleme der Elastizitätstheorie", *Zeitschrift fur angew. Math. und Phys. (ZAMP)*, **58**, 337–385, (in German).

Timoshenko, S. P. & Gere, J. M. [1961], *Theory of Elastic Stability*, McGraw-Hill, New York, 2nd edition.

Timoshenko, S. P. & Goodier, J. N. [1951], *Theory of Elasticity*, McGraw-Hill, New York.

Trefftz, E. [1935], "Über den Schubmittelpunkt in einem durch eine Einzellast gebogenen Balken", *Z. angew. Math. Mech.*, **55**, 220–225, (in German).

Vlasov, V. Z. [1961], *Thin-Walled Elastic Beams*, Israel Program for Scientific Translations Ltd., Jerusalem, first Russian edition (1940).

Wagner, H. [1936], "Torsion and Buckling of Open Sections", Technical Memorandum no. 807, National Advisory Committee for Aeronautics, Washington, D.C.

Washizu, K. [1982], *Variational Methods in Elasticity and Plasticity*, Pergamon Press, Oxford, 3rd edition.

Weinstein, A. [1947], "The Center of Shear and the Center of Twist", *Quart. Appl. Math.*, **5**, 97–99.

Young, W. C.; Budynas, R. & Sadegh, A. M. [2012], *Roark's Formulas for Stress and Strain*, McGraw Hill, New York, 8th edition.

Zbirohowski-Koscia, K. [1967], *Thin Walled Beams*, Crosby Lockwood and Son Ltd., London.

List of Figures

List of Tables

List of Boxes